

**CONSTITUTIVE MODELING AND FINITE
ELEMENT ANALYSIS OF THE DYNAMIC
BEHAVIOR OF SHAPE MEMORY ALLOYS**

by

BIJAN AZADI BORUJENI

**B.Sc., Sharif University of Technology, 2001
M.Sc., Sharif University of Technology, 2003**

**A THESIS SUBMITTED IN PARTIAL FULFILLMENT OF THE
REQUIREMENTS FOR THE DEGREE OF
DOCTOR OF PHILOSOPHY**

in

THE FACULTY OF GRADUATE STUDIES

(Mechanical Engineering)

THE UNIVERSITY OF BRITISH COLUMBIA

(Vancouver)

April 2008

© Bijan Azadi Borujeni, 2008

Abstract

Previous experimental observations have shown that the pseudoelastic response of NiTi shape memory alloys (SMA) is localized in nature and proceeds through nucleation and propagation of localized deformation bands. It has also been observed that the mechanical response of SMAs is strongly affected by loading rate and cyclic degradation. These behaviors significantly limit the accurate modeling of SMA elements used in various devices and applications. The aim of this work is to provide engineers with a constitutive model that can accurately describe the dynamic, unstable pseudoelastic response of SMAs, including their cyclic response, and facilitate the reliable design of SMA elements.

A 1-D phenomenological model is developed to simulate the localized phase transformations in NiTi wires during both loading and unloading. In this model, it is assumed that the untransformed particles located close to the transformed regions are less stable than those further away from the transformed regions. By consideration of the thermomechanical coupling among the stress, temperature, and latent heat of transformation, the analysis can account for strain-rate effects.

Inspired by the deformation theory of plasticity, the 1-D model is extended to a 3-D macromechanical model of localized unstable pseudoelasticity. An important feature of this model is the reorientation of the transformation strain tensor with changes in stress tensor. Unlike previous modeling efforts, the present model can also capture the propagation of localized deformation during unloading. The constitutive model is implemented within a 2-D finite element framework to allow numerical investigation of the effect of strain rate and boundary conditions on the overall mechanical response and evolution of localized transformation bands in NiTi strips. The model successfully captures the features of the transformation front morphology, and pseudoelastic response of NiTi strip samples observed in previous experiments. The 1-D and 3-D constitutive models are further extended to include the plastic deformation and degradation of material properties as a result of cyclic loading.

Table of Contents

Abstract	ii
List of Tables	vi
List of Figures	vii
List of Nomenclature and Abbreviations	xiii
Acknowledgements	xvii
Dedication	xviii
Co-Authorship Statement	xix
Chapter 1: Introduction	1
1.1. Macroscopic Behavior and Applications of Shape Memory Alloys.....	1
1.1.1. SMAs as actuators and sensors.....	3
1.1.2. Vibration control and seismic protection using SMAs	4
1.1.3. Medical applications of NiTi	5
1.2. Metallurgical Aspects and Thermomechanical Properties of SMAs	6
1.2.1. Microscopic origin of superelasticity and shape memory effect	6
1.2.2. Thermal sensitivity of SMAs behaviors	9
1.2.3. Instability and Lüders-like deformation in NiTi SMAs.....	12
1.2.4. Strain dependence of pseudoelastic behavior	19
1.2.5. Strain-rate sensitivity of SMAs.....	22
1.2.6. Effect of cyclic loading on pseudoelastic behavior	24
1.3. Constitutive Modeling of SMAs	28
1.3.1. Modeling of stable pseudoelastic behavior.....	29
1.3.2. Modeling of the unstable pseudoelastic behavior	34
1.4. Objective and Scope.....	37
1.5. Bibliography	39
Chapter 2: One-Dimensional Constitutive Model	49
2.1. Introduction.....	49
2.2. Constitutive Relations.....	52
2.2.1. Introduction of local martensitic fraction	52
2.2.2. Strain decomposition	54
2.2.3. Nucleation and evolution of transformation	57
2.2.4. Heat of transformation.....	63

2.3.	Numerical Examples	64
2.3.1.	Finite element model	65
2.3.2.	Displacement-controlled loading-unloading.....	69
2.3.3.	Temperature-induced transformation at constant stress.....	85
2.3.4.	Relaxation and restrained recovery in a partially transformed wire	90
2.4.	Bibliography	94
Chapter 3: Three-dimensional Constitutive Model.....		96
3.1.	Introduction.....	96
3.2.	General Remarks on Modeling of Reversible Inelastic Deformation	98
3.3.	A Total Deformation Constitutive Model	103
3.3.1.	General considerations.....	104
3.3.2.	Constitutive relation of transformation strain	105
3.3.3.	Kinetics of transformation	108
3.3.4.	Heat of transformation	114
3.4.	FEM Simulations	116
3.4.1.	Quasi-static extension of a short NiTi strip	116
3.4.2.	Effect of heat generation and loading rate	131
3.4.3.	Effect of boundary conditions	153
3.5.	Bibliography	155
Chapter 4: Modeling of Cyclic Effects.....		159
4.1.	Introduction.....	159
4.2.	Modification of the One-Dimensional Constitutive Model	162
4.2.1.	General considerations and stress-strain relationship	162
4.2.2.	Kinetics of transformation	166
4.2.3.	Heat of transformation.....	169
4.3.	Modification of the Three-Dimensional Constitutive Model.....	169
4.3.1.	General considerations and stress-strain relationship	169
4.3.2.	Kinetics of transformation	171
4.3.3.	Heat of transformation	173
4.4.	Numerical Simulations.....	173
4.4.1.	One-dimensional simulation of NiTi wire	173
4.4.2.	Three-dimensional simulation of the wire	197
4.5.	Bibliography	205
Chapter 5: Summary and Conclusions.....		208
5.1.	Summary of Model Development.....	208
5.2.	Conclusions.....	209
5.3.	Proposed Future Work	213

Appendix A. Details of Calculations Based on the Transformation Evolution Rule (One-Dimensional Model)	216
A.1. Forward Transformation	216
A.2. Reverse Transformation	220
Appendix B. Outline of Experiments	222
B.1. Displacement-Controlled Extension of NiTi wire (Shaw and Kyriakides, 1995).....	222
B.2. Uniaxial Tension of NiTi Strip (Shaw and Kyriakides, 1997).....	224
Appendix C. Finite Element Formulations.....	226
C.1. The Finite Element Formulations of Solid Continuum.....	226
C.2. Finite Element Formulations of Heat Transfer Problem.....	229
Appendix D. Numerical Solution of the Three-Dimensional Constitutive Relations.....	232
Appendix E. An Incremental Three-Dimensional Constitutive Model.....	236
E.1. General considerations.....	236
E.2. Flow rule of forward transformation.....	236
E.3. Flow rule of reverse transformation.....	238
E.4. Kinetics of transformation	240
Appendix F. Convergence Study of the Finite Element Solution.....	242

List of Tables

Table 2-1. Thermo-physical properties of the NiTi wire and ambient	68
Table 3-1. Summary of the constitutive model.	112
Table 3-2. Mechanical properties of the short NiTi strip at 25 °C.	118
Table 3-3. Mechanical and thermal properties of the NiTi strip.	139
Table 4-1. Mechanical and thermal properties of the NiTi wire	179
Table E-1. Summary of the incremental constitutive model.	241
Table F-1. Approximate CPU times for various mesh densities.	242

List of Figures

Figure 1-1. Schematic presentation of the thermomechanical behavior of SMAs at (a) low temperature (shape memory effect), and (b) high temperature (superelasticity).....	2
Figure 1-2. The principle of shape memory actuation. (a) Low temperature; (b) High temperature.	3
Figure 1-3. Temperature-induced transformation at zero stress.....	7
Figure 1-4. Schematic illustration of the austenite and martensite lattice structures, and different self-accommodation mechanisms. (a) Austenite; (b) Martensite without self-accommodation; (c) Self-accommodated martensite by twinning; (d) Self-accommodated martensite by slip.....	8
Figure 1-5. Influence of temperature and thermal history on mechanical behavior of SMAs. (a) $T < M_f$ or twinned martensite at $M_f < T < A_s$; (b) Austenite at $M_s < T < A_s$; (c) $T > A_f$; (d) $T_{plastic} < T$	10
Figure 1-6. The sensitivity of transition stresses to temperature in $Ti_{51\%}Ni$ wire specimens (adapted from Miyazaki et al., 1981a).....	12
Figure 1-7. Deformation localization (Lüders-like deformation) during stress-induced transformation in NiTi wire	13
Figure 1-8. Transformation fronts during uniaxial extension of NiTi strips. (a) Straight, inclined fronts; (b) Finger-type fronts.	15
Figure 1-9. Stress peak and valley at the onset of instability during the isothermal pseudoelastic response of NiTi wires (adapted from Iadicola and Shaw, 2002a).....	15
Figure 1-10. Various localization patterns observed during uniaxial loading/unloading of NiTi micro-tubes. (a) Initial helical band; (b) Cylindrical domain with branched fronts (adapted from Feng and Sun, 2006);.....	17
Figure 1-11. Dependence of the pseudoelastic responses of NiTi on the maximum applied strain.	20
Figure 1-12. The pseudoelastic response of NiTi wire at various strain rates (adapted from Leo et al., 1993).....	22
Figure 1-13. Effect of cyclic loading on pseudoelastic behavior of NiTi (reproduced with permission from Tobushi et al., 2005).	25
Figure 1-14. Effect of deformation localization on the cyclic behavior of a NiTi wire. (a) Full pseudoelastic loop in the first cycle; (b) 100 th pseudoelastic loop during the partial cyclic loading to a maximum strain of 3.3%; (c) Full pseudoelastic loop after 100 cycles to a maximum strain of 6% (adapted from Miyazaki et al., 1981b).	27

Figure 1-15. Trilinear stress-strain response used in the plasticity model of Shaw and Kyriakides (1998).....	36
Figure 2-1. Pseudoelasticity in NiTi shape memory alloy. (a) Isothermal quasi-static displacement-controlled response; (b) Stress-strain response at high strain rate; (c) Variation of transformation stresses with temperature (Shaw and Kyriakides, 1995).	50
Figure 2-2. A partially transformed one-dimensional element.....	53
Figure 2-3. Variations of stress-plateau length and transformation strain with temperature.	56
Figure 2-4. (a) Nucleation and propagation stresses during displacement-controlled tests of NiTi dog-bone strips (experimental data adapted from Shaw, 2000). (b) Schematic representation of nucleation and finish lines used in the model.....	58
Figure 2-5. Finite element discretization of the wire.....	66
Figure 2-6. Heat transfer mechanisms in a one-dimensional element.....	66
Figure 2-7. Nucleation and finish lines used in the simulations.....	69
Figure 2-8. Simulation of the pseudoelastic behavior of the NiTi wire at $\dot{\delta}/L_G = 4 \times 10^{-5} \text{ s}^{-1}$ in 70 °C water. (a) Stress-strain response (Experimental results adapted from Shaw and Kyriakides, 1995); (b) Temperature profiles.....	70
Figure 2-9. Evolution of A→M and M→A transformations in the pseudoelastic response of the NiTi wire at $\dot{\delta}/L_G = 4 \times 10^{-5} \text{ s}^{-1}$ in 70 °C water. (a) Simulation; (b) Experiment (adapted from Shaw and Kyriakides, 1995).....	71
Figure 2-10. Simulation of the pseudoelastic behavior of the NiTi wire at $\dot{\delta}/L_G = 4 \times 10^{-4} \text{ s}^{-1}$ in 70 °C water. (a) Stress-strain response (Experimental results adapted from Shaw and Kyriakides, 1995); (b) Temperature profiles.....	74
Figure 2-11. Evolution of A→M and M→A transformations in the pseudoelastic response of the NiTi wire at $\dot{\delta}/L_G = 4 \times 10^{-4} \text{ s}^{-1}$ in 70 °C water. (a) Simulation; (b) Experiment (adapted from Shaw and Kyriakides, 1995).....	75
Figure 2-12. Simulation of the transformation behavior of the NiTi wire at $\dot{\delta}/L_G = 4 \times 10^{-3} \text{ s}^{-1}$ in 70 °C water. (a) Evolution of transformation; (b) Temperature profiles.	77
Figure 2-13. Random deviation from the original cross-sectional area along the wire gauge length. .	78
Figure 2-14. Pseudoelastic behavior of the NiTi wire at $\dot{\delta}/L_G = 4 \times 10^{-3} \text{ s}^{-1}$ in 70 °C water based on simulation and experiment (experimental response adapted from Shaw and Kyriakides, 1995).79	

Figure 2-15. Simulation of the transformation behavior of the NiTi wire at $\dot{\delta}/L_G = 4 \times 10^{-3} \text{ s}^{-1}$ in 70 °C water. (a) Temperature profiles; (b) Evolution of transformation.	80
Figure 2-16. Pseudoelastic behavior of the NiTi wire at $\dot{\delta}/L_G = 4 \times 10^{-2} \text{ s}^{-1}$ in 70 °C water based on simulation and experiment (experimental response adapted from Shaw and Kyriakides, 1995).	81
Figure 2-17. Simulation of the transformation behavior of the NiTi wire at $\dot{\delta}/L_G = 4 \times 10^{-2} \text{ s}^{-1}$ in 70 °C water. (a) Temperature profiles; (b) Evolution of transformation.	83
Figure 2-18. The pseudoelastic response of the wire at various strain rates in 70 °C water. (a) Simulations; (b) Experiments.	84
Figure 2-19. Thermomechanical responses of the wire subjected to ambient cooling under constant stress ($\dot{T}_\infty = -2 \times 10^{-2} \text{ }^\circ\text{C s}^{-1}$). (a) Evolution of transformation; (b) Temperature profiles; (c) Strain response.	86
Figure 2-20. Thermomechanical responses of the wire subjected to ambient cooling under constant stress ($\dot{T}_\infty = -2 \times 10^{-1} \text{ }^\circ\text{C s}^{-1}$). (a) Evolution of transformation; (b) Temperature profiles; (c) Strain response.	88
Figure 2-21. Thermomechanical responses of the wire subjected to ambient cooling under constant stress ($\dot{T}_\infty = -5 \times 10^{-1} \text{ }^\circ\text{C s}^{-1}$). (a) Evolution of transformation; (b) Temperature profiles; (c) Strain response.	89
Figure 2-22. The strain response of the wire versus ambient temperature.	90
Figure 2-23. Simulation of relaxation in a partially transformed NiTi wire. (a) Evolution of transformation. (b) Stress response; (c) Time history of strain and ambient temperature.	92
Figure 2-24. Simulation of constrained recovery in a partially transformed NiTi wire. (a) Evolution of transformation. (b) Stress response; (c) Time history of strain and ambient temperature.	93
Figure 3-1. A continuum region occupied by an SMA.	100
Figure 3-2. Loading-unloading path in the stress space.	101
Figure 3-3. (a) Geometry and finite element discretization of the strip; (b) Corner imperfection.	117
Figure 3-4. Local uniaxial engineering stress-strain response of NiTi used in the simulation.	119
Figure 3-5. Nominal stress-strain response of the NiTi short strip.	120
Figure 3-6. Sequence of martensitic fraction contours during loading.	121
Figure 3-7. Sequence of logarithmic axial strain distribution during loading.	122

Figure 3-8. Sequence of martensitic fraction contours during unloading.	123
Figure 3-9. Distributions of effective stress at selected loading/unloading stages. (a) Loading; (b) Unloading	124
Figure 3-10. Variations of martensitic fraction, stress, and transformation strain at Point 1 and Point 2.	126
Figure 3-11. Nominal stress-strain response of the NiTi short strip based on the incremental constitutive model (Appendix E).....	127
Figure 3-12. Predicted evolution of transformation based on the incremental constitutive model (Appendix E). (a) Loading; (b) Unloading	129
Figure 3-13. Predicted distributions of equivalent stress based on the incremental constitutive model (Appendix E). (a) Loading; (b) Unloading	130
Figure 3-14. Geometry and finite element discretization of the dog-bone sample.....	132
Figure 3-15. Geometry and finite element discretization of the sample used for the calibration of the model in reverse transformation	135
Figure 3-16. Chosen 2nd Piola-Kirchhoff nucleation and completion stresses and their equivalent engineering values as determined by isothermal simulations.....	136
Figure 3-17. Local isothermal 1-D stress-strain behavior of SMA according to the constitutive model.	136
Figure 3-18. Pseudoelastic response of NiTi strip under isothermal conditions. (a) $T = 15\text{ }^{\circ}\text{C}$; (b) $T = 25\text{ }^{\circ}\text{C}$; (c) $T = 35\text{ }^{\circ}\text{C}$ (Experimental data are taken from Shaw, 2000).....	138
Figure 3-19. Pseudoelastic response of NiTi strip at $\dot{\delta}/L_G = 10^{-4}\text{ s}^{-1}$. Experimental data are taken from Shaw and Kyriakides (1997).	141
Figure 3-20. Sequence of events during forward transformation at $\dot{\delta}/L_G = 10^{-4}\text{ s}^{-1}$. (a) Martensitic fraction; (b) Temperature.....	142
Figure 3-21. Details of front morphology evolution during nucleation of forward transformation. (a) Distribution of phases; (b) Distorted mesh with lateral displacement multiplied by a factor of 20; (c) Bending moment at the upper end.....	143
Figure 3-22. Sequence of events during reverse transformation at $\dot{\delta}/L_G = -10^{-4}\text{ s}^{-1}$. (a) Martensitic fraction; (b) Temperature.....	145
Figure 3-23. Pseudoelastic response of NiTi strip at $\dot{\delta}/L_G = 10^{-3}\text{ s}^{-1}$. Experimental data are taken from Shaw and Kyriakides (1997).	147

Figure 3-24. Sequence of events during forward transformation at $\dot{\delta}/L_G = 10^{-3} \text{ s}^{-1}$. (a) Martensitic fraction; (b) Temperature.....	148
Figure 3-25. Sequence of events during reverse transformation at $\dot{\delta}/L_G = -10^{-3} \text{ s}^{-1}$. (a) Martensitic fraction; (b) Temperature.....	149
Figure 3-26. The simulated pseudoelastic response of NiTi strip at various elongation rates.	150
Figure 3-27. Sequence of events during forward transformation at $\dot{\delta}/L_G = 5 \times 10^{-3} \text{ s}^{-1}$. (a) Martensitic fraction; (b) Temperature.....	151
Figure 3-28. Sequence of events during reverse transformation at $\dot{\delta}/L_G = -5 \times 10^{-3} \text{ s}^{-1}$. (a) martensitic fraction; (b) temperature.	152
Figure 3-29. Transformation behavior of the specimen with misaligned grips during reverse transformation at $\dot{\delta}/L_G = -10^{-4} \text{ s}^{-1}$	155
Figure 4-1. (a) Experimental setup (adapted from Iadicola and Shaw, 2002a); (b) Finite element model.	174
Figure 4-2. Initial temperature distribution along the wire length (experimental data taken from Iadicola and Shaw, 2002a).....	181
Figure 4-3. Nominal stress-strain response of the NiTi wire during cyclic loading at $T_T = 16.5 \text{ }^\circ\text{C}$. (a) Simulation (b) Experiment (reproduced with permission from Iadicola and Shaw, 2002a).	182
Figure 4-4. Change in propagation stress relative to cycle 1 during cyclic loading at $T_T = 16.5 \text{ }^\circ\text{C}$. (a) Forward transformation; (b) Reverse transformation.	183
Figure 4-5. Evolution of (a) phases, and (b) nominal stress with cycles at $T_T = 16.5 \text{ }^\circ\text{C}$ (simulation).	185
Figure 4-6. Time history of stress during selected cycles.	188
Figure 4-7. (a) Infrared images of temperature variation at selected cycles (reproduced with permission from experiments of Shaw and Kyriakides, 2002a); (b) Simulated profiles of temperature variation during cyclic loading at $T_T = 16.5 \text{ }^\circ\text{C}$	189
Figure 4-8. Nominal stress-strain response of the NiTi wire under cyclic loading at $T_T = 24.6 \text{ }^\circ\text{C}$. (a) Simulation (b) Experiment (reproduced with permission from Iadicola and Shaw, 2002a).	191
Figure 4-9. Change in propagation stress relative to cycle 1 during cyclic loading at $T_T = 24.6 \text{ }^\circ\text{C}$. (a) Forward transformation; (b) Reverse transformation.	192

Figure 4-10. Evolution of (a) phases, and (b) nominal stress with cycles at $T_T = 24.6 \text{ }^\circ\text{C}$ (simulation).	194
Figure 4-11. (a) Infrared images of temperature variation at selected cycles (reproduced with permission from experiments of Shaw and Kyriakides, 2002a); (b) Simulated profiles of temperature variation during cyclic loading at $T_T = 24.6 \text{ }^\circ\text{C}$	196
Figure 4-12. Geometry of the wire and axisymmetric finite element mesh.	198
Figure 4-13. The nominal stress-strain response of the NiTi wire.	200
Figure 4-14. Sequence of martensitic fraction contours. (a) Loading; (b) Unloading.....	202
Figure 4-15. (a) Distribution of phases before the coalescence event; (b) Distributions of effective stress corresponding to figure (a); (c) Distributions of effective stress after the coalescence... ..	203
Figure 4-16. (a) Axial strain, $\varepsilon_x^{(p)}$; (b) Radial strain, $\varepsilon_r^{(p)}$; (c) Shear strain, $\gamma_{rx}^{(p)}$; (d) Hoop strain, $\varepsilon_\theta^{(p)}$	204
Figure A-1. Calculation of incremental changes during the forward transformation (elastic prediction and transformation correction).	217
Figure A-2. Calculation of incremental changes during the reverse transformation (elastic prediction and transformation correction).	221
Figure F-1. Distribution of martensitic fraction at selected loading stages.	243

List of Nomenclature and Abbreviations

t	Time
u, v, w	Displacement components
T	Temperature
M_s	Martensite start temperature
M_f	Martensite finish temperature
A_s	Austenite start temperature
A_f	Austenite finish temperature
γ	Martensitic fraction
λ	Cyclic identifier
σ	Uniaxial stress
$\boldsymbol{\sigma}, \sigma_{ij}$	Stress tensor
\mathbf{S}, S_{ij}	Deviatoric stress tensor
ε	Total uniaxial strain
$\boldsymbol{\varepsilon}, \varepsilon_{ij}$	Total strain tensor
$\varepsilon^{(e)}$	Uniaxial elastic strain
$\boldsymbol{\varepsilon}^{(e)}, \varepsilon_{ij}^{(e)}$	Tensor of elastic strain
$\varepsilon^{(t)}$	Uniaxial transformation strain

$\boldsymbol{\varepsilon}^{(t)}, \varepsilon_{ij}^{(t)}$	Tensor of transformation strain
$\varepsilon^{(p)}$	Uniaxial permanent strain
$\varepsilon_p^{(\infty)}$	Maximum permanent strain at cyclic saturation
$\boldsymbol{\varepsilon}^{(p)}, \varepsilon_{ij}^{(p)}$	Permanent/plastic strain tensor
$\Delta\varepsilon_t$	Maximum transformation-induced strain
$\Delta\varepsilon_t^{(0)}$	Maximum transformation-induced strain in the virgin material
$\Delta\varepsilon_t^{(\infty)}$	Maximum transformation-induced strain in the fully-trained material
$\Delta\varepsilon_p$	Cyclic plasticity multiplier
$\bar{\varepsilon}^{(t)}$	Effective transformation strain
$\tilde{\varepsilon}^{(t)}$	Path-dependent effective transformation strain
$\tilde{\varepsilon}^{(p)}$	Effective permanent strain
Q	Plastic potential function
P	Transformation potential function
\mathbf{C}, C_{ijkl}	Equivalent elastic stiffness tensor
\mathbf{D}, D_{ijkl}	Equivalent elastic compliance tensor
$\mathbf{D}^{(A)}, D_{ijkl}^{(A)}$	Elastic compliance tensor of austenite
$\mathbf{D}^{(M)}, D_{ijkl}^{(M)}$	Elastic compliance tensor of martensite

E_A	Elastic modulus of martensite
E_M	Elastic modulus of martensite
E	Effective elastic modulus of martensite-austenite mixture
σ_M	Instantaneous martensitic transformation stress
σ_{MN}	Martensite nucleation stress
σ_{MN}^*	Instantaneous martensite nucleation stress
σ_{MC}	Martensite completion stress
σ_{MF}	Martensite finish stress
σ_A	Instantaneous austenitic transformation stress
σ_{AN}	Austenite nucleation stress
σ_{AN}^*	Instantaneous austenite nucleation stress
σ_{AC}	Austenite completion stress
σ_{AF}	Austenite finish stress
$\Delta h_{A \rightarrow M}$	Stress-free enthalpy change during forward transformation
$\Delta h_{M \rightarrow A}$	Stress-free enthalpy change during reverse transformation
q_G	Generated heat
$u^{(i)}$	Specific internal energy
$u^{(e)}$	Elastic energy density

k	Thermal conductivity
C_p	Specific heat capacity
h_{conv}	Convective film coefficient
ρ	Mass density
a_λ, b_λ	Thermal parameters of cyclic deformation
SMA	Shape Memory Alloy
FE	Finite Element
FEM	Finite Element Method

Acknowledgements

I would like to express my sincere gratitude to my supervisor Prof. Nimal Rajapakse, for his guidance and support throughout my academic program. Without his encouragement and help this work would not have been possible. I am deeply indebted to Dr. Daan M. Maijer, whose insight and broad knowledge as the co-advisor have been of great value to me. His friendly advice and generous support are truly appreciated. I also would like to thank Prof. Mohamed S. Gadala, Prof. Reza Vaziri, and Prof. Farrokh Sassani who have provided useful comments, discussions, and encouragement during the course of this research.

This work has been supported by a grant from the Natural Science and Engineering Research Council of Canada, and by a fellowship from the University of British Columbia.

I am deeply grateful to my parents, Mansour and Zari, and my sisters, Elahe and Anna, for their constant love and inspiration throughout my life. I owe my warm gratitude to my friends at UBC, in particular Moritz Gadermann, Pirooz Darabi, Amer Ghavanini, Steven Ney, Ali Asadkarami, Chantal Beauregard, and Alfredo Franco-Cea.

To my beloved parents

Co-Authorship Statement

Some parts of this PhD dissertation have been published in scientific journals, or will be submitted for publication. With the exception of the PhD supervisors Prof. Nimal Rajapakse and Dr. Daan Maijer, who offered advice on analytical methods, numerical procedures, and interpretation of results, Bijan Azadi Borujeni is the primary contributor to the present work. During the course of this work, he conducted literature review, developed constitutive models, performed numerical simulations, compiled the results, prepared the text, and implemented the suggestions and/or corrections provided by the supervisors.

Chapter 1: Introduction

Owing to their unique thermomechanical behavior, shape memory alloys (SMAs) are being increasingly used in many engineering applications ranging from actuators and dampers, to medical devices, and orthodontic wires. Acquiring a thorough understanding of SMAs behavior has therefore been the subject of extensive research since the material was first discovered by Chang and Read (1951). In the next few sections, a detailed description of the extraordinary behavior of SMAs, and a survey of the state-of-the-art in material modeling and related challenges are presented.

1.1. MACROSCOPIC BEHAVIOR AND APPLICATIONS OF SHAPE MEMORY ALLOYS

SMAs are often classified as smart (functional/adaptive) materials, due to their ability to sense small changes in the environmental conditions, such as temperature, and respond by altering their mechanical/physical properties. SMAs are characterized by two important thermomechanical properties known as *shape memory effect*, and *pseudoelasticity* (or *superelasticity*), which take place over different temperature ranges. Shape memory effect is the ability of material to recover its original shape after large inelastic deformations (up to 10 %) upon raising the temperature of material by only a few degrees (Wayman, 1981). This behavior is observed below a certain transition temperature. At higher temperatures, pseudoelastic behavior is observed during which the material can accommodate a very large inelastic strain characterized by a long stress-plateau during mechanical loading and recovery of all the applied deformation through a lower stress-plateau during unloading (Otsuka and Shimizu, 1981). These two behaviors are schematically shown in Figure 1-1. The crystalline structures of the material at various stages are also marked on the diagram which will be explained in the subsequent sections.

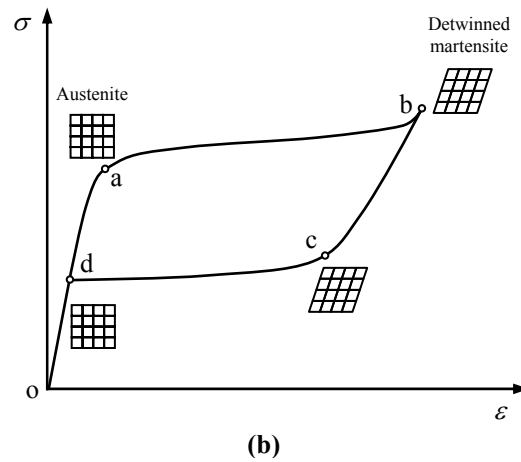
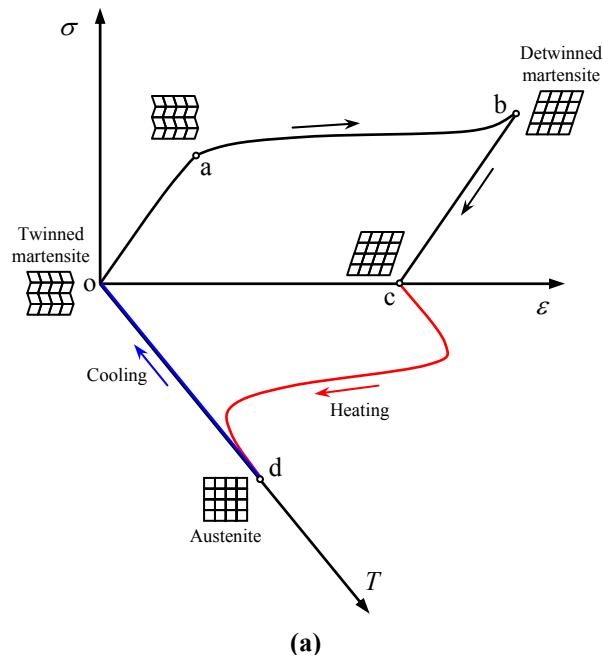


Figure 1-1. Schematic presentation of the thermomechanical behavior of SMAs at (a) low temperature (shape memory effect), and (b) high temperature (superelasticity).

Some examples of shape memory alloys are NiTi (also known as Nitinol), CuAlZn, CuAlZnMn, CuAlNi, and AuCd. Among these, NiTi is by far the most common SMA for practical applications in spite of its high cost. This is due to its exceptional strength and ductility, good fatigue

properties, high corrosion resistance, and excellent biocompatibility. Therefore, this research is mainly concerned with the thermomechanical behavior of NiTi.

The number of SMAs applications has become large, and a comprehensive overview is beyond the scope of this study. Only selected examples of the applications are briefly discussed here (for more examples see Duerig et al., 1990; Otsuka and Wayman, 1998; Van Humbeeck, 2001; Kohl, 2004).

1.1.1. SMAs as actuators and sensors

SMA actuators belong to the category of thermal actuators, which are capable of converting thermal energy into mechanical work. Since SMAs exhibit shape recovery over a large amount of strain, they can develop significant recovery stresses if they are restrained. The principles behind the application of SMA as actuators are shown in Figure 1-2. At low temperature (Figures 1-2a), the SMA can be easily deformed in the presence of a small biased force (represented by the spring in Figure 1-2). Upon heating, a solid-solid phase transformation takes place during which the material recovers its original shape and exerts a large amount of force if restrained (demonstrated by the stretched spring in Figure 1-2b). By cooling the actuator, the material transforms to its low-temperature phase again and releases the force (Figures 1-2a).

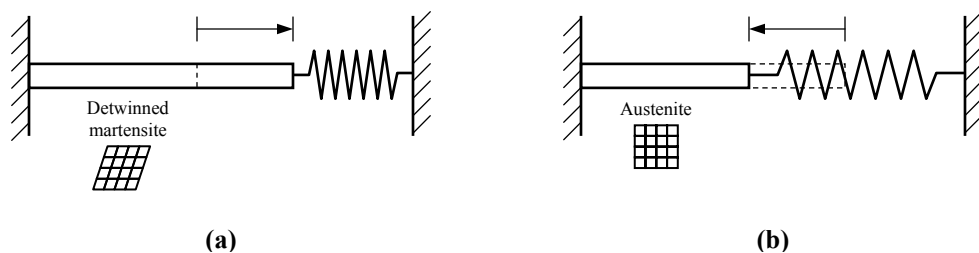


Figure 1-2. The principle of shape memory actuation. (a) Low temperature; (b) High temperature.

SMA actuators have been successfully used as electric switches for diesel engine radiator fans, thermostatic mixing valves, under-water robotic actuators (Ohkata and Suzuki, 1998), high pressure gas micro-valves (Kohl et al., 1999). SMA actuators are particularly attractive for aerospace applications due to their lightweight and small size (Jardine et al., 1997; Strelec et al., 2003). A recent example is Boeing's Variable Geometry Chevron which utilizes a NiTi actuator to reconfigure the shape of chevrons on the trailing edge of a jet engine to optimize nozzle performance for a variety of flight conditions (Calkins, 2006).

1.1.2. Vibration control and seismic protection using SMAs

The area enclosed by the pseudoelastic loop of Figure 1-1 is the dissipated mechanical work which converts to heat. Since SMAs display pseudoelastic hysteresis behavior over large strain ranges, a significant amount of energy dissipation can be obtained (Dolce and Cardone, 2001a,b). In recent years, considerable attention has been paid to the use of SMAs in the protection of structural systems against seismic loads, and also acoustic and vibration control of mechanical systems (see for example: Dolce et al., 2000; Saadat et al., 2001; Han et al., 2003; McCormick et al., 2006). Several types of seismic damping devices are available today; however, current technologies present some limitations mostly related to maintenance and reliability. Shape memory alloys have the potential to eliminate most of the limitations involved in current technologies, owing to their resistance to large strain cyclic fatigue, re-centering capability and high corrosion resistance. Bruno and Valente (2002) numerically compared the performance of a traditional damping system (steel-rubber damper) and SMA dampers. The analysis revealed that SMA dampers generally have better performance and less maintenance and functional costs. A state-of-the-art overview of different applications of NiTi SMAs in structural vibration control is given by Wilson and Wesolowsky (2005).

1.1.3. Medical applications of NiTi

The most commercially successful applications of NiTi SMAs in recent years have been in the biomedical engineering. The reason for this is the combination of biocompatibility, corrosion-resistance, and excellent pseudoelastic properties of NiTi which cannot be found in any other material.

An orthodontic arch wire made of NiTi was the first application in this field (Sachdeva and Miyazaki, 1990). In this application, the pseudoelastic property of NiTi is utilized as the material is capable of exerting a constant force over a large displacement range. This allows the NiTi arch wire to apply a constant force for a long time as the teeth gradually move. Stainless steel arch wires, on the other hand, quickly release the restoring force when teeth start moving.

NiTi tubes have been used as guide-wires in minimal invasive surgery (Song et al., 2003). Guide-wires are used to insert small surgical or endoscopic devices into the body for diagnostic or medical treatments. The superelastic property of NiTi provides an exceptional flexibility which prevents the guide-wire from being permanently deformed during the surgery.

A more recent application of NiTi is the self-expanding cardiovascular stent (Duerig et al., 2002). A stent is an intravascular tubular scaffold that supports the inner diameter of a blood vessel to prevent blockage. The NiTi stent is initially folded at a low temperature to occupy less space. As the stent enters the body, its temperature increases and the reverse transformation takes place which results in self-expansion and shape recovery. In some cases, the stent may also be compressed at a high temperature and then inserted into the body which will expand as it is released exhibiting pseudoelastic response.

NiTi elements are also largely used in orthopedic implants. In this application, the shape memory effect is exploited to exert compressive recovery forces on fractured bones or spinal

vertebrae to accelerate the healing process. A NiTi bone anchor, fixation nail, or bone staple is inserted at the fracture site in its low-temperature deformed phase, and then is heated by an external device. Upon heating, the material recovers its original shape and closes the gap.

1.2. METALLURGICAL ASPECTS AND THERMOMECHANICAL PROPERTIES OF SMAS

1.2.1. Microscopic origin of superelasticity and shape memory effect

Pseudoelasticity and shape memory effect in SMAs originate from a displacive (diffusionless) phase transformation between two solid phases called *austenite* and *martensite*. The transformation from austenite to martensite is often referred to as the *martensitic transformation* (or *forward transformation*), whereas the transformation from martensite to austenite is called the *austenitic transformation* or (*reverse transformation*).

The martensitic transformation and its inverse transformation can be induced by either changing the temperature or stress. In the absence of stress, an SMA material at high temperatures exists in the parent phase (austenite phase) and upon decreasing the temperature, the crystalline structure undergoes a phase transformation from austenite into martensite. The temperatures corresponding to the start and finish of the forward transformation in the stress-free condition are called the martensitic start and finish temperatures, which are denoted by M_s and M_f , respectively (see Figure 1-3). Similarly, the temperatures at which the reverse transformation starts and ends in the absence of stress are called the austenitic start and finish temperatures denoted by A_s and A_f , respectively. Since there is a hysteresis associated with the martensitic transformation in SMAs, the start and finish temperatures of forward and reverse transformations do not coincide. This hysteresis behavior is also shown in Figure 1-3. The parameter γ in Figure 1-3 indicates the extent of transformation and is called the *martensitic fraction*. Martensitic fraction by definition is the

volumetric fraction of martensite, i.e., it is equal to zero when the material is completely in the austenite phase and equal to one when the material is completely in the martensite phase. As shown, in a particular temperature range ($M_s < T < A_s$), both martensite and austenite phases are stable.

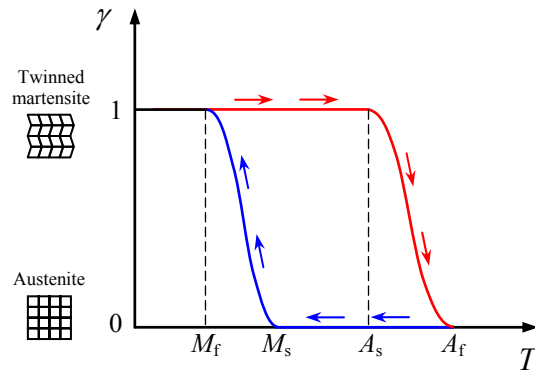


Figure 1-3. Temperature-induced transformation at zero stress.

The temperature-induced martensitic transformation in SMAs is a *self-accommodating* transformation. Self-accommodation is a mechanism by which the material preserves its original shape during the transformation and no macroscopic strain is produced as a result of the phase transformation in the stress-free condition. Since the lattice structures of austenite and martensite are of different shapes (Figure 1-4a and 1-4b), it is naturally expected that the newly produced martensite phase is stressed by the surrounding austenite phase due to strain mismatch. In order to accommodate itself inside the parent phase (self-accommodation), the martensite must undergo a severe deformation. In ordinary metals, such as steel, the self-accommodation is achieved through slip which is an irreversible process, and results in permanent deformation of martensite. In SMAs, the martensite phase has a low degree of lattice symmetry. As a result, the martensite phase can exist in multiple *variants* which are energetically equivalent but have different crystallographic orientations. This property allows for the formation of randomly distributed martensite variants at the microscopic

level (twinning), which gives rise to self-accommodation (Miyazaki et al., 1989a). The slip and twinning mechanisms of self-accommodation are schematically shown in Figure 1-4.

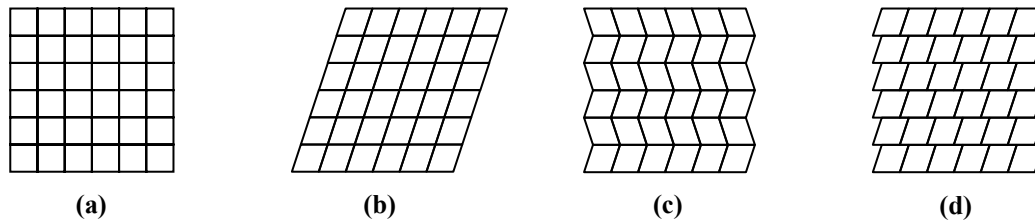


Figure 1-4. Schematic illustration of the austenite and martensite lattice structures, and different self-accommodation mechanisms. (a) Austenite; (b) Martensite without self-accommodation; (c) Self-accommodated martensite by twinning; (d) Self-accommodated martensite by slip.

The two adjacent martensitic plates with different crystallographic orientations (variants) are also called *twins* which are separated by a *twin boundary*. The ability of SMAs to exist in the twinned and detwinned martensitic states plays an important role in their observable macroscopic behaviors.

When shear stress is applied to a twinned martensite, the pairs of martensitic twins begin to convert into a single variant of martensite preferred by the direction of applied stress (Miyazaki et al., 1989b). This process is called *detwinning* or *reorientation*. During the detwinning process, a significant amount of strain is produced while the stress level remains almost constant (point “a” to “b” in Figure 1-1a). Unloading only recovers a small elastic strain, leaving the material with a large residual strain (point “c” in Figure 1-1a). If the temperature is increased, the material starts transforming from martensite back into austenite (point “c” to “d” in Figure 1-1a). Since the macroscopic strain associated with the austenite is the same as that of twinned martensite, the material recovers its original shape during the heating process (shape memory effect).

As mentioned earlier, the phase transformation may also be triggered by stress. To explain pseudoelasticity, consider an SMA material in the parent phase with $T > A_f$. When stress is applied to the austenite phase, the material initially behaves similar to a linear elastic solid (point “o” to “a” in

Figure 1-1b). At a critical stress level, the phase transformation from austenite into martensite initiates. Due to presence of stress during the transformation, the product phase is a single variant (detwinned) martensite which is oriented preferentially according to the direction of applied stress. As a result, a large amount of strain is produced during the stress-induced martensitic transformation in SMAs (point “a” to “b” in Figure 1-1b). During the unloading process, an inverse phenomenon takes place. The material deformation at the initial stages of unloading mainly consists of elastic deformations (point “b” to “c” in Figure 1-1b). The martensite phase loses its stability as the stress level drops to a critically low value. At this point, the inverse transformation starts and the martensite phase transforms back into austenite during which the transformation-induced strain is recovered (point “c” to “d” in Figure 1-1b). Similar to temperature-induced transformation, the stress-induced transformation also exhibits a hysteresis behavior which appears as the hysteresis loop shown in Figure 1-1b.

Further details on the crystallography of various SMAs and microscopic aspects of martensitic transformation, shape memory effect, and pseudoelasticity can be found in Miyazaki and Otsuka (1989), Miyazaki et al. (1989a,b), Otsuka and Wayman (1998), and Bhattacharya (2003).

1.2.2. Thermal sensitivity of SMAs behaviors

The mechanical behavior of SMAs is strongly dependent on temperature. This is primarily due to the fact that the initial microstructure of material (austenite/twinned martensite/detwinned martensite), and also the transformation stresses depend on temperature. Typical mechanical response of SMAs at various temperature ranges and initial conditions are schematically shown in Figure 1-5.

Below the martensitic finish temperature ($T < M_f$), the deformation mode for initially twinned martensite is mainly governed by the detwinning process. The stress-strain curves in this range exhibit a stress plateau associated with the martensite-to-martensite conversion (detwinning). The

residual strain after unloading is reversible by heating. The same type of mechanical behavior is also observed for twinned martensite in the range $M_f < T < A_s$. Experiments have shown that the flow stress for detwinning decreases with increasing temperature in NiTi alloys as shown in Figure 1-6 (Miyazaki et al., 1981a).

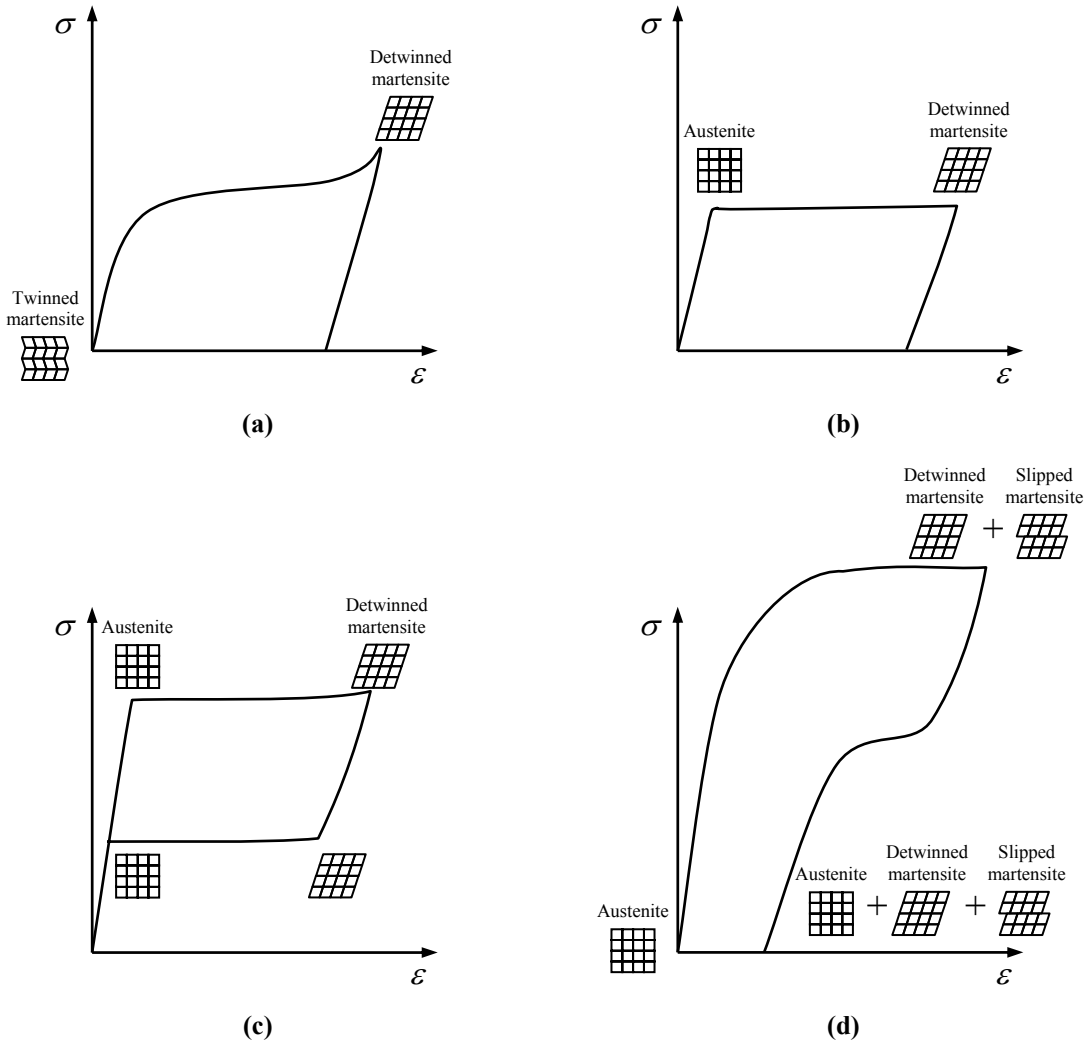


Figure 1-5. Influence of temperature and thermal history on mechanical behavior of SMAs. (a) $T < M_f$ or twinned martensite at $M_f < T < A_s$; (b) Austenite at $M_s < T < A_s$; (c) $T > A_f$; (d) $T_{plastic} < T$.

In the range $M_s < T < A_s$, when the material is initially in the austenitic phase, the stress-strain curve exhibits a plateau stress which corresponds to the stress-induced martensitic transformation.

The stress-induced transformation results in a large inelastic strain which remains after unloading (Figure 1-5b). The residual strain can only be recoverable by raising the temperature of material to above the austenite finish temperature (A_f). However, if the initial temperature is higher than the austenite finish temperature, i.e. $T > A_f$, the transformation strain is automatically recovered upon unloading due to reverse transformation (pseudoelastic behavior, Figure 1-5c). It is well known that the critical stresses at which the forward and reversing transformations start increase with increasing the temperature (Figure 1-6).

Above a certain limiting temperature (T_{plastic}), the stress required for inducing forward transformation becomes so high that plastic deformation through movement of dislocations and slip precedes the formation of stress-induced martensite. In that case, simultaneous plastic deformation and stress-induced transformation occur during loading. The introduction of plastic deformation creates an internal residual stress. The formation of an internal stress field by dislocations stabilizes the martensite, which prohibits the full transformation of martensite back to austenite during unloading. This results in a residual strain after unloading (Figure 1-5d). The residual strain consists of some permanent plastic deformation due to lattice slip, and some transformation strain associated with the residual pockets of detwinned martensite (Miyazaki et al., 1981a; Shaw and Kyriakides, 1995). The residual strain can be partially recovered by heating as the residual martensite transforms to austenite, but when the material is cooled the residual strain returns to its previous value (Shaw and Kyriakides, 1995).

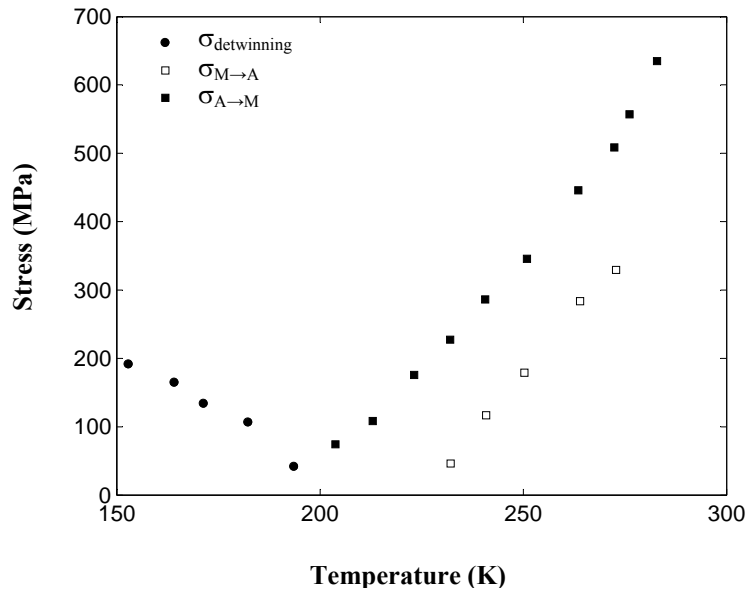


Figure 1-6. The sensitivity of transition stresses to temperature in Ti_{51%}Ni wire specimens (adapted from Miyazaki et al., 1981a)

1.2.3. Instability and Lüders-like deformation in NiTi SMAs

Experiments have shown that the stress-induced transformation in NiTi shape memory alloys is inhomogeneous in nature and proceeds through Lüders-type localized deformation. Lüders-type deformations are observed during the early stages of yielding in mild steel (Lomer, 1952; Butler, 1962; Hall, 1970; Kyriakides and Miller, 2000). The initiation of plastic deformation in mild steel under displacement-controlled conditions is characterized by a sudden drop in stress from the *upper yield stress* to the *lower yield stress*. This event is accompanied by the rapid formation of localized high-strain deformation bands which spread throughout the specimen as the loading continues. During the propagation of localized deformation, the nominal stress remains essentially constant at the lower yield stress. The localization of deformation in mild steel is due to instability of the mechanical behavior of material during yielding. The origin of such mechanical instability in mild

steel is related to certain micro-scale interactions between dislocations generated during yielding of the material (Kyriakides and Miller, 2000).

Similar localization phenomenon has also been observed in pseudoelastic response of NiTi samples during both forward and reverse transformations. Inhomogeneity of transformation in NiTi was first noticed by Miyazaki et al. (1981b) during the tensile testing of wire samples at a very low strain rate ($6 \times 10^{-5} \text{ s}^{-1}$). They observed that the phase transformations at this strain rate proceed through the propagation of a transformation front characterized by a narrow localized deformation band travelling from one side of the specimen to the other side. This behavior is shown schematically in Figure 1-7. Leo et al. (1993) confirmed the inhomogeneous nature of the stress-induced transformation by monitoring the local variations of temperature along the wire during loading. Since heat is released (absorbed) during the forward (reverse) transformation the localized transformations result in non-uniform temperature distributions.

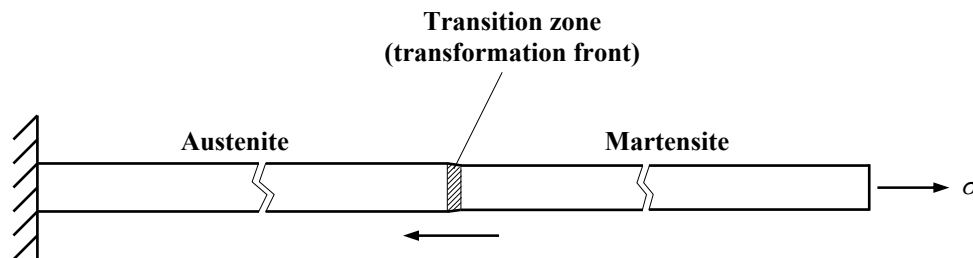


Figure 1-7. Deformation localization (Lüders-like deformation) during stress-induced transformation in NiTi wire

Shaw and Kyriakides (1995) presented a systematic study of the subject through in-situ local measurements of temperature and strain during the pseudoelastic response of NiTi wires. Multiple small thermocouples and miniature extensometers were mounted at discrete locations along the wire to accomplish this. They demonstrated that the stress-induced A→M and M→A phase transformations in NiTi wires are characterized by the nucleation and propagation of distinctly

nonuniform instabilities (locally transformed regions). It was shown that at low strain rates (of the order of 10^{-4} s^{-1} and smaller) the forward and reverse transformations proceed at essentially constant stresses. They also observed that the number of nucleation events and propagating fronts can vary depending on the loading rate. The effect of loading rate will be discussed in more detail in the following section.

The localization of transformation in thin strips of NiTi was later studied by Shaw and Kyriakides (1997) through full-field monitoring of the deformation and thermal changes. The inhomogenous evolution of the transformation was observed by recording the surface state of a brittle coating at prescribed time intervals using an optical camera. An infrared thermal camera was also used to simultaneously measure the full-field distributions of temperature. It was found that the transition fronts in uniaxial extension of NiTi strips are nearly straight sharp discontinuities at an angle of $\theta = 50^\circ \sim 60^\circ$ to the specimen axis (Figure 1-8a). They also observed that the fronts occasionally change their angle from $+\theta$ to $-\theta$ via formation of an intermediate *criss-cross* pattern (also referred to as *finger-type* pattern; see Figure 1-8b). In fact, the finger-type pattern is the prevailing shape of the transformation front in the case of strips with a small length to width ratio (Shaw and Kyriakides, 1998).

In their discussion of the experimental results, Shaw and Kyriakides (1997, 1998) associated the formation of localized deformations (sharp inclined bands of high strain) to nucleation of a new phase. Based on a set of isothermal experiments, Shaw and Kyriakides (1997) demonstrated that the nucleation of martensite requires a distinctly higher stress (*nucleation stress*) than the stress required subsequently to drive the existing transformation front(s) (*propagation stress*). Conversely, the nucleation of austenite during unloading occurs at a significantly lower stress than the stress observed during the propagation of the reverse transformation front(s) at a constant temperature. This behavior is shown in Figure 1-9.

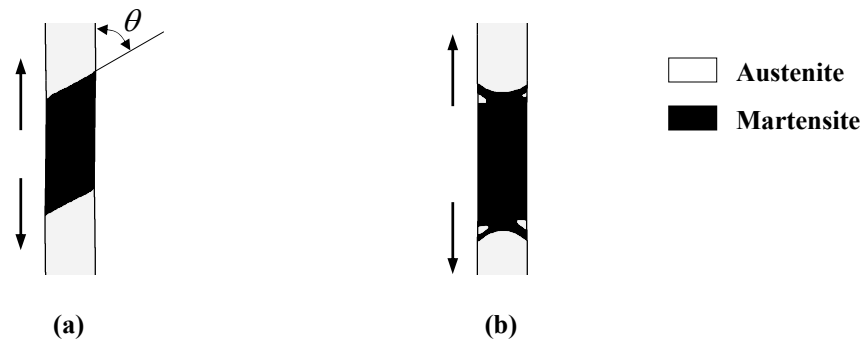


Figure 1-8. Transformation fronts during uniaxial extension of NiTi strips. (a) Straight, inclined fronts; (b) Finger-type fronts.

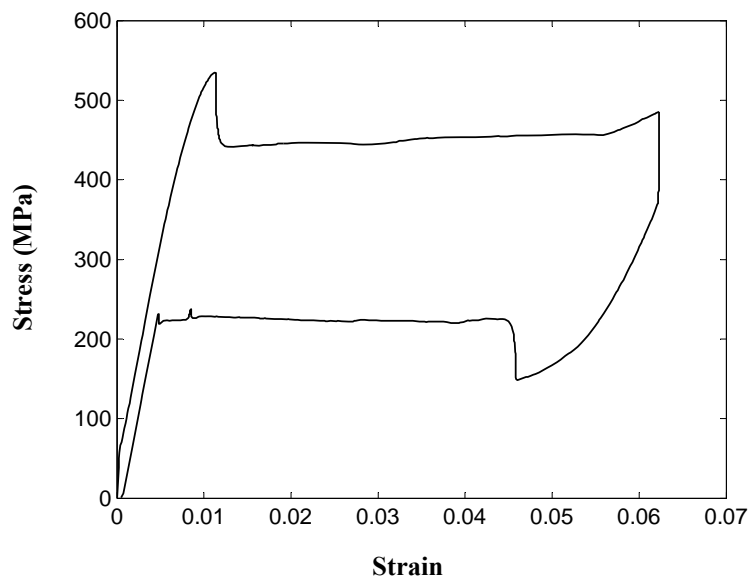


Figure 1-9. Stress peak and valley at the onset of instability during the isothermal pseudoelastic response of NiTi wires (adapted from Iadicola and Shaw, 2002a)

The experimental investigation of Lüders-like deformation in NiTi has gained considerable attention in recent years. Taking advantage of high-accuracy infrared imaging techniques, Pieczyska et al. (2004, 2006a) reported heterogeneous temperature distributions related to the nucleation and development of the new phase in NiTi sheet specimens during loading and unloading. It was shown

that even at relatively high strain rates (of the order of 10^{-2} s^{-1}) where the nominal stress-strain curves exhibit a stable mechanical behavior (positive slope during the transformation), both the forward and reverse transformations occurred in a localized manner. The number of nucleation events and coexisting transformation fronts increases dramatically at such high strain rates as compared to the rather low strain-rate experiments of Shaw and Kyriakides (1997). However, the shapes of localized deformation bands (characterized by high-temperature regions) were similar to those reported by Shaw and Kyriakides (1997), i.e., bands with straight transition fronts inclined at an angle of about 50° (Figure 1-8a). These phenomena were also observed during stress-controlled tests (Pieczyska et al., 2006b).

The formation of localized deformation bands has also been investigated in NiTi tubes by Li and Sun (2002), and Feng and Sun (2006) using high-speed in-situ optical imaging. The onset of the unstable mechanical behavior in a NiTi tube during displacement-controlled uniaxial extension is marked by a sudden drop in nominal stress accompanied by the rapid formation of a narrow helical localized band inclined at an angle of 60° to the axis of tube (Figure 1-10a). Upon further loading, the helical band grows in length and width followed by the domain self-merging into a cylindrical domain. This process is accompanied by the gradual branching of the fronts at the two ends of the cylindrical domain into several sharp tips (Figure 1-10b), which resemble the finger-type patterns observed during the uniaxial tests of NiTi strips (Figure 1-8b). It was shown that the sequence of events during unloading is not the exact opposite of that during loading. The reverse transformation starts with the inverse convoluted motion of the branched fronts, followed by a sudden switch to smooth inclined fronts (Figure 1-10c). Further unloading results in the merging of the two smooth fronts which is accompanied by a peak stress in stress-strain response. It was noticed that the topology of the localized domain depends on the previous loading/unloading history, and the change in the front morphology is an unstable process accompanied by the respective stress drop or jump.

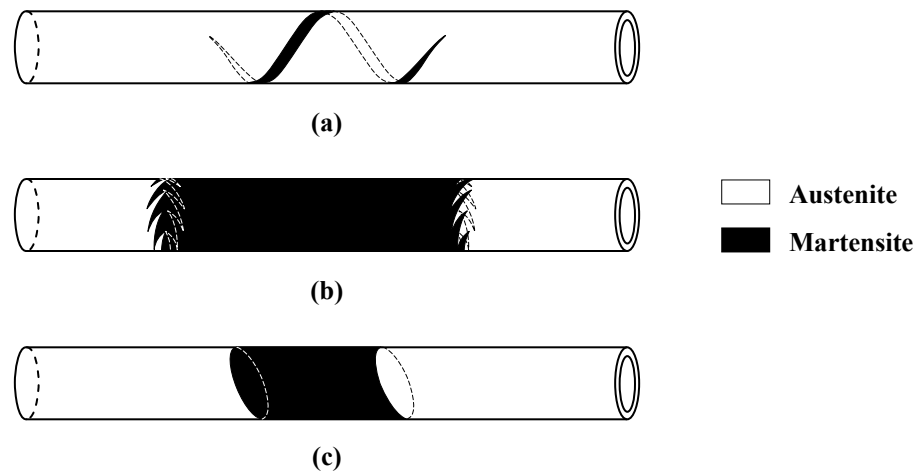


Figure 1-10. Various localization patterns observed during uniaxial loading/unloading of NiTi micro-tubes. (a) Initial helical band; (b) Cylindrical domain with branched fronts (adapted from Feng and Sun, 2006);

An interesting experimental technique has been recently presented by Daly et al. (2007) to establish the full-field quantitative strain maps of localization in thin sheets of NiTi. In this technique called *digital image correlation*, the displacement field is measured by optically tracking a random pattern on the surface of the specimen. It was shown that the stress-induced transformation initiates in a homogenous manner characterized by the deviation of stress-strain response from linearity prior to the nucleation of localized deformation bands. This observation is contrary to the conclusion of Shaw and Kyriakides (1995, 1997) which attributes the nucleation of localized bands to the nucleation of the new phase. The initiation of transformation prior to the nucleation of localized bands has also been supported by other experimental observations such as optical microscopy (Brinson et al., 2004), mechanical unloading just before the nucleation event (Li and Sun, 2002; Feng and Sun, 2006), and uniform temperature increase during the initial loading stage (Pieczyska et al., 2004, 2006a,b). Another important observation reported by Daly et al. (2007) was that once the localized bands nucleate, the transformation strain inside the bands does not jump to its maximum level but rather continues to increase as the stress increases.

Despite the similarities between the experimental observations on instability and Lüders-like deformation in NiTi alloys, various hypotheses have been proposed for the origin of deformation localization in NiTi. One possible reason for deformation localization in NiTi is the intrinsic instability of the material behavior (strain softening) during the phase transformation (Shaw and Kyriakides, 1998; Idesman et al., 2005; Feng and Sun, 2006). This hypothesis is supported mainly by the apparent resemblance between the Lüders-like behavior in NiTi and the propagation of instabilities in other material systems and structures such as neck-propagation in polymers and domino crushing of cellular solids (Kyriakides, 1993).

Another explanation is provided by researchers who believe that the strain-softening behavior in SMAs is an unrealistic assumption. According to this group, the underlying mechanism of deformation localization is the severe geometric distortion due to the large transformation strain (geometric instability) rather than the material instability (Sittner et al., 2005; Favier et al., 2001). They have shown that a positive (but small) tangential modulus in the stress-strain response during the transformation can also lead to localization. This theory is backed by some micro-mechanical calculations which rule out the possibility of strain softening. However, Shaw and Kyriakides (1998) reported that the relatively large drop in stress at the onset of the stress-plateau cannot be modeled by geometric instability alone. Through carefully designed experiments, Iadicola and Shaw (2002a) have demonstrated that the “true” load drop can be as high as 17% if the effects of stress concentrations at the gripped ends are eliminated.

The localization phenomena explained above are related to the stress-induced martensite transformation and its reverse transformation in NiTi. The Lüder-like deformation has also been observed during the loading of thermally induced martensite which includes detwinning and reorientation of martensite variants (Liu et al., 1998, 2000). However, this is not always the case and the deformation of martensite in some alloy compositions of NiTi has been reported to be

homogenous and characterized by stable stress-strain responses (Shaw and Kyriakides, 1995; Ng and Sun, 2006).

Regardless of its origin, the localization of deformation in NiTi has important implications on its application and modeling. This is because the true, local behavior of the material is quite different from what is observed on the bulk level. Therefore, the intrinsic instability of the material is an important issue which must be carefully accounted for in any modeling effort.

1.2.4. Strain dependence of pseudoelastic behavior

The deformation behavior of NiTi SMA is strongly affected by the maximum applied strain. From a macroscopic point of view, the deformation of a virgin NiTi sample during loading within the pseudoelastic regime ($T > A_f$) can be divided into four stages as shown schematically in Figure 1-11 (Miyazaki et al., 1981a; Liu et al., 1999; Tan et al., 2004). The mechanism of deformation and unloading behavior at each stage is explained as follows:

1.2.4.1. Stage I

The initial loading of material includes the elastic deformation of the austenite phase. The small non-linearity observed at the end of this stage is associated with some partial martensitic transformation which takes place in a homogenous manner (Brinson et al., 2004; Pieczyska et al., 2004, 2006a,b; Daly et al., 2007). Unloading at the end of this stage results in a narrow hysteresis loop which corresponds to the reverse transformation and elastic unloading (Li and Sun, 2002; Feng and Sun, 2006).

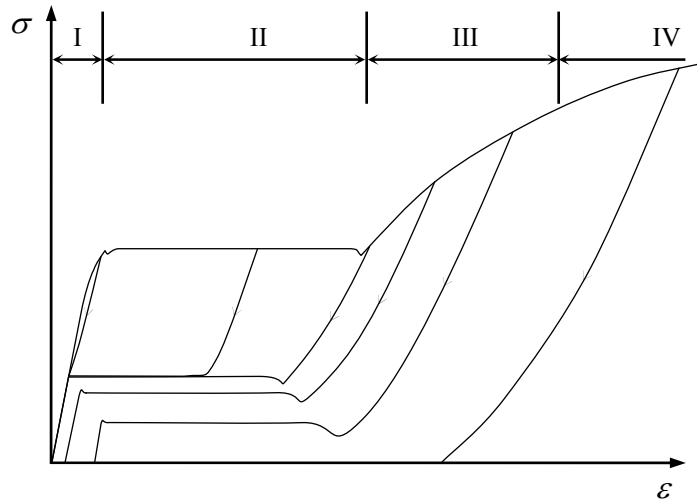


Figure 1-11. Dependence of the pseudoelastic responses of NiTi on the maximum applied strain.

1.2.4.2. Stage II:

In stage II, the deformation proceeds through a localized manner over a distinct stress plateau (Lüders-like deformation). Although the majority of stress-induced martensitic transformation occurs in this stage, the start and end of the stress-plateau are associated with the nucleation and eventual coalescence of one or several localized transformation bands rather than the initiation and completion of the transformation (Tan et al., 2004).

Unloading of a specimen loaded to this stage starts with elastic unloading of the stress-induced martensite, followed by the stress-induced reverse transformation exhibiting a stress plateau and Lüders-like behavior. It should be noted that the initial part of unloading is not a purely elastic deformation, and is accompanied by some homogenous reverse transformation, as well as some martensite-martensite conversion (reorientation) at microscopic levels.

For specimens deformed to the end of the stress-plateau during loading, the beginning of lower stress-plateau upon unloading is characterized by a pronounced stress-valley which corresponds

to the nucleation of localized deformation. For specimens unloaded prior to the ends of the upper stress-plateau, the inverse stress-peak is absent due to the existence of a localized austenite band from the previous partial martensitic transformation. However, the plateau stress during unloading does not depend on the maximum applied strain (Lin et al., 1994).

1.2.4.3. Stage III

It has been observed through various experimental techniques that the end of Lüders-like deformation in the pseudoelastic response is not the end of phase transformation, and that the stress-induced transformation continues beyond the stress plateau (Tan et al., 2004; Brinson et al., 2004; Khalil-Allafi et al., 2004). This is particularly apparent when considering the difference in the tangential modulus of loading and unloading at this stage (Daly et al., 2007).

The deformation in this stage is stable and the stress increases as the loading continues. The increase in stress results in slip and movement of dislocations which gives rise to some plastic deformation. The residual strain observed at the end of unloading in Figure 1-11 is attributed to this mechanism.

As shown in Figure 1-11, the reverse transformation stress (lower plateau stress) decreases with increasing maximum applied strain. The decrease in transformation stress is due to the residual stress field that is formed as a result of plastic deformations. The residual stress field has a similar effect on the forward transformation stress upon reloading (Miyazaki et al., 1981a).

In summary, the deformation mode in stage III is a combination of elastic deformation, slip, and stress-induced martensitic transformation.

1.2.4.4. Stage IV

The amount of recoverable strain rapidly decreases in this stage and the lower stress plateau completely disappears due to severe plastic deformation. Most of the deformation in this stage is plastic through the movement of dislocations.

1.2.5. Strain-rate sensitivity of SMAs

It has been experimentally shown that the pseudoelastic stress-strain responses of SMAs depend strongly on the applied strain rate (Leo et al., 1993; Shaw and Kyriakides, 1995, 1997; Tobushi et al., 1998; Pieczyska et al., 2006a,b). A typical strain rate sensitivity of NiTi is shown in Figure 1-12. It can be seen that both the transition stress and the size of the pseudoelastic hysteresis in NiTi shape-memory wires depend on the strain rate.

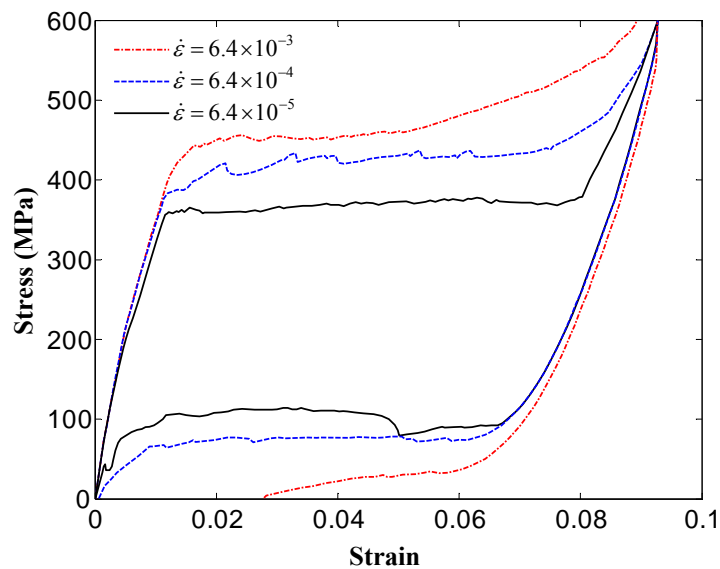


Figure 1-12. The pseudoelastic response of NiTi wire at various strain rates (adapted from Leo et al., 1993)

Tobushi et al. (1998) attributed the strain-rate dependency of SMA behavior to the inherent rate-dependency of material resistance against the motion of the austenite/martensite interface (*internal friction resistance*). Based on the similarities between the stress-induced martensitic transformation and Lüders deformation in mild steel, they argued that the increase in transformation stress with strain rate is similar to the increase in resistance against the progress of plastic deformation with strain rate for normal metals. In contrast to this theory, Leo et al. (1993) and Shaw and Kyriakides (1995) attributed the nature of such sensitivity to transient heating effects caused by the release or absorption of the latent heat of transformation. Similar to most solid-state transformations, some amount of heat is released during the transformation from austenite to martensite, or absorbed during the reverse transformation. As explained in Section 1.2.2, the transformation stress strongly depends on temperature. Therefore, the latent heat of transformation can severely influence the pseudoelastic response of SMAs due to internal self-heating (or cooling) of the material.

Through in-situ optical microscopy, Brinson et al. (2004) investigated the microstructural evolution of NiTi during the stress-induced martensitic transformation at various loading rates and various loading stages. It was found that the strain rate had a little effect on the microstructure of martensite. Based on this observation they concluded that strain rate effects are largely due to the latent heat in the specimen.

Shaw and Kyriakides (1995, 1997) demonstrated that the localization of deformation during the transformation causes the local strain rate in the transition region to be significantly amplified compared to the global strain rate. Consequently, the rate of heat generation/absorption, and therefore the magnitude of temperature variations at the active transformation fronts can be significantly higher than expected. Their observations revealed that the uniaxial pseudoelastic response of NiTi at low strain rates is characterized by a distinct stress-plateau, and the propagation of only one or two

transformation fronts. At high strain rates, the latent heat could not be removed (or supplied) fast enough and therefore the temperature variations are large enough to significantly increase/decrease the stress level. This can result in the nucleation of the new phase at other sites along the specimen, and propagation of several transformation fronts at the same time. At very high strain rates, numerous nucleation events take place which makes the deformation more homogeneous. In that case, the overall mechanical response of the material also becomes more stabilized as the stress-strain curves maintain a positive slope during the transformation (Pieczyska et al., 2006a,b).

1.2.6. Effect of cyclic loading on pseudoelastic behavior

Repetitive loading-unloading cycle has a pronounced effect on the subsequent thermomechanical behavior of SMAs. In general, mechanical cycling reduces the critical stresses needed to induce the forward and reverse transformations, as well as the size of the hysteresis loop. Moreover, the residual strain usually observed at the end of unloading increases with increasing the number of cycles (Miyazaki et al., 1986; Strnadel et al., 1995; Tobushi et al., 1996, 2005; Gong et al., 2002). As an example, the stress-strain responses from a NiTi specimen subjected to cyclic loading are shown in Figure 1-13. The cyclic changes are more severe during the early stages of cyclic loading. As the number of cycles increases, the material behavior approaches a saturation limit beyond which the pseudoelastic response does not significantly change with the number of cycles.

The cause for the effect of cyclic deformation is the generation of dislocations during the stress-induced transformation. Microstructural observations have revealed that even at low strain levels (Stage II in Figure 1-11) mechanical cycling produces a strongly oriented pattern of dislocations (Miyazaki et al., 1986; Sittner et al., 2003). The gradual accumulation of dislocations around infinitesimal defects produces a microscopic residual stress field. The residual stress field

assists the stress-induced martensitic transformation while resisting the inverse transformation. As a result, the transformation stresses during both loading and unloading are reduced.

The microscopic residual stress field also causes some residual pockets of martensite which do not transform back into austenite during unloading. Therefore, the total permanent strain is caused by a combination of micro-plasticity and residual martensite.

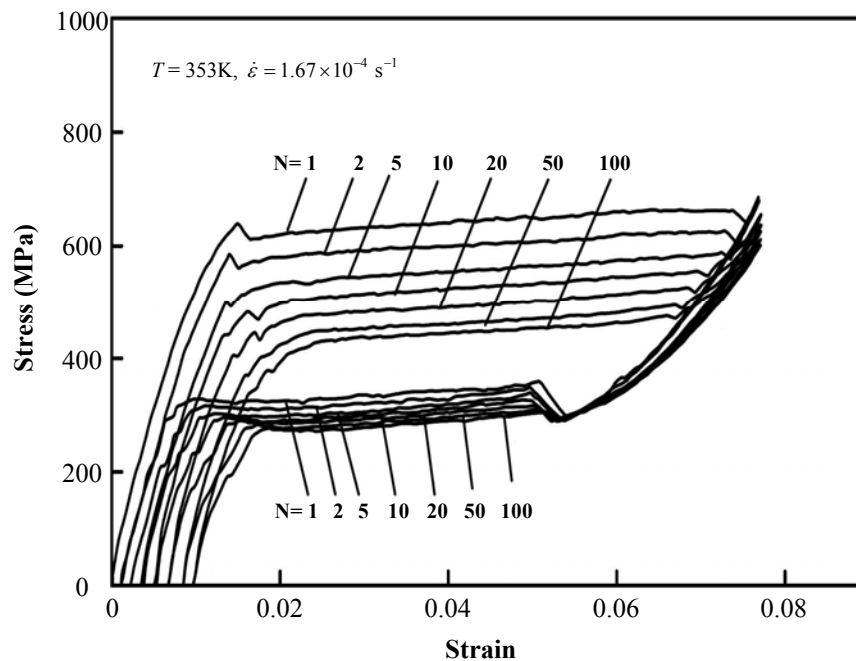
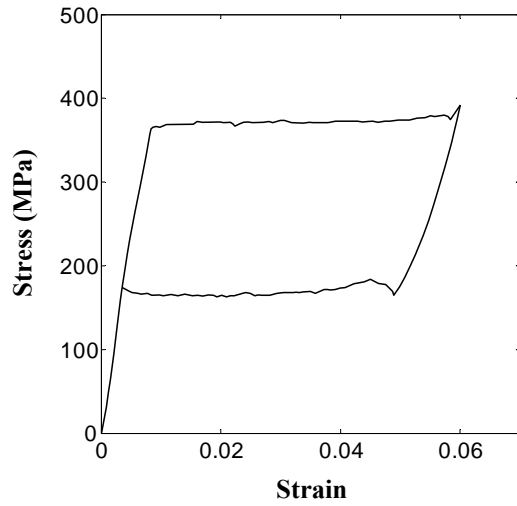


Figure 1-13. Effect of cyclic loading on pseudoelastic behavior of NiTi (reproduced with permission from Tobushi et al., 2005).

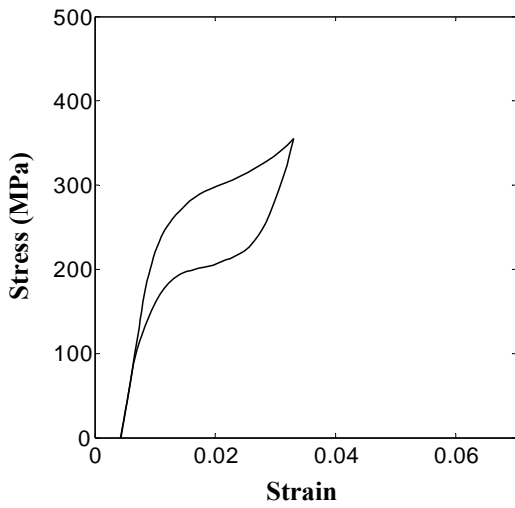
The residual stresses produced during the cyclic deformation may be used to induce the *two-way shape memory effect*. In that case, the biased external force shown in Figure 1-2 is replaced by the internal residual stresses to create a stand-alone actuating system (for examples see Hebda and white, 1995; Tobushi et al., 1996; Inaba et al., 2002). Therefore, the cyclic loading is also sometimes referred to as *training effect* in order to reflect this phenomenon.

For some NiTi alloys that have been subjected to special heat treatments, the cyclic deformation also tends to stabilize the overall pseudoelastic response of the material. That is, the flat stress plateau disappears after a number of cycles and the stress-strain curve exhibits a positive slope during loading and unloading (Miyazaki et al., 1986; Liu et al., 1999). It is tempting to conclude based on this observation that the phase transformation occurs homogeneously after cyclic training. However, it has been experimentally shown that the stress-induced transformation still results in deformation localization in spite of the overall stable pseudoelastic response of the material (Iadicola and Shaw, 2002b).

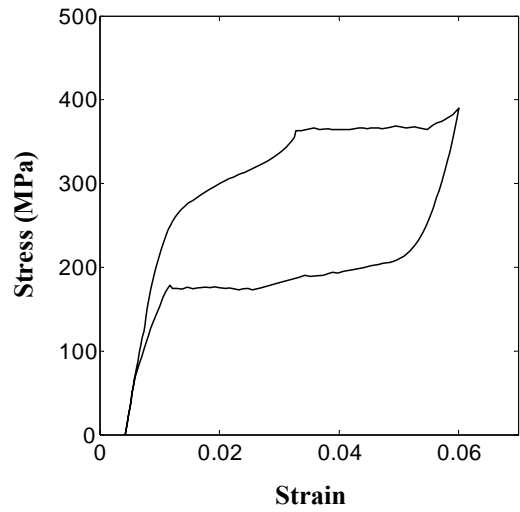
Figure 1-14 shows the effect of localization during cycling loading on the overall pseudoelastic response of a NiTi wire. The full pseudoelastic response of the “virgin” material in the first cycle is shown in Figure 1-4(a). The pseudoelastic response of the wire after being cycled up to a maximum strain of 3.3% for N=100 cycles is also given in Figure 1-14(b). During the 100th cycle, the stress plateaus have almost disappeared and the material seems to exhibit a mechanically stable behavior. Also the height of the hysteresis loop has significantly decreased compared to the first cycle. However, if the wire is loaded beyond the strain limit of the initial cycles (3.3%) a completely different behavior is observed as shown in Figure 1-14(c). The reason for this behavior is as follows: since the wire is only partially transformed during the first 100 cycles only some parts of the sample experience the phase transformation due to the localization, and other sections deform elastically. As the wire is loaded beyond the 3.3% strain, the transformation fronts enter parts of the wire which have not been transformed more than once. Therefore, the stress plateau appears again in the pseudoelastic loop and the transformation stresses reach the same values as those seen in the first cycle.



(a)



(b)



(c)

Figure 1-14. Effect of deformation localization on the cyclic behavior of a NiTi wire. (a) Full pseudoelastic loop in the first cycle; (b) 100th pseudoelastic loop during the partial cyclic loading to a maximum strain of 3.3%; (c) Full pseudoelastic loop after 100 cycles to a maximum strain of 6% (adapted from Miyazaki et al., 1981b).

Iadicola and Shaw (2002b) investigated the effect of cyclic loading on the nucleation and propagation of localized transformation bands in NiTi wires through full-field infrared measurements of temperature. They observed that even after stabilization of the pseudoelastic response, the stress-induced transformation proceeds via a non-uniform and localized manner. They explained that the positive slope of the stress-strain response after cyclic conditioning is due to the gradual progression of the transformation fronts into regions that have experienced a limited number of transformations and therefore require a higher stress for transformation. Another important observation is that the rate of cyclic change depends strongly on the test temperature. They observed that at higher temperatures the material approaches its fully-trained state at a faster rate (fewer cycles). They attributed this trend to the increase in transformation stress with increase in temperature. It was observed that the evolution of the transformation fronts during cyclic loading is also dependent on the temperature. That is, the number of propagating fronts tends to increase with increasing test temperature.

The above experimental observations suggest that the Lüders-like deformation and localization of deformation are important factors in the cyclic response of NiTi shape memory alloys.

1.3. CONSTITUTIVE MODELING OF SMAS

In order to exploit the superior mechanical properties of SMAs in various applications, it is essential to have a reliable constitutive model that is both accurate and convenient to incorporate into engineering tools such as the finite element method (FEM). The desirable model must be able to describe such important behaviors as mechanical instability, localization of transformation, thermomechanical coupling, strain rate effects, and cyclic degradations as explained in detail in Section 1.2.

There are two approaches to establish a constitutive relation for any material. One is the microscopic physical method. The other is the macroscopic phenomenological method. In

micromechanical models, the behavior of individual microstructural grains in polycrystalline SMAs are modeled based on the behavior of single-crystalline SMA and lattice parameters. This solution is then used to analyze a boundary value problem for a polycrystalline SMA. Micromechanical methods can successfully explain the underlying mechanism of fundamental phenomena, but their numerical simulations of macroscopic problems are often complex and deviate from experimental observations.

The phenomenological methods are based on continuum thermomechanics and internal variables that reflect the microstructural changes on the macroscopic level. These methods are often used in engineering applications; however, they require experimental data to find the model parameters. During the past two decades, several models of the behavior of SMAs have been developed based on one of these two approaches or a combination of both. A common feature of most of these models is that they have been developed for the case of “stable” mechanical behavior, and therefore they do not account for the localization of deformation. However, as explained earlier the “true” local behavior of NiTi SMA is quite different from the global response of a NiTi specimen. Some of these models will now be briefly explained, followed by an assessment of the state-of-the-art on the modeling of unstable pseudoelastic behavior.

1.3.1. Modeling of stable pseudoelastic behavior

Tanaka (1986) and Tanaka et al. (1986) developed a one-dimensional phenomenological constitutive model based on the Helmholtz free energy function for an SMA material of finite length. The Helmholtz free energy is the summation of the non-chemical energy, such as the strain energy and the thermal energy, and the chemical free energy. They argued that the phase transformation is basically governed by the minimization of the free energy. By using this assumption and basic thermodynamic laws, they derived an incremental constitutive relation that related the increment of

stress ($d\sigma$) to those of strain ($d\varepsilon$), temperature (dT), and an internal variable (γ) which characterizes the extent of phase transition (martensitic fraction) as:

$$d\sigma = D d\varepsilon + \Omega d\gamma + \Theta dT \quad (1-1)$$

The coefficients of the constitutive equation are the elastic modulus D (Young's modulus), the thermal expansion modulus Θ , and the transformation modulus Ω , which must be determined through experiments. They also expressed the martensitic fraction during the forward and reverse transformations in terms of exponential functions of stress and temperature (kinetics equations) as:

$$\begin{cases} \gamma = 1 - \exp[b_M c_M (M_s - T) + b_M \sigma], & \text{Forward transformation } (d\gamma > 0) \\ \gamma = \exp[b_A c_A (A_s - T) + b_A \sigma], & \text{Reverse transformation } (d\gamma < 0) \end{cases} \quad (1-2)$$

where b_A , b_M , c_A , c_M are material parameters.

The nucleation criteria for both direct and reverse transformations were formulated using the kinetics equations and the assumption that the transformations are completed when the martensitic fraction reaches a value of 0.99 (martensitic transformation) or 0.01 (reverse transformation). Substituting $\gamma = 0.01$ and $\gamma = 0.99$ in the kinetics equations (1-2) defines a set of four lines on a σ - T diagram which correspond to the start and finish of the transformations. The incremental constitutive equation was integrated by assuming that the coefficients are constant to derive a simple finite relation. Later, Sato and Tanaka (1988) relaxed this assumption and suggested that the elastic and thermoelastic moduli in this finite form could be expressed as linear functions of the martensitic fraction. The model of Tanaka was later used to qualitatively predict the overall pseudoelastic and shape memory behavior of a NiTi alloy wire (Tanaka, 1990).

Liang and Rogers (1990) modified the Tanaka model to provide a more accurate and quantitative description of SMAs. They employed the finite constitutive equation of Tanaka, but

replaced the exponential form of the transformation kinetics with a cosine relation. They also considered the transformation of a material with mixed austenite and martensite phases.

Liang and Rogers (1992) extended their one-dimensional constitutive relation to a multi-dimensional thermomechanical constitutive relation. They utilized the concept of the Helmholtz free energy and the first and second laws of thermodynamics to derive a three-dimensional rate equation that related the rate of change of the second Piola-Kirchhoff stress tensor to the rates of the Green-Lagrange strain tensor, temperature, and martensitic fraction. Based on experimental observations that the hydrostatic pressure had a small influence on the phase transformation, they expressed the second law of thermodynamics in terms of the J_2 equivalent Green-Lagrange strain. Furthermore, they also assumed that the increment of strain could be decomposed into elastic and transformation components. The coefficients that appeared in the constitutive equation were the tensors of elastic and thermoelastic moduli, and the transformation tensor. For the transformation kinetics, they expressed the martensitic fraction as the cosine functions of temperature and the equivalent Piola-Kirchhoff stress. The application of the model was limited to simple loading cases such as the torsion of a circular SMA rod.

The models introduced by Tanaka and Liang-Rogers were not able to simulate the detwinning of thermally-induced martensite and the subsequent shape memory effect. Based on the incremental constitutive relation of Tanaka, a one-dimensional constitutive model was developed by Brinson (1993) to describe both the pseudoelastic and reorientation of thermal martensite. In this model, the total martensitic fraction was divided into two components: one corresponding to the temperature-induced martensite (twinned martensite), and the other associated with the stress-induced martensite (detwinned martensite). Two types of constitutive relations were developed. The first relation was obtained by integrating the incremental equation assuming that the material coefficients are constant, which resulted in a relation similar to the models of Tanaka (1990) and Liang-Rogers (1992). In the

second model it was assumed that the elastic modulus and transformation modulus are linear functions of martensitic fraction prior to the integration. The transformation kinetics used in the model were based on the kinetics introduced by Liang and Rogers (1992), which were modified to account for the conversion between the austenite, twinned martensite, and detwinned martensite at various temperature ranges. The model was further refined by Bekker and Brinson (1998) to account for combined thermal and mechanical loading, and also partial transformations.

A “practical” three-dimensional constitutive model was developed by Boyd and Lagoudas (1994a) and Lagoudas et al. (1996). They extended the constitutive model of Tanaka (1986) and Sato and Tanaka (1988) by rewriting the incremental constitutive equation in (1-1) as:

$$d\sigma_{ij} = C_{ijkl} d\varepsilon_{kl} - C_{ijkl} d\varepsilon_{kl}^{(t)} - \alpha_{ij} dT \quad (1-3)$$

where C_{ijkl} is the elastic stiffness tensor and α_{ij} is the thermoelastic expansion tensor.

The transformation strain tensor $\varepsilon_{ij}^{(t)}$ in above equation is given by,

$$d\varepsilon_{ij}^{(t)} = \begin{cases} -\frac{3}{2} \frac{\Omega}{D} \frac{s_{ij}}{\bar{\sigma}} d\gamma, & \text{Forward trans. } (d\gamma > 0) \\ -\frac{\Omega}{D} \frac{\varepsilon_{ij}^{(t)}}{\bar{\varepsilon}^{(t)}} d\gamma, & \text{Reverse trans. } (d\gamma < 0) \end{cases} \quad (1-4)$$

where $\bar{\sigma}$ is the von-Mises equivalent stress, and $\bar{\varepsilon}^{(t)}$ is an equivalent transformation strain defined as,

$$\bar{\varepsilon}^{(t)} = \sqrt{\frac{2}{3} \varepsilon_{ij}^{(t)} \varepsilon_{ij}^{(t)}} \quad (1-5)$$

The kinetics of transformation are similar to those from Tanaka (1986) except that the uniaxial stress in equation (1-2) is replaced by the von-Mises equivalent stress $\bar{\sigma}$ (J_2 transformation surface). From equation (1-4) it can be seen that the transformation strain tensor does not change if

the transformation does not proceed ($d\gamma = 0$). However, in general three-dimensional non-proportional loading the martensite variants convert to each other (reorientation) to accommodate the change in the direction of applied load. This results in reorientation of transformation strain tensor without changing the overall martensitic fraction.

To address the simultaneous transformation and reorientation of variants, Boyd and Lagoudas (1996) developed a general micromechanics-based model that considers the transformation of austenite into a number of martensitic variants, as well as the conversion of variants to each other. For the special case of only one martensite variant, they proposed a particular non-associated flow rule during unloading to account for the reorientation of the transformation strain tensor (Boyd and Lagoudas, 1994b).

An extension of the model of Boyd and Lagoudas (1996) was presented by Qidwai and Lagoudas (2000) where the tensile-compression asymmetry observed in the pseudoelastic response of SMAs was included. They considered several different transformation surfaces based on J_2 , I_1 and J_3 invariants.

A completely different approach to model three-dimensional behavior of SMAs was presented by Brocca et al. (2002) based on the *microplane* theory. In this theory, the three dimensional behavior of a material is obtained by superimposing the effects of inelastic deformations calculated on several planes of different orientations called microplanes. The normal and shear components of stress acting on each plane are first found based on the macroscopic stress tensor. The normal and shear components of strain are then calculated based on a one-dimensional model. The particular one-dimensional model that was used in this model was that of Bekker and Brinson (1998). However, any other one-dimensional model could also be used to describe the behavior of SMAs on each microplane.

Recently, Kadkhodaei et al. (2007) presented a micro-plane theory in which only one shear stress component (the resultant shear component) is considered on each micro-plane rather than two shear components. They showed that unlike other micro-plane theories, this approach does not cause shear strain during uniaxial loading or axial strain during shear loading.

1.3.2. Modeling of the unstable pseudoelastic behavior

While most of the constitutive models developed in the past have focused on the overall mechanical response of shape memory alloys, there have been a few notable efforts to model the localized unstable transformation behavior of the material. Abeyaratne and Knowles (1993) developed a one-dimensional thermodynamic framework based on the Helmholtz free energy to simulate the isothermal transformation in an SMA bar. They constructed an explicit form of the Helmholtz free energy with two wells, corresponding to the equilibrium states of the austenite phase and martensite phase. The kinetics relation is also determined a priori by expressing the speed of the interface as a function of the driving force (stress) and temperature. They treated the propagating phase boundaries as traveling field discontinuities, across which jump conditions are enforced. Therefore in their model a point inside the body is either martensite or austenite and the concept of martensitic fraction does not appear. Kim and Abeyaratne (1995) extended the model to consider the heat generation during transformation. This time, the kinetics of transformation (speed of phase boundaries) was not specified a priori but was determined as part of the solution which was obtained using a finite difference method. Based on their results the following conclusions were drawn: the phase boundary temperature increased with the loading rate; the area of the hysteresis loop in the pseudoelastic response increased with the loading rate; an increase in the environment temperature resulted in a shift of the hysteresis loop to the higher stresses. Although this model proved to be successful in capturing the propagation of the transformation front in SMAs, it is not suited for

implementation in the finite element method. Moreover, its practical application is limited to one-dimensional problems.

A different type of analysis has been presented by Sun and Zhong (2000) to simulate the nucleation and propagation stresses for a single transformation band in a NiTi wire. The wire was modeled as an elastic rod containing a single cylindrical transformation inclusion with a uniform axisymmetric transformation strain. The FEM was implemented to calculate the elastic energy associated with strain discontinuity across the austenite/martensite interface. The total elastic energy and Gibbs free energy of the composite were obtained by superposition. They assumed that the nucleation event at a stress peak is accompanied by the formation of a localized martensite band with finite length. Based on the calculations, they related the magnitude of the stress drop to the length of the initial nucleation band. By comparing the results to the experimental observations of Shaw and Kyriakides (1995) they concluded that this length must be approximately equal to half the radius of the wire. The effect of specimen aspect ratio on the load drop was also discussed based on the numerical analysis. A similar approach was implemented by Messner et al. (2000), this time using Helmholtz free energy to analyze the nucleation of martensite bands in SMA flat strips. They found that the inclination of the transformation front with respect to the loading direction (54°) helps to minimize the total elastic energy of the system.

Shaw and Kyriakides (1998) proposed a plasticity-based model to capture the material instability observed in NiTi strips. Based on the similarities between the localized unstable propagation of Lüders bands in fine-grained mild steel and the localized deformation in SMA strips, they concluded that continuum level strain localization based on a shear mechanism (rather than microstructure) is the dominant player in the observed behavior of NiTi strips. The material was assumed to behave as an isothermal, rate independent J_2 -type elasto-plastic solid with isotropic softening. The key ingredient of the constitutive model is a trilinear stress-strain response that has two

stable elastic branches, and an intermediate unstable softening branch as shown schematically in Figure 1-15. The heat generation during the phase transformation and the thermal interaction of an SMA specimen with the environment and the sensitivity of the transformation stress to temperature were neglected in their model. Explicit transformation kinetics were not employed in this approach, and the extent of transformation was calculated from the amount of plastic deformation at any point in the specimen. The model was implemented with a three-dimensional finite element mesh to simulate the propagation of transformation front(s) in quasi-static extension of NiTi strips. In this case, the transformation front was a local propagating neck with a finite length. The same type of approach has also been recently used by Hu et al. (2007) to simulate the nucleation and propagation of localized helical bands in uniaxial loading of NiTi tubes.

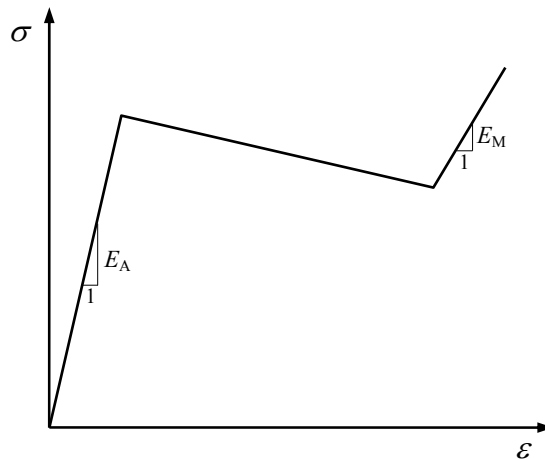


Figure 1-15. Trilinear stress-strain response used in the plasticity model of Shaw and Kyriakides (1998)

Shaw (2000), and Iadicola and Shaw (2004) extended the work of Shaw and Kyriakides (1998) by considering the temperature variations and thermomechanical coupling of the material with its environment. Several trilinear stress-strain characteristic responses at various temperatures similar to that shown in Figure 1-15 were considered to account for the thermal effects. They numerically

investigated the effect of the latent heat of transformation, heat transfer, and loading rate on the evolution of instabilities in NiTi dog-bone strip samples using FEM.

Due to the inherent irreversibility of plastic deformation, the approaches implemented by Shaw and Kyriakides (1998), Shaw (2000), Iadicola and Shaw (2004), and Hu et al. (2007) are limited to the forward transformation case (loading), i.e., the reverse transformation and strain recovery upon unloading cannot be modeled by these methods. Moreover, the J_2 incremental plasticity theory does not recognize the reorientation of plastic strain (transformation strain in this case) which occurs during the general non-proportional loading.

1.4. OBJECTIVE AND SCOPE

Despite the extensive experimental and theoretical work in the past two decades, some aspects of SMA behavior are still subject to intense research. Among these are the instability in the mechanical behavior of some SMAs during stress-induced transformation, the sensitivity of their response to loading rate, and the degradation of material properties due to repeated loading-unloading cycles. In some important applications such as microactuators, stents, guidewires, and other biomedical applications, relatively slender structures are subjected to rather complex deformations. Also, in some other applications, SMA elements are often subjected to dynamic loading, which involves localized heating/cooling. Given the small length scale of most applications involving SMAs, accurate modeling of localized deformation behavior of SMAs becomes critical.

The local nature of stress-induced transformation plays an important role in the dynamic pseudoelastic response of shape memory alloys due to the local generation/absorption of heat. The existing models which recognize the instability and localized nature of stress-induced transformations are either inconvenient for use in engineering numerical packages or limited only to the case of forward transformation. Therefore, one of the objectives of this research is to develop a convenient

continuum-level engineering model to study the unstable dynamic pseudoelastic response of NiTi SMAs over a wide range of loading rates. The proposed one-dimensional and multi-dimensional models are primarily intended for implementation in a finite element framework, which can then be applied to model complex geometries. In this work, the modeling efforts are focused on the behavior of NiTi alloys at temperatures above A_f where the material exhibits a full pseudoelastic hysteresis. The current study is also limited to the unstable regime and therefore deformations beyond the stress-plateau (Stage III, and IV in Figures 1-11) are neglected.

While the propagation of instabilities in various material systems during mechanical loading have been extensively studied using various numerical and analytical methods in the past, the inverse phenomena during unloading has not received enough attention from a mechanical point of view. Another objective of this study is to provide an in-depth understanding of the mechanical origin of the propagation of localized deformation bands during pseudoelastic response, particularly during the reverse transformation. This goal is achieved by numerically studying the problem using a continuum-level three-dimensional model and FEM.

In Chapter 2, the derivation of a one-dimensional phenomenological model is presented, and the numerical examples are compared to the experimental observations. The extension of the model to the three-dimensional case is explained in Chapter 3, where simulations of the nucleation and propagation of transformation bands in thin sheets of NiTi during both forward and reverse transformations are presented. The effects of cyclic loading on unstable behavior of material are incorporated into the models in Chapter 4. Chapter 5 contains a concluding summary of the contributions and results obtained throughout this research. Potential future work to extend and enhance the present modeling effort is also included in Chapter 5.

1.5. BIBLIOGRAPHY

- Abeyaratne, R., Knowles, J.K., 1993. Continuum model of a thermoelastic solid capable of undergoing phase transitions. *Journal of the Mechanics and Physics of Solids* 41, 541-571.
- Bhattacharya, K., 2003. *Microstructure of martensite: why it forms and how it gives rise to the shape memory effect*. Oxford University Press, Oxford.
- Bekker, A., Brinson, L.C., 1998. Phase diagram based description of the hysteresis behavior of shape memory alloys. *Acta Materialia* 46, 3649-3665.
- Boyd, J.G., Lagoudas, D.C., 1994a. Thermomechanical response of shape memory composites, *Journal of Intelligent Material Systems and Structures* 5, 333-346.
- Boyd, J.G., Lagoudas, D.C., 1994b. A thermodynamical constitutive model for the shape memory effect due to transformation and reorientation. *Proceedings of the SPIE - The International Society for Optical Engineering* 2189, 276-88.
- Boyd, J.G., Lagoudas, D.C., 1996. Thermodynamical constitutive model for shape memory materials. Part 1. The monolithic shape memory alloy. *International Journal of Plasticity* 12, 805-842.
- Brinson, L.C., 1993. One-dimensional constitutive behavior of shape memory alloys: Thermomechanical derivation with non-constant material functions and redefined martensite internal variable. *Journal of Intelligent Material Systems and Structures* 4, 229-242.
- Brinson, L.C., Schmidt, I., Lammering, R., 2004. Stress-induced transformation behavior of a polycrystalline NiTi shape memory alloy: micro and macromechanical investigations via in situ optical microscopy. *Journal of the Mechanics and Physics of Solids* 52, 1549-1571.

- Brocca, M., Brinson, L.C., Bazant, Z.P., 2002. Three-dimensional constitutive model for shape memory alloys based on microplane model. *Journal of the Mechanics and Physics of Solids* 50, 1051-1077.
- Bruno, S., Valente, C., 2002. Comparative response analysis of conventional and innovative seismic protection strategies. *Earthquake Engineering and Structural Dynamics* 31, 1067-1092.
- Butler, J. F., 1962. Lüders front propagation in low carbon steels, *Journal of the Mechanics and Physics of Solids* 10, 313–334.
- Calkins, F.T., Mabe, J.H., Butler, G.W., 2006. Boeing's variable geometry chevron: Morphing aerospace structures for jet noise reduction. *Proceedings of SPIE - The International Society for Optical Engineering* 6171, 61710O.
- Chang, L.C., Read, T.A., 1951. Plastic deformation and diffusionless phase changes in metals - Gold-cadmium beta phase, *American Institute of Mining and Metallurgical Engineers - Journal of Metals* 191, 47-52.
- Daly, S., Ravichandran, G., Bhattacharya, K., 2007. Stress-induced martensitic phase transformation in thin sheets of Nitinol. *Acta Materialia* 55, 3593-3600.
- Dolce, M., Cardone, D., 2001a. Mechanical behaviour of shape memory alloys for seismic applications 1. Martensite and austenite NiTi bars subjected to torsion. *International Journal of Mechanical Sciences* 43, 2631-2656.
- Dolce, M., Cardone, D., 2001b. Mechanical behaviour of shape memory alloys for seismic applications 2. Austenite NiTi wires subjected to tension, *International Journal of Mechanical Sciences* 43 2657-2677.

- Dolce, M., Cardone, D., Marnetto, R., 2000. Implementation and testing of passive control devices based on shape memory alloys. *Earthquake Engineering and Structural Dynamics* 29, 945-968.
- Duerig, T. W., Melton, K. N., Stockel, D., Wayman, C. M. (eds), 1990. *Engineering Aspects of Shape Memory Alloys*. Butterworth-Heinemann Co., London.
- Duerig, T., Stoeckel, D., Johnson, D., 2002. SMA - Smart materials for medical applications. *Proceedings of SPIE - The International Society for Optical Engineering* 4763, 7-15.
- Favier, D., Liu, Y., Orgeas, L., Rio, G., 2001. Mechanical instability of NiTi in tension, compression and shear. *Solid Mechanics and its Applications*, vol. 101. *Proceedings of IUTAM Symposium*. Kluwer Academic Publishers, Dordrecht, 205–212.
- Feng, P., Sun, Q.P., 2006. Experimental investigation on macroscopic domain formation and evolution in polycrystalline NiTi microtubing under mechanical force. *Journal of the Mechanics and Physics of Solids* 54, 1568-1603.
- Gong, J.M., Tobushi, H., Takata, K., Okumura, K., Endo, M., 2002. Cyclic superelastic deformation of TiNi shape-memory alloy. *Materials Science Forum* 394-395, 245-248.
- Hall, E. O., 1970. *Yield point phenomena in metals and alloys*. Macmillan, London.
- Han, Y.L., Li, A.Q., Lin, P.H., Li, Q.S., Leung, A.Y.T., 2003. Structural vibration control by shape memory alloy damper. *Earthquake Engineering and Structural Dynamics* 32, 483-494.
- Hebda, D.A., White, S.R., 1995. Effect of training conditions and extended thermal cycling on nitinol two-way shape memory behavior. *Smart Materials and Structures* 4, 298-304.
- Hu, Z., Sun, Q.P., Zhong, Z., 2007. Numerical simulation for stress-induced phase transformation of SMAs tube under tension. *Key Engineering Materials* 340-341, 1181-1186.

- Iadicola, M.A., Shaw, J.A., 2002a. An experimental setup for measuring unstable thermo-mechanical behavior of shape memory alloy wire. *Journal of Intelligent Material Systems and Structures* 13, 157-166.
- Iadicola, M.A.; Shaw, J.A., 2002b. The effect of uniaxial cyclic deformation on the evolution of phase transformation fronts in pseudoelastic NiTi wire. *Journal of Intelligent Material Systems and Structures* 13, 143-155.
- Iadicola, M.A., Shaw, J.A., 2004. Rate and thermal sensitivities of unstable transformation behavior in a shape memory alloy. *International Journal of Plasticity* 20, 577-605.
- Idesman, A.V., Levitas, V.I., Preston, D.L., Cho, J.-Y., 2005. Finite element simulations of martensitic phase transitions and microstructures based on a strain softening model. *Journal of the Mechanics and Physics of Solids* 53, 495-523.
- Inaba, T., Tokuda, M., Sugino, S., Warita, T., Sittner, P., Bundara, B., 2002. Experimental research on two-way shape memory effect of Cu-based SMA polycrystal. *Key Engineering Materials* 233-236, 553-558.
- Jardine, A.P., Flanagan, J., Martin, C.A., Carpenter, B.F., 1997. Smart wing shape memory alloy actuator design and performance. *Proceedings of SPIE - The International Society for Optical Engineering* 3044, 48-55.
- Kadkhodaei, M., Salimi, M.H., Rajapakse, R.K, Mahzoon, M., 2007. Modeling of shape memory alloys based on microplane theory. *Journal of Intelligent Material Systems and Structures*
- Khalil-Allafi, J., Hasse, B., Klönne, M., Wagner, M., Pirling, Th., Predki, W., Schmahl, W.W., 2004. In-situ diffraction investigation of superelastic NiTi shape memory alloys under mechanical stress with neutrons and with synchrotron radiation. *Materialwissenschaft und Werkstofftechnik* 35, 280-283.

- Kim, S.J., Abeyaratne, R., 1995. On the effect of the heat generated during a stress-induced thermoelastic phase transformation. *Continuum Mechanics and Thermodynamics* 7, 311-332.
- Kohl, M., Skrobanek, K.D., Miyazaki, S., 1999. Development of stress-optimized shape memory microvalves. *Sensors and Actuators, A: Physical* 72, 243-250.
- Kohl, M., 2004. *Shape Memory Microactuators*. Springer, Berlin.
- Kyriakides, S., 1993. Propagating instabilities in structures. *Advances in Applied Mechanics*, (ed. J.W. Hutchinson and T.Y. Wu) 30, 67-189. Academic Press, Boston.
- Kyriakides, S., Miller, J.E., 2000. On the propagation of Lüders bands in steel strips. *Journal of Applied Mechanics* 67, 645-654.
- Lagoudas, D.C., Bo, Z., Qidwai, M.A., 1996. Unified thermodynamic constitutive model for SMA and finite element analysis of active metal matrix composites. *Mechanics of Composite Materials and Structures* 3, 153-179.
- Leo, P.H., Shield, T.W., Bruno, O.P., 1993. Transient heat transfer effects on the pseudoelastic behavior of shape-memory wires. *Acta Metallurgica et Materialia* 41, 2477-2485.
- Li, Z.Q., Sun, Q.P., 2002. The initiation and growth of macroscopic martensite band in nano-grained NiTi microtube under tension. *International Journal of Plasticity* 18, 1481-1498.
- Liang, C., Rogers, C.A., 1990. One-dimensional thermomechanical constitutive relations for shape memory materials. *Journal of Intelligent Material Systems and Structures* 1, 207-234.
- Liang, C., Rogers, C.A., 1992. A Multi-dimensional constitutive model for shape memory alloys. *Journal of Engineering Mathematics* 26, 429-443.

- Lin, P.H., Tobushi, H., Tanaka, K., Hattori, T., Makita, M., 1994. Pseudoelastic behaviour of TiNi shape memory alloy subjected to strain variations. *Journal of Intelligent Material Systems and Structures* 5, 694-701.
- Liu, Y., Liu, Y., Van Humbeeck, J., 1998. Lüders-like deformation associated with martensite reorientation in NiTi. *Scripta Materialia* 39, 1047-1055.
- Liu, Y., Houver, I., Xiang, H., Bataillard, L., Miyazaki, S., 1999. Strain dependence of pseudoelastic hysteresis of NiTi. *Metallurgical and Materials Transactions A: Physical Metallurgy and Materials Science* 30, 1275-1282.
- Liu, Y., Xie, Z., Van Humbeeck, J., Delaey, L., Liu, Y., 2000. On the deformation of the twinned domain in NiTi shape memory alloys. *Philosophical Magazine A: Physics of Condensed Matter, Structure, Defects and Mechanical Properties* 80, 1935-1953.
- Lomer, W. M., 1952. The yield phenomenon in polycrystalline mild steel. *Journal of the Mechanics and Physics of Solids* 1, 64-73.
- McCormick, J., DesRoches, R., Fugazza, D., Auricchio, F., 2006. Seismic vibration control using superelastic shape memory alloys. *Journal of Engineering Materials and Technology, Transactions of the ASME* 128, 294-301.
- Messner, C., Reisner, G., Sun, Q.P., Werner, E., 2000. On instabilities and autocatalytic effects associated with the nucleation of martensite bands in polycrystalline SMA flat tensile specimens. *Computational Materials Science* 19, 313-319.
- Miyazaki, S., Otsuka, K., 1989, Development of shape memory alloys. *ISIJ International* 29, 353-377.

- Miyazaki, S., Otsuka, K., Suzuki, Y., 1981a. Transformation pseudoelasticity and deformation behavior in a Ti-50.6at%Ni alloy. *Scripta Metallurgica* 15, 287-292.
- Miyazaki, S., Imai, T., Otsuka, K., Suzuki, Y., 1981b. Lüders-like deformation observed in the transformation pseudoelasticity of a Ti-Ni alloy. *Scripta Metallurgica* 15, 853-856.
- Miyazaki, S., Imai, T., Igo, Y., Otsuka, K., 1986. Effect of cyclic deformation on the pseudoelasticity characteristics of Ti-Ni alloys. *Metallurgical Transactions A (Physical Metallurgy and Materials Science)* 17A, 115-120.
- Miyazaki, S., Otsuka, K., Wayman, C.M., 1989a. Shape memory mechanism associated with the martensitic transformation in Ti-Ni alloys. I. Self-accommodation. *Acta Metallurgica* 37, 1873-1884.
- Miyazaki, S., Otsuka, K., Wayman, C.M., 1989b. Shape memory mechanism associated with the martensitic transformation in Ti-Ni alloys. II. Variant coalescence and shape recovery. *Acta Metallurgica* 37, 1885-1890.
- Ng, K.L., Sun, Q.P., 2006. Stress-induced phase transformation and detwinning in NiTi polycrystalline shape memory alloy tubes. *Mechanics of Materials* 38, 41-56.
- Ohkata, I., Suzuki, Y., 1998. The design of shape memory alloy actuators and their applications. in Otsuka, K., Wayman, C.M., *Shape Memory Materials*. Cambridge University Press, UK, 240-266.
- Otsuka, K., Shimizu, K., 1981. Pseudoelasticity. *Metals Forum* 4, 142-152.
- Otsuka, K., Wayman, C.M., 1998. *Shape Memory Materials*. Cambridge University Press, UK.
- Pieczyska, E.A., Gadaj, S.P., Nowacki, W.K., Tobushi, H., 2004. Thermomechanical investigations of martensitic and reverse transformations in TiNi shape memory alloy. *Bulletin of the Polish Academy of Sciences: Technical Sciences* 52, 165-171.

- Pieczyska, E.A., Tobushi, H., Gadaj, S.P., Nowacki, W.K., 2006a. Superelastic deformation behaviors based on phase transformation bands in TiNi shape memory alloy. *Materials Transactions* 47, 670-676.
- Pieczyska, E.A., Gadaj, V., Nowacki, W.K., Tobushi, H., 2006b. Phase-transformation fronts evolution for stress- and strain-controlled tension tests in TiNi shape memory alloy. *Experimental Mechanics* 46, 531-542.
- Qidwai, M.A., Lagoudas, D.C., 2000. On thermomechanics and transformation surfaces of polycrystalline NiTi shape memory alloy material. *International Journal of Plasticity* 16, 1309-1343.
- Saadat, S., Noori, M., Davoodi, H., Hou, Z., Suzuki, Y., Masuda, A., 2001. Using NiTi SMA tendons for vibration control of coastal structures. *Smart Materials and Structures* 10, 695-704.
- Sachdeva, R.C.L., Miyazaki, S., 1990. Superelastic Ni-Ti alloys in orthodontics. in Duerig, T. W., Melton, K. N., Stockel, D., Wayman, C. M. (eds). *Engineering Aspects of Shape Memory Alloys*. Butterworth-Heinemann Co., London, 452-469.
- Sato, Y., Tanaka, K., 1988. Estimation of energy dissipation in alloys due to stress-induced martensitic transformation. *Res Mechanica* 23, 381-93.
- Shaw, J.A., 2000. Simulations of localized thermo-mechanical behavior in a NiTi shape memory alloy. *International Journal of Plasticity* 16, 541-562.
- Shaw, J.A., Kyriakides, S., 1995. Thermomechanical aspects of NiTi. *Journal of the Mechanics and Physics of Solids* 43, 1243-1281.
- Shaw, J.A., Kyriakides, S., 1997. On the nucleation and propagation of phase transformation fronts in a NiTi alloy. *Acta Materialia* 45, 683-700.

- Shaw, J.A., Kyriakides, S., 1998. Initiation and propagation of localized deformation elasto-plastic strips under uniaxial tension. *International Journal of Plasticity* 13, 837-871.
- Sittner, P., Lukas, P., Neov, D., Lugovyy, D., 2003. Martensitic transformations in NiTi polycrystals investigated by in-situ neutron diffraction. *Materials Science Forum* 426-432, 2315-20.
- Sittner, P., Liu, Y., Novak, V., 2005. On the origin of Lüders-like deformation of NiTi shape memory alloys. *Journal of the Mechanics and Physics of Solids* 53, 1719-1746.
- Song, C., Frank, T.G., Cuschieri, A., 2003. Application of high-pushing-force NiTi for minimal access surgery. *Journal De Physique IV* 112 1133-1136.
- Strelec, J.K., Lagoudas, D.C., Khan, M.A., Yen, J., 2003. Design and implementation of a shape memory alloy actuated reconfigurable airfoil. *Journal of Intelligent Material Systems and Structures* 14, 257-273.
- Strnadel, B., Ohashi, S., Ohtsuka, H., Miyazaki, S., Ishihara, T., 1995. Effect of mechanical cycling on the pseudoelasticity characteristics of Ti-Ni and Ti-Ni-Cu alloys. *Materials Science & Engineering A (Structural Materials: Properties, Microstructure and Processing)* A203, 187-96.
- Sun, Q.P., Zhong, Z., 2000. An inclusion theory for the propagation of martensite band in NiTi shape memory alloy wires under tension. *International Journal of Plasticity* 16, 1169-1187.
- Tan, G., Liu, Y., Sittner, P., Saunders, M., 2004. Lüders-like deformation associated with stress-induced martensitic transformation in NiTi. *Scripta Materialia* 50, 193-198.
- Tanaka, K., 1986. A thermomechanical sketch of shape memory effect: one-dimensional tensile behavior, *Res Mechanica* 18, 251-263.
- Tanaka, K., 1990. A phenomenological description on thermomechanical behavior of shape memory alloys. *Transactions of the ASME, Journal of Pressure Vessel Technology* 112, 158-163.

- Tanaka, K., Kobayashi, S., Sato, Y., 1986. Thermomechanics of transformation pseudoelasticity and shape memory effect in alloys. *International Journal of Plasticity* 2, 59-72.
- Tobushi, H., Yamada, S., Hachisuka, T., Ikai, A., Tanaka, K., 1996. Thermomechanical properties due to martensitic and R-phase transformations of TiNi shape memory alloy subjected to cyclic loadings. *Smart Materials and Structures* 5, 788-795.
- Tobushi, H., Shimeno, Y., Hachisuka, T., Tanaka, K., 1998. Influence of strain rate on superelastic properties of TiNi shape memory alloy. *Mechanics of Materials* 30, 141-50.
- Tobushi, H., Pieczyska, E., Gadaj, S., Nowacki, W.K., Hoshio, K., Makino, Y., 2005. Characteristics of energy storage and dissipation in TiNi shape memory alloy. *Science and Technology of Advanced Materials* 6, 889-94.
- Van Humbeeck, J., 2001. Shape memory alloys: a material and a technology. *Advanced Engineering Materials* 3, 837-50.
- Wayman, C. M., 1981. Shape Memory Effect. *Metals Forum* 4, 135-141.
- Wilson, J.C., Wesolowsky, M.J., 2005. Shape memory alloys for seismic response modification: A state-of-the-art review. *Earthquake Spectra* 21, 569-601.

Chapter 2: One-Dimensional Constitutive Model¹

This chapter describes the development of a one-dimensional constitutive model to capture the thermomechanical coupling and the localized phase transformations that occur during the dynamic response of shape memory alloys. The model is then implemented into a finite element code to simulate the dynamic behavior of a NiTi wire subjected to various thermomechanical loading conditions. The numerical simulations of the pseudoelastic response show close qualitative agreement with previously reported experimental data. Relaxation and restrained recovery in a partially transformed wire are also simulated to show the versatility of the model.

2.1. INTRODUCTION

Experiments have shown that the mechanical response of shape memory alloys is highly sensitive to loading rate (Leo et al., 1993; Shaw and Kyriakides, 1995, 1997; Tobushi et al., 1998; Pieczyska et al., 2006a,b). The origin of this rate-dependent behavior, however, is not the usual viscoelastic effect, but rather it arises from the complex coupling that exists among stress, temperature, and the rate of heat generation during stress-induced phase transformations.

A typical quasi-static (isothermal) pseudoelastic behavior of NiTi SMA is shown schematically in Figure 2-1(a). When a unidirectional stress is applied to an SMA sample at a very slow strain rate, the forward (a-b) and reverse (d-e) transformations propagate at constant stresses manifested by two stress plateaus.

¹ Parts of this chapter have been published in the following paper: Azadi, B., Rajapakse R.K.N.D., Maijer, D. M., 2006. One-dimensional thermomechanical model for dynamic pseudoelastic response of SMA. *Smart Materials and Structures* 15, 996-1008.

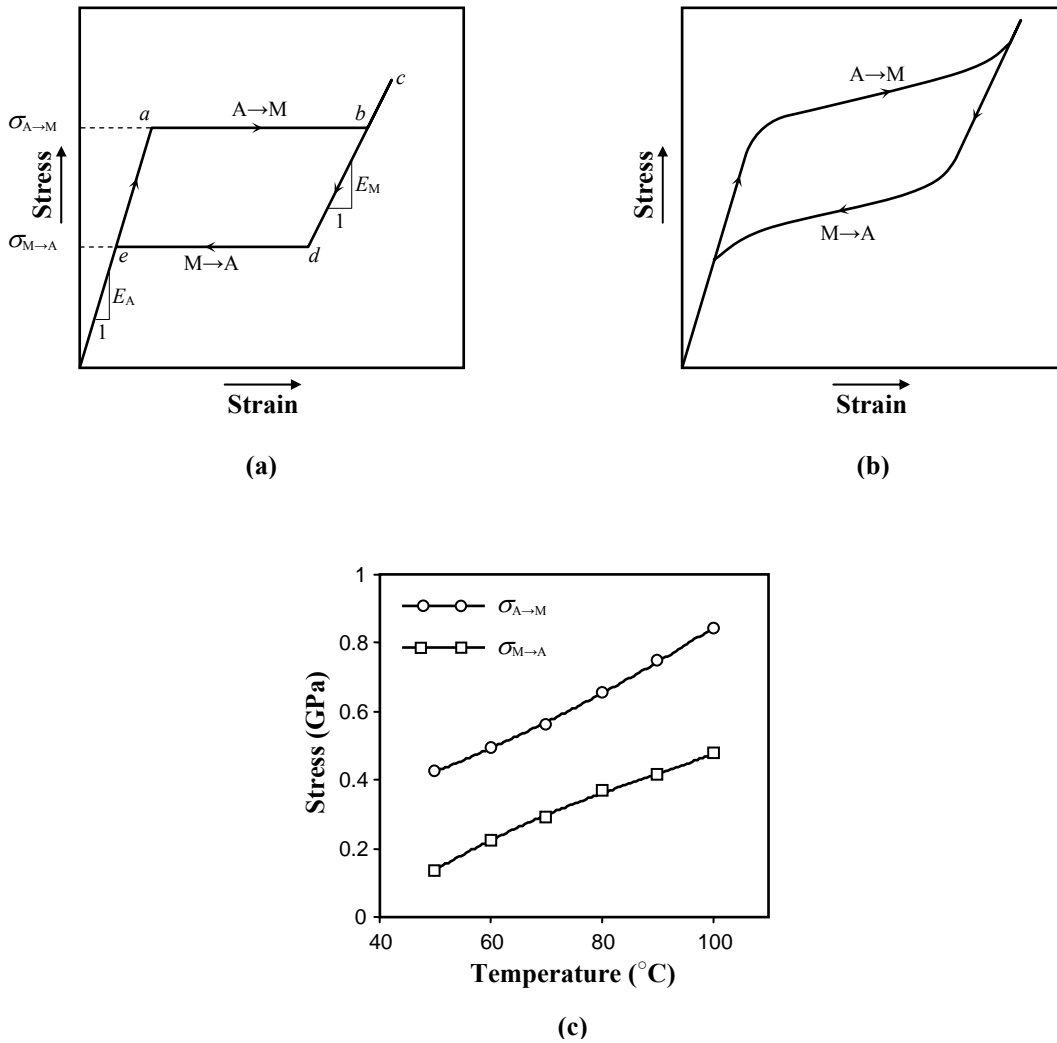


Figure 2-1. Pseudoelasticity in NiTi shape memory alloy. (a) Isothermal quasi-static displacement-controlled response; (b) Stress-strain response at high strain rate; (c) Variation of transformation stresses with temperature (Shaw and Kyriakides, 1995).

Similar to other solid-state transformations, some amount of heat is released during the transformation from austenite to martensite, or absorbed during the reverse transformation. Because the forward and reverse transformation stresses ($\sigma_{A \rightarrow M}$ and $\sigma_{M \rightarrow A}$) are strongly dependent on temperature (see Figure 1c), the internal self-heating or cooling that occur during the transformation can influence the mechanical response of the material. At very slow strain rates with effective heat

transfer to the environment, the latent heat of transformation is dissipated fast enough to prevent a significant change in temperature. At higher strain rates on the other hand, the effect of local heating/cooling on the transformation stress is not negligible, and a distinct stress plateau is no longer distinguishable as shown in Figure 1(b).

Experiments have shown that the stress-induced transformations in NiTi shape memory alloys are inhomogeneous in nature and result in distinctly nonuniform and propagating deformations (Shaw and Kyriakides, 1995, 1997; Tan et. al., 2004; Pieczyska et al., 2004, 2006a,b; Feng and Sun, 2006). This localization phenomenon, also known as Lüders-like deformation, adds to the complexity of the SMAs' behavior. Due to localization of deformation, the local strain rate at the transformation front is significantly amplified compared to the global strain rate. Consequently, even at fairly low strain rates the local temperature changes at transformation fronts become large enough to change the magnitude of the stress required to transform the rest of the material. In order for a constitutive model to capture such localized behaviors and the rate dependency of shape memory alloys, both the mutual interaction of stress-temperature, and the inhomogeneous nature of phase transformation must be taken into account.

In this chapter, a one-dimensional thermomechanical model of SMAs is developed in order to simulate the nucleation and propagation of transformation front(s) in an SMA wire. The thermomechanical coupling among the transformation stress, internal heating/cooling, and the heat exchanges with the ambient medium are considered thus allowing the model to capture the strain rate effects. The *local* martensitic fraction is a basic variable which is defined as the volume fraction of martensite at a point. Based on the definition of martensitic fraction and by using the basic continuum mechanics method, a constitutive relation is derived that relates the increment of total strain to those of stress, temperature, and martensitic fraction. The kinetics of transformation is controlled by a transformation evolution rule which determines the increment of stress in terms of the increments of

temperature and martensitic fraction during the phase transformation. The transformation evolution rule is expressed in terms of a set of transformation surfaces in the stress-temperature space. The model allows for the determination of the amount of phase transformation under a constant mechanical load and varying ambient temperature. The model also includes a variable nucleation criterion for the initiation of transformation, which is dependent on the distance of a material point from the fully transformed regions.

2.2. CONSTITUTIVE RELATIONS

In this section, the derivation of constitutive relations for a simplified one-dimensional element of SMA material is presented.

2.2.1. Introduction of local martensitic fraction

The observation of unstable propagation of the transformation fronts in SMAs suggests that it is necessary to consider the stress-induced transformation as a local phenomenon which takes place at a material point. Although there is evidence of some small homogeneous phase transformations in the stable part of the pseudoelastic response (Brinson et al., 2004; Daly et al., 2007), it is assumed here that in general, phase transformation occurs in an inhomogeneous fashion. Therefore, *the local martensitic fraction* γ is introduced to describe the volumetric fraction of the martensitic phase at a point. The average martensitic fraction over a volume V , which is denoted by $\bar{\gamma}$ may be expressed in terms of the local martensitic fraction γ as:

$$\bar{\gamma} = \frac{1}{V} \int_V \gamma \, dV \quad (2-1)$$

Consider an incremental one-dimensional element of material that has been partially transformed as shown in Figure 2-2. If a uniaxial stress denoted by σ is applied to this element, the total elastic strain of the element $\varepsilon^{(e)}$ is obtained as:

$$\varepsilon^{(e)} = \left(\frac{\gamma}{E_M} + \frac{1-\gamma}{E_A} \right) \sigma \quad (2-2)$$

where E_M and E_A are the elastic modulus of martensite and austenite, respectively (see Figure 2-1).

The local martensitic fraction γ is also defined as:

$$\gamma = \frac{dL_M}{dL_M + dL_A} \quad (2-3)$$

where dL_M and dL_A are proportional to the volume of martensite and austenite phases, as shown in Figure 2-2. The value of γ therefore can vary from 0 to 1 with $\gamma=0$ corresponding to a fully austenite phase and $\gamma=1$ corresponding to a fully martensite phase.

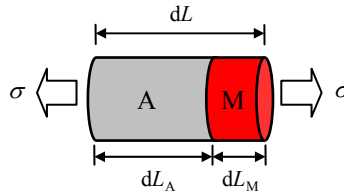


Figure 2-2. A partially transformed one-dimensional element.

Equation (2-2) can be rewritten in the following form:

$$\varepsilon^{(e)} = \frac{\sigma}{E(\gamma)} \quad (2-4)$$

where E is the *effective elastic modulus* of the element given by:

$$E(\gamma) = \frac{E_A E_M}{\gamma E_A + (1-\gamma) E_M} \quad (2-5)$$

Note that the effective elastic modulus, E , is obtained as a nonlinear function of γ .

2.2.2. Strain decomposition

It is well known that during the stress-induced martensitic transformation some amount of seemingly permanent strain is produced due to the formation of detwinned single variant martensite. If this transformation-induced strain is denoted by $\Delta\varepsilon_t$, the total transformation strain for the element shown in Figure 2-2 will be equal to:

$$\varepsilon^{(t)} = \frac{dL_M \Delta\varepsilon_t}{dL_M + dL_A} = \gamma \Delta\varepsilon_t \quad (2-6)$$

Next, it is assumed that the total strain of the element (ε) can be expressed as the summation of elastic and transformation strains as:

$$\varepsilon = \varepsilon^{(e)} + \varepsilon^{(t)} = \frac{\sigma}{E(\gamma)} + \gamma \Delta\varepsilon_t \quad (2-7)$$

Parameter $\Delta\varepsilon_t$ in the above equations is a material property and must be determined through experimental data. In order to experimentally measure the value of $\Delta\varepsilon_t$, consider the typical stress-strain response of a shape memory wire during a slow strain-rate isothermal loading-unloading experiment, as shown in Figure 2-1(a). Ideally, the experimental stress-strain response used to calibrate the model must be obtained through the local measurements of stress and strain at a point similar to the measurements of Shaw and Kyriakides (1995) by miniature extensometers. As an approximation, it is assumed that the forward transformation starts at point *a* and ends at the end of the stress plateau, point *b*. Based on previous equations, the total strain at point *b* ($\gamma = 1$) is given by:

$$\varepsilon|_b = \frac{\sigma_{A \rightarrow M}}{E_M} + \Delta\varepsilon_t$$

which can be used to find $\Delta\varepsilon_t$ as,

$$\Delta\varepsilon_t = \varepsilon|_b - \frac{\sigma_{A \rightarrow M}}{E_M} \quad (2-8)$$

Alternatively, the information related to point d can also be used to find $\Delta\varepsilon_t$ as,

$$\Delta\varepsilon_t = \varepsilon|_d - \frac{\sigma_{M \rightarrow A}}{E_M} \quad (2-9)$$

It should be noted that the value of transformation strain $\Delta\varepsilon_t$ differs from the length of stress plateau observed during the forward or reverse transformations. From the above equations, it can be shown that the length of stress plateau during loading is given by,

$$\varepsilon|_b - \varepsilon|_a = \Delta\varepsilon_t + \left(\frac{1}{E_M} - \frac{1}{E_A} \right) \sigma_{A \rightarrow M} \quad (2-10)$$

and during unloading by,

$$\varepsilon|_d - \varepsilon|_e = \Delta\varepsilon_t + \left(\frac{1}{E_M} - \frac{1}{E_A} \right) \sigma_{M \rightarrow A} \quad (2-11)$$

Therefore, the lengths of both stress plateaus are greater than the amount of transformation-induced strain in the present model. It can also be seen from equations (2-10) and (2-11) that the upper stress plateau is longer than the lower one, which is due to the change in the elastic portion of strain upon unloading at a lower stress. Interestingly, this result is in agreement with the experimental stress-strain curves which often exhibit shorter reverse plateaus (Tan et al., 2002). Experimental results have also revealed that the length of the stress plateau increases with increasing test temperatures (Shaw and Kyriakides, 1995; Tan et al., 2002). This observation has led to a common belief that the amount of transformation-induced strain ($\Delta\varepsilon_t$) also depends on temperature (or stress level). Figure 2-3 compares the measured length of the stress plateau during loading and the calculated transformation strain based on equation (2-8) at various temperatures. The values of $\varepsilon|_a$,

$\varepsilon|_b$, $\sigma_{A \rightarrow M}$, and E_M are taken from the experimental stress-strain curves reported by Shaw et al., (2003). In this figure, the transformation strain calculated from equation (2-8) or (2-10) does not exhibit such a strong temperature-dependency. Therefore, it is assumed that the transformation strain ($\Delta\varepsilon_t$) is independent of temperature or stress.

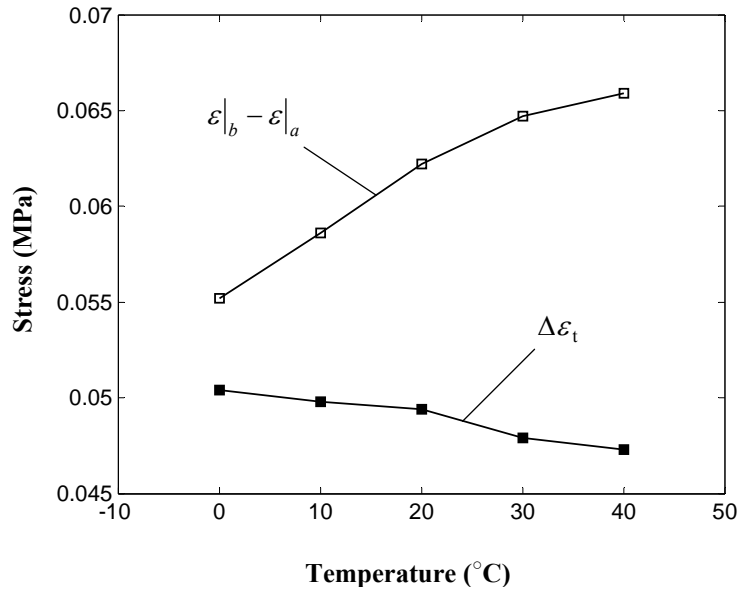


Figure 2-3. Variations of stress-plateau length and transformation strain with temperature.

Since the constitutive relations described in the above equations are non-linear, it is more appropriate to express them in incremental form in order to facilitate the numerical solutions. The incremental relation obtained from equations (2-5) and (2-7) is,

$$d\varepsilon = \left(\frac{\gamma}{E_M} + \frac{1-\gamma}{E_A} \right) d\sigma + \left(\frac{\sigma}{E_M} - \frac{\sigma}{E_A} + \Delta\varepsilon_t \right) d\gamma \quad (2-12)$$

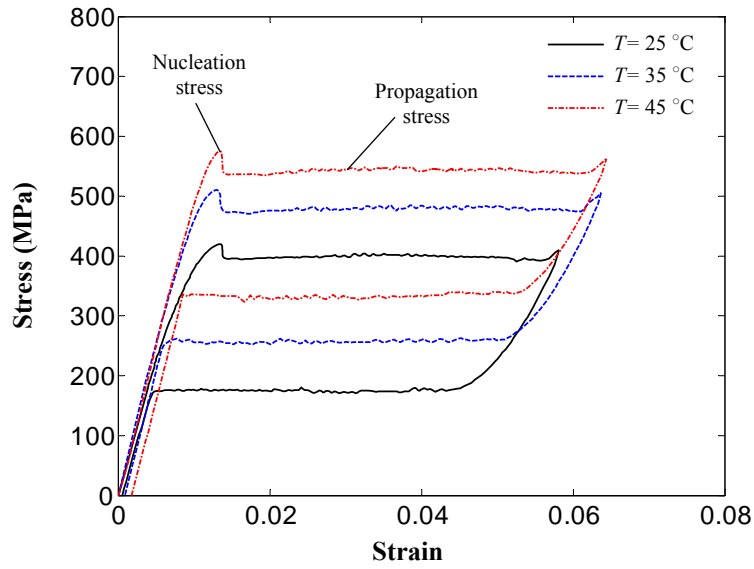
which is the increment of total strain in terms of the increments of stress, temperature, and martensitic fraction at a point. This relationship holds at any instant whether the material point is undergoing an elastic deformation ($d\gamma = 0$) or a phase transformation ($d\gamma \neq 0$). It will be shown in the next section

that the increment of stress is related to the increments of temperature and martensitic fraction via the transformation evolution rule.

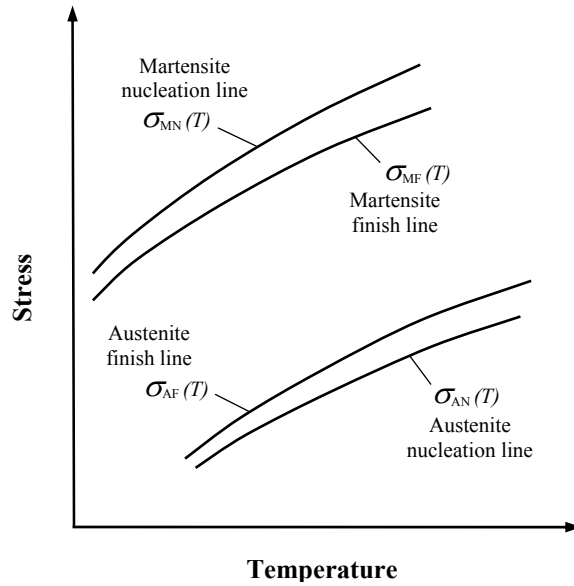
2.2.3. Nucleation and evolution of transformation

In an isothermal quasi-static test, once the transformation starts (nucleation), the level of stress is kept constant and the transformation appears to be more strain-driven than stress-driven. However, it is the level of stress that determines whether the current phase is stable or not. On the other hand, stress is not the only factor that makes the microstructure unstable: a change in temperature may also result in instability and initiation of transformation. At higher strain rates, where both stress and temperature are varying during the phase transformation, the effect of temperature on the production of detwinned martensite must also be considered (temperature-induced martensitic transformation). In this section, the governing incremental equations of phase transformation (kinetic relations) are developed for the most general case in which the temperature may also change and result in transformation; that is, both the stress-induced and temperature-induced transformations are taken into account.

Using carefully designed experiments, Shaw and Kyriakides (1997) and Iadicola and Shaw (2002) have shown that during the loading stage, the nucleation of martensite occurs at a distinctly higher stress than that required to subsequently continue the transformation, as shown in Figure 2-4(a) and also Figure 1-9. By contrast, the nucleation stress of austenite in a martensitic region during unloading is lower than the stress required to propagate the transformation (Because of the particular shape of the specimen used in the experiments, a stress valley at the beginning of the reverse transformation is not observed in Figure 2-4(a), however, the inverse stress peak during unloading is clearly seen in Figure 1-9).



(a)



(b)

Figure 2-4. (a) Nucleation and propagation stresses during displacement-controlled tests of NiTi dog-bone strips (experimental data adapted from Shaw, 2000). (b) Schematic representation of nucleation and finish lines used in the model

Shaw and Kyriakides (1997) mentioned that these characteristics are similar to the properties of other propagating structural instabilities such as neck propagation in polymers or mild steel. All of these quasi-static displacement-controlled loading examples exhibit initiation (nucleation) loads that are distinctly higher than the lowest load required to propagate the instability.

Based on these observations, it is assumed here that at any temperature, the nucleation stress for untransformed particles $\gamma = 0$ (or $\gamma = 1$ for reverse transformation) is slightly higher (or lower) than the stress required to complete the transformation of a partially transformed particle ($0 < \gamma < 1$). In order to specify a stability margin for the nucleation of the new phase, an idea similar to the concept of a yield surface in plasticity theory is introduced here. In the case of a forward transformation, a *martensite nucleation surface (line)* is defined in the stress-temperature space, which determines the highest possible energy level for an austenite particle to be stable. Once the stress-temperature vector reaches the nucleation surface, martensite is nucleated and further loading results in the *continuation of transformation*. During the continuation of transformation, the stress-temperature vector moves towards a lower energy state. The lowest energy level, which determines the completion of transformation for a partially transformed particle is defined by another surface in the stress-temperature space, which is called the *martensite finish surface (line)*. Similarly, *austenite nucleation and finish surfaces (lines)* are also defined for reverse transformation. In one-dimensional cases, in which only one stress component exists, these surfaces are reduced to a set of four curved lines, which are schematically shown in Figure 2-4(b). These curves can be determined through a set of quasi-static tests at various temperatures (similar to those shown in Figure 2-4a).

So far, the qualitative transformation behavior of a material during nucleation and propagation was described. In order to quantify the direction of incremental changes during the transformation at a local material point, it is necessary to introduce the corresponding *transformation evolution rule* for forward and reverse transformations. In other words, it is required to fix the path of

incremental changes in the stress-temperature space from the nucleation line towards the finish line. To this end, it is assumed that the stress-temperature vector always lies on an *instantaneous transformation line* during the evolution from the highest energy level (nucleation line) to the lowest energy level (finish line). The location of this instantaneous transformation line is somewhere between the nucleation and finish lines and is determined by the martensitic fraction γ . The instantaneous martensite transformation line for a given value of γ is defined by the following equation:

$$F_{A \rightarrow M}(\sigma, \gamma, T) \equiv \sigma - \sigma_M(\gamma, T) = 0 \quad (2-13)$$

For the first nucleation of forward transformation in an austenite area, σ_M satisfies the following conditions:

$$\begin{cases} \sigma_{MF}(T) \leq \bar{\sigma}_M(\gamma, T) \leq \sigma_{MN}(T) \\ \sigma_M(0, T) = \sigma_{MN}(T) \\ \sigma_M(1, T) = \sigma_{MF}(T) \end{cases} \quad (2-14)$$

σ_{MN} and σ_{MF} in the above equation determine the martensite nucleation and finish lines as depicted in Figure 2-4(b). Similarly, the instantaneous austenite transformation line is also defined as:

$$F_{M \rightarrow A}(\sigma, \gamma, T) \equiv \sigma - \sigma_A(\gamma, T) = 0 \quad (2-15)$$

and σ_A satisfies the following conditions for the nucleation of first austenitic element in a fully martensite region:

$$\begin{cases} \sigma_{AN}(T) \leq \bar{\sigma}_A(\gamma, T) \leq \sigma_{AF}(T) \\ \sigma_A(1, T) = \sigma_{AN}(T) \\ \sigma_A(0, T) = \sigma_{AF}(T) \end{cases} \quad (2-16)$$

where σ_{AN} and σ_{AF} are the austenite nucleation and finish stresses as shown in Figure 2-4(b).

The simplest way to specify the form of instantaneous transformation lines is through the linear interpolation of nucleation and finish stresses. That is,

$$\sigma_M(\gamma, T) = (1 - \gamma)\sigma_{MN}(T) + \gamma\sigma_{MF}(T) \quad (2-17)$$

and,

$$\sigma_A(\gamma, T) = \gamma\sigma_{AN}(T) + (1 - \gamma)\sigma_{AF}(T) \quad (2-18)$$

Shaw and Kyriakides (1997) argued that once the new phase is nucleated, the stress field associated with each transition front provides a trigger mechanism for transforming the untransformed adjacent grains. Thus, as in other problems of this class, it is expected that the initiation stress for transformation of austenitic particles located adjacent to the fully transformed regions be smaller than the nucleation stress of those surrounded by the parent phase. The same scenario is also expected for the partially transformed particles. Therefore, it is assumed that there is an *instantaneous martensite nucleation line* $\sigma_{MN}^*(T)$ defined for partially transformed particles ($0 < \gamma < 1$), or austenitic particles ($\gamma = 0$) that are located close² to the interface of two phases (transformation front). For austenite particles surrounded by other austenite aggregates, this line coincides with the nucleation line $\sigma_{MN}(T)$. In other cases, the instantaneous martensite nucleation line is located somewhere between the martensite nucleation line $\sigma_{MN}(T)$ and martensite finish line $\sigma_{MF}(T)$ depending on the current state of stress, temperature, martensitic fraction, and distance from the transformation fronts (see Appendix A for details). The transformation evolution rule in this

² The region that is affected by the transformation front is physically characterized by a narrow transition zone which separates the austenite and martensite phases (Figure 1-7). It is needed to mathematically clarify the meaning of “close”. For a fully transformed material particle located at point x , a radius of influence ξ is defined so that for particles located in $[x - \xi, x + \xi]$, the instantaneous nucleation surface is used rather than the nucleation surface. Later in the FEM analysis it will be assumed that ξ is equal to the length of each element.

case is applied to calculate the amount of transformation by replacing $\sigma_{MN}(T)$ by $\sigma_{MN}^*(T)$ in equation 2-17. Similarly, an *instantaneous austenite nucleation line* $\sigma_{AN}^*(T)$ is also defined for the reverse transformation of partially transformed particles ($0 < \gamma < 1$), or martensite particles ($\gamma = 1$) that are close² to the austenite/martensite interface. Hence, the instantaneous transformation stresses in the general case are replaced by,

$$\sigma_M(\gamma, T) = (1 - \gamma)\sigma_{MN}^*(T) + \gamma\sigma_{MF}(T) \quad (2-19)$$

and,

$$\sigma_A(\gamma, T) = \gamma\sigma_{AN}^*(T) + (1 - \gamma)\sigma_{AF}(T) \quad (2-20)$$

where $\sigma_{MN}^*(T)$ and $\sigma_{AN}^*(T)$ may or may not coincide with $\sigma_{MN}(T)$ and $\sigma_{AN}(T)$, respectively.

The instantaneous transformation lines defined in equations (2-13) and (2-15) together with (2-19) and (2-18) determine the onset of transformations in the stress-temperature space. Once the transformation starts, the evolution of transformation is governed by the following evolution rules:

$$\begin{cases} dF_{M \rightarrow A}(\sigma, \gamma, T) = 0, & \text{Forward transformation (d } \gamma > 0) \\ dF_{A \rightarrow M}(\sigma, \gamma, T) = 0, & \text{Reverse transformation (d } \gamma < 0) \end{cases} \quad (2-21)$$

The above transformation evolution rules together with the constitutive relation in equation (2-12) can be used to calculate the increments of stress ($d\sigma$) and martensitic fraction ($d\gamma$) in terms of the increments of total strain ($d\varepsilon$) and temperature (dT). The details of numerical calculations based on the concepts of instantaneous nucleation line and transformation evolution rule are presented in Appendix A.

It should be noted that the observed nucleation and propagation stresses in a uniaxial experiment, such as those shown in Figure 2-4(a), dependent on both the microstructure of the material and its geometry. Therefore in the present one-dimensional model, the nucleation and finish stresses (σ_{MN} , σ_{AN} , σ_{MF} , σ_{MF}) are measured/chosen for a particular wire geometry.

2.2.4. Heat of transformation

In order to consider the effect of heat released during phase transformation, the conservation of energy must be ensured. The incremental form of the conservation equation is,

$$\sigma d\varepsilon = du^{(e)} + du^{(i)} + dq_G \quad (2-22)$$

where $u^{(e)}$ (J/m^3) is the elastic energy density, $u^{(i)}$ (J/m^3) is the specific internal energy (excluding the elastic energy), and q_G (J/m^3) is the heat generated per unit volume. The elastic energy density is given by,

$$u^{(e)} = \frac{1}{2} E(\gamma) [\varepsilon^{(e)}]^2 \quad (2-23)$$

Using (2-4), (2-5) and (2-23) the change in the elastic energy density is obtained as,

$$du^{(e)} = \sigma d\varepsilon^{(e)} - \frac{1}{2} \left(\frac{1}{E_M} - \frac{1}{E_A} \right) \sigma^2 d\gamma \quad (2-24)$$

Substituting (2-7 and (2-24) in equation (2-22) gives,

$$dq_G = -du^{(i)} + \frac{1}{2} \left(\frac{1}{E_M} - \frac{1}{E_A} \right) \sigma^2 d\gamma + \sigma \Delta\varepsilon_t d\gamma$$

or,

$$\dot{q}_G = -\dot{u}^{(i)} + \left[\frac{1}{2} \left(\frac{1}{E_M} - \frac{1}{E_A} \right) \sigma^2 + \sigma \Delta\varepsilon_t \right] \dot{\gamma} \quad (2-25)$$

where ($\dot{}$) denotes the time derivative ($\frac{d}{dt}$). Next, it is assumed that the rate of change in the specific internal energy $\dot{u}^{(i)}$ (W/m³) is proportional to the rate of transformation ($\dot{\gamma}$). That is,

$$\dot{u}^{(i)} = \begin{cases} \rho \Delta h_{A \rightarrow M} \dot{\gamma}, & \text{Forward transformation } (\dot{\gamma} > 0) \\ -\rho \Delta h_{M \rightarrow A} \dot{\gamma}, & \text{Reverse transformation } (\dot{\gamma} < 0) \end{cases} \quad (2-26)$$

where ρ (Kg/m³) is the material density, and $\Delta h_{A \rightarrow M}$ and $\Delta h_{M \rightarrow A}$ (J/Kg) are the total changes in enthalpy during the forward and reverse transformation at zero stress, respectively.

The values of $\Delta h_{A \rightarrow M}$ and $\Delta h_{M \rightarrow A}$ can be determined through Differential Scanning Calorimetry (DSC) tests. The rate of heat generation is therefore given by,

$$\dot{q}_G = \begin{cases} \left[-\rho \Delta h_{A \rightarrow M} + \frac{1}{2} \left(\frac{1}{E_M} - \frac{1}{E_A} \right) \sigma^2 + \sigma \Delta \varepsilon_t \right] \dot{\gamma}, & \text{Forward transformation } (\dot{\gamma} > 0) \\ \left[\rho \Delta h_{M \rightarrow A} + \frac{1}{2} \left(\frac{1}{E_M} - \frac{1}{E_A} \right) \sigma^2 + \sigma \Delta \varepsilon_t \right] \dot{\gamma}, & \text{Reverse transformation } (\dot{\gamma} < 0) \end{cases} \quad (2-27)$$

2.3. NUMERICAL EXAMPLES

In this section, the pseudoelastic response of a NiTi wire subjected to various thermomechanical loadings is determined based on the proposed model. The capabilities of the model in simulating the rate effects, propagation of instabilities, and temperature-induced transformations are demonstrated. Some of the simulation results are compared with the experimental observations of Shaw and Kyriakides (1995). A summary of their experimental procedure is provided in Appendix B.

2.3.1. Finite element model

The constitutive model was implemented in a nonlinear finite element (FE) code, which was developed by using FORTRAN as an in-house numerical tool. The wire was discretized into one-dimensional rod elements with linear shape functions. The coupled mechanical and thermal equilibrium equations were solved using a modified Newton-Raphson non-linear iterative scheme. The step-by-step integration of the heat transfer equation with time was calculated using the Backward Euler method which is unconditionally stable. A summary of the finite element formulation and the non-linear calculations are given in Appendix C. The convergence with respect to time was obtained by choosing a small enough time step for each simulation. The chosen time step was equal to $10^{-6} / \dot{\epsilon}$ (s) where $\dot{\epsilon}$ is the applied strain-rate measured in s^{-1} . The effect of inertia was neglected due to its minor effects.

For each of the following simulations, the numerical analysis was repeated with different element sizes to ensure the convergence of the results. Further refinement of the mesh did not alter the results of the simulations reported here. In each case, the radius of influence (ξ), which is used to determine whether a Gauss integration point is close to a fully transformed region (see the footnotes in Section 2.3.3), was assumed to be equal to the length of each element.

The diameter and the gauge length of the wire were assumed to be $D=1.07$ mm and $L_G=63.5$ mm, respectively. These values were chosen based on the specimen used by Shaw and Kyriakides (1995). The gripped ends of the wire were each assumed to have a length of $0.2L_G$. The gauge length and the gripped lengths of the wire were discretized respectively into 50 and 10 elements, as shown in Figure 2-5. In order to produce stress concentrations at the grips, the cross-sectional area of the very first and last elements of the gauge length were reduced by 10% and 15%, respectively (the elements

with reduced cross-sectional areas are shown by “v” in Figure 2-5). These values were chosen arbitrarily to cause a stress concentration in one end that was higher than the other end.

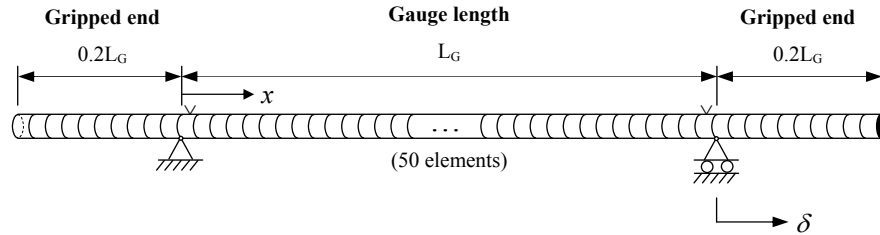


Figure 2-5. Finite element discretization of the wire.

The thermal interaction between the wire and the environment was taken into account by assigning a constant heat transfer coefficient (h) to the external surface of each element as shown in Figure 2-6. The heat transfer was considered by employing the following one-dimensional equation:

$$-\frac{\partial}{\partial x} \left(k \frac{\partial T}{\partial x} \right) + \rho C_p \dot{T} + \frac{4h}{D} (T - T_\infty) = \dot{q}_G \quad (2-28)$$

where k is the conductivity (W/m K), C_p is the heat capacity (J/kg K), T_∞ is the ambient temperature (K), and \dot{q}_G is the heat generation term given in equation (2-27).

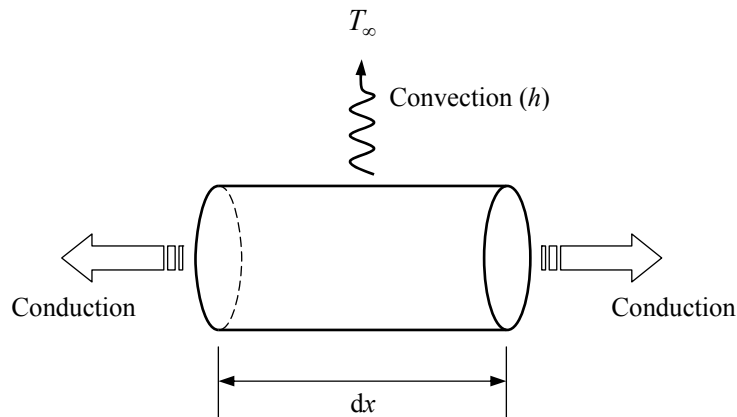


Figure 2-6. Heat transfer mechanisms in a one-dimensional element.

The ambient temperature was held constant at $T_\infty = 70^\circ\text{C}$. The temperatures of the two ends of the rod ($x = -0.2L_G, 1.2L_G$) were also assumed to be constant and equal to the ambient temperature (70°C). This is a reasonable assumption since the grips were also held inside the thermal bath during the actual experiments. The thermal expansion/contraction was neglected in the following simulations due to its minor effect on the results.

The thermo-physical properties of a material in general depend on the phase (martensite or austenite), temperature, stress and strain. However, as a first approximation, the thermo-physical properties are considered to be independent of all state variable. Table 2-1 shows the chosen thermal and mechanical parameters. The thermal conductivity (k), specific heat (C_p), density (ρ), and enthalpy change during forward transformation ($\Delta h_{A \rightarrow M}$) were taken from Shaw (2000), although the composition of NiTi alloy used by Shaw and Kyriakides (1995) is slightly different from that used in Shaw (2000). It was assumed that the zero-stress enthalpy change during the reverse transformation ($\Delta h_{M \rightarrow A}$) is the same as that during the forward transformation ($-\Delta h_{A \rightarrow M}$). A few different values of heat transfer coefficient (h) in the range typical for stagnant air and water environments (Incropera and DeWitt, 1996) were tried. The values of h were chosen based on the best fit to the experimental results. The values of elastic modulus (E_A, E_M) and transformation strain ($\Delta \varepsilon_t$) are the average values calculated based on the local measurements reported by Shaw and Kyriakides (1995). It was assumed that $\Delta \varepsilon_t$ is constant and does not change with temperature. The transformation finish stresses (σ_{MF}, σ_{AF}) were assumed to be the same as the propagation stresses given in Figure 2-1, approximated by the following linear functions of temperature:

$$\sigma_{MF}(T) = \sigma_{MP}(T) = 8.1682 \times 10^6 T - 9.6269 \times 10^6 \quad (2-29)$$

$$\sigma_{AF}(T) = \sigma_{AP}(T) = 7.1248 \times 10^6 T - 1.9524 \times 10^8 \quad (2-30)$$

Due to stress concentrations at the gripped ends of the specimens in the experiments of Shaw and Kyriakides (1995), the exact measurements of nucleation stresses are not possible from the experimental data. Based on the experimental results presented by Shaw and Kyriakides (1997) and Iadicola and Shaw (2002), it is known that the apparent nucleation stress during forward transformation σ_{MN} is approximately between 10% to 20% higher than the propagation stress σ_{MP} . In the case of reverse transformation the nucleation stress σ_{AN} is between 17% to 30% lower than the propagation stress σ_{AP} . In the following simulation it was assumed that σ_{MN} and σ_{AN} respectively are 14% higher and 20% lower than the corresponding propagation stresses. That is,

$$\sigma_{MN} = 1.14\sigma_{MF}(T) = 9.3117 \times 10^6 T - 10.9747 \times 10^6 \quad (2-31)$$

$$\sigma_{AN} = 0.8\sigma_{AF}(T) = 5.6998 \times 10^6 T - 1.5619 \times 10^8 \quad (2-32)$$

The above values seemed to give reasonable results. The variation of nucleation and finish stresses with temperature are plotted in Figure 2-7.

Table 2-1. Thermo-physical properties of the NiTi wire and ambient

Parameter		Value
Elastic modulus of austenite	E_A (GPa)	74.21
Elastic modulus of martensite	E_M (GPa)	25.53
Transformation strain	$\Delta\varepsilon_t$	0.0415
Stress-free enthalpy change	$\Delta h_{A \rightarrow M}, -\Delta h_{M \rightarrow A}$ (J kg ⁻¹)	12300
Density	ρ (kg m ⁻³)	6500
Thermal conductivity	k (W m ⁻¹ K ⁻¹)	18
Specific heat capacity	C_p (J kg ⁻¹ K ⁻¹)	837
Heat convection coefficient in air	h_{air} (W m ⁻² K ⁻¹)	15
Heat convection coefficient in water	h_{water} (W m ⁻² K ⁻¹)	400

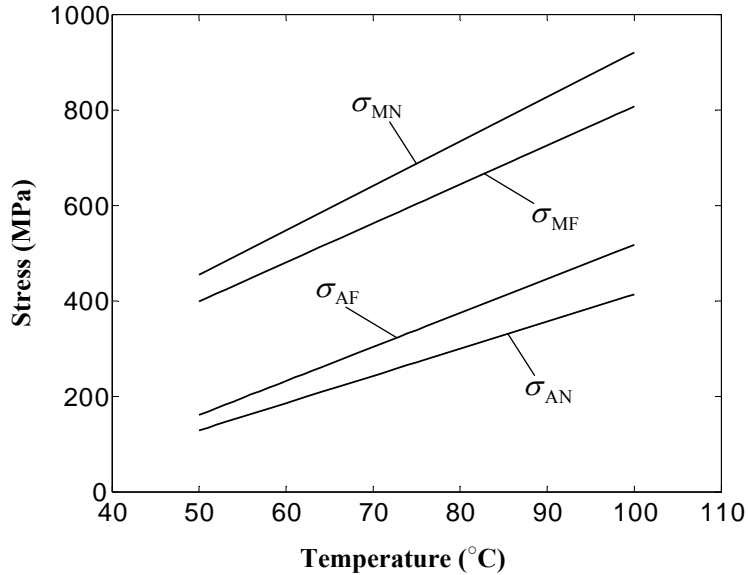


Figure 2-7. Nucleation and finish lines used in the simulations.

2.3.2. Displacement-controlled loading-unloading

A series of displacement controlled loading-unloading simulations at various displacement rates were conducted. The results compared to the experimental data from Shaw and Kyriakides (1995) are presented in this section.

2.3.2.1. Simulation of pseudoelastic behavior at low strain-rate

The behavior of the NiTi wire during one loading-unloading cycle at a constant displacement rate of $\dot{\delta}/L_G = 4 \times 10^{-5} \text{ s}^{-1}$ was simulated. The simulated stress-strain response is compared with experimental data in Figure 2-8(a). The temperature profile along the wire at various times is shown in Figure 2-8(b). As can be seen the variation in temperature is very small, which agrees with the experimental observations of Shaw and Kyriakides (1995). The predicted evolution of phase transformation is compared with experimental observations in Figure 2-9. In these plots, δ is the displacement of the end point and x shows the location along the wire as defined in Figure 2-5.

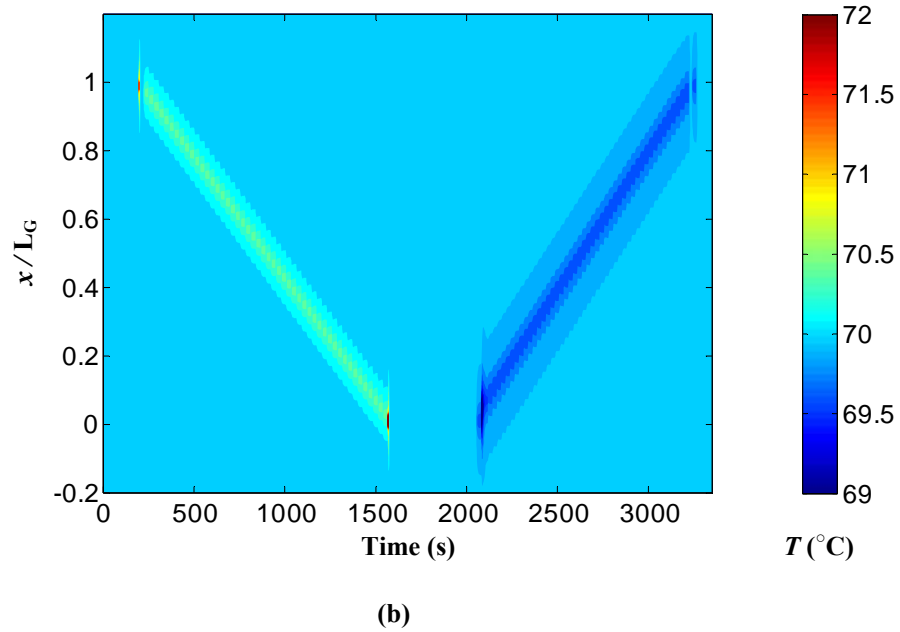
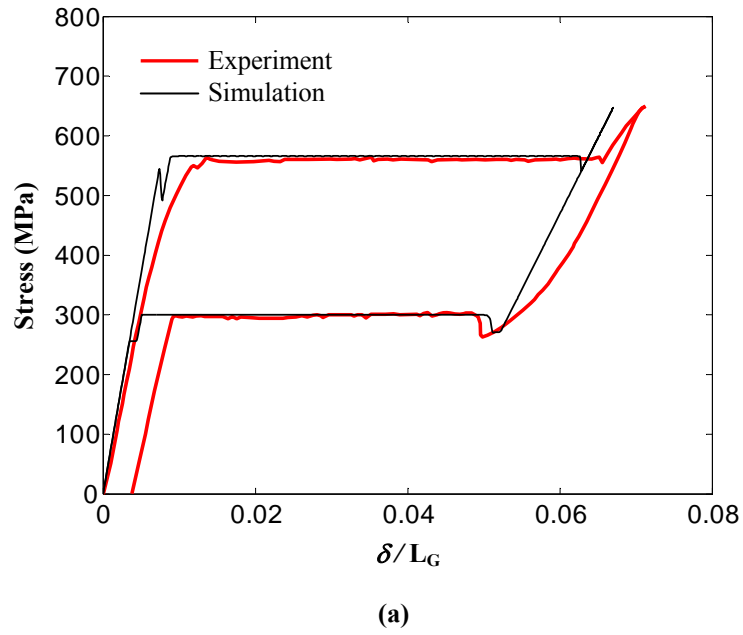
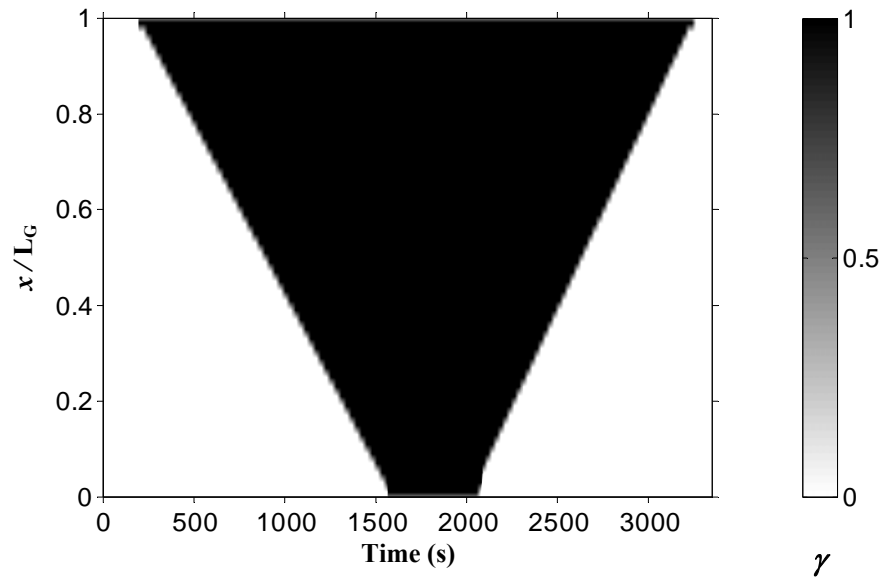
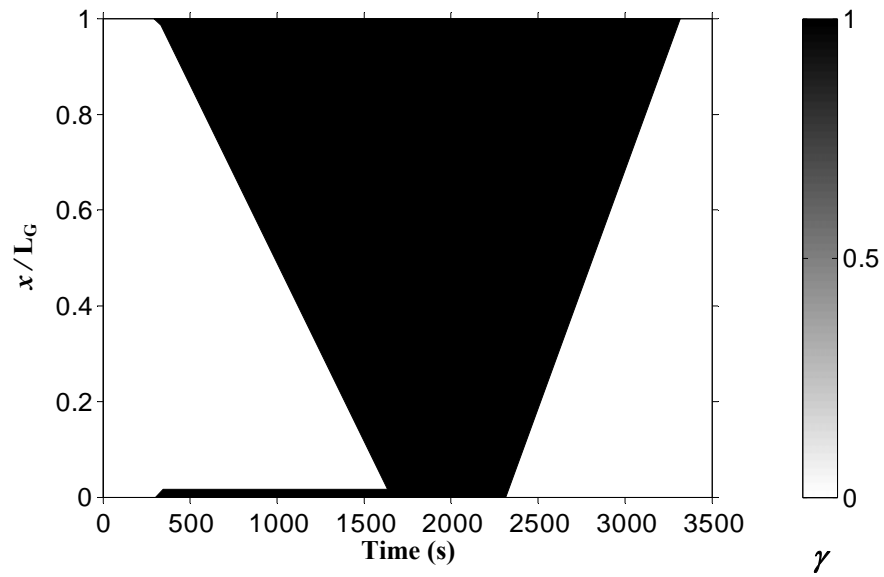


Figure 2-8. Simulation of the pseudoelastic behavior of the NiTi wire at $\dot{\delta}/L_G = 4 \times 10^{-5} \text{ s}^{-1}$ in 70°C water.
(a) Stress-strain response (Experimental results adapted from Shaw and Kyriakides, 1995); (b) Temperature profiles.



(a)



(b)

Figure 2-9. Evolution of A→M and M→A transformations in the pseudoelastic response of the NiTi wire at $\dot{\delta}/L_G = 4 \times 10^{-5} \text{ s}^{-1}$ in 70 °C water. (a) Simulation; (b) Experiment (adapted from Shaw and Kyriakides, 1995).

The forward transformation in this simulation is first nucleated at $x=L_G$ where the highest stress concentration exists. After the nucleation, the level of stress remains almost constant since the change in temperature at the transformation front is very small. As the transformation front progresses along the wire from $x=0$, the driving force does not become large enough to nucleate the transformation at other points along the wire. This behavior is also seen in the experiment, except that in the experimental result the forward transformation is nucleated at both ends but only one of them propagates. During unloading, both ends are adjacent to austenitic regions (i.e., the gripped ends), which means that the level of stress required for nucleation of austenite is higher at these end points compared to the middle points. However, the reverse transformation is nucleated at $x=0$ which has a lower level of stress than the other end due to a lower stress concentration.

It is seen that the length of the stress plateau in the experimental result is slightly longer than in the simulation, and there is also some residual strain at the end of the loading cycle in the experimental result. These effects are mainly attributed to the slippage at the grips (Shaw and Kyriakides, 1995), which is not modeled in the present simulations, and could be partly due to the approximate material properties.

A small stress peak followed by a dip is observed at the beginning of the stress plateau in the simulation, which corresponds to the nucleation of martensite and is not exhibited in the experimental result. In the experiment, the complicated state of stress at the grips results in early transformation of the adjacent particles during the stable part of the response where stress is still increasing. This early transformation in turn results in deviation from linear elastic behavior and suppression of the stress peak. However, at the beginning of the reverse transformation a small stress valley is seen in both the experiment and the simulation, which corresponds to nucleation of austenite in martensite phase. Two small valleys at the end of stress plateaus in both the forward and reverse transformations are also seen, which are due to the reduction in cross-sectional areas of the end elements.

2.3.2.2. Simulation of pseudoelastic behavior at moderate strain-rate

The results of the simulation for a moderate strain rate of $\dot{\delta}/L_G = 4 \times 10^{-4} \text{ s}^{-1}$ are shown in Figures 2-10 and 2-11. It can be seen that at this strain rate the transformation is first nucleated at the upper end, and soon after that another transformation front emanates from the lower end and the two transformation fronts propagate simultaneously. This behavior is also seen in the experiment. This is due to the increase in temperature at the initial transformation front, which tends to stop the propagation of the current front and initiate the transformation at another location with lower temperature. The predicted nucleation point in the reverse transformation is quite close to the experimental observation. Since the middle point is the final point to start transforming into martensite and does not complete the transformation, a small amount of residual parent phase remains untransformed in the middle element. This makes the middle element a preferred point for initiation of the reverse transformation (in addition to the end elements which are adjacent to the austenitic region). On the other hand, since the level of stress is slightly lower in the intermediate elements compared to the first and last elements of the gauge length, the reverse transformation is nucleated at the middle point rather than the end points.

It should be emphasized that nucleation of the reverse transformation is a complicated phenomenon, which depends on the location of defects in the microstructure. Therefore, accurate prediction of the nucleation point in the reverse transformation (and even the forward transformation) requires a knowledge of the imperfections and impurities in the specimen. These factors, however, are not considered in the present simulations, and the nucleation of transformation is imposed only by such factors as stress concentrations or residual untransformed phases.

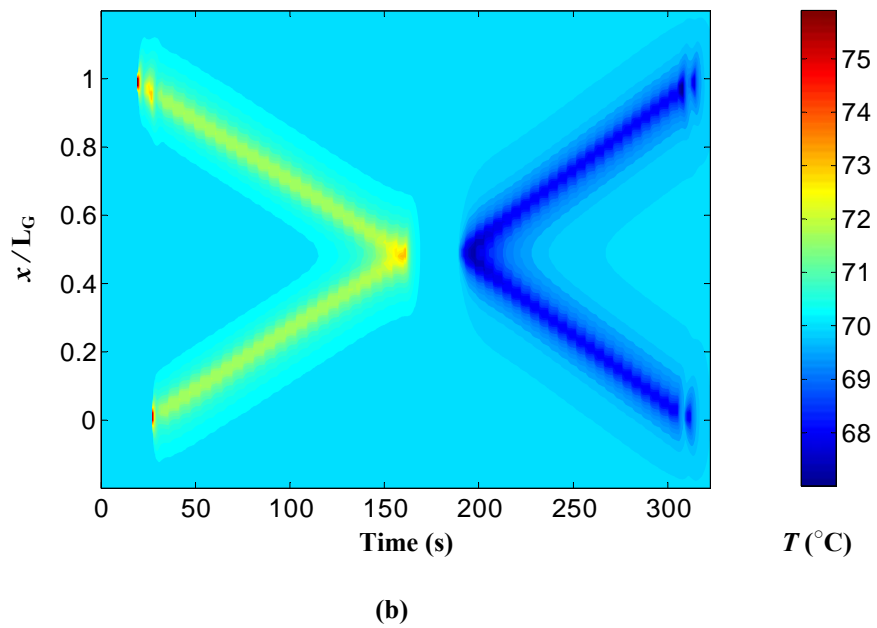
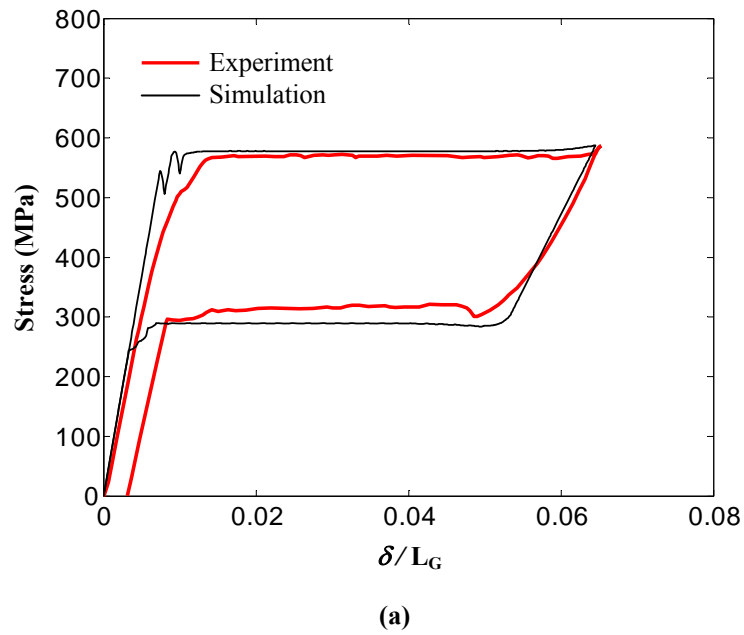


Figure 2-10. Simulation of the pseudoelastic behavior of the NiTi wire at $\dot{\delta}/L_G = 4 \times 10^{-4} \text{ s}^{-1}$ in 70°C water. (a) Stress-strain response (Experimental results adapted from Shaw and Kyriakides, 1995); (b) Temperature profiles.

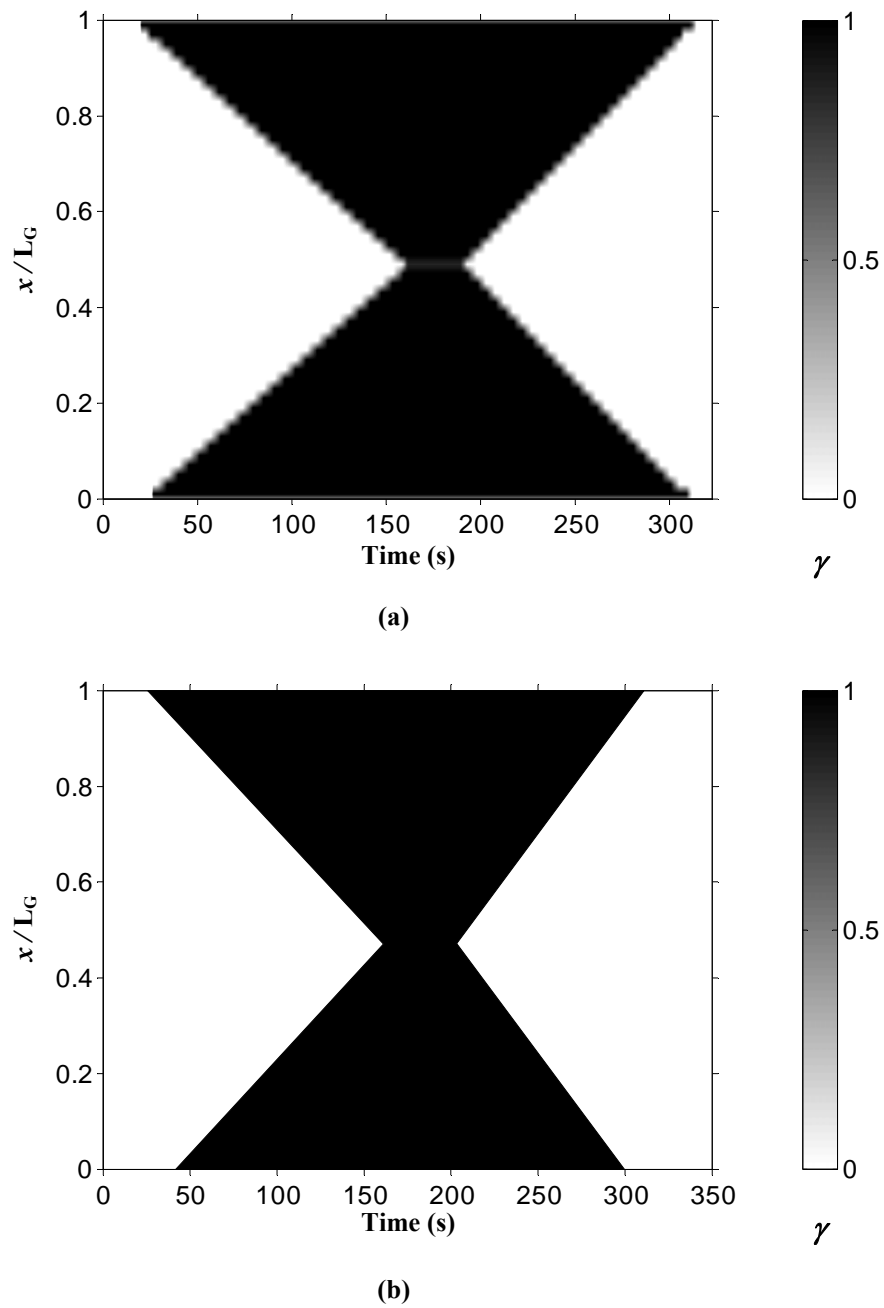


Figure 2-11. Evolution of A→M and M→A transformations in the pseudoelastic response of the NiTi wire at $\dot{\delta}/L_G = 4 \times 10^{-4} \text{ s}^{-1}$ in 70 °C water. (a) Simulation; (b) Experiment (adapted from Shaw and Kyriakides, 1995).

2.3.2.3. Simulation of pseudoelastic behavior at high strain-rates

The simulation of pseudoelastic response at strain rates higher than $\dot{\delta}/L_G = 4 \times 10^{-4} \text{ s}^{-1}$ resulted in severe self-heating/cooling at the propagating transformation fronts. Figure 2-12 shows the simulated transformation behavior at a strain rate of $\dot{\delta}/L_G = 4 \times 10^{-3} \text{ s}^{-1}$. Similar to the moderate strain rate case, two transformation fronts initiate at the top and bottom ends of the wire. As the fronts propagate, the temperature and stress increase. At some point during the loading, the stress becomes so high that nucleation occurs in the middle portion of the wire. As observed in Figure 2-12(a), the nucleation of transformation in the mid-span is uniform. This is the result of the uniform temperature field in the mid-span and the fact that there is no preferred nucleation site. In practice however, a random distribution of defects and impurities exists along the wire length which results in non-uniform nucleation of transformation. These effects cannot be explicitly considered in the present model. In order to force the transformation to occur non-uniformly, a random deviation from the original cross-sectional area was introduced along the wire gauge length. The amplitude of the deviation was $\pm 0.5\%$ from the original cross-sectional area, as shown in Figure 2-13.

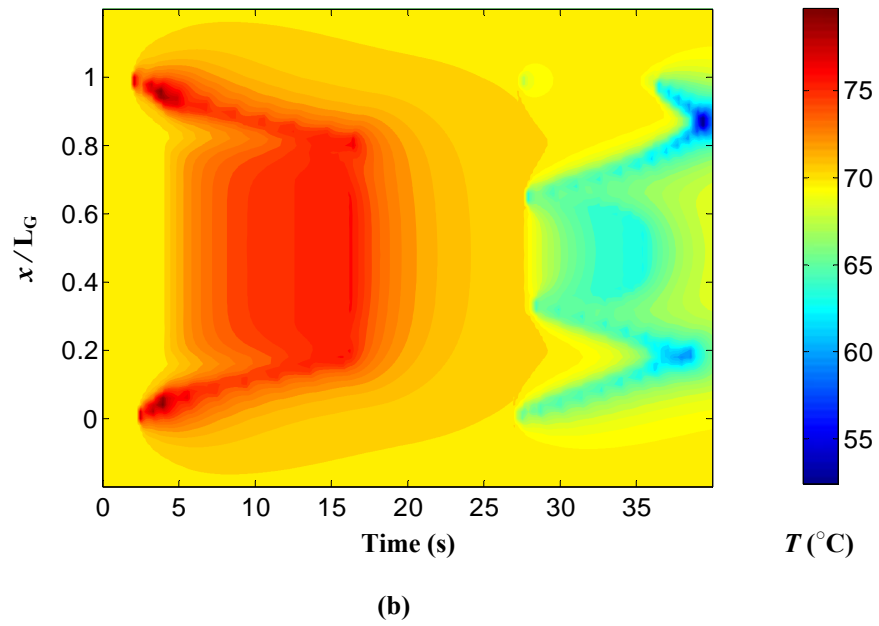
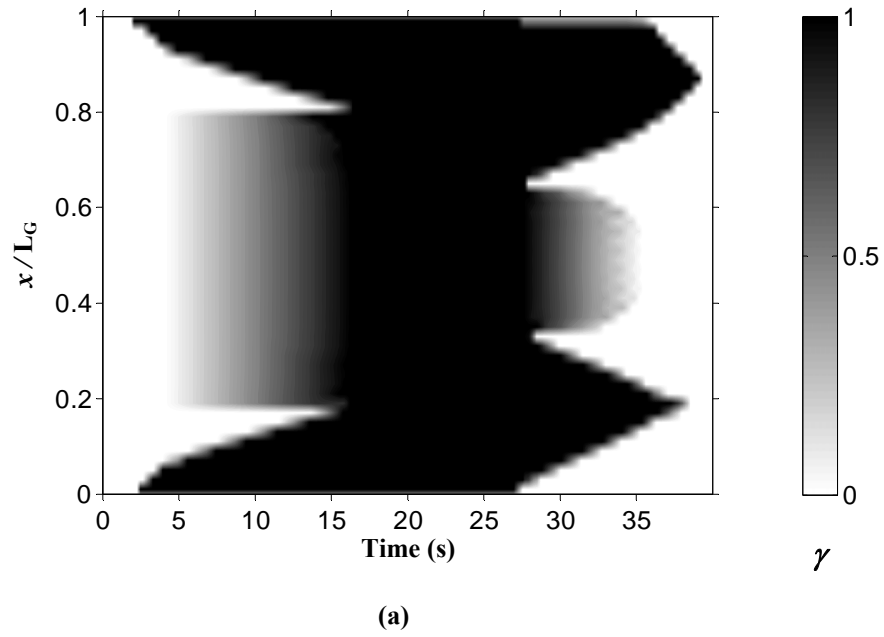


Figure 2-12. Simulation of the transformation behavior of the NiTi wire at $\dot{\delta}/L_G = 4 \times 10^{-3} \text{ s}^{-1}$ in $70 \text{ }^\circ\text{C}$ water. (a) Evolution of transformation; (b) Temperature profiles.

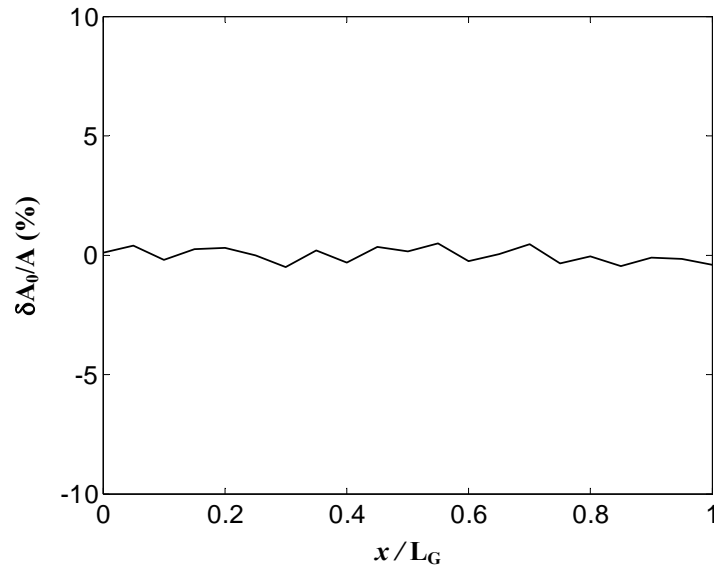


Figure 2-13. Random deviation from the original cross-sectional area along the wire gauge length.

The simulation was repeated at a strain rate $\dot{\delta}/L_G = 4 \times 10^{-3} \text{ s}^{-1}$ with the new distribution of cross-sectional area along the wire gauge length. In order to achieve the convergence in the finite elements solution, the number of elements in the gripped end and the gauge length of the wire were increased to 20 and 100 respectively. The results of the simulation are shown in Figures 2-14 and 2-15. The stress-strain response is in good agreement with the experimental results. It is seen from the simulation results that up to six transformation fronts may simultaneously propagate in this case. The experimental observations of Shaw and Kyriakides (1995) also verify the propagation of multiple transformation fronts at this strain rate. However, the spatial resolution of the measurements in their experiments did not allow for accurate tracking of the transformation fronts.

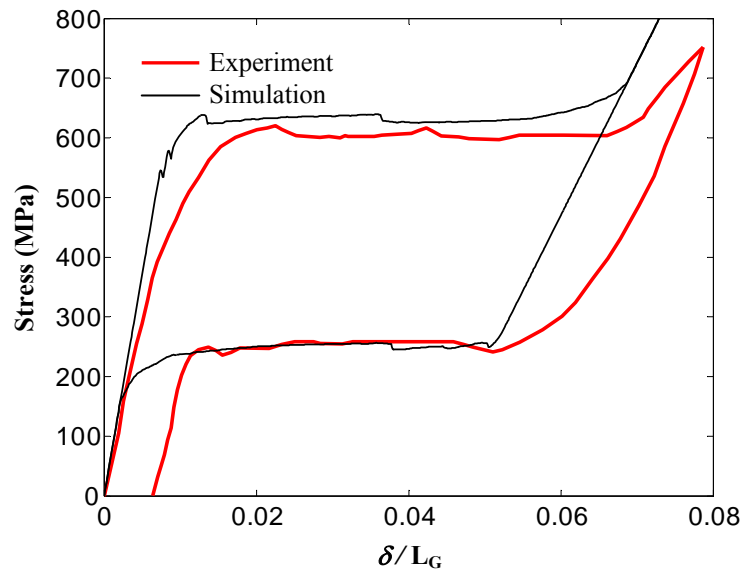
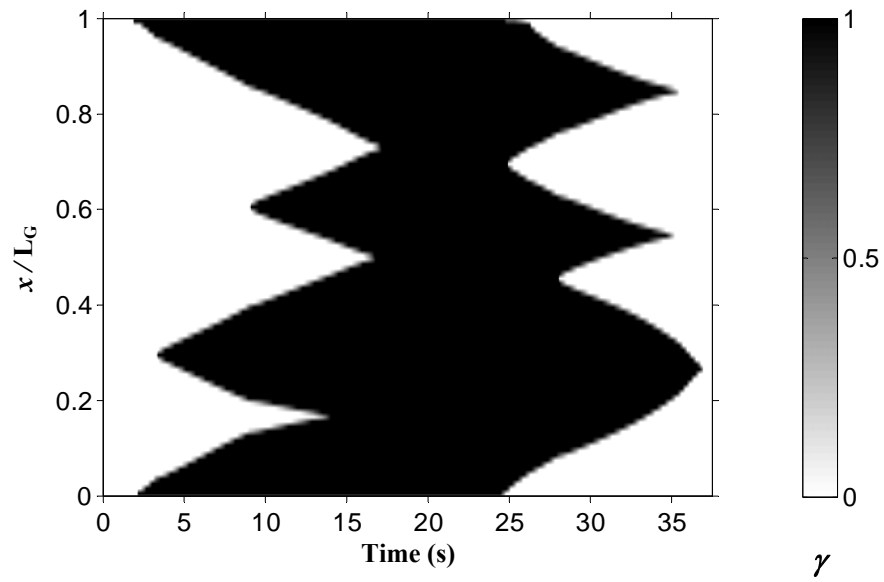
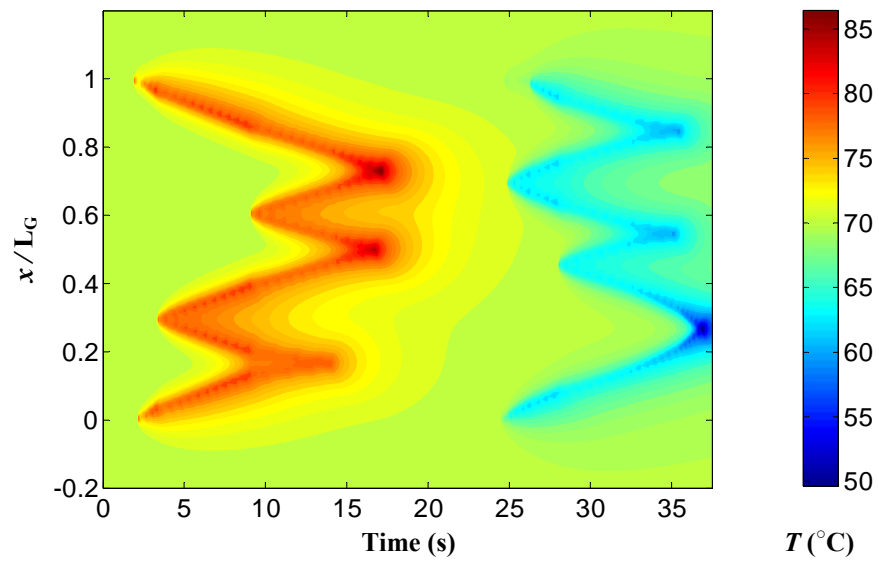


Figure 2-14. Pseudoelastic behavior of the NiTi wire at $\dot{\delta}/L_G = 4 \times 10^{-3} \text{ s}^{-1}$ in 70 °C water based on simulation and experiment (experimental response adapted from Shaw and Kyriakides, 1995).



(a)



(b)

Figure 2-15. Simulation of the transformation behavior of the NiTi wire at $\dot{\delta}/L_G = 4 \times 10^{-3} \text{ s}^{-1}$ in 70°C water. (a) Temperature profiles; (b) Evolution of transformation.

For simulating the pseudoelastic response of the wire at the very high strain rate of $\dot{\delta}/L_G = 4 \times 10^{-2} \text{ s}^{-1}$ an even finer mesh density was required to achieve convergence. The same distribution of defects was used as shown earlier in Figure 2-13, and the number of elements in the gripped end and gauge section of the wire were increased to 30 and 200 respectively. The simulated pseudoelastic response compared to the experimental results is shown in Figure 2-16. The evolution of transformation and the temperature profiles predicted by the model are also shown in Figure 2-17.

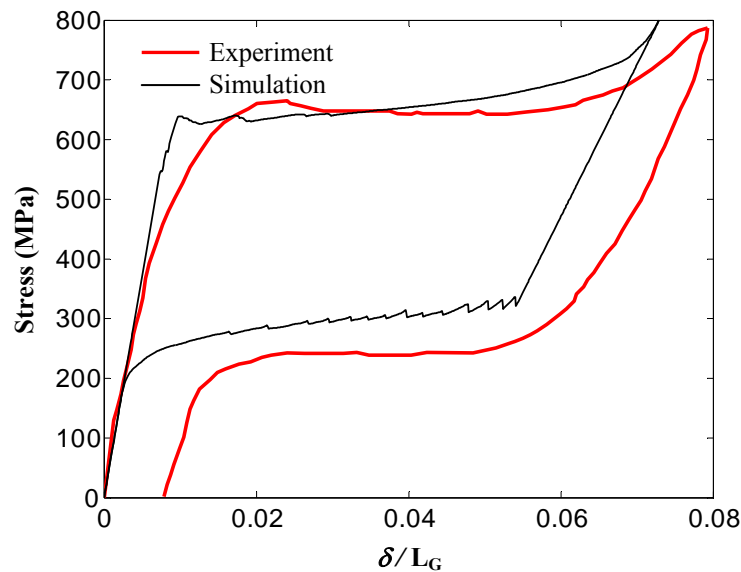
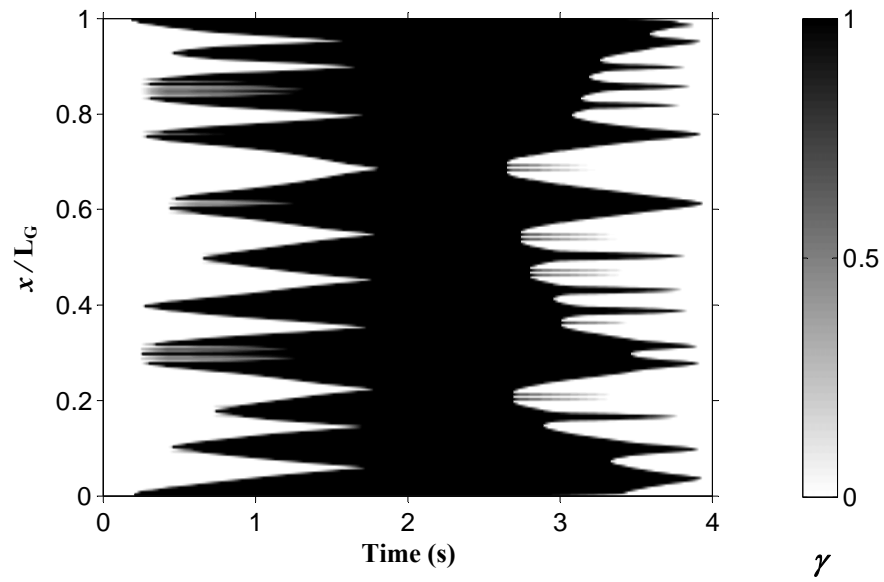


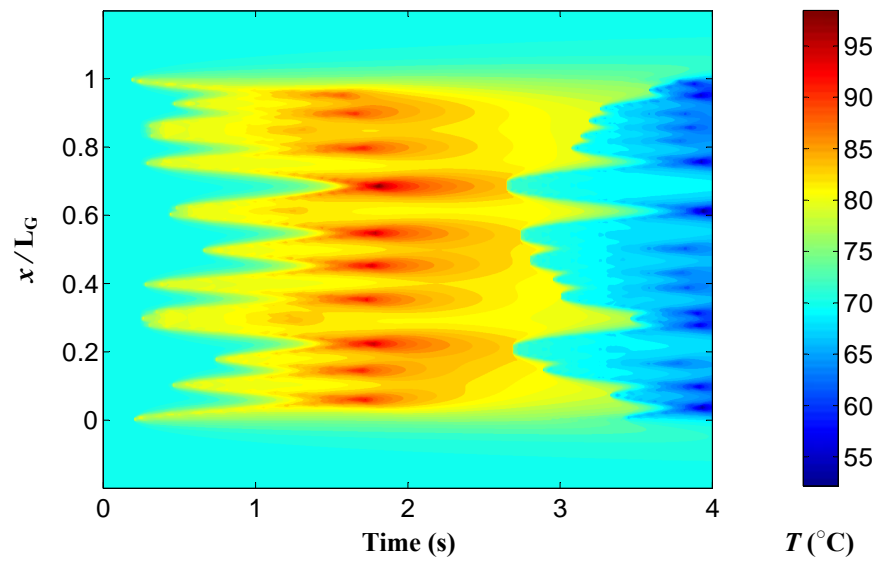
Figure 2-16. Pseudoelastic behavior of the NiTi wire at $\dot{\delta}/L_G = 4 \times 10^{-2} \text{ s}^{-1}$ in 70 °C water based on simulation and experiment (experimental response adapted from Shaw and Kyriakides, 1995).

The stress level of the simulated pseudoelastic response during the reverse transformation is higher than that in the experimental response. Also it is higher than the reverse stress plateaus predicted at the lower strain rates (Figure 2-18a). The reason for this is found from Figure 2-17(b) which shows that the overall temperature of the wire is still quite high at the beginning of reverse transformation. It is seen from Figure 2-17(b) that the maximum temperature reaches about 98.5°C during the forward transformation. The heat transfer during the elastic portion of unloading, however, is not efficient enough to dissipate the produced heat. In contrast, the temperature of the wire measured at a point during the experiments of Shaw and Kyriakides (1995) exhibits a drop to the ambient temperature during elastic unloading. Therefore, the difference between the simulation and experimental results may be attributed to the chosen heat transfer coefficients.

The pseudoelastic response of the wire at various strain rates based on the simulations and experimental results are compared to each other in Figure 2-18. The model successfully describes the strain rate effects and thermal interactions with the ambient environment. As mentioned earlier, the residual strains at the end of unloading in the experimental results are mainly due to grip slippage as pointed out by Shaw and Kyriakides (1995). The same effect is probably responsible for the difference between the widths of the hysteresis loops measured in the experiments and those predicted by the simulations.



(a)



(b)

Figure 2-17. Simulation of the transformation behavior of the NiTi wire at $\dot{\delta}/L_G = 4 \times 10^{-2} \text{ s}^{-1}$ in 70°C water. (a) Temperature profiles; (b) Evolution of transformation.

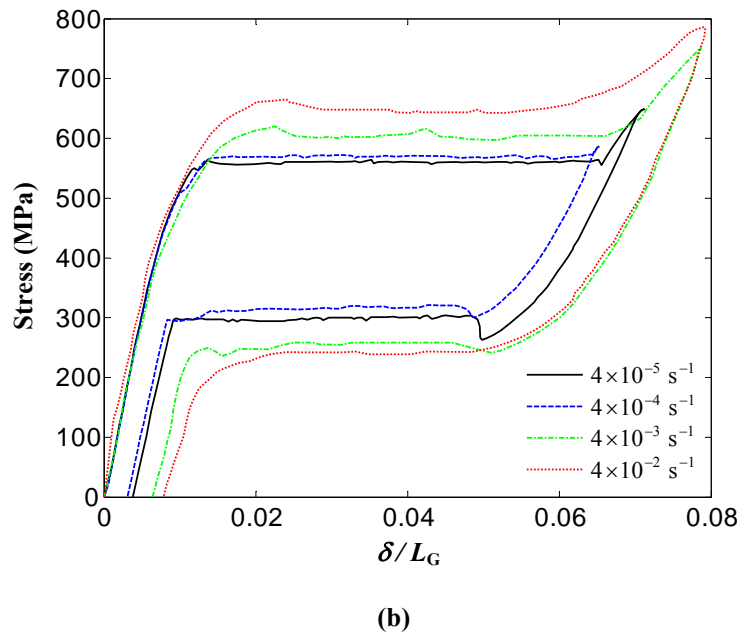
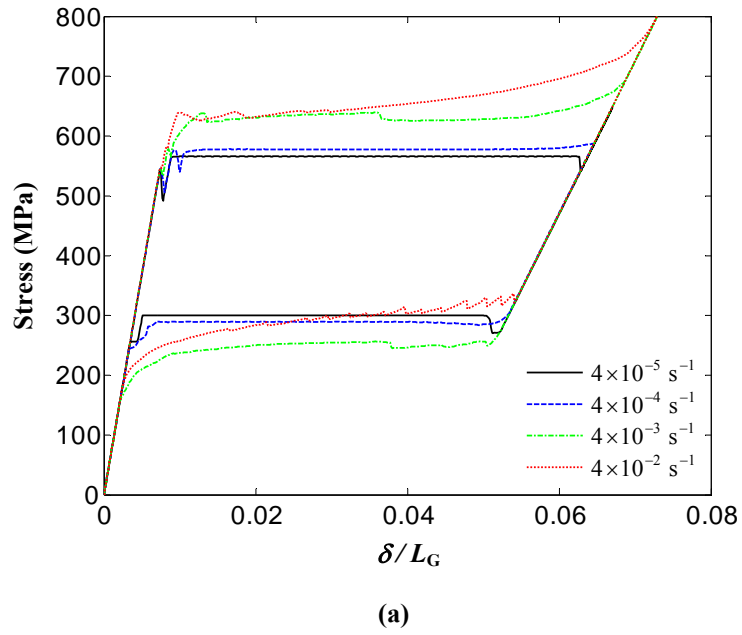


Figure 2-18. The pseudoelastic response of the wire at various strain rates in 70 °C water. (a) Simulations; (b) Experiments.

2.3.3. Temperature-induced transformation at constant stress

In this section the results of a simulation at constant applied stress and variable ambient temperature are shown. The wire is initially stressed to a level that is slightly lower than the stress required to initiate the martensitic transformation. The ambient temperature is then decreased with constant cooling rates to start the transformation while the stress is held constant. The initial temperature of the wire and environment (water) is 70 °C, and the applied stress is:

$$\sigma = 543 \text{ (MPa)}$$

The thermo-physical properties and the thermal boundary conditions are the same as before. The finite element mesh density was similar to that used in the simulation of pseudoelastic response at the highest strain-rate in the previous section (i.e., 40 elements in the gripped ends and 240 elements in the gauge length). The results of simulation for a number of different cooling rates are shown in Figure 2-19 through 2-21. It is seen from the results that the temperature-induced transformation under constant stress is sensitive to the rate of cooling and involves nucleation and propagation of one or more transformation fronts.

At $\dot{T}_\infty = -2 \times 10^{-2} \text{ }^\circ\text{C s}^{-1}$ transformation starts at the point with the highest stress concentration (i.e., at $x=L_G$) and propagates towards the other end. As the transformation front propagates, the temperature becomes low enough to nucleate the transformation at the other end. The second nucleation happens at $T_\infty = 65.9 \text{ }^\circ\text{C}$, and the transformation of the gauge length completes at $T_\infty = 63.9 \text{ }^\circ\text{C}$.

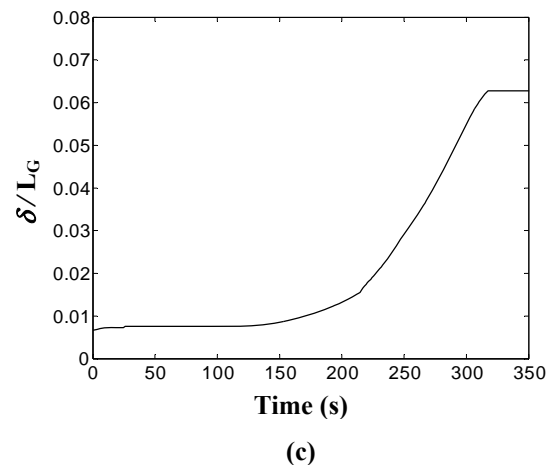
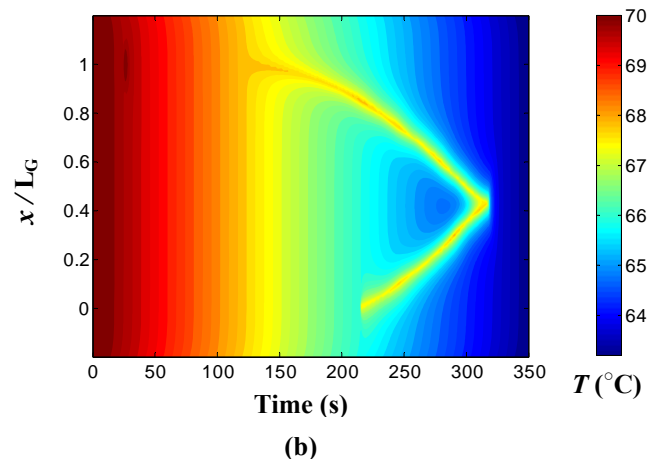
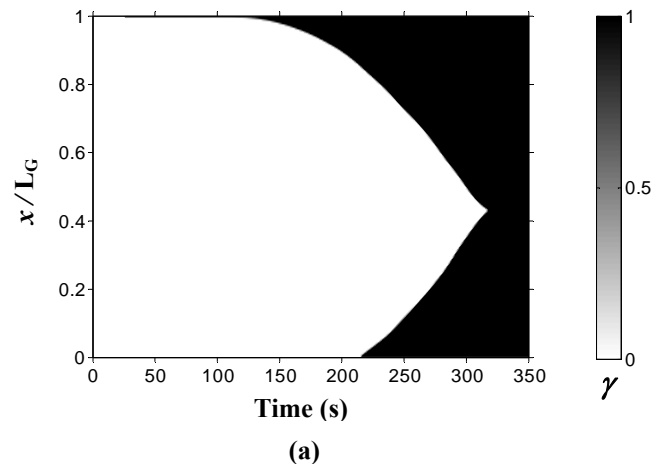


Figure 2-19. Thermomechanical responses of the wire subjected to ambient cooling under constant stress ($\dot{T}_\infty = -2 \times 10^{-2} \text{ }^\circ\text{C s}^{-1}$). (a) Evolution of transformation; (b) Temperature profiles; (c) Strain response.

At $\dot{T}_{\infty} = -2 \times 10^{-1} \text{ }^{\circ}\text{C s}^{-1}$, the forward transformation is again nucleated at $x=L_G$, and the second nucleation occurs at the other end at $T_{\infty} = 65.3 \text{ }^{\circ}\text{C}$. In this case, just before the full transformation of the gauge length at $T_{\infty} = 57 \text{ }^{\circ}\text{C}$, another nucleation occurs in the mid-span of the wire and four transformation fronts propagate simultaneously until the end of transformation.

At the highest cooling rate $\dot{T}_{\infty} = -5 \times 10^{-1} \text{ }^{\circ}\text{C s}^{-1}$ the first and second nucleations occur at almost the same time in the upper and lower ends of the gauge length. Before the completion of the transformation, the transformation also nucleates at several middle points in the wire at about $T_{\infty} = 57.9 \text{ }^{\circ}\text{C}$. The transformation eventually completes at $T_{\infty} = 54.6 \text{ }^{\circ}\text{C}$.

The strain responses of the wire versus ambient temperature at various cooling rates are compared to each other in Figure 2-22. A common feature in all of the curves is a sharp turn which corresponds to the nucleation of martensite at new sites during the cooling process. It is interesting to observe that the range of ambient temperature over which the transformation completes increases with increasing cooling rate. This is mainly due to the self-heating of the wire during the forward transformation. As the cooling rate increases, the rate of transformation also increases which in turn results in an increase in the temperature of the propagating transformation front(s). This effect, which is clearly seen in the temperature profiles of the wire, opposes the transformation and prohibits the rapid transformation of the wire at high cooling rates.

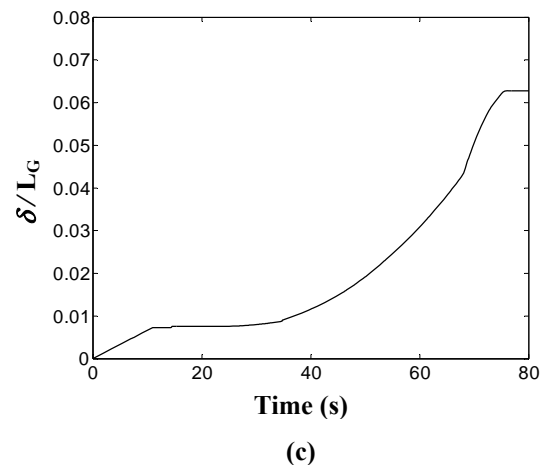
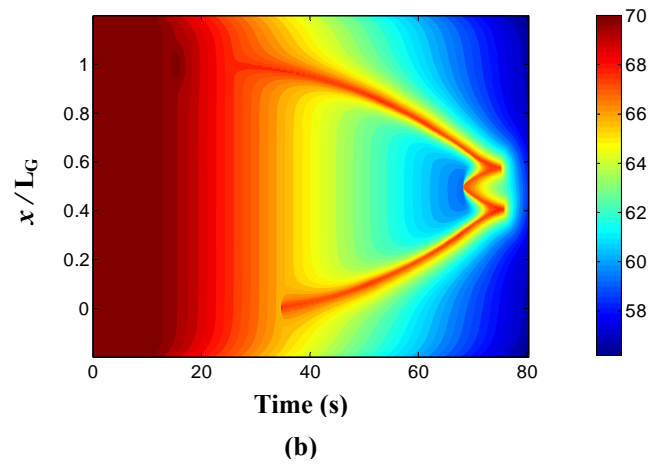
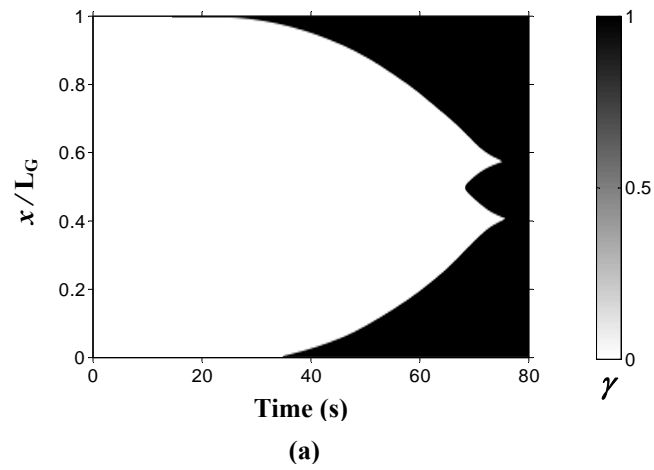


Figure 2-20. Thermomechanical responses of the wire subjected to ambient cooling under constant stress ($\dot{T}_\infty = -2 \times 10^{-1} \text{ }^\circ\text{C s}^{-1}$). (a) Evolution of transformation; (b) Temperature profiles; (c) Strain response.

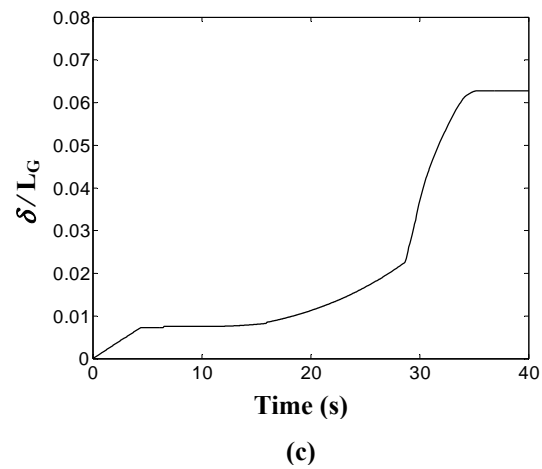
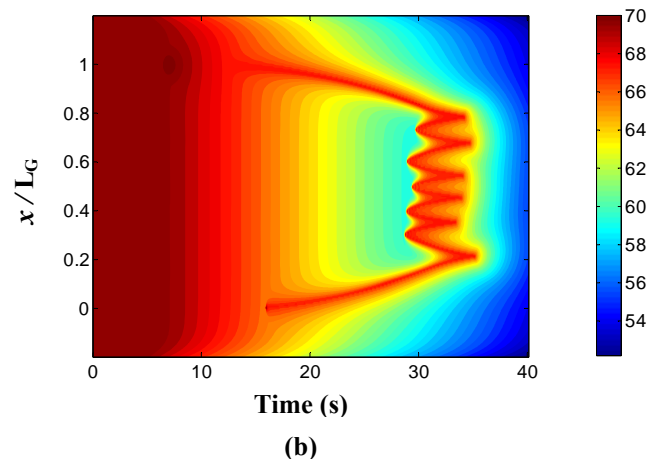
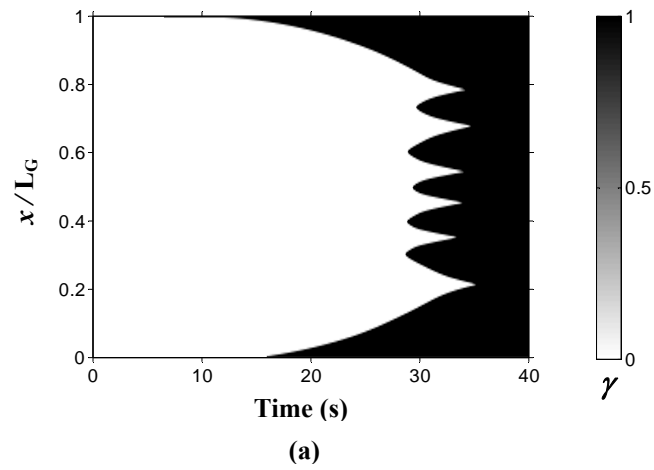


Figure 2-21. Thermomechanical responses of the wire subjected to ambient cooling under constant stress ($\dot{T}_\infty = -5 \times 10^{-1} \text{ }^\circ\text{C s}^{-1}$). (a) Evolution of transformation; (b) Temperature profiles; (c) Strain response.

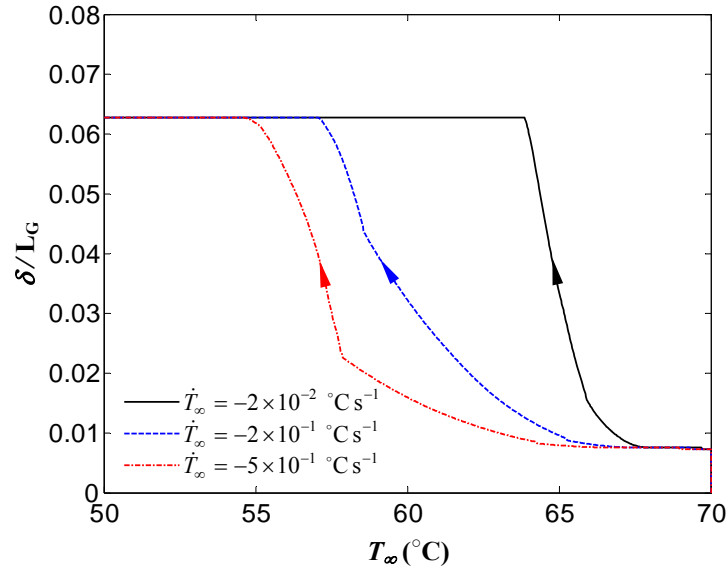


Figure 2-22. The strain response of the wire versus ambient temperature.

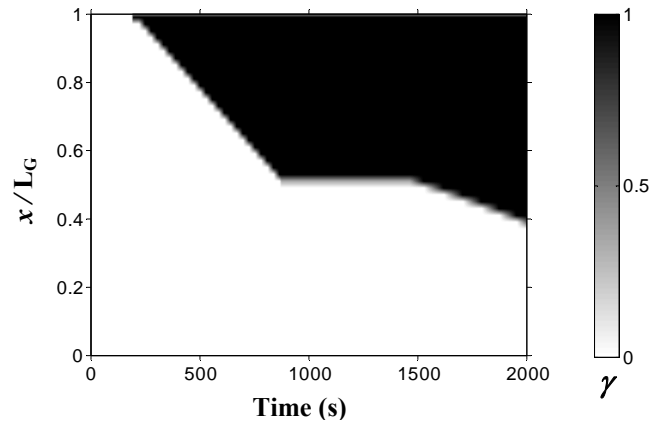
2.3.4. Relaxation and restrained recovery in a partially transformed wire

The last set of results corresponds to the simulation of relaxation in a constrained partially transformed specimen subjected to temperature variations. Thermo-physical properties and thermal boundary conditions are the same as those in the previous simulations. The finite element mesh density is set back to its original size (10 elements in the gripped ends and 50 elements in the gauge length). In the present simulations, the specimen is first partially transformed by a displacement-controlled loading at a low strain rate of $\dot{\delta}/L_G = 4 \times 10^{-5} \text{ s}^{-1}$ in 70 °C water until $\delta/L_G = 3.5\%$, followed by an unloading to $\delta/L_G = 3\%$. In the second stage, the ambient temperature is increased or decreased to induce the forward or reverse transformation while the total strain is held constant at $\delta/L_G = 3\%$. Figure 2-23 shows the results of the simulation for a drop in the ambient temperature of 50 °C at a cooling rate of $\dot{T}_\infty = -5 \times 10^{-2} \text{ °C s}^{-1}$. A single transformation front nucleates in the upper end and propagates toward the mid-span as a result of the initial loading of the wire. The existing

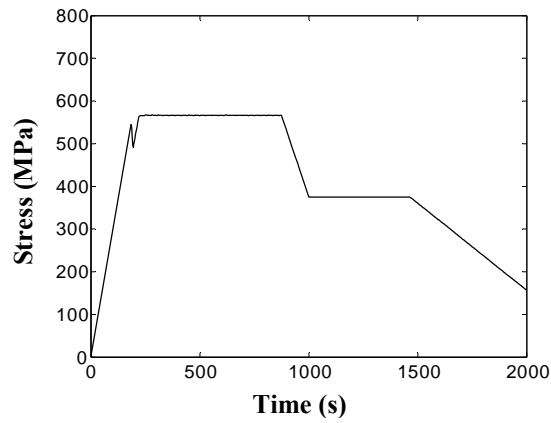
transformation front further propagates toward the other end as the ambient temperature decreases. As a result of the transformation, the total inelastic strain in the wire increases. However, since the total strain is constant, the elastic strain in the wire decreases, which lowers the stress level of the wire (relaxation).

If the ambient temperature increases, the reverse transformation occurs. This recovers the transformation strain and elevates the stress level in the wire. This phenomenon is called *constrained recovery*. The simulation results in this case are shown in Figure 2-24. The ambient temperature is increased by 50 °C at a rate of $\dot{T}_\infty = -5 \times 10^{-2} \text{ }^\circ\text{C s}^{-1}$ while the total strain is kept constant.

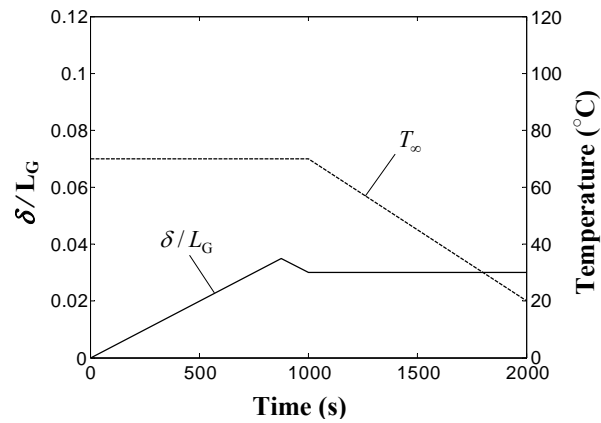
These simulations show that the local temperature changes at the transformation front are negligible compared to the variations in wire temperature. The amount of temperature-induced transformation in these simulations is very small compared to the results of constant stress simulations in the previous section, where small changes in temperature resulted in full transformation of the specimen. This can be explained by noting that during the decrease in temperature, further transformation of austenite to martensite lowers the level of stress, which makes the austenite phase more stable. During the reverse transformation (increase in ambient temperature) a similar self-prohibiting mechanism also exists; that is, the recovery of transformation strain raises the level of stress, which makes the martensite phase more stable.



(a)

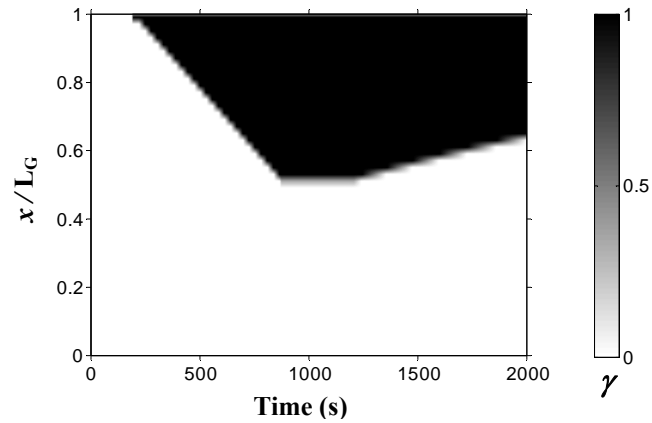


(b)

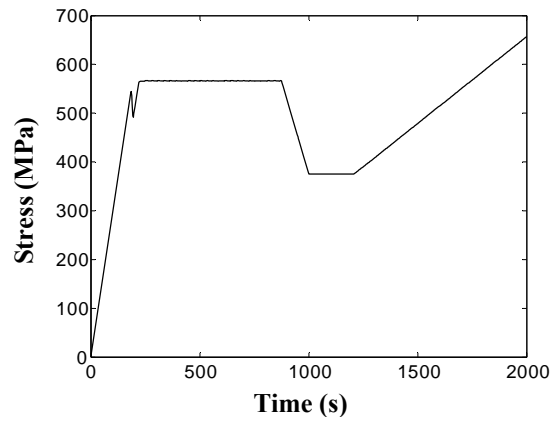


(c)

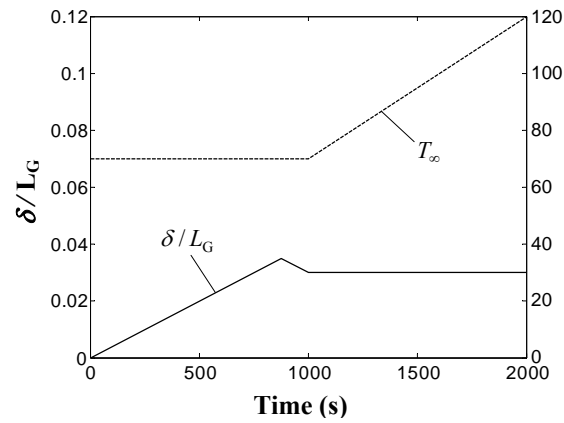
Figure 2-23. Simulation of relaxation in a partially transformed NiTi wire. (a) Evolution of transformation. (b) Stress response; (c) Time history of strain and ambient temperature.



(a)



(b)



(c)

Figure 2-24. Simulation of constrained recovery in a partially transformed NiTi wire. (a) Evolution of transformation. (b) Stress response; (c) Time history of strain and ambient temperature.

2.4. BIBLIOGRAPHY

- Brinson, L.C., Schmidt, I., Lammering, R., 2004. Stress-induced transformation behavior of a polycrystalline NiTi shape memory alloy: micro and macromechanical investigations via in situ optical microscopy. *Journal of the Mechanics and Physics of Solids* 52, 1549-1571.
- Daly, S., Ravichandran, G., Bhattacharya, K., 2007. Stress-induced martensitic phase transformation in thin sheets of Nitinol. *Acta Materialia* 55, 3593-3600.
- Feng, P., Sun, Q.P., 2006. Experimental investigation on macroscopic domain formation and evolution in polycrystalline NiTi microtubing under mechanical force. *Journal of the Mechanics and Physics of Solids* 54, 1568-1603.
- Iadicola, M.A., Shaw, J.A., 2002. An experimental setup for measuring unstable thermo-mechanical behavior of shape memory alloy wire. *Journal of Intelligent Material Systems and Structures* 13, 157-166.
- Incropera, F.P., DeWitt, D.P., 1996. *Introduction to heat transfer*. Wiley, New York.
- Leo, P.H., Shield, T.W., Bruno, O.P., 1993. Transient heat transfer effects on the pseudoelastic behavior of shape-memory wires. *Acta Metallurgica et Materialia* 41, 2477-2485.
- Pieczyska, E.A., Gadaj, S.P., Nowacki, W.K., Tobushi, H., 2004. Thermomechanical investigations of martensitic and reverse transformations in TiNi shape memory alloy. *Bulletin of the Polish Academy of Sciences: Technical Sciences* 52, 165-171.
- Pieczyska, E.A., Tobushi, H., Gadaj, S.P., Nowacki, W.K., 2006a. Superelastic deformation behaviors based on phase transformation bands in TiNi shape memory alloy. *Materials Transactions* 47, 670-676.

- Pieczyska, E.A., Gadaj, V., Nowacki, W.K., Tobushi, H., 2006b. Phase-transformation fronts evolution for stress- and strain-controlled tension tests in TiNi shape memory alloy. *Experimental Mechanics* 46, 531-542.
- Shaw, J.A., 2000. Simulations of localized thermo-mechanical behavior in a NiTi shape memory alloy. *International Journal of Plasticity* 16, 541-562.
- Shaw, J.A., Kyriakides, S., 1995. Thermomechanical aspects of NiTi. *Journal of the Mechanics and Physics of Solids* 43, 1243-1281.
- Shaw, J.A., Kyriakides, S., 1997. On the nucleation and propagation of phase transformation fronts in a NiTi alloy. *Acta Materialia* 45, 683-700.
- Shaw, J.A., Chang, B.C., Iadicola, M.A., Leroy, Y.M., 2003. Thermodynamics of a 1-D shape memory alloy: Modeling, experiments, and application. *Proceedings of SPIE - The International Society for Optical Engineering* 5049, 76-87.
- Tan, G.S., Suseno, T., Liu, Y., 2002. Mechanical hysteresis in the pseudoelasticity of Ti-50.2at%Ni. *Materials Science Forum* 394-395, 249-252.
- Tan, G., Liu, Y., Sittner, P., Saunders, M., 2004. Lüders-like deformation associated with stress-induced martensitic transformation in NiTi. *Scripta Materialia* 50, 193-198.
- Tobushi, H., Shimeno, Y., Hachisuka, T., Tanaka, K., 1998. Influence of strain rate on superelastic properties of TiNi shape memory alloy. *Mechanics of Materials* 30, 141-50.

Chapter 3: Three-dimensional Constitutive Model³

A three-dimensional macroscopic-level constitutive model of shape memory alloys exhibiting unstable pseudoelastic behavior is presented in this chapter. A mechanical approach is used to develop the constitutive relations based on the deformation theory of plasticity. The model is used to simulate the localized deformation and transformation front propagation in NiTi strips subjected to various loading conditions. Special attention is paid to the multi-axiality of stress state at the transformation fronts during the forward and reverse transformations.

3.1. INTRODUCTION

The transformation fronts observed during the uniaxial loading of NiTi wire samples are in the form of narrow axisymmetric transition zones which separate the highly deformed martensitic areas from the low-strain parent phase as shown earlier in Figure 1-7. It is clear that the state of stress at the transformation front is three-dimensional due to the strain mismatch between the austenite and martensite regions. Based on the hypothesis proposed by Shaw and Kyriakides (1997), the stress concentration at the transformation front during loading transforms the nearby austenitic grains and prohibits the homogenous nucleation of martensite throughout the sample. However, because of the large aspect ratios (length to diameter) of wire specimens, and that the details of transformation fronts were not the focus of study, the one-dimensional constitutive model presented in the previous chapter was developed without explicitly calculating the complex stress-state at the transformation fronts.

³ Parts of this chapter appear in the following papers:

- 1- Azadi, B., Rajapakse R.K.N.D., Maijer, D. M., 2007. Multi-dimensional constitutive modeling of SMA during unstable pseudoelastic behavior. *International Journal of Solid and Structures* 44, 6473-6490.
- 2- Azadi, B., Maijer, D. M., Rajapakse R.K.N.D., Finite element simulation of strain-rate effects on localized unstable pseudoelastic response of shape memory alloys. *Journal of Mechanics of Materials and Structures* (submitted on Oct 14, 2007; 29 pages; submission number: 071014).

For non-wire specimens, such as strips and hollow cylinders, the shape of the transformation fronts are more versatile and complex than in wires as shown in Figures 1-8 and 1-10 (see also Shaw and Kyriakides, 1997, 1998; Pieczyska et al., 2004, 2006a,b; Feng and Sun 2006; Daly et al., 2007). The pattern of the transformation fronts can potentially affect the performance of the NiTi elements that have small aspect ratios. Studying the details of the stress distributions at the transformation fronts is also important for understanding the fundamental behavior of material.

The first attempt to analytically study the nucleation and propagation of transformation bands in NiTi strip was presented by Shaw and Kyriakides (1998). They proposed a plasticity-based model to capture the material instability during the uniaxial loading of NiTi strips under isothermal conditions. The material was assumed to behave as an isothermal, rate independent J_2 -type elasto-plastic solid with isotropic softening during the forward transformation. Based on the similarities between the unstable propagation of Lüders bands in fine-grained mild steel and the transformation bands in NiTi strips, they concluded that continuum level strain localization is the dominant mechanism in the observed behavior of NiTi strips during the martensitic transformation. The analysis, however, was limited to the forward transformation and the strain recovery upon the reverse transformation was ignored.

Shaw (2000), and Iadicola and Shaw (2004) extended the analysis of Shaw and Kyriakides (1998) by considering the thermomechanical coupling of the material with its environment, and investigated the effect of loading rate on the evolution of instabilities. The same approach has also been used recently by Hu et al. (2007) to simulate the nucleation and propagation of localized helical transformation bands in NiTi tubes.

While the role of material instability and stress-concentration in propagation of transformation fronts during the forward transformation has been analytically established, it is not yet

clear how the propagation of transformation fronts during the reverse transformation is governed by the complex multi-axial stress field developed at the transformation fronts. Answering this question is the main motivation behind developing a multi-axial constitutive model of unstable pseudoelastic behavior in this chapter. Characteristics of the incremental constitutive relations in modeling the unstable pseudoelastic response are first discussed. It is shown that the path-dependent nature of the inelastic deformation (transformation strain) in incremental constitutive models may prohibit the full recovery of inelastic deformation in a continuum body. Derivation of a *total transformation strain* constitutive model is then presented. The present model aims to overcome the deficiency of previous plasticity-based analyses in modeling of the reverse transformation through nucleation and propagation of localized austenite bands. The model is implemented in a finite element code to simulate the nucleation and propagation of a single transformation front during the forward and reverse transformation of a short NiTi strip under isothermal conditions. The effect of heat generation on the pseudoelastic response and propagation of transformation fronts in dog-bone specimens are then considered in numerical simulations. The morphology of the transformation front and the effect of loading rate and boundary conditions on its evolution are studied in detail.

3.2. GENERAL REMARKS ON MODELING OF REVERSIBLE INELASTIC DEFORMATION

Based on the classical flow rule of plasticity, the increment of the plastic strain tensor $d\boldsymbol{\varepsilon}^{(p)}$ is related to the gradient of a plastic potential function Q through following equation:

$$d\varepsilon_{ij}^{(p)} = d\lambda \frac{\partial Q(\boldsymbol{\sigma})}{\partial \sigma_{ij}} \quad (3-1)$$

where $\boldsymbol{\sigma}$ is the stress tensor and $d\lambda$ is a positive scalar known as the plastic multiplier. The multiplier factor $d\lambda$ is determined using the yield criterion in plasticity theory. Depending on the

choice of the plastic potential function Q and the yield criterion, various plasticity theories can be developed. If the chosen potential function and yield surface are expressed by the same functions, the corresponding flow rule is known as an *associated flow rule*. If different functions are used for the plastic potential and the yield surface, the resulting flow rule is called a *non-associated flow rule*.

For ordinary metals, plastic strain is produced because of the movement of dislocations inside the microstructure. Therefore, it is irreversible and cannot be recovered by mechanical unloading. In contrast with this, the transformation strain observed during the pseudoelastic behavior of SMAs is produced by simultaneous stress-induced martensitic transformation and reorientation of martensitic variants, which can be recovered during the reverse transformation.

The question that naturally arises is whether a similar flow rule can also be implemented to describe the pseudoelastic behavior of SMAs. In that case, equation (3-1) can be modified to give the increment of transformation strain during the forward or reverse transformation as:

$$d\varepsilon_{ij}^{(t)} = d\lambda \frac{\partial P(\boldsymbol{\sigma}, T, \gamma)}{\partial \sigma_{ij}} \quad (3-2)$$

where $\boldsymbol{\varepsilon}^{(t)}$ is the transformation strain tensor, P is the *transformation potential function*, and γ is the volume fraction of martensite phase which is a positive scalar varying between 0 and 1. The fundamental difference between the above equation and the flow rule of plasticity in (3-1) is that the scalar multiplier $d\lambda$ in equation (3-2) can be either positive or negative depending on the direction of transformation (forward or reverse). The increment of transformation strain ($d\varepsilon^{(t)}$) is proportional to the increment of martensite phase production ($d\gamma$). Therefore, equation (3-2) can be rewritten in the following form:

$$d\varepsilon_{ij}^{(t)} = A \frac{\partial P(\boldsymbol{\sigma}, T, \gamma)}{\partial \sigma_{ij}} d\gamma \quad (3-3)$$

where the proportionality factor A is a function of material properties, state variables, and loading history in general. Similar to the concept of a yield surface in plasticity, the evolution of transformation in the forward or reverse directions is governed by the corresponding kinetic relations, which control the extent of transformation (γ) in terms of all state variables.

Consider a continuum region R occupied by an SMA as shown in Figure 3-1. Within R , consider a material point denoted by p .

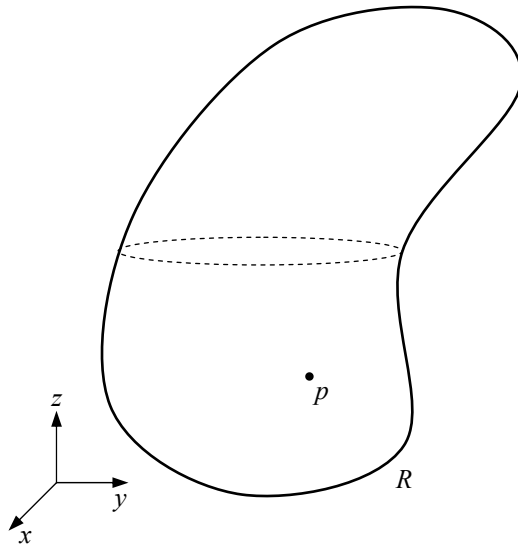


Figure 3-1. A continuum region occupied by an SMA

In general, material point p may be subjected to a general three-dimensional loading-unloading path in the six-dimensional stress space, which corresponds to the six components of stress tensor, σ_{ij} 's. To make it easier to visualize, consider a plane-stress loading-unloading path in the three-dimensional stress space ($\sigma_1 - \sigma_2 - \sigma_{12}$) as shown Figure 3-2. The loading path is denoted by l (from point o to point o'), and the unloading path is denoted by u (from point o' back to o).

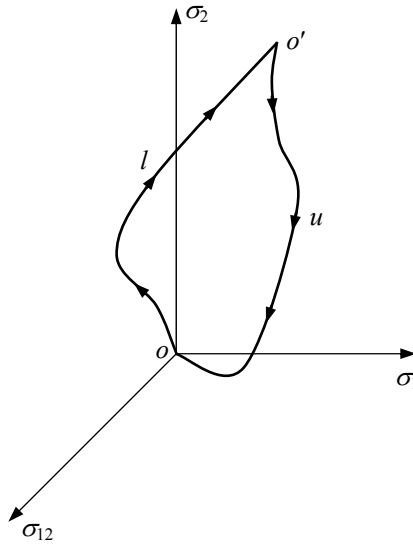


Figure 3-2. Loading-unloading path in the stress space.

The total transformation strain at the end of the loading-unloading loop is found by integrating equation (3-3) as,

$$\varepsilon_{ij}^{(t)} \Big|_o = \int_l A \frac{\partial P(\boldsymbol{\sigma}, T, \gamma)}{\partial \sigma_{ij}} d\gamma + \int_u A \frac{\partial P(\boldsymbol{\sigma}, T, \gamma)}{\partial \sigma_{ij}} d\gamma \quad (3-4)$$

It can be seen from the above equation that the total transformation strain $\boldsymbol{\varepsilon}^{(t)}$ depends on the integration path and loading history. In order to ensure the reversibility of the transformation strain, the sum of integrals in equation (3-4) must be equal to zero at the end of any loading-unloading path (where γ becomes zero again). This is of course a mathematical constraint which must be satisfied regardless of the physical properties of material. Since the loading path l does not necessarily coincide with the unloading path u , the potential functions and yielding criterion usually used in plasticity theories cannot be used to model shape recovery. Thus determining a proper transformation

potential function and corresponding yield surfaces (transformation surfaces) during the forward and reverse transformations is more complex than in plasticity theory.

So far, the necessary mathematical condition for the reversibility of transformation strain at a material point has been discussed. In problems with uniform stress fields, the above condition is sufficient to ensure the full recovery of transformation strain throughout the spatial domain R . However, multi-dimensional problems generally involve non-uniform stress fields, and individual points in the continuum body may experience different loading paths. This is especially true when localization of transformation and/or stress concentrations result in peculiar and complex stress distributions in the continuum domain. Unlike the elastic deformation, the transformation strain described by the incremental flow rule in equation (3-3) is not a functional of the final state of stress and temperature, but depends on the integration path. It is possible that the distribution of inelastic deformation left at the end of the loading path produces local areas of high stress concentration which prohibits the reverse transformation at those sites. Therefore, the mathematical reversibility of constitutive relations for a single point like p does not automatically ensure the shape recovery over the entire volume R .

A few three-dimensional constitutive models based on equation (3-3) have been developed in the past which can successfully capture the recovery of transformation strain at a material point along complex multi-axial loading loops (for notable examples see Boyd and Lagoudas, 1994; Auricchio et al., 1997; Helm and Haupt, 2003; Bouvet et al., 2004a). These models have been developed and used for analyzing the stable pseudoelastic behavior of SMAs. However, the performance of these models for the mechanically unstable regimes with transformation localization is open to question. In fact, it will be shown in the subsequent sections that the numerical simulations based on a path-dependent incremental constitutive equation similar to the model of Boyd and Lagoudas (1994), which is

reversible for a material point, fails to fully recover the transformation strain in the entire domain during the localized pseudoelastic behavior.

Finding a proper transformation flow rule that is truly reversible and guarantees the recovery of transformation strain during the unstable pseudoelastic response for any loading path and geometry seems to be a challenging problem. In the following section, the aim is to propose a multi-dimensional constitutive model that is not only mathematically reversible at a single material point, but also gives a consistent solution over the entire domain during the unstable pseudoelastic response.

3.3. A TOTAL DEFORMATION CONSTITUTIVE MODEL

The flow rule given in equation (3-3) relates the increments of transformation strain tensor to the increment of martensitic fraction γ and the gradient of a potential function. Since the gradient of the potential function is not constant during the loading path, the components of the final transformation strain depend on the integration path and loading history. If the potential function and kinetic relations are not carefully chosen, it is highly possible that the transformation strain does not recover along some integration paths, unless model use is limited to proportional loading-unloading cases.

In this section, a different type of constitutive relation is proposed in which the “total” transformation strain is related to the gradient of a potential function. The constitutive model is inspired by the deformation theory of plasticity, with two sets of yielding criteria for forward and reverse transformations. The model is intended to describe the material behavior at a local point subjected to general thermomechanical loading. The major assumptions and equations governing the stress-strain-temperature relations in this model are summarized in the following sections.

3.3.1. General considerations

Conventional additive strain decomposition is used to relate the total strain tensor $\boldsymbol{\varepsilon}$ to the elastic $\boldsymbol{\varepsilon}^{(e)}$ and transformation $\boldsymbol{\varepsilon}^{(t)}$ components as,

$$\boldsymbol{\varepsilon}_{ij} = \boldsymbol{\varepsilon}_{ij}^{(e)} + \boldsymbol{\varepsilon}_{ij}^{(t)} \quad (3-5)$$

The elastic strain tensor is related to the stress tensor through the fourth-order equivalent compliance tensor (\mathbf{D}) as,

$$\boldsymbol{\varepsilon}_{ij}^{(e)} = D_{ijkl}(\gamma) \sigma_{kl} \quad (3-6)$$

It is assumed that the equivalent compliance of the material \mathbf{D} is a linear function of martensitic fraction γ , given by:

$$D_{ijkl}(\gamma) = \gamma D_{ijkl}^{(M)} + (1 - \gamma) D_{ijkl}^{(A)} \quad (3-7)$$

where $\mathbf{D}^{(A)}$ and $\mathbf{D}^{(M)}$ are the elastic compliance tensors of the pure austenite and martensite phases, respectively. The martensitic fraction γ is a positive number between 0 and 1, which characterizes the extent of transformation, i.e., $\gamma = 0$ corresponds to the full austenitic phase and $\gamma = 1$ corresponds to the full martensitic phase at a point. In this study, the individual phases are assumed to be isotropic. Therefore, the equivalent compliance tensor \mathbf{D} defined in (3-7) is also an isotropic tensor. The equivalent Young's modulus, E , and Poisson's ratio, ν , of the mixture of two phases can be calculated from equation (3-7) to be:

$$E(\gamma) = \frac{E_A E_M}{\gamma E_A + (1 - \gamma) E_M} \quad (3-8)$$

and,

$$\nu = \frac{\gamma \nu_M E_A + (1-\gamma) \nu_A E_M}{\gamma E_A + (1-\gamma) E_M} \quad (3-9)$$

(E_A, ν_A) and (E_M, ν_M) in the above equations are the Young's modulus and Poisson's ratio of the individual martensite and austenite phases, respectively. It should be noted that the equivalent elastic modulus, E , obtained by the assumption made in equation (3-7) is consistent with the relation proposed by in Chapter 2 for the one-dimensional model.

3.3.2. Constitutive relation of transformation strain

The total transformation strain is assumed to be expressed in terms of other variables by the following equation:

$$\varepsilon_{ij}^{(t)} = A \frac{\partial P}{\partial \sigma_{ij}} \gamma \quad (3-10)$$

where P is the transformation potential function, and A is a scalar quantity. In general, A is a function of all state variables $(\varepsilon_{ij}, \sigma_{ij}, T, \gamma)$ and deformation history. Note that the reversibility of the transformation strain has already been guaranteed since for $\gamma=0$ the components of the total transformation strain tensor $\varepsilon_{ij}^{(t)}$ become zero from equation (3-10).

In fact, the constitutive relation assumed in equation (3-10) is similar to the equation used in *deformation theories of plasticity* (Khan and Huang, 1995), in which the finite form of plastic strain is given as a function of final stress state. Such constitutive structures are generally inappropriate for plastic deformation since the path dependency of plastic strain is ignored. However, the deformation theory of plasticity is applicable in problems with nearly proportional loading where elastic unloading never occurs (Budiansky, 1959). The theory was also implemented in a study of bifurcation phenomenon and plastic buckling (Hutchinson, 1974).

In order to find the proportionality factor A in equation (3-10), it is assumed that:

$$\bar{\varepsilon}^{(t)} = \Delta\varepsilon_t \gamma \quad (3-11)$$

where $\bar{\varepsilon}^{(t)}$ is called *the effective transformation strain*, and provides a scalar measure of the total transformation strain. This quantity is defined in the following form:

$$\bar{\varepsilon}^{(t)} = \sqrt{\frac{2}{3} \varepsilon_{ij}^{(t)} \varepsilon_{ij}^{(t)}} \quad (3-12)$$

The parameter $\Delta\varepsilon_t$ in equation (3-10) is a material property, which indicates the maximum attainable transformation strain during a uniaxial tension test. Substituting equation (3-10) in (3-12) and the subsequent result in (3-11) gives the proportionality factor as,

$$A = \frac{\Delta\varepsilon_t}{\sqrt{\frac{2}{3} \frac{\partial P}{\partial \sigma_{ij}} \frac{\partial P}{\partial \sigma_{ij}}}} \quad (3-13)$$

Therefore, the transformation strain is given by:

$$\varepsilon_{ij}^{(t)} = \frac{\Delta\varepsilon_t}{\sqrt{\frac{2}{3} \frac{\partial P}{\partial \sigma_{kl}} \frac{\partial P}{\partial \sigma_{kl}}}} \frac{\partial P}{\partial \sigma_{ij}} \gamma \quad (3-14)$$

Note that the above relation holds at any time during the general multi-axial loading-unloading of SMA. This means that the components of the transformation strain tensor $\varepsilon_{ij}^{(t)}$ can continuously change without any change in the extent of martensitic fraction (γ), and even after the completion of transformation ($\gamma = 1$). This way, the direction of the transformation strain tensor is always adjusted according to the current direction of the potential gradient. This mode of deformation is referred to as *reorientation*.

It should be noted however that the value of the effective transformation strain $\bar{\varepsilon}^{(t)}$ depends only on the extent of transformation (γ), and does not change without progress in transformation (see equation 3-11). In other words, forward (reverse) transformation increases (decreases) the magnitude of the effective transformation strain $\bar{\varepsilon}^{(t)}$, while the current gradient of the potential function controls the orientation of the transformation strain tensor $\varepsilon_{ij}^{(t)}$. The reorientation of transformation strain in stress-induced martensite (oriented martensite) based on the applied stress state has been experimentally observed for some SMAs (Bouvet et al., 2002). It has been shown that the martensite variants evolved and oriented during the stress-induced martensitic transformation can transform to other variants with different orientations upon change in the direction of applied load (Zheng et al., 2000). An incremental form of equation (3-14) is given below to better illustrate the reorientation feature of the model:

$$d\varepsilon_{ij}^{(t)} = \frac{\Delta\varepsilon_t}{\sqrt{\frac{2}{3} \frac{\partial P}{\partial \sigma_{kl}} \frac{\partial P}{\partial \sigma_{kl}}}} \frac{\partial P}{\partial \sigma_{ij}} d\gamma + \Delta\varepsilon_t \gamma \frac{\partial}{\partial \sigma_{rs}} \left(\frac{\frac{\partial P}{\partial \sigma_{ij}}}{\sqrt{\frac{2}{3} \frac{\partial P}{\partial \sigma_{kl}} \frac{\partial P}{\partial \sigma_{kl}}}} \right) d\sigma_{rs} \quad (3-15)$$

This equation applies to both the forward ($d\gamma > 0$) and reverse ($d\gamma < 0$) transformations, and also when neither of the transformations is taking place ($d\gamma = 0$). The first term on the right hand side of this equation corresponds to the phase transformation, and the second term characterizes the reorientation of transformation strain, which may happen independently from the transformation. Hence, there can be a non-zero change in transformation strain $d\varepsilon_{ij}^{(t)}$ while $d\gamma$ is zero. It must be reemphasized that according to equation (3-11), the magnitude of the effective transformation strain does not change if reorientation without transformation is the only mechanism of deformation.

Note that an expression of transformation strain similar to equation (3-15) has been previously proposed by Auricchio et al. (1997) with a different derivation. In their model however, the reorientation is active only during loading, and the reorientation of transformation during reverse transformation has been neglected. As shown later by numerical examples, the reorientation of transformation strain during reverse transformation is as important and needs to be considered for full recovery of the transformation strain during unstable pseudoelastic response.

The choice of transformation potential function P is described in the next section after introducing the kinetics of transformation.

3.3.3. Kinetics of transformation

It has been verified by experiments that the stress-induced martensitic transformation under multi-axial stress state is triggered and controlled by the input mechanical work (Sittner et al., 1995). For yielding of ordinary metals, this mechanical work is characterized by a kind of equivalent stress. A similar approach is followed here in the case of initiation and completion of the martensitic transformation and its reverse transformation. For example, in the case of forward transformation it is assumed that the transformation starts when the equivalent stress reaches a critical value, known as the *martensite nucleation stress* (σ_{MN}), and the transformation ends at another critical value called the *martensite completion stress* (σ_{MC}). For intermediate stages (i.e., during the evolution of transformation) the value of equivalent stress must be somewhere between these two critical values, depending on the extent of transformation identified by γ . It must be noted that these critical stresses are functions of temperature, and the variation of temperature during the transformation affects the stress required to continue the transformation.

Based on the above discussion, the initiation of forward transformation is marked by the following conditions:

$$F_{A \rightarrow M}(\sigma_{ij}, \gamma, T) = 0, \quad \gamma < 1 \quad (3-16)$$

where,

$$F_{A \rightarrow M} = \bar{\sigma} - \sigma_M(\gamma, T) \quad (3-17)$$

In above equation, $\bar{\sigma}$ is an equivalent stress which is assumed to be the Von-Mises effective stress defined as,

$$\bar{\sigma} = \sqrt{\frac{3}{2} S_{ij} S_{ij}} \quad (3-18)$$

S is the deviatoric stress tensor given by,

$$S_{ij} = \sigma_{ij} - \frac{\sigma_{kk}}{3} \delta_{ij} \quad (3-19)$$

The choice of the Von-Mises effective stress is mainly driven by the strong macroscopic similarities between Lüders bands in steel (dislocation plasticity) and localized transformation bands in NiTi (displacive phase transformation). However, other types of effective stress can also be used without loss of generality in the present model.

In equation (3-17), $\sigma_M(\gamma, T)$ is the *instantaneous martensitic transformation stress*, which satisfies the following conditions:

$$\begin{cases} \sigma_M(0, T) = \sigma_{MN}(T) \\ \sigma_M(1, T) = \sigma_{MC}(T) \end{cases} \quad (3-20)$$

It is assumed that $\sigma_M(\gamma, T)$ is linear in terms of γ , that is,

$$\sigma_M(\gamma, T) = (1 - \gamma) \sigma_{MN}(T) + \gamma \sigma_{MC}(T) \quad (3-21)$$

Similarly, the initiation of reverse transformation is characterized by the following condition,

$$F_{M \rightarrow A}(\sigma_{ij}, \gamma, T) = 0, \quad \gamma > 0$$

where,

$$F_{M \rightarrow A} = \bar{\sigma} - \sigma_A(\gamma, T) \quad (3-22)$$

and the *instantaneous austenitic transformation stress* σ_A is:

$$\sigma_A(\gamma, T) = \gamma \sigma_{AN}(T) + (1 - \gamma) \sigma_{AC}(T) \quad (3-23)$$

where σ_{AN} and σ_{AC} are the *austenite nucleation* and *austenite completion* stresses, respectively.

During the evolution of transformation, the effective stress must be somewhere between the nucleation and completion stresses, depending on the extent of transformation and an associated hardening/softening rule. Once the transformation starts, the conditions that govern the evolution of the transformation are,

$$\begin{cases} dF_{A \rightarrow M}(\sigma_{ij}, \gamma, T) = 0, & \text{Forward transformation (d } \gamma > 0) \\ dF_{M \rightarrow A}(\sigma_{ij}, \gamma, T) = 0, & \text{Reverse transformation (d } \gamma < 0) \end{cases} \quad (3-24)$$

For materials such as NiTi, which exhibit localization of deformation and unstable mechanical behavior, the local stress-strain relation loses its positive slope during the transformation. It has been experimentally shown that the stress required to nucleate the martensite is higher than the stress associated with the completion of martensitic transformation. By contrast, the stress required to trigger the nucleation of austenite during unloading is lower than the stress required to propagate the reverse transformation (Shaw and Kyriakides, 1997; Iadicola and Shaw, 2002). Such unstable behaviors imply that the nucleation stress in the above kinetics relations must be higher (lower) than the completion stress during the forward (reverse) transformation. As shown later, such a “softening” feature in the kinetic of transformation results in localization and propagation of transformation

front(s) in the simulations. The nucleation and completion stresses are material properties and can be measured or calculated based on carefully designed and executed uniaxial loading-unloading tests at different temperatures (Iadicola and Shaw, 2002). Note that the nucleation and completion stresses in the present three-dimensional model are dependent only on the microstructure of the material. They cannot be directly measured from the experimental values which are also geometry-dependent. As will be seen in Section 3.4, calibration is required to find the nucleation and completion stresses using the numerical simulations of a sample with particular geometry.

It should be noted that the concept of an instantaneous nucleation stress defined in the one-dimensional model (Chapter 2) does not appear in the present three-dimensional model. The instantaneous nucleation stresses were used to account for the effect of stress concentration at the transformation front on the nearby particles. However, in the three-dimensional analysis the effect of stress concentrations are automatically considered. Also note that the transformation completion stresses (σ_{MC} , σ_{AC}) defined for the three-dimensional model are quantitatively different from the transformation finish stresses defined for the one-dimensional model (σ_{MF} , σ_{AF}) in Chapter 2.

For materials which exhibit hardening behavior during forward (reverse) transformation, the completion stress is higher (lower) than the nucleation stress. The localization is unlikely in those cases, and the form of $\sigma_M(\gamma, T)$ and $\sigma_A(\gamma, T)$ must be carefully chosen in order to fit the experimental data.

As stated earlier, the stored elastic energy, which is identified by the equivalent stress, controls the nucleation and evolution of transformation through kinetic relations. In the present model it is assumed that the same equivalent stress also controls the direction of the transformation strain, and the transformation potential function is chosen to be the Von-Mises effective stress. This

assumption is similar to the assumptions used in the associated flow rules of plasticity. Therefore, the transformation potential function is given by:

$$P \equiv \bar{\sigma} \quad (3-25)$$

A simplified summary of the constitutive equations and kinetic relations based on the above assumption is given in Table 3-1.

Table 3-1. Summary of the constitutive model.

Constitutive Relations	
Finite form:	$\varepsilon_{ij} = \left\{ \gamma D_{ijkl}^{(M)} + (1-\gamma) D_{ijkl}^{(A)} \right\} \sigma_{kl} + \frac{3}{2} \Delta \varepsilon_t \frac{S_{ij}}{\bar{\sigma}} \gamma$
Incremental form:	$d\varepsilon_{ij} = \bar{D}_{ijkl}(\gamma) d\sigma_{kl} + \left\{ \left(D_{ijkl}^{(M)} - D_{ijkl}^{(A)} \right) \sigma_{kl} + \frac{3}{2} \Delta \varepsilon_t \frac{S_{ij}}{\bar{\sigma}} \right\} d\gamma$ <p style="margin-left: 20px;">where,</p> $\bar{D}_{ijkl}(\gamma) = D_{ijkl}(\gamma) + \frac{3}{2} \frac{\Delta \varepsilon_t}{\bar{\sigma}} \left(\delta_{ik} \delta_{jl} - \frac{1}{3} \delta_{ij} \delta_{kl} - \frac{3}{2} \frac{S_{ij} S_{kl}}{\bar{\sigma}^2} \right) \gamma$
Kinetic Relations	
Forward transformation:	$dF_{A \rightarrow M} = 0 \Rightarrow \frac{3}{2} \frac{S_{ij}}{\bar{\sigma}} d\sigma_{ij} - [(1-\gamma)\sigma'_{MN}(T) + \gamma\sigma'_{MC}(T)]dT - [\sigma_{MC}(T) - \sigma_{MN}(T)]d\gamma = 0$
Reverse transformation:	$dF_{M \rightarrow A} = 0 \Rightarrow \frac{3}{2} \frac{S_{ij}}{\bar{\sigma}} d\sigma_{ij} - [\gamma\sigma'_{AN}(T) + (1-\gamma)\sigma'_{AC}(T)]dT - [\sigma_{AN}(T) - \sigma_{AC}(T)]d\gamma = 0$

The stress-strain relation coupled with the kinetic relations form a set of highly nonlinear equations. These equations can be linearized and numerically solved by expressing them in differential form as shown in Table 3-1. However, numerical errors may develop due to strong non-

linearity. An efficient iterative method is provided in Appendix D for solving this set of simultaneous nonlinear equations, which has been used in the FEM analyses of the next section.

A few remarks regarding the limitations and validity of the assumptions in this constitutive model are necessary:

Remark 1. The details of the microstructure of material are not considered in deriving the relationships in this constitutive model, and the transformation-related phenomena at the lattice and on the grain levels are ignored. The derivation of the model from the deformation theory of plasticity solely originates from the similarities between plastic yielding and stress-induced transformation on the macroscopic level. As mentioned earlier, the idea of using plasticity theory in the modeling of unstable localized pseudoelastic behavior of NiTi is not new (Shaw and Kyriakides 1998; Shaw 2000; Iadicola and Shaw 2004; Hu et al., 2007). However, the mathematical irreversibility of plastic deformation in incremental theories of plasticity limits their application to forward transformation only. To overcome this deficiency, the present total deformation theory is employed rather than its incremental counterpart.

Remark 2. Although the transformation strain in this model is expressed in a finite form (equation 3-14), the constitutive model is not totally path-independent. From the kinetic relations it is apparent that the martensitic fraction is path-dependent and must be calculated incrementally. However, the orientation of the transformation strain tensor is a function of the final stress state and independent of the loading path.

Remark 3. The present constitutive model is intended to model the macroscopic, but local pseudoelastic behavior of an SMA at a material point. Due to the localization of deformation, the material behavior as described by equations (3-10) through (3-25) is not representative of the bulk

material response. Therefore, this constitutive model may not be the best choice for analyzing SMAs that exhibit stable mechanical behavior (such as most copper-based SMAs).

Remark 4. The use of the Von-Mises effective stress in the yield criteria limits the application of the model to materials that behave symmetrically in tension and compression. A number of researchers (see for example Liu et al., 1998) have reported that NiTi alloys exhibit tension-compression asymmetry. Different yield surfaces have also been proposed to describe this asymmetry based on either micromechanical calculations (Lexcellent and Blanc, 2004) or experimental data (Bouvet et al., 2004b). The tension-compression asymmetry, however, does not impact on the current work which focuses on tension. Although the local stress field at the transformation front is multi-dimensional, as shown later the localized stress field only deviates slightly from the uniaxial state, and therefore, the use of the Von-Mises effective stress is justified here.

Remark 5. It has been shown through experiment that phase transformation in NiTi starts homogeneously prior to the nucleation of localized deformation bands through stable mechanical behavior and homogeneous deformation (Feng and Sun, 2006; Daly et al., 2007). Tan et al. (2004) also reported that the end of the stress plateau in pseudoelastic response is not the end of phase transformation and that the stress-induced transformation continued beyond the stress plateau. The mechanically stable stress-induced phase transformation is not considered in this current analysis. However, it would be straightforward to incorporate into the constitutive model by revising the form of the yield criteria in equations (3-21) through (3-23).

3.3.4. Heat of transformation

The heat generation/consumption during the transformation may be calculated by writing the energy conservation law as,

$$\sigma_{ij} \dot{\epsilon}_{ij} = \dot{u}^{(e)} + \dot{u}^{(i)} + \dot{q}_G \quad (3-26)$$

where $u^{(e)}$ (J/m³) is the elastic energy density, $u^{(i)}$ (J/m³) is the specific internal energy (excluding the elastic energy), q_G (J/m³) is the generated heat, and $(\dot{})$ denotes the time derivative ($\frac{d}{dt}$). The elastic energy density is given by,

$$u^{(e)} = \frac{1}{2} \sigma_{ij} \epsilon_{ij}^{(e)} \quad (3-27)$$

Equations (3-26), and (3-27) together with (3-5) and (3-6) give the heat generation term as,

$$\dot{q}_G = \sigma_{ij} \dot{\epsilon}_{ij}^{(i)} + \frac{1}{2} \sigma_{ij} (D_{ijkl}^{(M)} - D_{ijkl}^{(A)}) \sigma_{kl} \dot{\gamma} - \dot{u}^{(i)} \quad (3-28)$$

It is assumed that the rate of change in specific internal energy, $\dot{u}^{(i)}$ (W/m³), can be expressed as,

$$\begin{cases} \dot{u}^{(i)} = \rho \Delta h_{A \rightarrow M} \dot{\gamma}, & \dot{\gamma} > 0 \\ \text{or,} \\ \dot{u}^{(i)} = -\rho \Delta h_{M \rightarrow A} \dot{\gamma}, & \dot{\gamma} < 0 \end{cases} \quad (3-29)$$

where ρ (kg/m³) is the density, and $\Delta h_{A \rightarrow M}$, $\Delta h_{M \rightarrow A}$ (J/kg) are the total change in enthalpy due to phase transformation at zero-stress state during forward and reverse transformations, respectively.

According to (3-29), the rate of heat generation is obtained to be:

$$\begin{cases} \dot{q}_G = \sigma_{ij} \dot{\epsilon}_{ij}^{(i)} + \left\{ \frac{1}{2} \sigma_{ij} (D_{ijkl}^{(M)} - D_{ijkl}^{(A)}) \sigma_{kl} - \rho \Delta h_{A \rightarrow M} \right\} \dot{\gamma}, & \dot{\gamma} > 0 \\ \text{or,} \\ \dot{q}_G = \sigma_{ij} \dot{\epsilon}_{ij}^{(i)} + \left\{ \frac{1}{2} \sigma_{ij} (D_{ijkl}^{(M)} - D_{ijkl}^{(A)}) \sigma_{kl} + \rho \Delta h_{M \rightarrow A} \right\} \dot{\gamma}, & \dot{\gamma} < 0 \end{cases} \quad (3-30)$$

Note that $\Delta h_{A \rightarrow M}$, and $\Delta h_{M \rightarrow A}$ are material properties that can be measured by Differential Scanning Calorimetry (DSC).

3.4. FEM SIMULATIONS

In this section, the proposed constitutive model is used to numerically study the Lüders-like deformations in NiTi shape memory alloys during pseudoelastic response. An in-house FEM code was developed in FORTRAN for the numerical simulations. The FEM code is capable of handling non-linear problems with coupled thermomechanical fields. The modified Newton-Raphson method was used to solve the set of non-linear equations. A summary of the finite element formulations and the non-linear calculations are given in Appendix C.

3.4.1. Quasi-static extension of a short NiTi strip

A short strip of NiTi subjected to displacement-controlled uniaxial extension under isothermal conditions is simulated using the proposed constitutive model. The simulation results based on an incremental constitutive model are also provided for comparison. The details of the incremental constitutive model are given in Appendix E.

The strip geometry and FE mesh are depicted in Figure 3-3. The strip dimensions ($14 \times 4 \times 0.4$ mm³) and boundary conditions are similar to the strip modeled by Shaw and Kyriakides (1998):

$$u|_{x=0} = 0, \quad u|_{x=L} = \delta$$

$$v|_{x=0, y=0} = 0, \quad v|_{x=L, y=0} = 0$$

where u and v are displacement components in the x - and y - directions, and δ is the applied end displacement.

The strip was discretized with two-dimensional, 8-node isoparametric plane-stress (serendipity) elements. The number of elements in the axial and transverse directions is 70 and 20, respectively, which is the same as the mesh density used in the simulation of Shaw and Kyriakides (1998). They used three-dimensional 20-node elements with two elements in the thickness direction. However, it is shown that the two-dimensional plane-stress finite element analysis used here is successful in capturing the features of the transformation front, and a three-dimensional analysis is not necessary. Note that although the finite element modeling is two-dimensional, the normal component of transformation strain in the transverse direction still exists due to the incompressibility of transformation-induced deformation, and therefore, all important quantities are accounted for in the analysis.

The sensitivity of the finite element analysis to mesh-size was investigated by trying a number of different mesh densities. The mesh density selected in the present analysis (70×20) is computationally efficient and captures the important features of the transformation fronts. The details of the convergence study are provided in Appendix F.

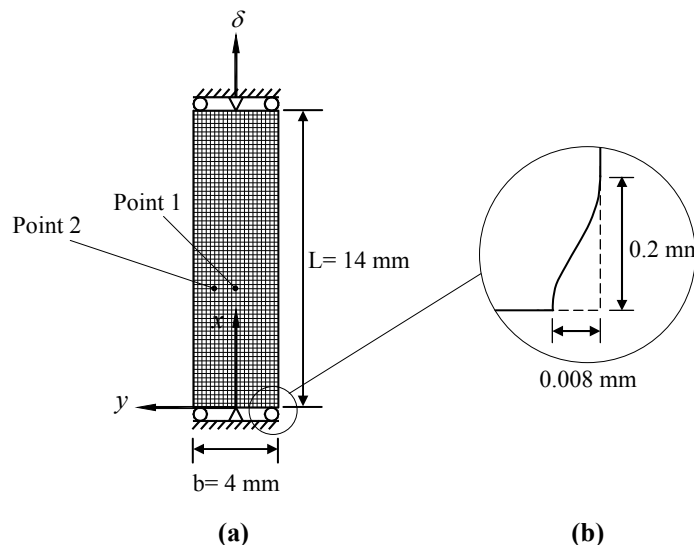


Figure 3-3. (a) Geometry and finite element discretization of the strip; (b) Corner imperfection.

A very small geometric imperfection is introduced at the lower right corner of the strip ($x=0$, $y=-b/2$) in order to initiate the transformation at this point as a result of the stress concentration (Figure 3-3b). The imperfection has the shape of a cosine function (half period) with amplitude of 4×10^{-3} mm and width of 0.4 mm.

The elastic behavior of the individual austenite and martensite phases was assumed isotropic and homogeneous. The mechanical parameters chosen for this analysis are given in Table 3-2. The critical values of stress for nucleation and completion of transformations (σ_{MN} , σ_{MC} , σ_{AN} , σ_{AC}) were obtained by fitting the results of the simulations to the nucleation and propagation stresses of NiTi strips at 25 °C observed in the experimental results reported by Shaw and Kyriakides (1997) (see Figure 2-4a). The elastic moduli of austenite and martensite, and maximum engineering transformation strain ($\Delta\varepsilon_t$) were also chosen based on the tri-linear stress-strain model used in the simulation of Shaw and Kyriakides (1998). Note that the measures of stress and strain in Table 3-2 are the second Piola-Kirchhoff and Green, respectively. This is because the FEM program has been developed for general large-deformation problems in anticipation of future research.

Table 3-2. Mechanical properties of the short NiTi strip at 25 °C.

Parameter		Value
Elastic modulus of Austenite	E_A (GPa)	62.7
Elastic modulus of Martensite	E_M (GPa)	38.7
Poisson's ratio	ν_A, ν_M	0.3
Transformation strain	$\Delta\varepsilon_t$	0.0398
Martensite nucleation stress	σ_{MN} (MPa)	424.7
Martensite completion stress	σ_{MC} (MPa)	353.1
Austenite nucleation stress	σ_{AN} (MPa)	143.6
Austenite completion stress	σ_{AC} (MPa)	221.6

For better illustration of the material properties given in Table 3-2, the local one-dimensional engineering stress-strain response for one complete loading-unloading cycle is shown in Figure 3-4. The upper and lower intermediate branches correspond to the forward and reverse transformations. The intermediate branches slightly deviate from perfect straight lines due to variation of the elastic modulus with martensitic fraction (see equation 3-8).

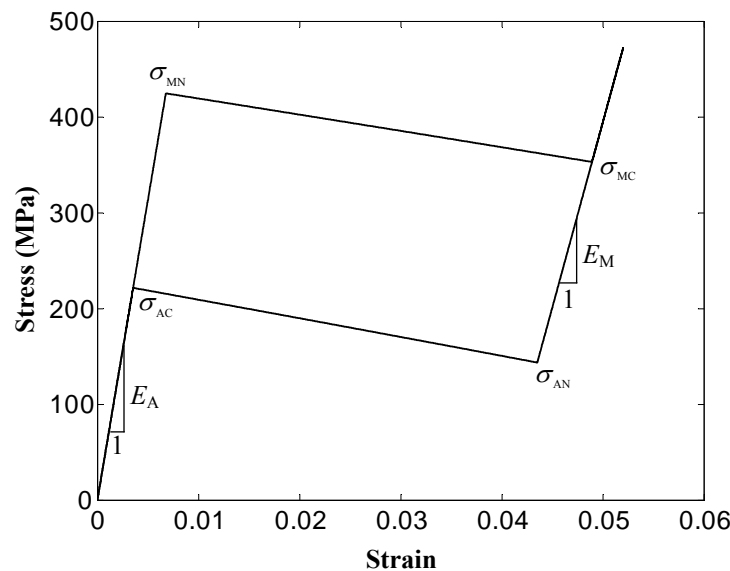


Figure 3-4. Local uniaxial engineering stress-strain response of NiTi used in the simulation.

The force-displacement responses from the present simulation and the simulation of Shaw and Kyriakides (1998) are shown in Figure 3-5. Since Shaw and Kyriakides (1998) only simulated the forward transformation, the comparison with their work is possible only for the forward transformation. As seen in Figure 3-5, the result of the present model shows fully recovery of deformation upon unloading. A stress peak at the nucleation of forward transformation and a small dip at the end of the upper stress plateau that are typically observed in the experiments can also be found in the results corresponding to both simulations.

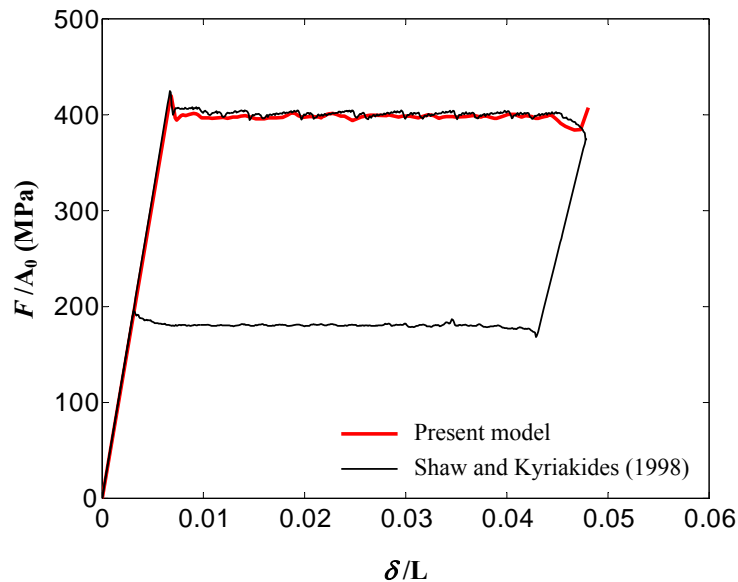


Figure 3-5. Nominal stress-strain response of the NiTi short strip.

A set of contour plots showing the martensitic fraction during the loading (forward transformation) is shown in Figure 3-6. Each contour represents the extent of transformation corresponding to various applied displacements. Transformation is first nucleated at the lower right corner due to the stress concentration. Initially, a Hill-type special localization is formed which later switches to a finger-type pattern as the transformation propagates. This type of transformation pattern is also observed in the experimental observations (Shaw and Kyriakides, 1998). As the inclined transformation band grows, the lateral deflection of the strip increases at the lower end of the strip. On the other hand, the axial force opposes the growth of lateral deflection. Eventually some transformation bands in the opposite direction are also nucleated to minimize the lateral deflection. This process is repeated as the loading continues. The mechanism of successive formation of finger-like edges in alternate directions is described in detail by Shaw and Kyriakides (1998).

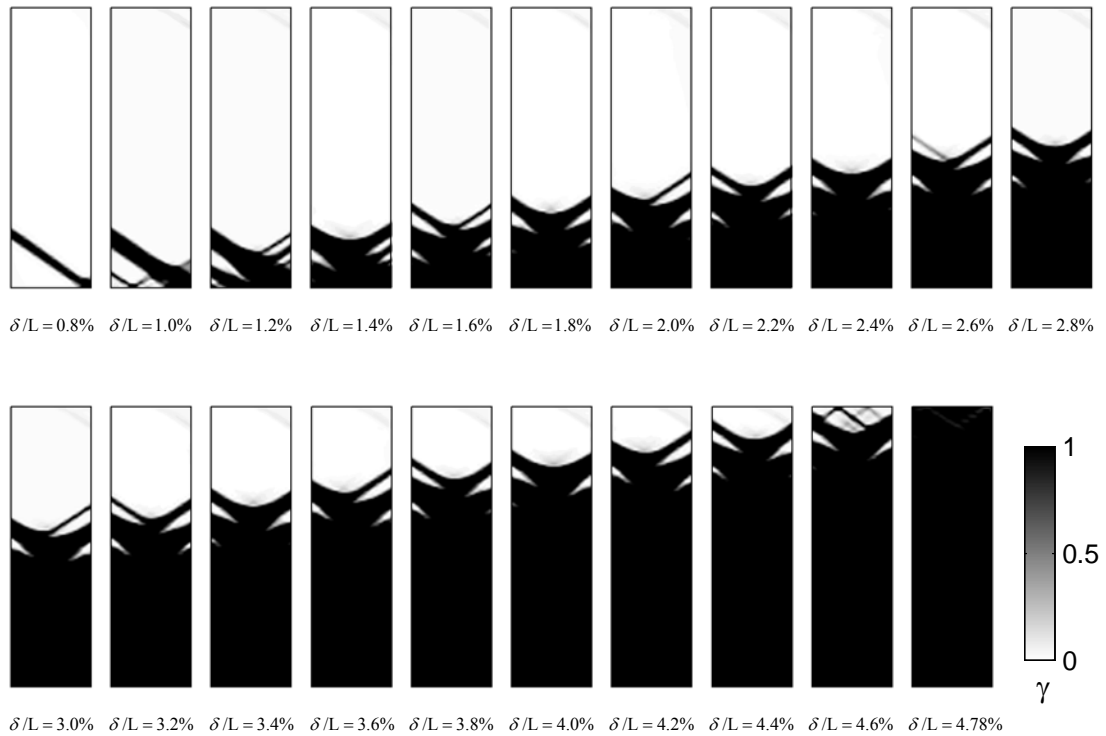


Figure 3-6. Sequence of martensitic fraction contours during loading.

In Figure 3-7, black and white regions of axial strain at selected loading stages are compared with those from Shaw and Kyriakides (1998). The Green-Lagrange strains were converted to true strains (logarithmic strains) for this purpose. The regions with axial strain of 2% or higher are shown in black, and those with lower axial strains are in white. In the first three plots, the transformation patterns from the two simulations are identical. The axial strain contours then start showing some deviation from each other, although the overall pattern of the transformation front remains similar.

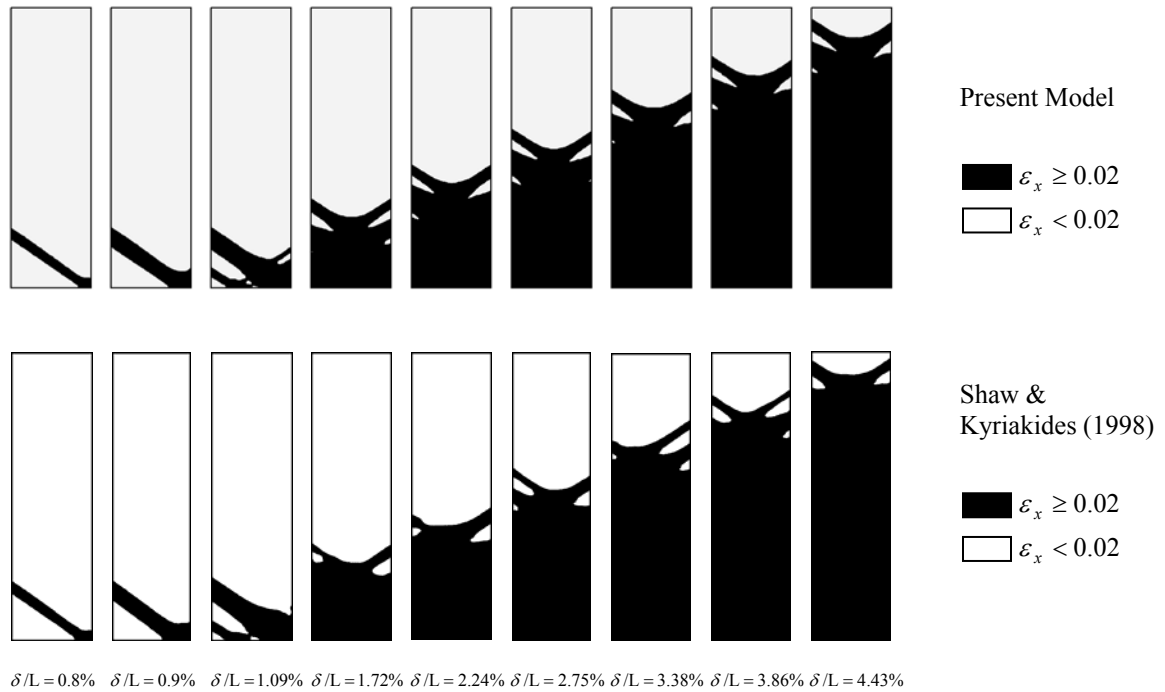


Figure 3-7. Sequence of logarithmic axial strain distribution during loading.

The loading is terminated at $\delta/L = 4.78\%$, just before the entire domain transforms into martensite. This leaves some small partially untransformed areas near the $x=L$ end.

The evolution of martensitic fraction during unloading (reverse transformation) is plotted in Figure 3-8. The reverse transformation started at the partially untransformed regions (martensite-austenite mixture) left at the end of loading phase. As shown later, this is because the level of stress is lower in these partially transformed regions. The reverse transformation initially proceeds along an inclined band, but soon after a rather symmetric criss-cross pattern is formed. This criss-cross pattern continues during the propagation of the reverse transformation front, and the sharp finger-type edges that were seen during loading are not present. Unfortunately, the experimental data are not available to verify the predicted shape of transformation fronts during the reverse transformation of the short NiTi strips.

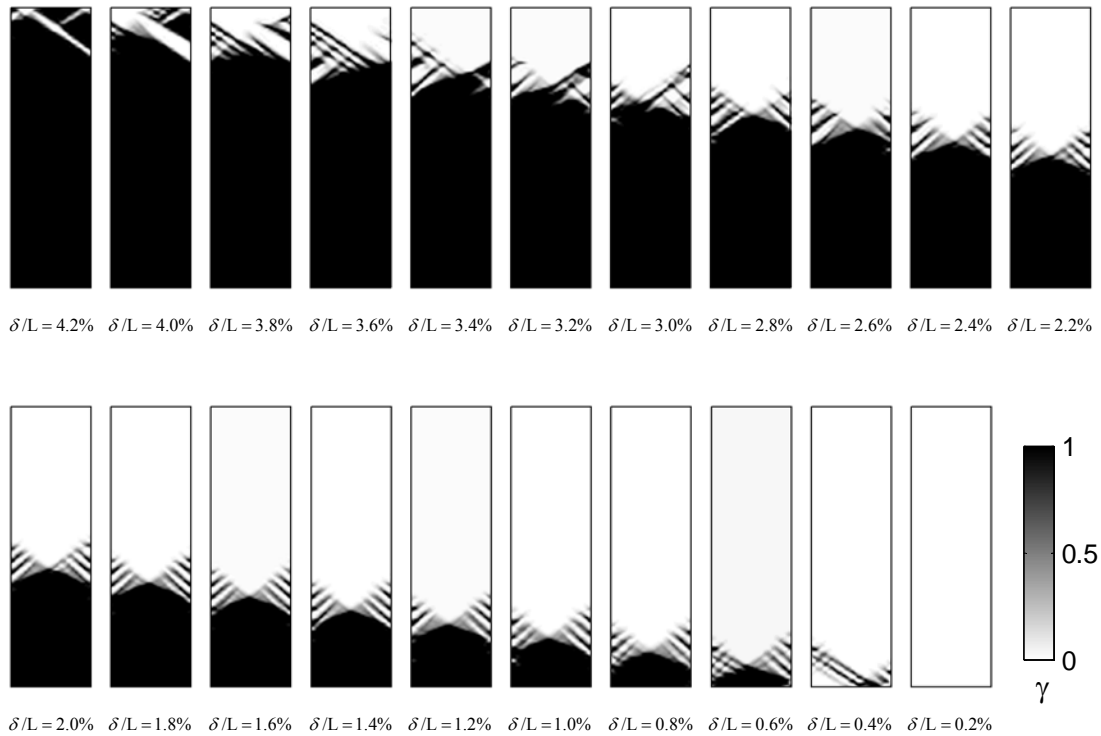
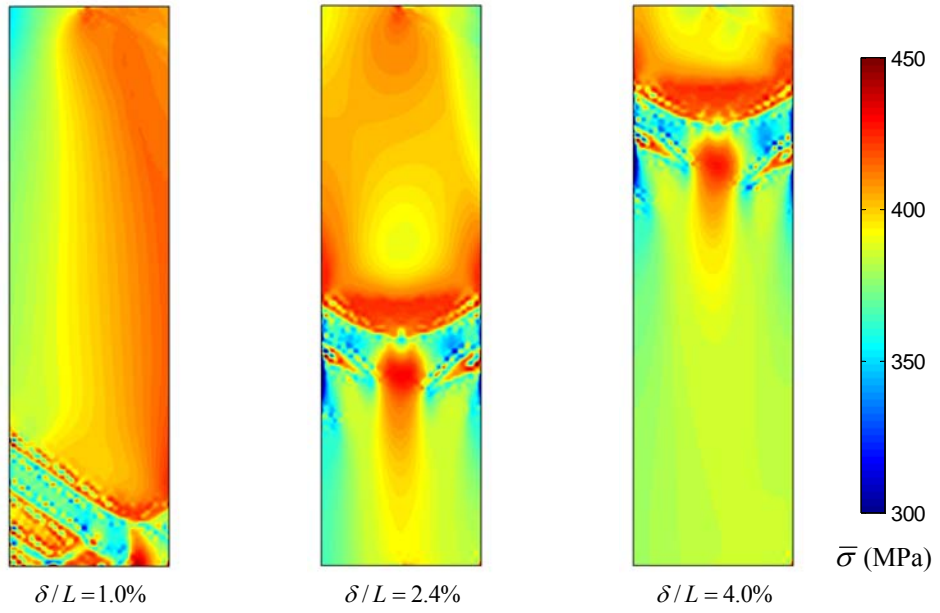
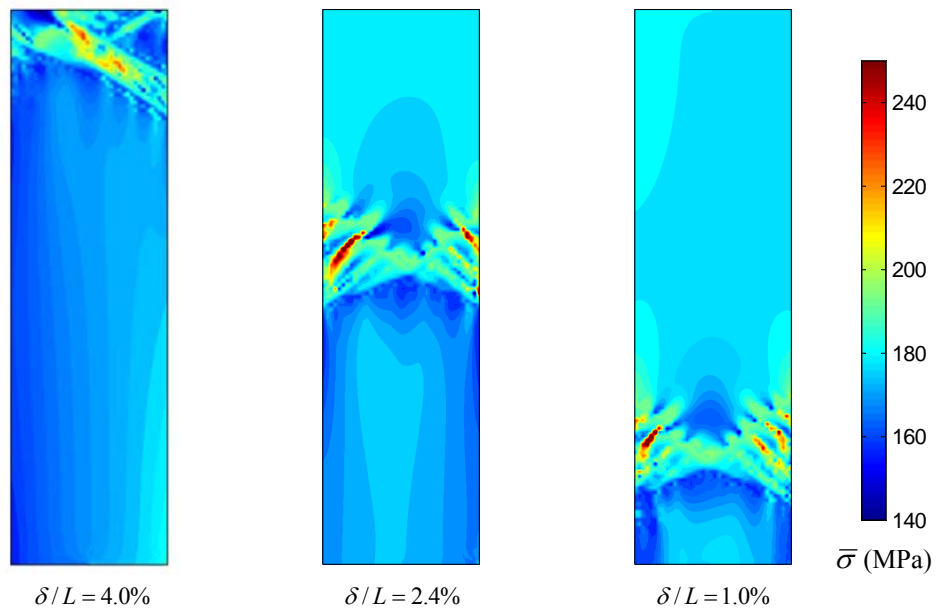


Figure 3-8. Sequence of martensitic fraction contours during unloading.

To understand the role of the stress distribution in the propagation of transformation fronts, contours of effective stress ($\bar{\sigma}$) during forward and reverse transformations at selected loading/unloading stages are shown in Figure 3-9. In Figure 3-9(a), the stress level is higher on the untransformed (austenite) side of the transformation front during the forward transformation. This effect transforms the austenite regions close to the transformation front and prohibits the nucleation of martensite bands at other places. Therefore, only one transformation front moves upward. During unloading on the other hand, the level of stress is lower on the martensite side of the front, which makes the adjacent martensitic particles unstable. Therefore, the reverse transformation occurs only at the propagating transformation front which moves downward.



(a)



(b)

Figure 3-9. Distributions of effective stress at selected loading/unloading stages. (a) Loading; (b) Unloading.

It should be noted that the high or low stress concentrations seen at the transformation fronts in Figure 3-9 are caused by the localization of deformation. Deformation localization also results in a complex multi-axial state of stress at the transformation fronts despite the uniaxial nature of the applied extension. In order to better illustrate the multi-axiality of the stress state, the variation in stress, transformation strain, and martensitic fraction during loading and unloading at two sample points are shown in Figure 3-10. The location of sample points are denoted by “Point 1” and “Point 2” in Figure 3-3(a). Point 1 is located at $(x=0.4L, y=0)$ and Point 2 is located at $(x=0.4L, y=b/4)$.

The transformation from austenite to martensite during loading occurs quite suddenly at these two points. The state of stress is initially two-dimensional during the forward transformation. As explained earlier, the multi-axiality of the stress state during the transformation is due to the localization of deformation. Therefore, the transformation strain tensor is also initially multi-axial and has three non-zero components. The stress tensor gradually becomes uniaxial again as the transformation front passes over and transformation ends. It is seen that the components of transformation strain tensor also change to align themselves with the evolving stress tensor. This behavior is due to reorientation of transformation strain embedded in the proposed constitutive model. In fact, it is the reorientation of transformation strain tensor that results in a uniform distribution of stress in the transformed areas despite the non-uniformity of the stress distribution at the transformation fronts (see Figure 3-9).

During the reverse transformation, it is seen that the state of stress becomes two-dimensional again due to deformation localization at the transformation front. Eventually, the transformation strains are fully recovered at Points 1 and 2.

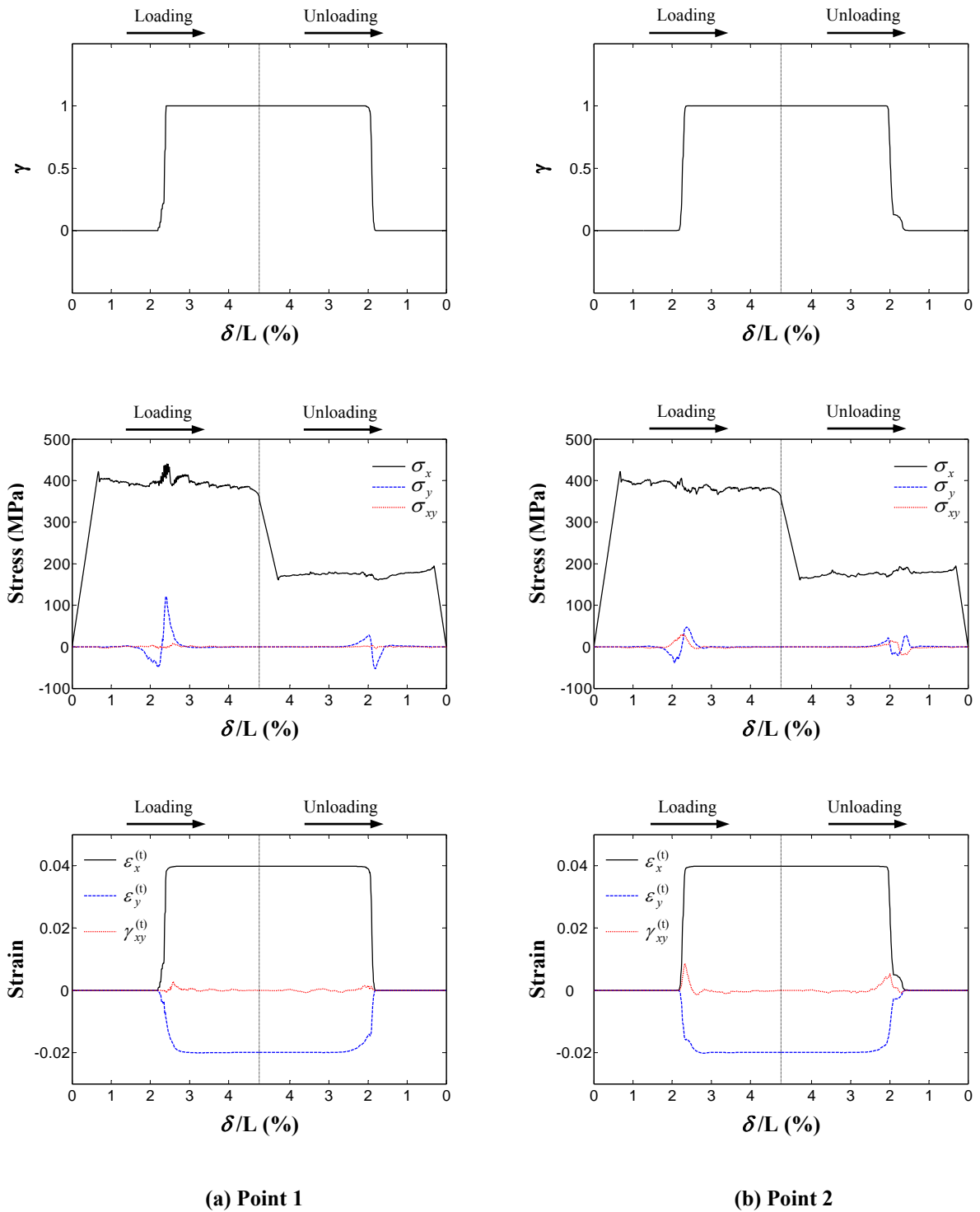


Figure 3-10. Variations of martensitic fraction, stress, and transformation strain at Point 1 and Point 2.

For the purpose of comparison, a path-dependent incremental constitutive model was also employed to simulate this problem. The incremental constitutive relations which are similar to those in the model of Boyd and Lagoudas (1994) are described in Appendix E. The material parameters used with the incremental model are the same as those provided in Table 3-2.

The predicted engineering stress-strain response based on the incremental constitutive model is shown in Figure 3-11. Despite the reversibility of the transformation strain in this model, the overall pseudoelastic response exhibits a large residual strain upon unloading. This can be explained by looking at the distribution of martensitic fraction throughout the sample.

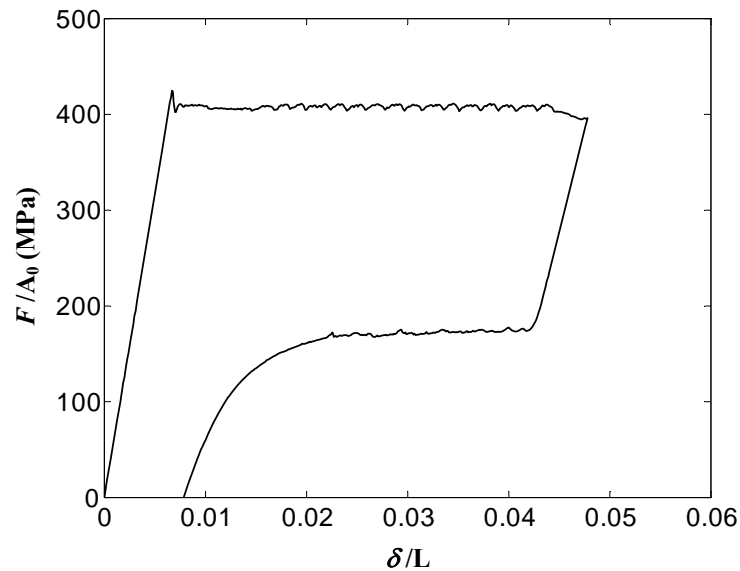


Figure 3-11. Nominal stress-strain response of the NiTi short strip based on the incremental constitutive model (Appendix E).

Two sets of contour plots showing the evolution of martensitic fraction during the forward and reverse transformations are shown in Figure 3-12. The results of simulation based on the incremental model are similar to those predicted by the total deformation model during the forward transformation (see Figure 3-6). However, the transformation behavior during unloading based on the

incremental model (Figure 3-12b) is quite different from that predicted by the total deformation model (Figure 3-8). During unloading, the reverse transformation initiates at numerous points throughout the sample, and a distinct moving front does not exist anymore. Although the transformation occurs in a localized manner, it is not limited to the vicinity of a single propagating transformation front. By the end of unloading, the majority of the sample has transformed back into austenite, however, some isolated pockets of martensitic phase still remain throughout the sample. The reason for this behavior is the presence of a biased non-uniform stress distribution produced during the forward transformation.

The predicted distributions of equivalent stress based on the incremental constitutive model at select instants are shown in Figure 3-13. As the transformation front propagates during loading, local regions of high stress concentration are formed inside the transformed areas (Figure 3-13a). These high-stress regions are found to be along the finger-like edges nucleated during the forward transformation. Upon unloading, the mismatch in strain between the neighboring transformed and untransformed regions further intensifies the stress concentration (Figure 3-13b). The high stress concentration prohibits the occurrence of the inverse transformation. Consequently, some localized martensitic areas are locked inside the parent phase, and the transformation strain is not recovered at every point (Figure 3-12b). In contrast, the reorientation of transformation strain in the total deformation model (Figure 3-10) results in a fairly uniform distribution of stress across the transformed areas as seen in Figure 3-9. This prevents particles from being locked in the localized high stress concentration zones during reverse transformation.

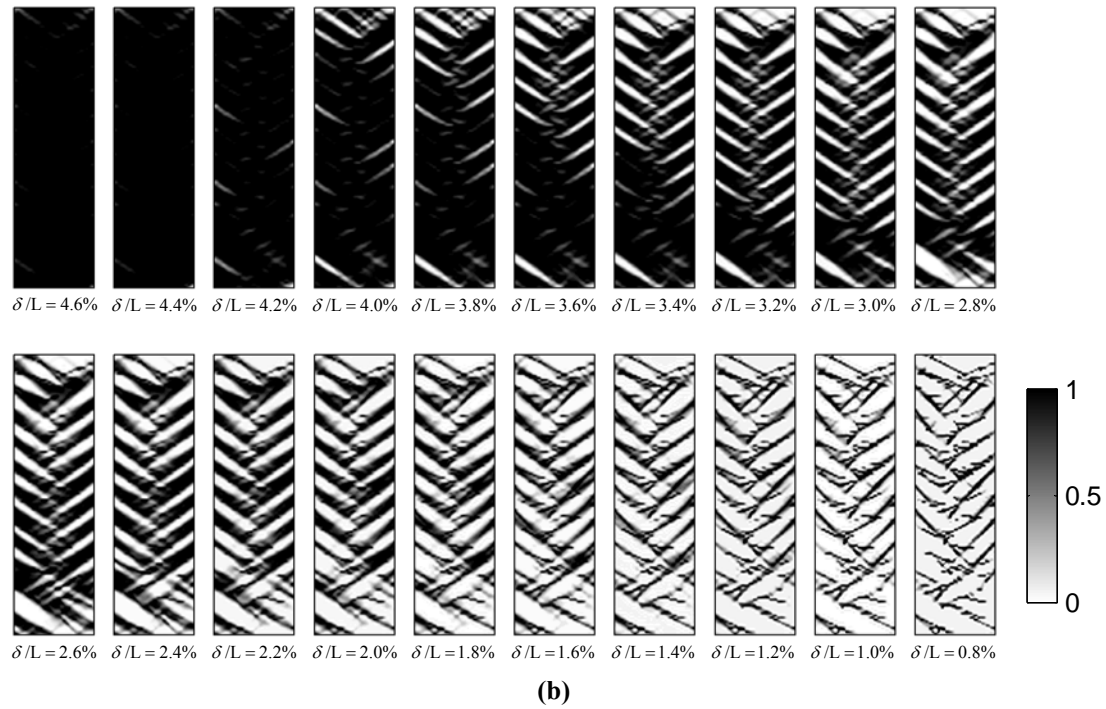
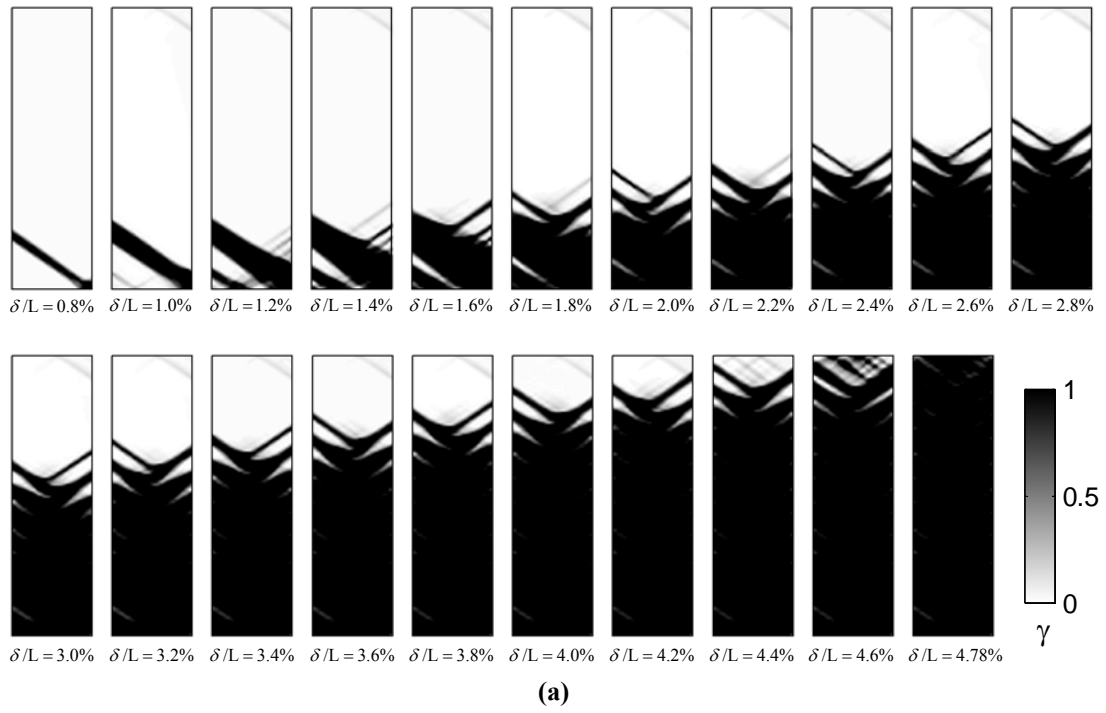
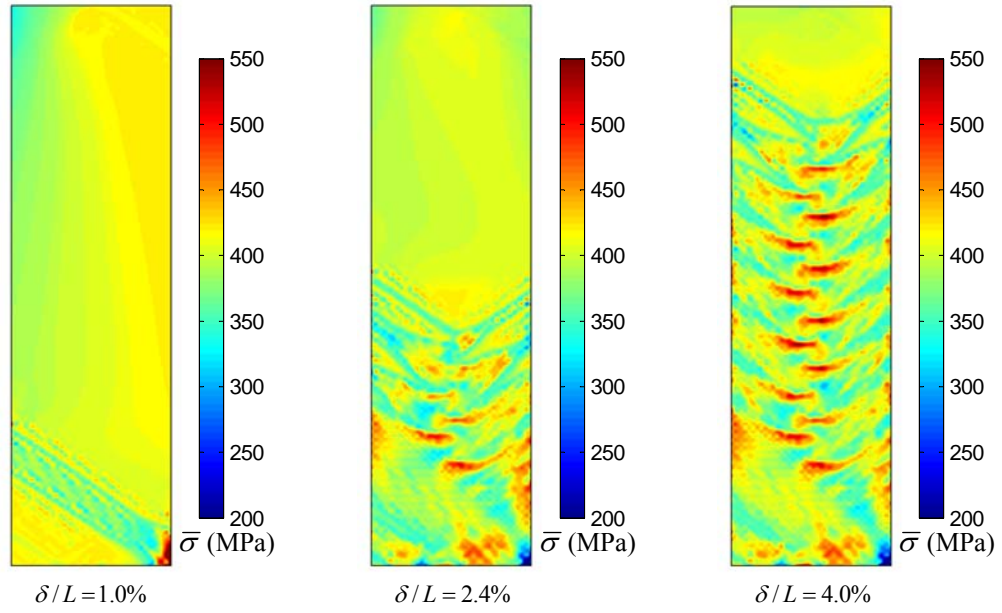
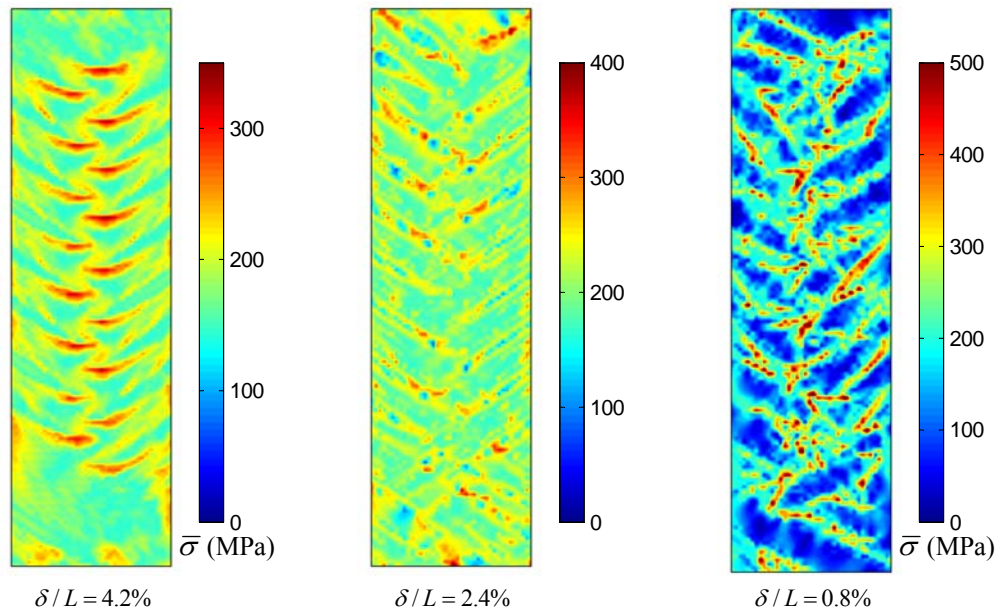


Figure 3-12. Predicted evolution of transformation based on the incremental constitutive model (Appendix E). (a) Loading; (b) Unloading.



(a)



(b)

Figure 3-13. Predicted distributions of equivalent stress based on the incremental constitutive model (Appendix E). (a) Loading; (b) Unloading.

3.4.2. Effect of heat generation and loading rate

After verifying the ability of the model to capture unstable pseudoelastic response in the previous section, the analysis is extended to include the internal heat generation/consumption and thermal interactions with environment. The constitutive model is implemented within an FEM simulation to predict the nucleation and propagation of transformation-induced instabilities during the pseudoelastic response of NiTi dog-bone samples at various loading rates. The simulation results are compared with the experimental observations of Shaw and Kyriakides (1997). A brief description of the experimental procedure used by them can be found in Appendix B.

The geometry of the sample and FE mesh are shown in Figure 3-14. The sample is similar to the one used in the experiments of Shaw and Kyriakides (1997), which has a uniform thickness of 0.4 mm. The two-dimensional spatial domain was discretized with 8-node serendipity plane-stress elements. The gauge section was discretized with 150 elements along the length and 10 elements across the width. A small dent with a depth of 0.04 mm was introduced at the top right corner of the gauge section as shown in Figure 3-14. The purpose of this geometric imperfection is to control the location of the first nucleation. Physically, this imperfection manifests itself as a manufacturing defect at the junction of the gauge section and fillet. There is no other artificial imperfection and all the events following the first nucleation take place naturally as a result of the numerical solution.

The nodal displacements along the bottom end of the specimen ($x = 0$) are fixed while those across the top end ($x = L_0$) are pulled at a constant rate. The temperatures of both ends are fixed at the ambient temperature (25 °C). Shaw (2000) justified this assumption based on the large size of the metallic grips used in the experiments. The heat loss due to natural convection has been considered by assuming a constant convective film coefficient, $h_{\text{conv}} = 4$ (W/m² K), for all the exposed surfaces and free edges of the sample (Shaw, 2000). The imposed mechanical and thermal boundary conditions may be expressed as,

$$\begin{aligned}
 u|_{x=0} &= 0, & v|_{x=0, y=0} &= 0 \\
 u|_{x=L_0} &= \delta, & v|_{x=L_0, y=0} &= 0 \\
 T|_{x=0} &= 25^\circ\text{C} \\
 T|_{x=L_0} &= 25^\circ\text{C} \\
 \dot{q}|_{\text{surface}} &= h_{\text{conv}}(T - 25^\circ\text{C}) \\
 \dot{q}|_{\text{edge}} &= h_{\text{conv}}(T - 25^\circ\text{C})
 \end{aligned}$$

where u and v are the displacement components in the x - and y - directions, respectively, δ is the applied end displacement, T ($^\circ\text{C}$) is the temperature, and \dot{q} (W/m^2) is the rate of heat loss per unit area.

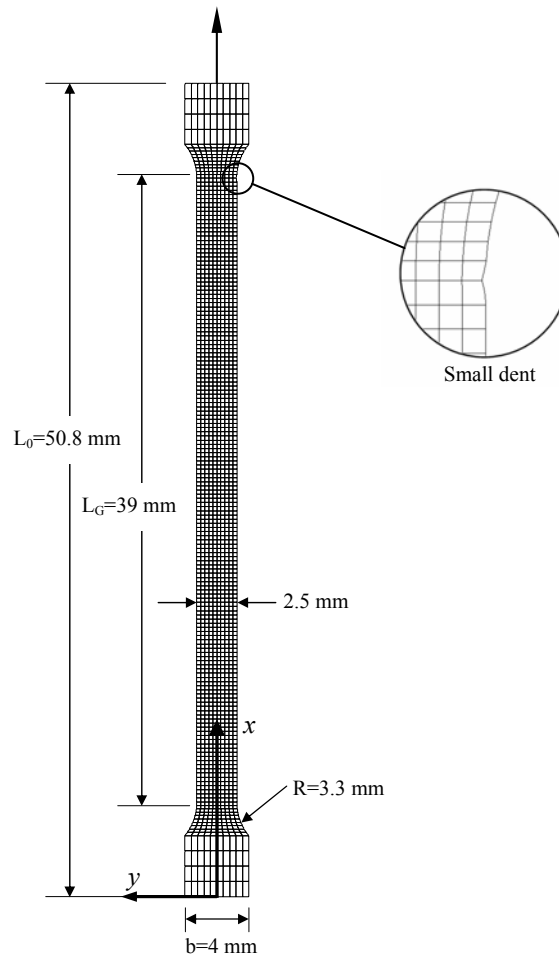


Figure 3-14. Geometry and finite element discretization of the dog-bone sample.

In the experiments of Shaw and Kyriakides (1997), the variation in temperature at the moderate strain rate was in the range of +12 °C and -5 °C. Therefore, heat transfer through radiation was assumed to be negligible. Thermal expansion/contraction was also ignored in the following analysis due to its minor effect on the results.

The sensitivity of the present numerical analysis to mesh size, and the uniqueness of the solution were examined. Despite the instability of mechanical behavior, only minor mesh sensitivity was observed in the numerical simulations conducted with finer meshes. As pointed out by Shaw (2000), the generation or absorption of heat during the transformation stabilizes the mechanical response. Additionally, the recovery of material stability at the end of phase transformation has an overall stabilizing effect on the solution. As a result, the overall force-displacement response, temperature variation, the number of nucleation events, and the basic features of the front morphology are not affected by mesh size. However, the exact location and timing of nucleation events, and also the orientation of transformation fronts (+ θ or - θ) are sensitive to mesh size.

3.4.2.1. Material parameters and calibration of the constitutive model

In the present analysis, it is assumed that individual solid phases behave as isotropic materials. A set of stress-strain curves derived from the isothermal (low strain rate) uniaxial tensile tests on NiTi dog-bone samples reported by Shaw (2000) have been used to find the mechanical parameters of the constitutive model (see Figure 2-4a). The mechanical responses of the material at three different temperatures (15, 25, and 35 °C) have been considered for this purpose. The elastic modulus of individual phases (E_A, E_M), and the transformation strain ($\Delta\varepsilon_t$) are the average values measured directly from the experimental results.

In order to find the nucleation and completion stresses during the forward transformation, a set of isothermal simulations at various temperatures were run on the dog-bone sample shown in

Figure 3-14. By best-fitting the nominal nucleation stress and propagation stress (Maxwell stress) obtained from the numerical analysis to those from the experiments at the above mentioned temperatures, the following linear relationships were established,

$$\sigma_{MN}(T) = 9.4258 T + 189.13 \quad (\text{MPa})$$

$$\sigma_{MC}(T) = 4.8158 T + 232.73 \quad (\text{MPa})$$

The tapered sections of the sample in Figure 3-14 experience a lower level of stress. Therefore, some residual austenite remains in those areas at the end of stress plateau. This effect masks a visible stress valley at the onset of reverse transformation in the stress-strain response, both in the simulations and experiments. In order to eliminate the end effects, Shaw and Kyriakides (1997) used straight specimens to experimentally measure the nucleation stress during reverse transformation. During these tests, austenite nucleation upon unloading occurs in the middle of test section and is accompanied by a distinct stress valley. To calibrate the model for reverse transformation, a straight specimen was also used in the isothermal simulations, as depicted in Figure 3-15. The dimensions and FE mesh of the specimen are similar to those of the gauge section of the dog-bone sample. A slight side imperfection in the form a bump was introduced at $x=L/5$ to control the location of the first nucleation. The height of the bump was 0.04 mm. The specimen was first loaded until the entire domain was fully transformed into martensite, and then was unloaded.

The following linear relationships were found to best fit the nucleation and propagation stresses of the reverse transformation obtained from the isothermal experiments at different temperatures,

$$\sigma_{AN}(T) = 7.5128 T - 44.22 \quad (\text{MPa})$$

$$\sigma_{AC}(T) = 10.276 T - 35.31 \quad (\text{MPa})$$

In above relations T is in $^{\circ}\text{C}$ and $\sigma_{MN}, \sigma_{MC}, \sigma_{AN}, \sigma_{AC}$ are the second Piola-Kirchhoff stresses. The variations of the nucleation and completion stresses with temperature are shown in Figure 3-16. In Figure 3-16, the nominal (engineering) nucleation and propagation stresses (Maxwell stress) as determined by the isothermal simulations are also shown. Notice the large difference between the engineering nucleation stress and the second Piola-Kirchhoff nucleation stress during the reverse transformation. This difference is due to the large amount of strain induced during the forward transformation. The local isothermal behavior of the material according to the constitutive model is shown in Figure 3-17.

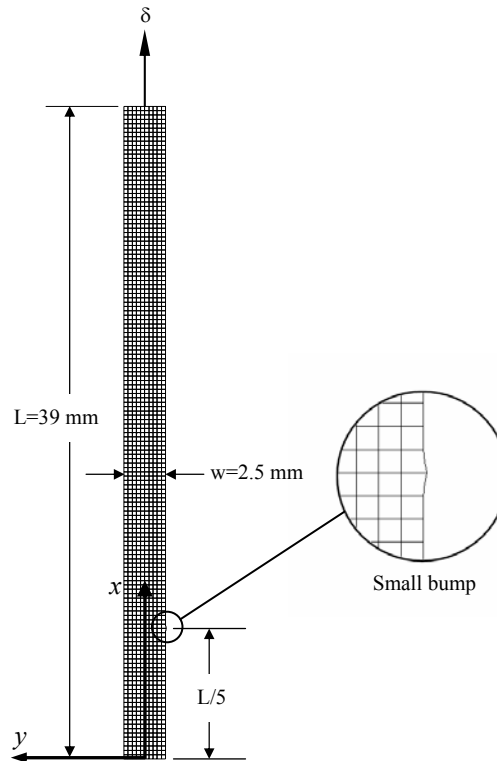


Figure 3-15. Geometry and finite element discretization of the sample used for the calibration of the model in reverse transformation

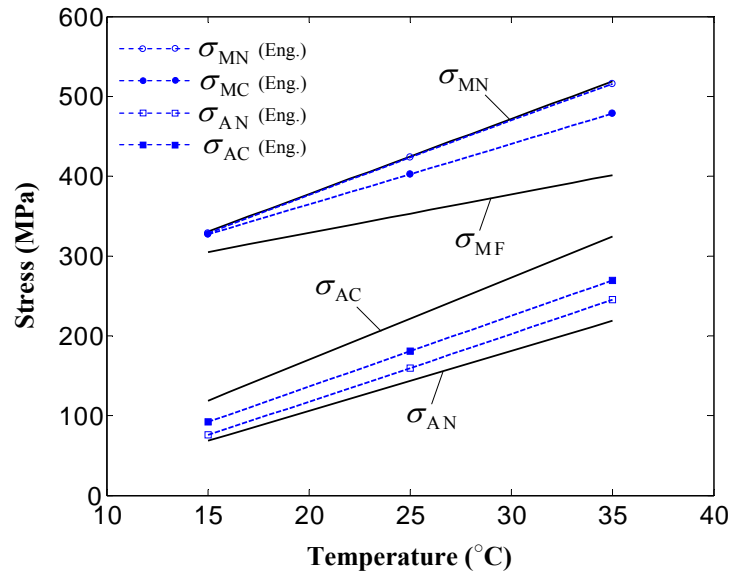


Figure 3-16. Chosen 2nd Piola-Kirchhoff nucleation and completion stresses and their equivalent engineering values as determined by isothermal simulations.

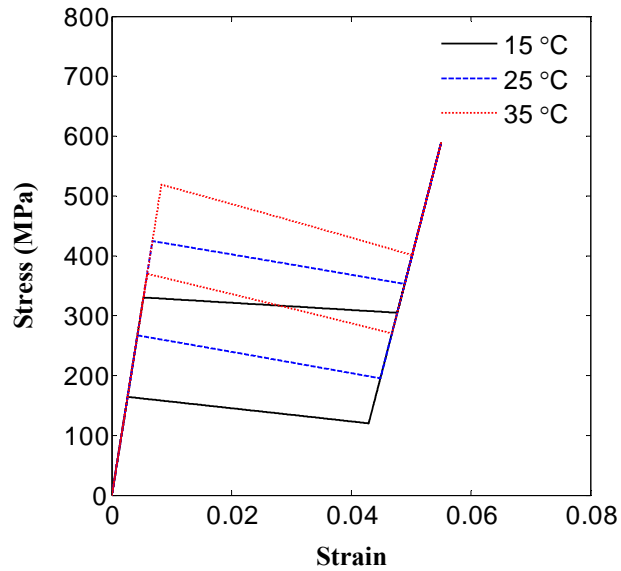


Figure 3-17. Local isothermal 1-D stress-strain behavior of SMA according to the constitutive model.

In order to show the close fit of the chosen mechanical properties, the overall pseudoelastic responses of the dog-bone sample based on the isothermal simulations are compared to the experimental results in Figure 3-18. The deviation from linear elasticity during loading at 15 °C is probably due to the rhombohedral phase transformation (A→R) that occurs prior to martensitic transformation at this low temperature (further details can be found in Shaw and Kyriakides, 1995). Also, the deviation from linearity during loading at 25 °C is due to the early phase transformation which occurs homogeneously prior to the nucleation of localized transformation bands (Feng and Sun, 2006; Daly et al., 2007; also Remark 5 at the end of Section 3.3.3.).

Thermal parameters of the NiTi strip, including zero-stress enthalpy change, $\Delta h_{A \rightarrow M}$, the thermal conductivity, k , specific heat capacity, C_p , and density, ρ , were taken from Shaw (2000). It was also assumed that the stress-free enthalpy change for the martensite to austenite transformation, $\Delta h_{M \rightarrow A}$, is the negative of that for the austenite to martensite transformation. As an approximation, all thermal parameters were assumed to be independent of phase, temperature, or other state variables. Table 3-3 summarizes the chosen mechanical and thermal properties.

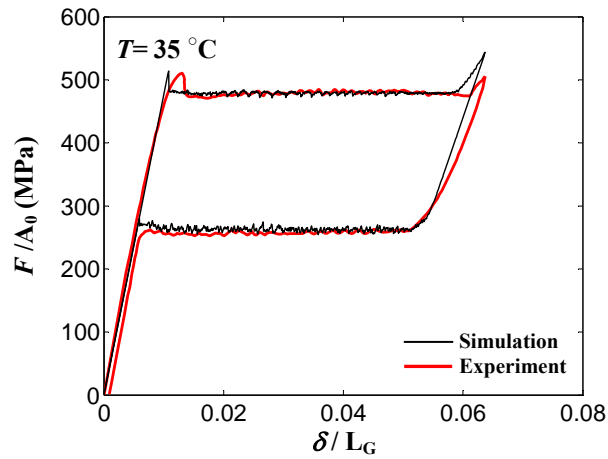
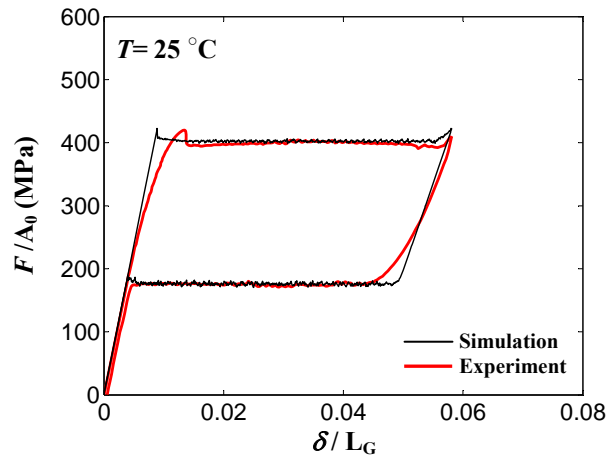
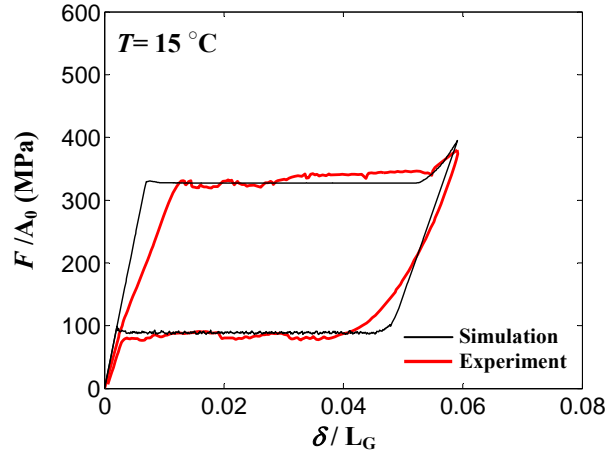


Figure 3-18. Pseudoelastic response of NiTi strip under isothermal conditions. (a) $T = 15\text{ }^{\circ}\text{C}$; (b) $T = 25\text{ }^{\circ}\text{C}$; (c) $T = 35\text{ }^{\circ}\text{C}$ (Experimental data are taken from Shaw, 2000).

Table 3-3. Mechanical and thermal properties of the NiTi strip.

Parameter		Value
Elastic modulus of Austenite	E_A (GPa)	57.55
Elastic modulus of Martensite	E_M (GPa)	28.00
Poisson's ratio	ν_A, ν_M	0.3
Transformation strain	$\Delta\varepsilon_t$	0.0429
Martensite nucleation stress	σ_{MN} (MPa)	$9.4258 T^{(C)} + 189.13$
Martensite completion stress	σ_{MC} (MPa)	$4.8158 T^{(C)} + 232.73$
Austenite nucleation stress	σ_{AN} (MPa)	$7.5128 T^{(C)} - 44.22$
Austenite completion stress	σ_{AC} (MPa)	$10.276 T^{(C)} - 35.31$
Enthalpy change at zero-stress	$\Delta h_{A \rightarrow M}, -\Delta h_{M \rightarrow A}$ (J kg ⁻¹)	-12.3×10^3
Thermal conduction coefficient	k (W m ⁻¹ K ⁻¹)	18
Specific heat capacity	C_p (J kg ⁻¹ K ⁻¹)	837
Density	ρ (kg m ⁻³)	6.5×10^3

3.4.2.2. Simulation of loading-unloading at low strain-rate

The pseudoelastic response of the dog-bone sample, shown in Figure 3-14, was simulated for low strain-rate displacement-controlled loading-unloading. The ambient air temperature surrounding the sample and the temperature of the grips was 25 °C. The specimen was loaded at a constant rate of $\dot{\delta}/L_G = 10^{-4} \text{ s}^{-1}$. The deformation was paused at $\delta/L_G = 6.4\%$ for 5 minutes to allow the sample to reach thermal equilibrium, followed by unloading at a constant rate of $\dot{\delta}/L_G = -10^{-4} \text{ s}^{-1}$.

The predicted force-displacement response is compared with the experimental measurements of Shaw and Kyriakides (1997) in Figure 3-19. A sequence of 14 contour graphs showing the distribution of phase and temperature corresponding to the deformed configurations of the specimen during the forward transformation are provided in Figure 3-20. The contours are separated by

intervals of $\delta/L_G = 0.4\%$ with the first and last contour corresponding to $\delta/L_G = 0.8\%$ and $\delta/L_G = 6\%$, respectively. The first region to transform to martensite nucleates at the geometric imperfection described earlier, and a sharp inclined deformation band forms with the well-known angle of 55° to the specimen axis. Upon additional loading, the single, well-defined transformation front evolves into an alternating criss-cross pattern, which is similar to the pattern Shaw and Kyriakides (1997) observed in their experiments. As loading continues, the temperature at the transformation front increases (Figure 3-21), which in turn results in an increase in the nominal stress as shown in Figure 3-19. At $\delta/L_G \approx 2.7\%$, a second transformation front nucleates at the lower end of the gauge section due to the stress concentration near the round fillet. The second nucleation event causes the drop in the load observed in both the experiment and the simulation results (refer to Figure 3-19). As the fronts approach each other, they become straight and inclined across the width with the same orientation to minimize the mismatch between them. At the instant of coalescence, the fronts make an angle of 57.5° with the loading axis. Overall, the mechanical response, distribution of temperature, evolution of transformation, and details of the transformation fronts are in good agreement with the experimental observations of Shaw and Kyriakides (1997).

The sequence of events leading to the initial shape change of the transformation front is particularly interesting. Figure 3-21 shows a close up view of the transformation front (phase distribution contour) and distorted mesh, as well as the predicted bending moment at the top end of the specimen ($x=L_0$) as a function of loading. The contour and mesh image labels correspond to various loading stages which are marked in Figure 3-21(c). In the distorted mesh images, the lateral displacement (v) has been multiplied by a factor of 20 to accentuate the lateral deflection in Figure 3-21(b). When the inclined transformation band nucleates at time ① and begins to spread, the lateral deflection increases continuously at the front. The lateral deflection causes a bending moment to build up at the specimen end, which tends to straighten the specimen. The bending moment and lateral

deflection reach their maximum between times ⑤ and ⑥, where the first finger emanates from the upper front in order to balance the lateral deflection, and straighten the specimen. As a result, the bending moment and lateral deflection decrease from time ⑥ to ⑧. The subsequent evolution of the transformation front can be described as successive nucleation and growth of finger patterns in alternative directions in order to keep the lateral deflection minimum.

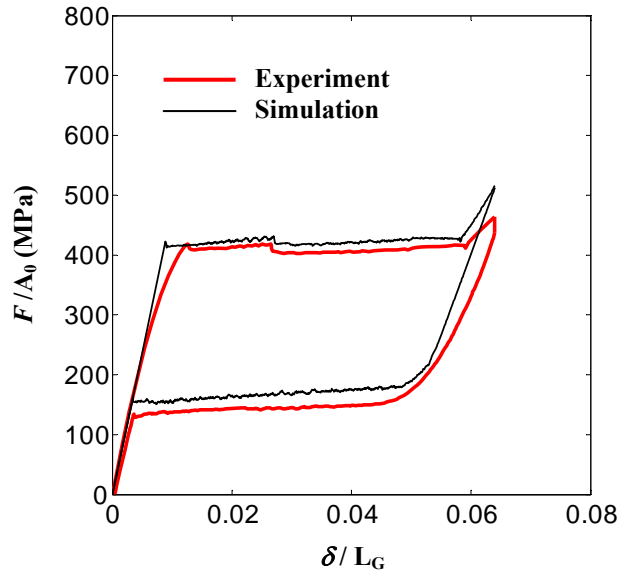
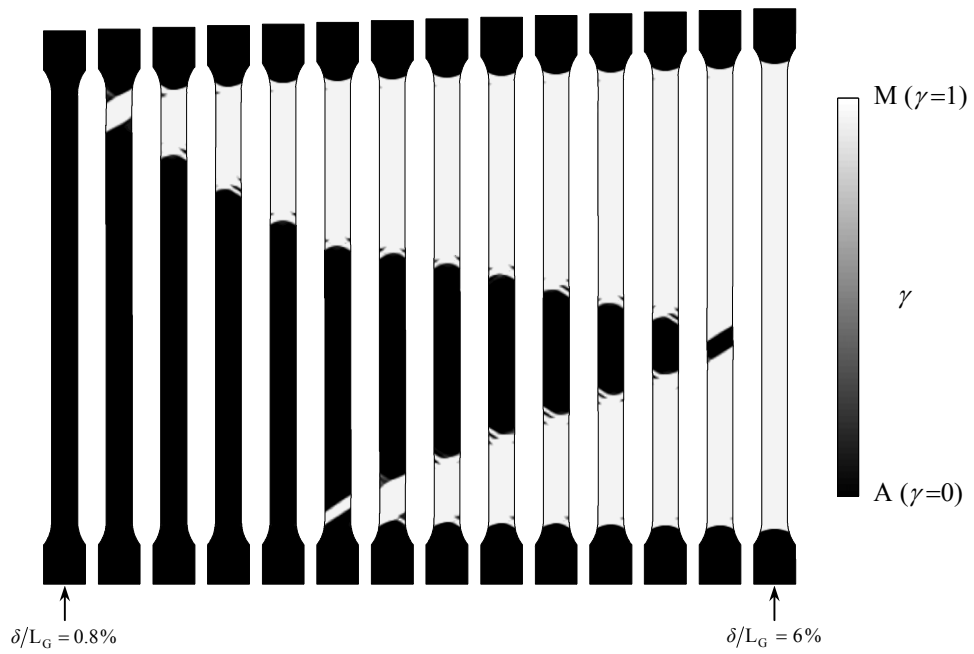
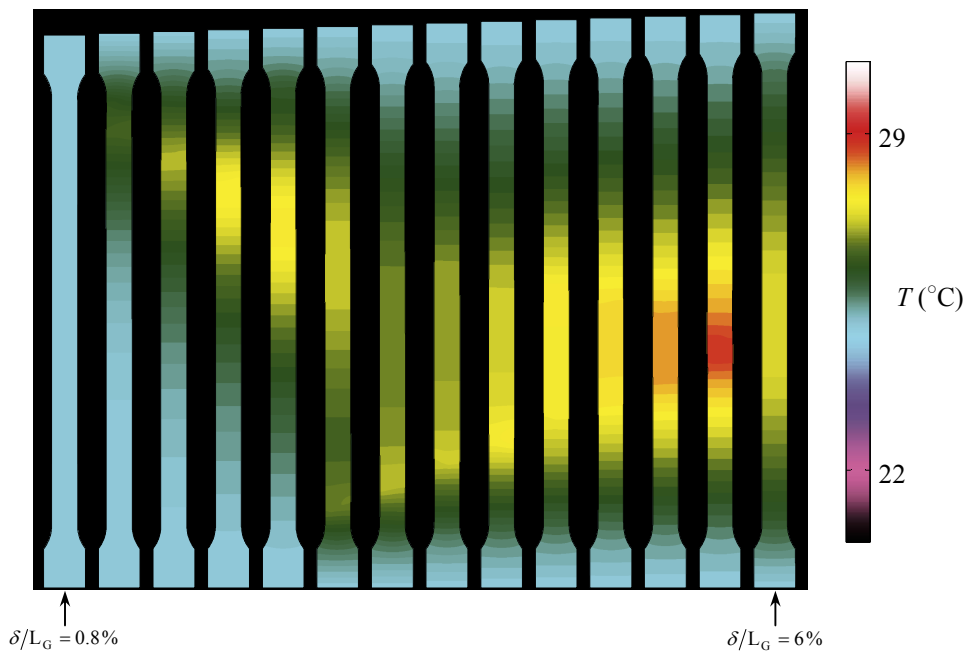


Figure 3-19. Pseudoelastic response of NiTi strip at $\dot{\delta}/L_G = 10^{-4} \text{ s}^{-1}$. Experimental data are taken from Shaw and Kyriakides (1997).

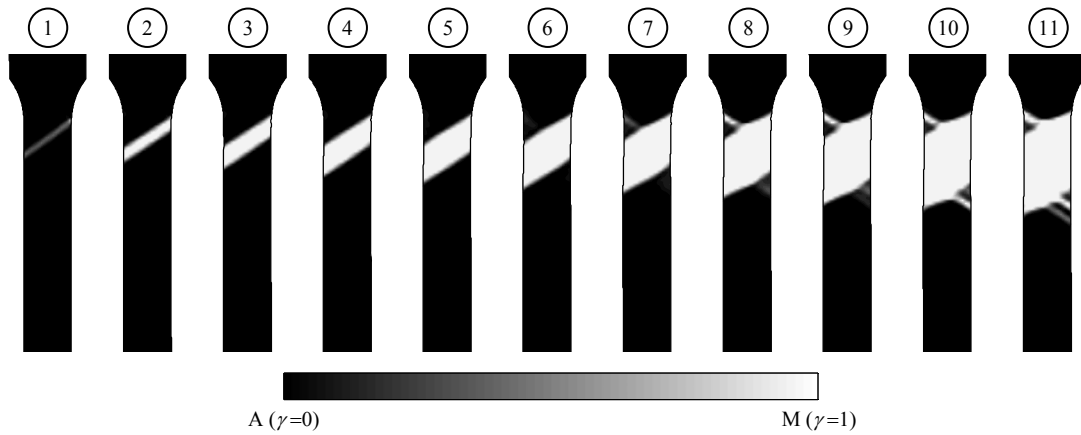


(a)

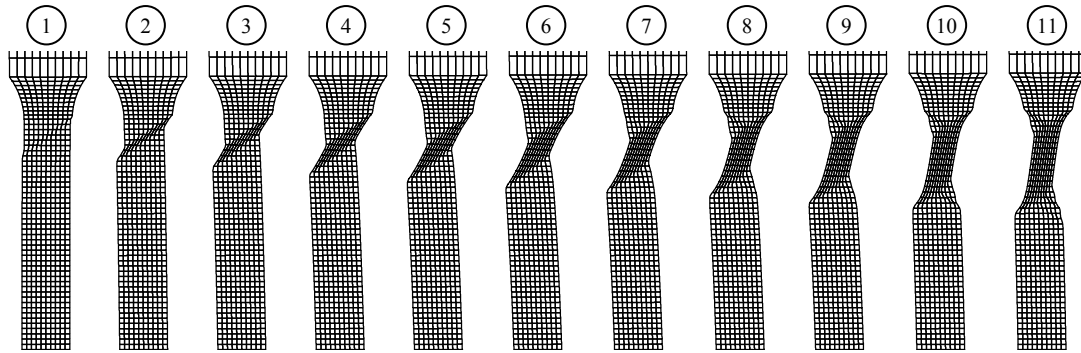


(b)

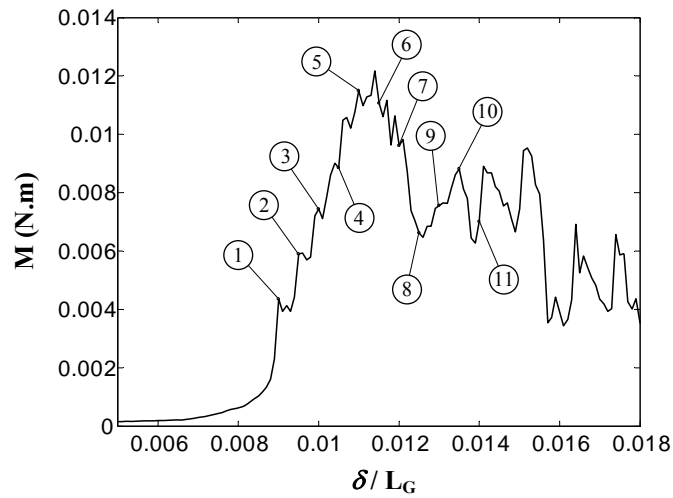
Figure 3-20. Sequence of events during forward transformation at $\dot{\delta}/L_G = 10^{-4} \text{ s}^{-1}$. (a) Martensitic fraction; (b) Temperature.



(a)



(b)

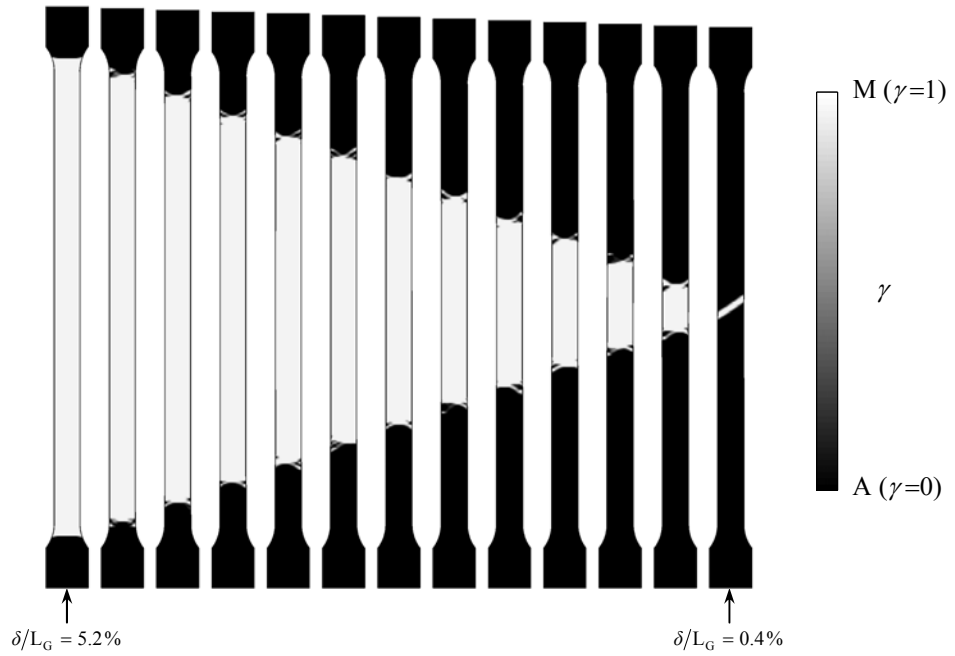


(c)

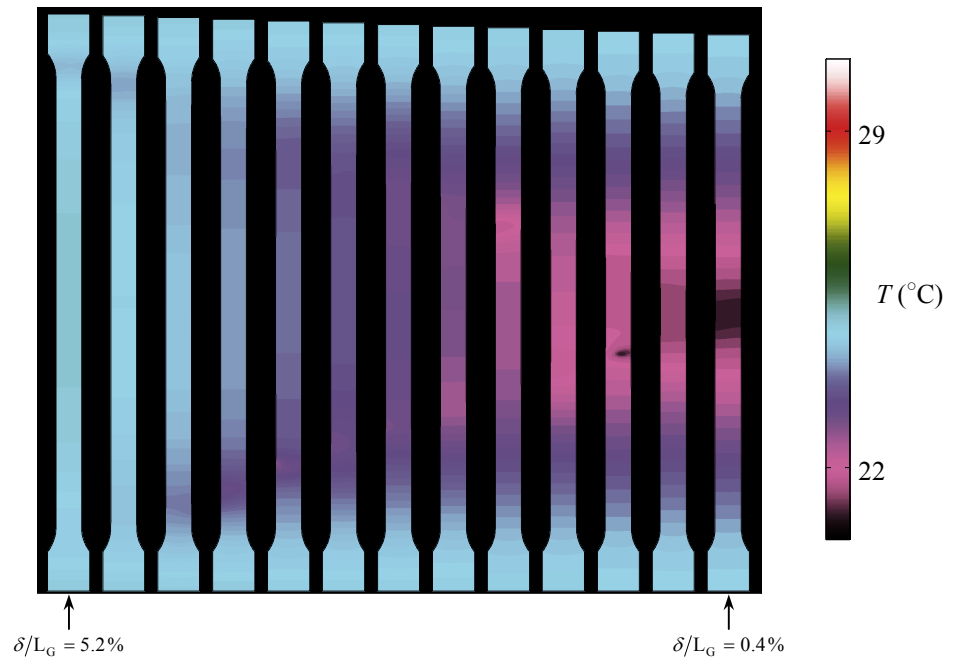
Figure 3-21. Details of front morphology evolution during nucleation of forward transformation. (a) Distribution of phases; (b) Distorted mesh with lateral displacement multiplied by a factor of 20; (c) Bending moment at the upper end.

During the pause between loading and unloading, the temperature of the sample returns to the ambient temperature. The evolution of the phase transformation and temperature distributions during the reverse transformation are shown in Figure 3-22. As expected, the reverse transformation initiates at the tapered ends of the sample due to the reduced stress at these regions. The two transformation fronts propagate toward each other at the same speed. During most of the unloading part, the converging fronts are predicted to propagate through inverse shrinkage of the finger-type patterns observed during the forward transformation. However, experimental results of Shaw and Kyriakides (1997) suggested that the fronts during reverse transformation are quite sharp and straight with an inclination angle of approximately 56° . This discrepancy between the predicted and observed results is probably due to the lack of information on the exact boundary conditions at the gripped ends in the model. As will be discussed later, small misalignments in the boundary conditions may result in sharp inclined fronts during the reverse transformation.

In addition to difference in the shape of the transformation fronts, the magnitude of the predicted temperature drop during reverse transformation is also different from the measurements of Shaw and Kyriakides (1997). The maximum temperature drop observed during the experiment was -2°C whereas in the simulation it was predicted to reach -3.6°C . This discrepancy may be partly due to uncertainties in the thermo-physical properties of the specimen and thermal boundary conditions, and/or partly due to the assumption that zero-stress latent heat in forward and reverse transformations have the same value.



(a)



(b)

Figure 3-22. Sequence of events during reverse transformation at $\delta/L_G = -10^{-4} \text{ s}^{-1}$. (a) Martensitic fraction; (b) Temperature.

3.4.2.3. Simulation of loading-unloading at moderate strain-rate

The pseudoelastic response of the dog-bone SMA specimen was simulated for a moderate strain rate condition. A constant loading rate of $\dot{\delta}/L_G = 10^{-3} \text{ s}^{-1}$ was applied until $\delta/L_G = 7.65\%$, followed by a 5-minute hold, and then unloading at the same constant rate. The ambient air temperature was 25 °C. The nominal stress-strain response is shown in Figure 3-23. The evolution of phase transformation and distribution of temperature during the forward and reverse transformations are depicted in Figures 3-24 and 3-25. The transformation behavior is very similar to the experimental observations of Shaw and Kyriakides (1997). The localized transformation is first nucleated at the top corner followed by a second nucleation event at the lower end and two nucleation events in the mid-span. The shape of transformation fronts match those observed in the experiment. For the duration of the loading phase, they are sharp and straight, with an inclination angle ranging from 55° to 65° to the vertical axis. Only occasionally will one or two fingers develop at the front. This can be explained by noticing that the lateral deflection developed in each front compensate the lateral deflection in another front, and therefore the sharply inclined fronts can survive without branching and developing crossing fingers.

An interesting feature of the stress-strain response in Figure 3-23 is the stress-relaxation during the break time between loading and unloading, which can be seen in both the simulation and experimental results. This stress-relaxation is caused by the phase transformation due to the temperature decrease during the pause period (Pieczyska, 2006c).

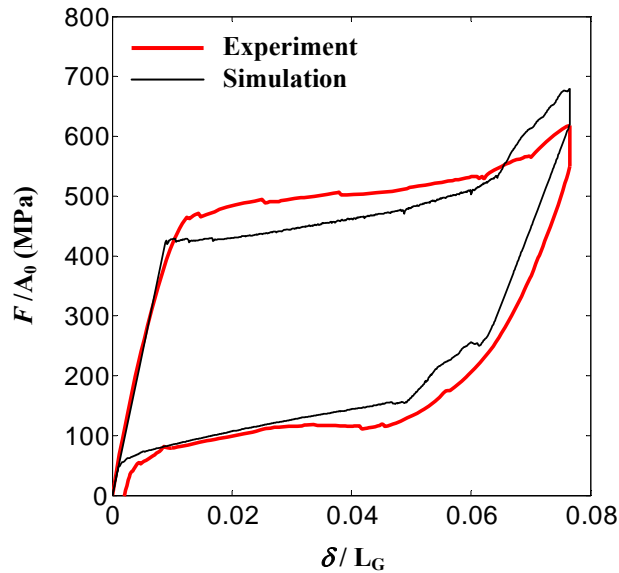
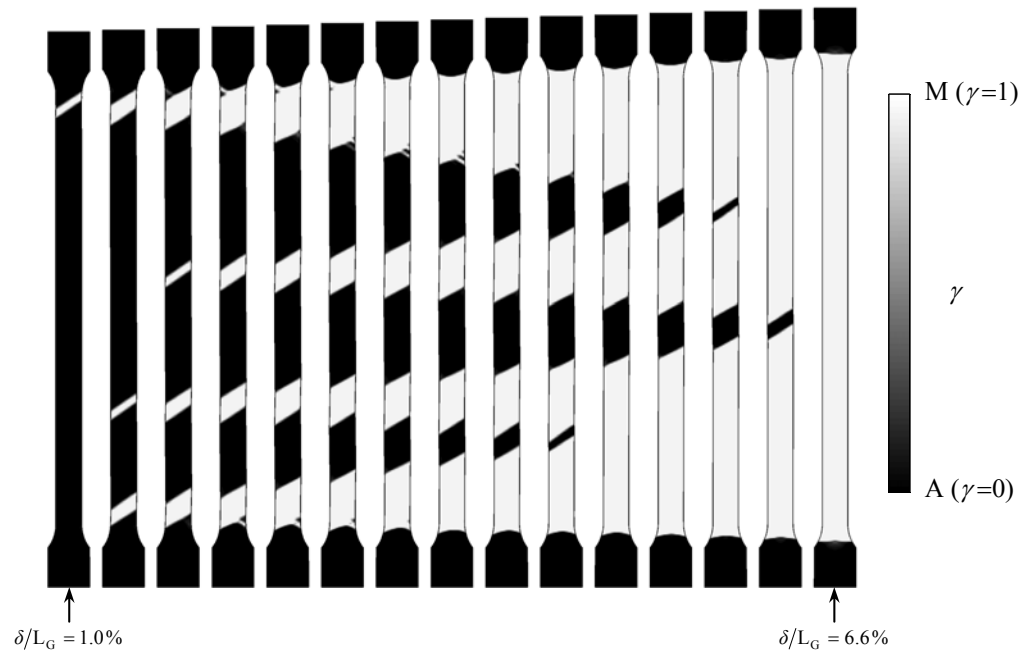


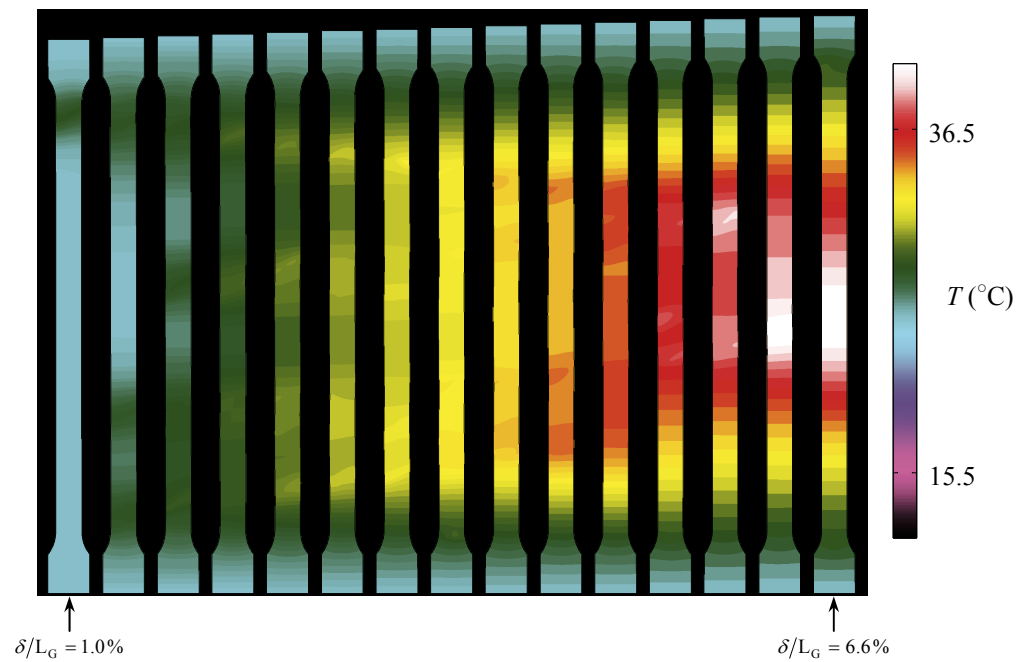
Figure 3-23. Pseudoelastic response of NiTi strip at $\dot{\delta}/L_G = 10^{-3} \text{ s}^{-1}$. Experimental data are taken from Shaw and Kyriakides (1997).

Unlike the low strain rate case, the transformation fronts during unloading at this moderate strain rate are mostly straight, with an inclination angle between 54° and 62° . The fronts emanating from the sample ends, however, are initially fingered and gradually become straight as they approach the middle fronts.

The temperature distributions during forward transformation agree with the measurements of Shaw and Kyriakides (1997). But as in the previous simulation, the predicted temperatures exhibit a much larger temperature drop (-13°C) during the reverse transformation as compared to the experiments (-5°C). This large deviation from the experimental measurements suggests that the stress-free enthalpy change during the reverse transformation ($\Delta h_{M \rightarrow A}$) must be substantially smaller than its counterpart during forward transformation. The DSC measurements reported in Shaw (2000), however, do not show such a large difference. Further investigation is needed to clarify this issue.



(a)



(b)

Figure 3-24. Sequence of events during forward transformation at $\dot{\delta}/L_G = 10^{-3} \text{ s}^{-1}$. (a) Martensitic fraction; (b) Temperature.

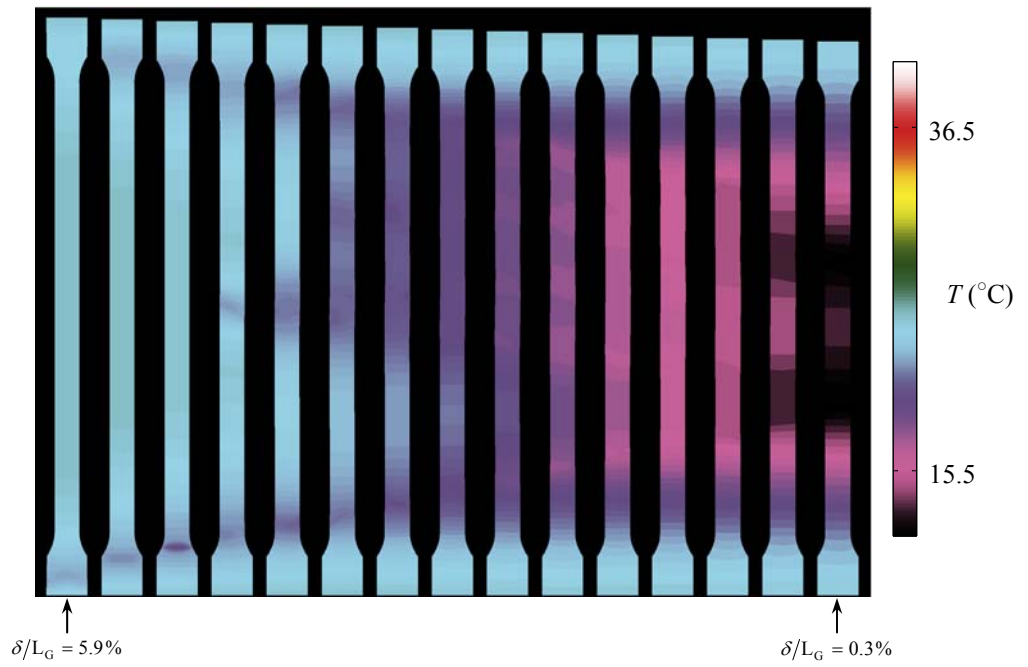
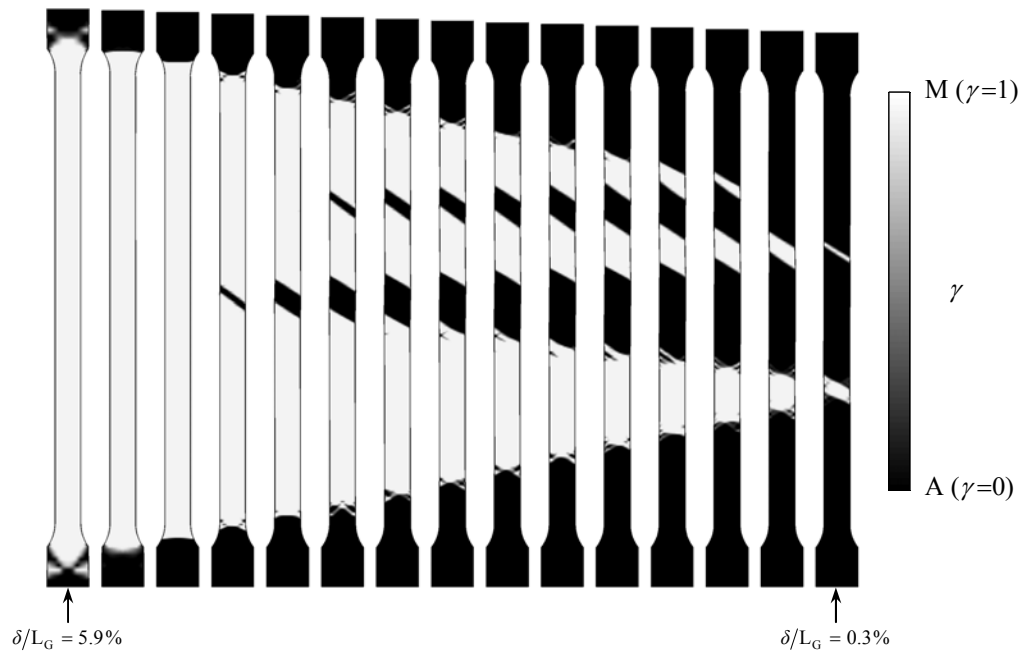


Figure 3-25. Sequence of events during reverse transformation at $\delta/L_G = -10^{-3} \text{ s}^{-1}$. (a) Martensitic fraction; (b) Temperature.

3.4.2.4. Simulation of loading-unloading at high strain-rate

This simulation was performed for a high strain rate beyond the loading rates applied in the experiments of Shaw and Kyriakides (1997). The elongation rate in this case was $\dot{\delta}/L_G = 5 \times 10^{-3} \text{ s}^{-1}$, which is five times faster than the moderate strain rate case. The loading was stopped at $\delta/L_G = 7.65\%$, followed by a 5-minute hold and then unloading. The predicted nominal stress-strain response at this rate is compared to those at the low and moderate strain rates in Figure 3-26. The evolution of the phase transformations and temperature during loading and unloading are shown in Figures 3-27 and 3-28, respectively.

Similar to the previous cases, the first nucleation event occurs at the top end of the gauge section where the geometric imperfection is located. Shortly after that, seven narrow bands, some parallel and some opposing each other are nucleated almost simultaneously in the gauge section. The number of nucleation events in this case is substantially larger than those observed in the previous two cases.

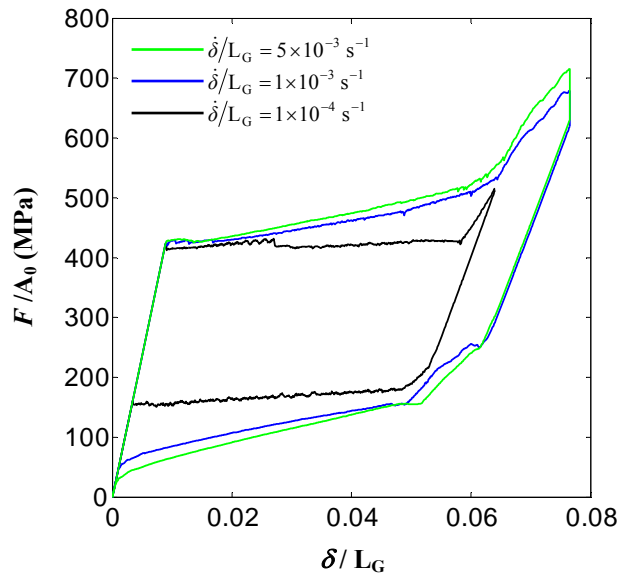
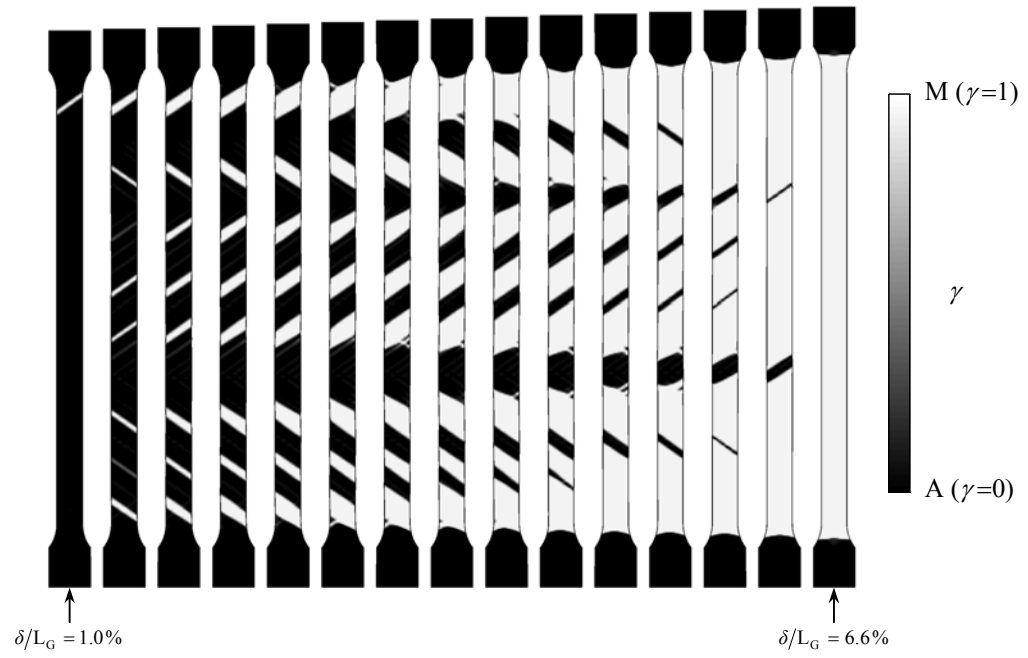
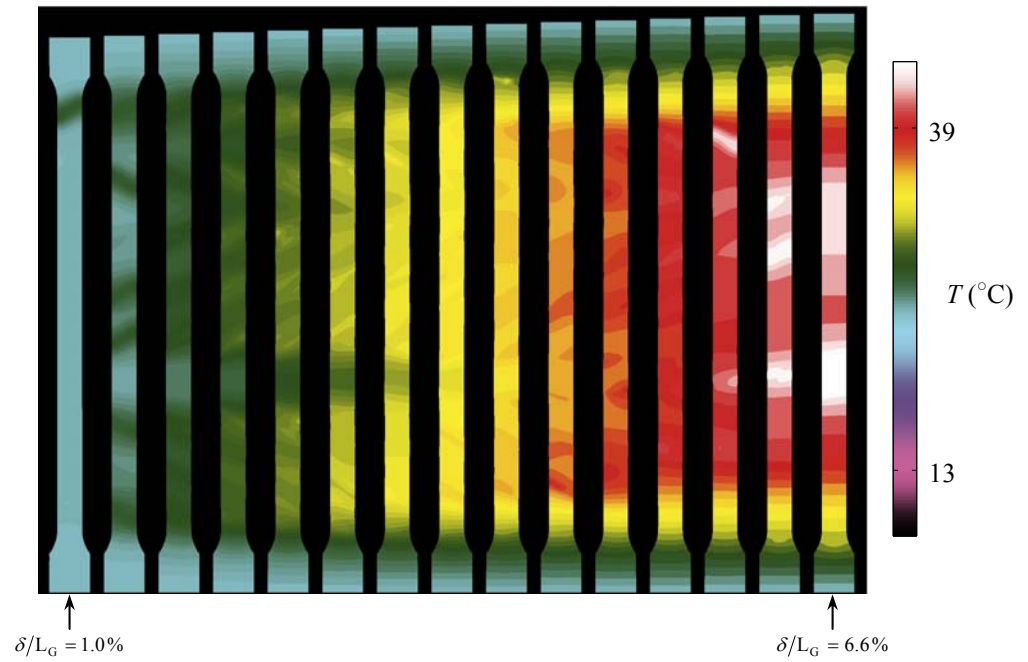


Figure 3-26. The simulated pseudoelastic response of NiTi strip at various elongation rates.

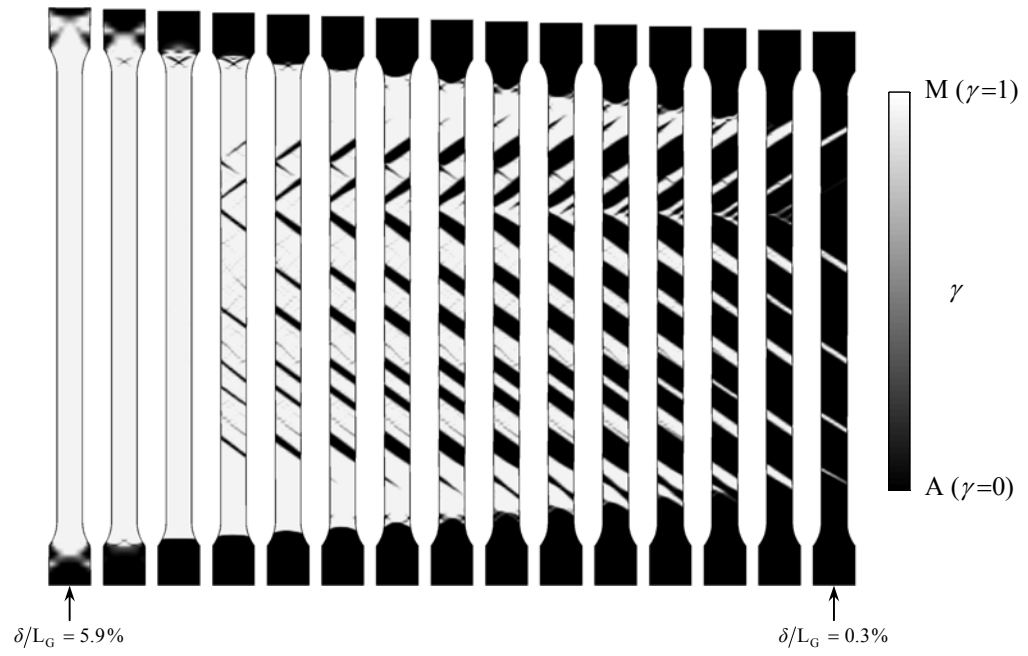


(a)

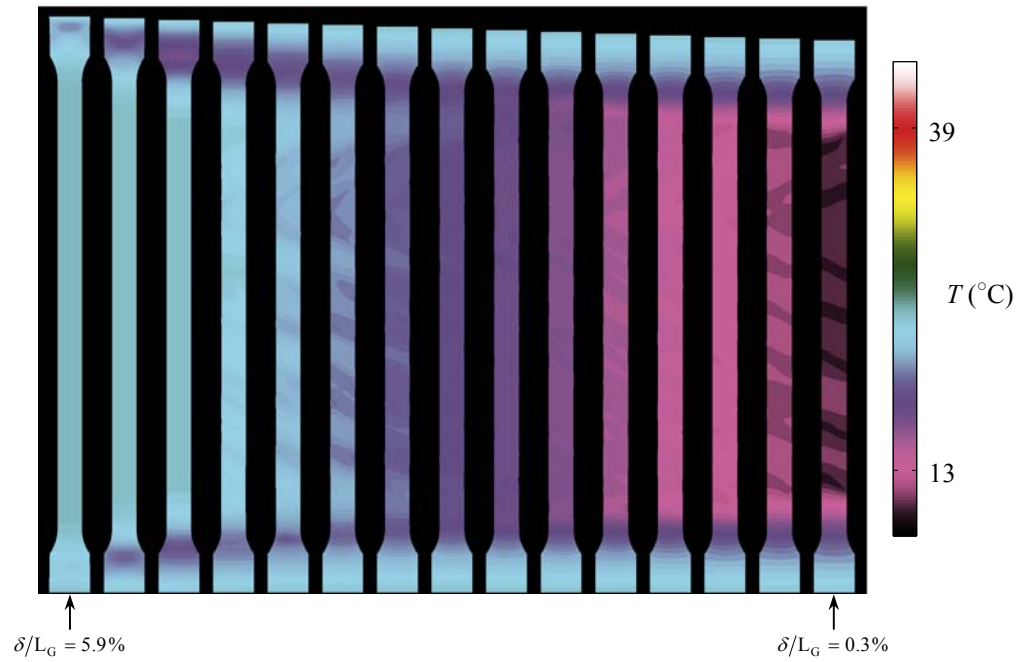


(b)

Figure 3-27. Sequence of events during forward transformation at $\dot{\delta}/L_G = 5 \times 10^{-3} \text{ s}^{-1}$. (a) Martensitic fraction; (b) Temperature.



(a)



(b)

Figure 3-28. Sequence of events during reverse transformation at $\dot{\delta}/L_G = -5 \times 10^{-3} \text{ s}^{-1}$. (a) martensitic fraction; (b) temperature.

Figure 3-26 indicates that the change in the nominal stress-strain response with strain rate does not exhibit a linear trend. The difference between the stress-strain curves at the low and moderate strain rates is more pronounced than the difference between those at the moderate and high strain rates. As explained earlier, the increase or decrease in plateau stress is caused by the increase or decrease in temperature at the transformation fronts. The magnitude of temperature variation at the front depends on the rate of transformation, which is proportional to the speed at which the transformation front propagates. The propagation speed, on the other hand, decreases with the number of coexisting transformation fronts (Shaw and Kyriakides 1995, 1997, 1998). Consequently, the increase of the transformation front temperature in the high strain rate case is hampered by the increase in the number of transformation fronts, which in turn results in a relatively small increase in the nominal stress.

By increasing the elongation rate, it is seen that the transformation fronts become even sharper, and emanating fingers disappear during the reverse transformation. This is due to the fact that the number of nucleation events increases by an increase in the strain rate. As explained earlier, concurrent transformation fronts tend to maintain the overall straightness of the sample, and reduce the bending moment that cause the fronts to branch. Hence, the sharp inclined transformation fronts survive for long periods before finally merging.

3.4.3. Effect of boundary conditions

When performing uniaxial tension tests, it is important to minimize grip misalignment in order to reduce the out-of-axis loading. However in practice, a pure uniaxial test may be difficult to achieve. For most materials which exhibit stable mechanical behavior, a small variation in loading conditions does not usually affect the observed behavior. But it is suspected that the transformation behavior of NiTi samples undergoing uniaxial tensile tests may be sensitive to grip misalignments

due to the instability of mechanical response. The dog-bone simulation has been used to evaluate the possible effects of misalignment on the transformation behavior. A lateral misalignment of 0.35 mm was applied to the lower end of the sample shown in Figure 3-14. The new displacement boundary conditions are now given by,

$$\begin{aligned} u|_{x=0} &= 0, & v|_{x=0, y=0} &= 0.35 \text{ mm} \\ u|_{x=L_0} &= \delta, & v|_{x=L_0, y=0} &= 0 \end{aligned}$$

All other boundary conditions were applied as previously described. The simulations for the low and moderate strain-rate conditions were repeated with new boundary conditions. The overall force-displacement response, the number of transformation fronts, and distribution of temperature were hardly affected by the new boundary conditions in any of the simulations. During the forward transformation at the moderate strain rate, only the orientation (+ θ or - θ) of the intermediate transformation bands were affected by the misalignment. On the other hand, the reverse transformation for both strain-rates exhibited dramatic change in the morphology of transformation fronts (especially at the low strain rate). Figure 3-29 shows the evolution of the reverse transformation. The two transformation fronts become sharp and straight shortly after exiting the tapered ends of the specimen. As shown previously, a straight inclined front tends to increase the amount of lateral deflection, which in turn helps to compensate for the misalignment of the specimen ends. The axial load acts as a restorative force which resists the growth of lateral deflection. During the forward transformation, where the axial load is quite large, lateral deflection is opposed, and the straight inclined band eventually converts to a criss-cross front in order to reduce the lateral deflection. During the reverse transformation, the transformation proceeds at a much smaller axial load, and therefore a larger amount of lateral deflection can exist. The kinking of the specimen due to lateral deflection is visible in Figure 3-29, which can also be observed in the experiments of Shaw and Kyriakides (1997).

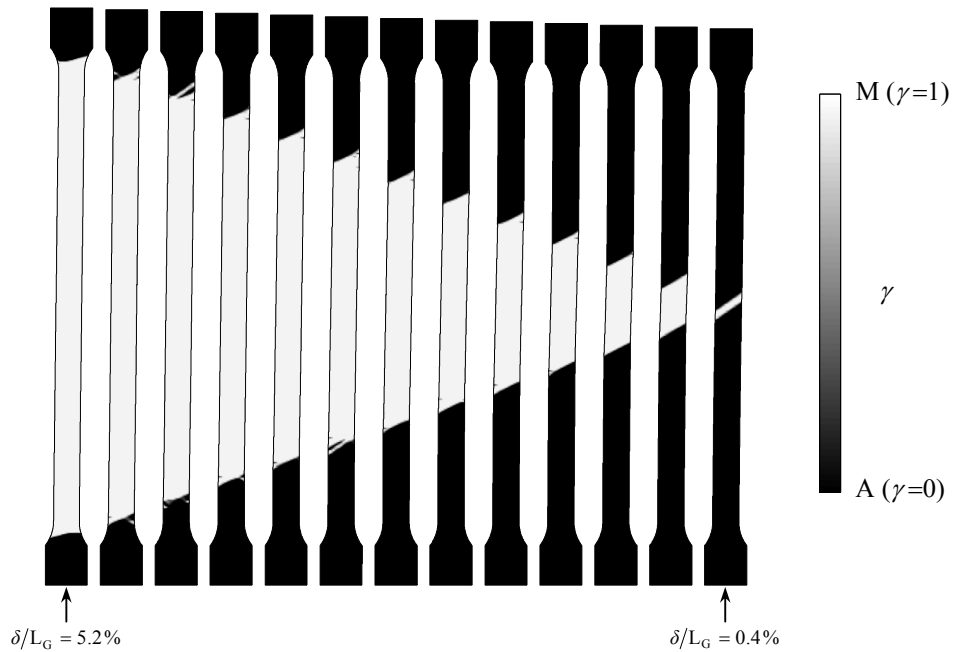


Figure 3-29. Transformation behavior of the specimen with misaligned grips during reverse transformation at $\dot{\delta}/L_G = -10^{-4} \text{ s}^{-1}$.

3.5. BIBLIOGRAPHY

Auricchio, F., Taylor, R., Lubliner, J., 1997. Shape-memory alloys: Macromodelling and numerical simulations of the superelastic behavior. *Computer Methods in Applied Mechanics and Engineering* 146, 281-312.

Bouvet, C., Calloch, S., LExcellent, C., 2002. Mechanical behavior of a Cu-Al-Be shape memory alloy under multiaxial proportional and nonproportional loadings. *Journal of Engineering Materials and Technology, Transactions of the ASME* 124, 112-124.

Bouvet, C., Calloch, S., LExcellent, C., 2004a. A phenomenological model for pseudoelasticity of shape memory alloys under multiaxial proportional and nonproportional loadings. *European Journal of Mechanics, A/Solids* 23, 37-61.

- Bouvet, C., Calloch, S., Taillard, K., Lexcellent, C., 2004b. Experimental determination of initial surface of phase transformation of SMA. *Journal de Physique IV* 115, 29-36.
- Boyd, J.G., Lagoudas, D.C., 1994. Thermomechanical response of shape memory composites, *Journal of Intelligent Material Systems and Structures* 5, 333-346.
- Budiansky, B., 1959. A reassessment of deformation theories of plasticity. *Journal of Applied Mechanics* 26, 259-264.
- Daly, S., Ravichandran, G., Bhattacharya, K., 2007. Stress-induced martensitic phase transformation in thin sheets of Nitinol. *Acta Materialia* 55, 3593-3600.
- Feng, P., Sun, Q.P., 2006. Experimental investigation on macroscopic domain formation and evolution in polycrystalline NiTi microtubing under mechanical force. *Journal of the Mechanics and Physics of Solids* 54, 1568-1603.
- Helm, D., Haupt, P., 2003. Shape memory behaviour: Modelling within continuum Thermomechanics. *International Journal of Solids and Structures* 40, 827-849.
- Hu, Z., Sun, Q.P., Zhong, Z., 2007. Numerical simulation for stress-induced phase transformation of SMAs tube under tension. *Key Engineering Materials* 340-341, 1181-1186.
- Hutchinson, J.W., Plastic buckling, 1974. *Advances in Applied Mechanics* 14, 67-144.
- Iadicola, M.A., Shaw, J.A., 2002. An experimental setup for measuring unstable thermo-mechanical behavior of shape memory alloy wire. *Journal of Intelligent Material Systems and Structures* 13, 157-166.
- Iadicola, M.A., Shaw, J.A., 2004. Rate and thermal sensitivities of unstable transformation behavior in a shape memory alloy. *International Journal of Plasticity* 20, 577-605.

- Khan, A. S., Huang, S., 1995. Continuum theory of plasticity. John Wiley & Sons Inc., New York, 177-179.
- Lexcellent, C., Blanc, P., 2004. Phase transformation yield surface determination for some shape memory alloys. *Acta Materialia* 52, 2317-2324.
- Liu, Y., Van Humbeeck, J., Delaey, L., 1998. Asymmetry of stress-strain curves under tension and compression for NiTi shape memory alloys. *Acta Materialia* 46 4325-4338.
- Pieczyska, E.A., Gadaj, S.P., Nowacki, W.K., Tobushi, H., 2004. Thermomechanical investigations of martensitic and reverse transformations in TiNi shape memory alloy. *Bulletin of the Polish Academy of Sciences: Technical Sciences* 52, 165-171.
- Pieczyska, E.A., Tobushi, H., Gadaj, S.P., Nowacki, W.K., 2006a. Superelastic deformation behaviors based on phase transformation bands in TiNi shape memory alloy. *Materials Transactions* 47, 670-676.
- Pieczyska, E.A., Gadaj, V., Nowacki, W.K., Tobushi, H., 2006b. Phase-transformation fronts evolution for stress- and strain-controlled tension tests in TiNi shape memory alloy. *Experimental Mechanics* 46, 531-542.
- Pieczyska, E.A., Gadaj, S.P., Nowacki, W.K., Tobushi, H., 2006c. Stress relaxation during superelastic behavior of TiNi shape memory alloy. *International Journal of Applied Electromagnetics and Mechanics* 23, 3-8.
- Shaw, J.A., 2000. Simulations of localized thermo-mechanical behavior in a NiTi shape memory alloy. *International Journal of Plasticity* 16, 541-562.
- Shaw, J.A., Kyriakides, S., 1995. Thermomechanical aspects of NiTi. *Journal of the Mechanics and Physics of Solids* 43, 1243-1281.

- Shaw, J.A., Kyriakides, S., 1997. On the nucleation and propagation of phase transformation fronts in a NiTi alloy. *Acta Materialia* 45, 683-700.
- Shaw, J.A., Kyriakides, S., 1998. Initiation and propagation of localized deformation elasto-plastic strips under uniaxial tension. *International Journal of Plasticity* 13, 837-871.
- Sittner, P., Hara, Y., Tokuda, M., 1995. On the transformation path of reverse thermoelastic martensitic transformation. *Scripta Metallurgica et Materialia* 33, 433-439.
- Tan, G., Liu, Y., Sittner, P., Saunders, M., 2004. Lüders-like deformation associated with stress-induced martensitic transformation in NiTi. *Scripta Materialia* 50, 193-198.
- Zheng, Y.F., Cai, W., Zhang, J.X., Zhao, L.C., Ye, H.Q., 2000. Microstructural development inside the stress induced martensite variant in a Ti-Ni-Nb shape memory alloy. *Acta Materialia* 48, 1409-1425.

Chapter 4: Modeling of Cyclic Effects⁴

In many engineering applications, SMA elements are subjected to periodic loading-unloading cycles which results in the alteration and/or degradation of material properties. In this chapter, the one-dimensional and three-dimensional constitutive models developed in the previous chapters are extended to incorporate the effects of mechanical cycling during the unstable pseudoelastic behavior. The generalized one-dimensional constitutive model is used to simulate the cyclic behavior of a NiTi wire at different temperatures. The role of transformation-induced plasticity in determining the location of nucleation events is also studied numerically by using the three-dimensional model.

4.1. INTRODUCTION

As explained in Chapter 1, the pseudoelastic characteristics of SMAs are strongly affected by cyclic loading (Miyazaki et al., 1986; Strnadel et al., 1995; Tobushi et al., 1996, 2005; Liu et al., 1999; Gong et al., 2002; Iadicola and Shaw, 2002a). The forward and reverse transformation stresses, the size of the hysteresis stress, and the amount of the transformation-induced strain are all affected by the preceding cyclic deformation as shown in Figure 1-13. The origin of cyclic effects is the introduction of microscopic plastic deformation during the stress-induced transformation which is referred to as *the transformation-induced plasticity*. The dislocations are formed during the forward transformation due to the incompatibility of transformation strain at the grain boundaries (Miyazaki et al., 1986; Sittner et al., 2003).

The residual stress field formed by the microscopic plastic deformation influences the stresses required to induce the phase transformations. As a result, both the forward and reverse

⁴ A version of this chapter will be submitted for publication: Azadi, B., Rajapakse R.K.N.D., Maijer, D. M., Modeling of the Cyclic Behavior of Shape Memory Alloys during Localized Unstable Mechanical Response.

transformation stresses and the size of the hysteresis stress decrease with increasing number of cycles. Additionally, the residual stress field shields some pockets of martensite and prevents them from being transformed into austenite during unloading. The residual martensitic phase and the microscopic plastic deformation result in the macroscopic permanent strain at the end of the loading-unloading cycles in Figure 1-13.

In some engineering applications where it is necessary for the material to exhibit a uniform steady-state behavior, cyclic loading may be used to condition or “train” the SMA prior to service. However, the process of cyclic training deteriorates the superior pseudoelastic characteristics of the virgin material, such as the large dissipation capacity, and eventually leads to fatigue damage. It is therefore reasonable to try to exploit the excellent properties of the material during the early cycles in some potential applications. For this purpose, it is important to understand the nature of the cyclic effects and incorporate them in the constitutive modeling in order to effectively predict the material response.

One of the first attempts to model the cyclic behavior of SMAs was the phenomenological model presented by Tanaka et al. (1992, 1995). They extended a one-dimensional model also developed by Tanaka (1986, 1990) to include cyclic effects by introducing three internal variables associated with the residual stress, residual strain, and the volume fraction of the irreversible residual martensite. They assumed that the evolution of the internal variables could be expressed as exponentially decaying functions of the number of forward and reverse transformations.

Lexcellent and Bourbon (1996) used a thermodynamic approach and employed the concept of the free energy of the specimen in a one-dimensional model. They assumed that a portion of the martensitic volume fraction is not recovered after each cycle. This behavior eventually saturates with the number of cycles. The residual strain was attributed to residual martensite only.

Bo and Lagoudas (1999) and Lagoudas and Bo (1999) developed a one-dimensional model of cyclic behavior based on a framework provided earlier by Boyd and Lagoudas (1994a). This is the first model that allows the plastic strain and transformation strain to develop simultaneously during the forward and reverse transformations. The model has been extended to three dimensions by Lagoudas and Entchev (2004). The flow rules for transformation and plastic strains are both based on the flow rules presented in Boyd and Lagoudas (1994b). The transformation conditions and yield surfaces were also assumed to be described by the same functions.

As discussed in the previous chapters, the localization of deformation and kinetics of transformation are important factors in determining the dynamic pseudoelastic response of NiTi shape memory alloys. The inhomogeneous nature of the phase transformation also has important implications on the cyclic behavior of the material. As shown experimentally by Miyazaki et al. (1986) and Iadicola and Shaw (2002a), the localization of deformation during cyclic loading of NiTi wires can result in an inhomogeneous change in the material properties. That is, some parts of the sample are affected by the cyclic changes while other parts remain unaffected. This can produce serious errors when attempting to predict the material response if the localization phenomenon is not properly accounted for in the model. However, the constitutive models reviewed earlier do not consider these effects during the cyclic loading.

A one-dimensional model that takes into account the inhomogeneous nature of transformations was developed by Abeyaratne and Kim (1997) based on the concept of the Helmholtz free energy function. They generalized the thermoelastic model of Abeyaratne and Knowles (1993) by assuming that the energy barriers between the austenite and martensite are changed by the defects generated during cyclic deformation, so that the nucleation of the forward transformation becomes easier while nucleation of the reverse transformation becomes more difficult with increasing number of cycles. Only one internal variable associated with the cyclic effects was introduced, which was the number of

times that a material point has undergone the forward transformation. The model was able to qualitatively capture the effects of localized partial cyclic loading on transformation stress such as demonstrated in Figure 1-14. However, the effect of cyclic loading on transformation strain, generation of residual strain, and strain rate effects were neglected. The model also is not suitable for use within a finite element framework.

The objective of this chapter is to generalize the one-dimensional and multi-dimensional constitutive models developed in the previous chapters to account for the cyclic effects and transformation-induced plasticity. For the first time, the effect of temperature on the rate of cyclic changes is also considered in the following generalized constitutive models. The one-dimensional model is used within a finite element framework to simulate the dynamic pseudoelastic response of a NiTi wire subjected to partial cyclic loading. The strain-rate effects and thermal interactions with the ambient environment are also considered. The results of the simulations are then compared with the experimental observations reported by Iadicola and Shaw (2002a). The results of a simulation employing the multi-dimensional model are also presented to study the effects of transformation induced plasticity and the impact of the residual macroscopic stress field on the nucleation of transformations.

4.2. MODIFICATION OF THE ONE-DIMENSIONAL CONSTITUTIVE MODEL

4.2.1. General considerations and stress-strain relationship

To account for the macroscopic residual strain produced during cyclic loading, it is assumed that the total strain contains a *permanent strain* component denoted by $\epsilon^{(p)}$. The permanent strain is introduced to account for microscopic plastic deformations and residual martensitic pockets locked at the grain boundaries. Therefore, the total strain (ϵ) is expressed as,

$$\varepsilon = \varepsilon^{(e)} + \varepsilon^{(t)} + \varepsilon^{(p)} \quad (4-1)$$

where the elastic strain ($\varepsilon^{(e)}$) is related to the stress (σ) by,

$$\varepsilon^{(e)} = \left(\frac{\gamma}{E_M} + \frac{1-\gamma}{E_A} \right) \sigma \quad (4-2)$$

and the recoverable transformation strain ($\varepsilon^{(t)}$) is obtained according to,

$$\varepsilon^{(t)} = \Delta\varepsilon_t(\lambda) \gamma \quad (4-3)$$

where $\Delta\varepsilon_t$ is the maximum recoverable transformation strain as defined in Chapter 2. As mentioned in the previous section, some amount of the stress-induced martensite does not transform back into austenite at the end of each cycle. Therefore, it is assumed that $\Delta\varepsilon_t$ is a function of the cyclic effects which are characterized by a new state variable called the *cyclic identifier*. The cyclic identifier denoted by λ is a function of the number of preceding cycles and other state variables in general. In particular, the amount and rate of cyclic change has been shown to be strongly dependent on temperature (Miyazaki et al., 1986; Iadicola and Shaw, 2002a). Therefore, the mathematical expression for the parameter λ is assumed to be given by,

$$\lambda = \int (a_\lambda T + b_\lambda) H(d\gamma) d\gamma \quad (4-4)$$

where H is the Heaviside step function defined as,

$$H(x) = \begin{cases} 1 & x > 0 \\ 0 & x \leq 0 \end{cases} \quad (4-5)$$

The parameters a_λ and b_λ are material properties which define the effect of temperature on the evolution of the cyclic identifier during martensitic transformation. The physical meaning of the

cyclic identifier λ and parameters a_λ and b_λ should become clearer in the next few paragraphs. For isothermal cycling, the cyclic identifier is given by,

$$\lambda = (a_\lambda T + b_\lambda) \int H(d\gamma) d\gamma$$

where the integral on the right hand side is the accumulated martensitic fraction during forward transformation. If the material particle undergoes a sequence of full forward and reverse transformations in each cycle ($\gamma = 0 \rightarrow 1 \rightarrow 0$) the above equation simply gives the number of times the particle has undergone the forward transformation.

Differentiating equation (4-4) gives,

$$d\lambda = \begin{cases} (a_\lambda T + b_\lambda) d\gamma & d\gamma > 0 \\ 0 & d\gamma \leq 0 \end{cases} \quad (4-6)$$

According to this equation the cyclic identifier λ does not change during the reverse transformation. This is, of course, a reasonable assumption as the reverse transformation does not eliminate the defects generated during the forward transformation nor does it generate any additional defect (Miyazaki et al., 1986).

In the next step, other material parameters which are sensitive to cyclic deformation are expressed in terms of the parameter λ . The changes in the pseudoelastic behavior and permanent strain during the cyclic loading have been experimentally shown to be exponentially decaying functions of the number of cycles. That is, with increasing cycles the pseudoelastic response approaches a limiting state which is referred to as the *fully-trained response* throughout this text. Therefore, the maximum transformation strain ($\Delta\varepsilon_t$) is assumed to be given by the following exponential expression,

$$\Delta\varepsilon_t(\lambda) = \Delta\varepsilon_t^{(0)} - [\Delta\varepsilon_t^{(0)} - \Delta\varepsilon_t^{(\infty)}](1 - e^{-\lambda}) \quad (4-7)$$

where $\Delta\varepsilon_t^{(0)}$ is the initial transformation strain corresponding to the virgin material ($\lambda = 0$), and $\Delta\varepsilon_t^{(\infty)}$ is the transformation strain at the saturation limit ($\lambda = \infty$).

Similarly, the evolution of the permanent strain is also given by the following equation:

$$\varepsilon^{(p)} = \varepsilon_p^{(\infty)}(1 - e^{-\lambda}) \quad (4-8)$$

where $\varepsilon_p^{(\infty)}$ is the maximum permanent strain at the saturation limit.

The incremental form of the evolution equation for transformation strain is obtained by differentiating equation (4-3) as,

$$d\varepsilon^{(t)} = \left[\Delta\varepsilon_t(\lambda) + \gamma \frac{d\Delta\varepsilon_t(\lambda)}{d\gamma} \right] d\gamma \quad (4-9)$$

where,

$$\frac{d\Delta\varepsilon_t(\lambda)}{d\gamma} = \begin{cases} -(a_\lambda T + b_\lambda) [\Delta\varepsilon_t^{(0)} - \Delta\varepsilon_t^{(\infty)}] e^{-\lambda} & d\gamma > 0 \\ 0 & d\gamma \leq 0 \end{cases} \quad (4-10)$$

The incremental evolution rule of the permanent strain is also given by,

$$d\varepsilon^{(p)} = \Delta\varepsilon_p(\lambda) d\gamma \quad (4-11)$$

where $\Delta\varepsilon_p(\lambda)$ is called the *cyclic plasticity multiplier* and is given by,

$$\Delta\varepsilon_p(\lambda) = \begin{cases} (a_\lambda T + b_\lambda) \varepsilon_p^{(p)} e^{-\lambda} & d\gamma > 0 \\ 0 & d\gamma \leq 0 \end{cases} \quad (4-12)$$

Using equations (4-1), (4-2), (4-9), and (4-11), the incremental stress-strain relationship may be expressed as:

$$d\varepsilon = \begin{cases} \left(\frac{\gamma}{E_M} + \frac{1-\gamma}{E_A} \right) d\sigma + \left(\frac{\sigma}{E_M} - \frac{\sigma}{E_A} + \Delta\varepsilon_t(\lambda) + \Delta\varepsilon_p(\lambda) + \gamma \frac{d\Delta\varepsilon_t}{d\gamma} \right) d\gamma, & d\gamma > 0 \\ \left(\frac{\gamma}{E_M} + \frac{1-\gamma}{E_A} \right) d\sigma + \left(\frac{\sigma}{E_M} - \frac{\sigma}{E_A} + \Delta\varepsilon_t(\lambda) \right) d\gamma & d\gamma \leq 0 \end{cases} \quad (4-13)$$

4.2.2. Kinetics of transformation

The nucleation criteria and the transformation evolution rules in this model are essentially the same as those described in Chapter 2 and Appendix A. The only difference is that the evolution of the transformation nucleation and finish stresses with cyclic deformation are also taken into account in the generalized model.

The martensite nucleation and finish stresses are described by the following equations,

$$\sigma_{MN}(\lambda, T) = \sigma_{MN}^{(0)}(T) - [\sigma_{MN}^{(0)}(T) - \sigma_{MN}^{(\infty)}(T)](1 - e^{-\lambda}) \quad (4-14)$$

$$\sigma_{MF}(\lambda, T) = \sigma_{MF}^{(0)}(T) - [\sigma_{MF}^{(0)}(T) - \sigma_{MF}^{(\infty)}(T)](1 - e^{-\lambda}) \quad (4-15)$$

and the nucleation and finish stresses of the reverse transformation are given by,

$$\sigma_{AN}(\lambda, T) = \sigma_{AN}^{(0)}(T) - [\sigma_{AN}^{(0)}(T) - \sigma_{AN}^{(\infty)}(T)](1 - e^{-\lambda}) \quad (4-16)$$

$$\sigma_{AF}(\lambda, T) = \sigma_{AF}^{(0)}(T) - [\sigma_{AF}^{(0)}(T) - \sigma_{AF}^{(\infty)}(T)](1 - e^{-\lambda}) \quad (4-17)$$

In the above equations, the ⁽⁰⁾ and ^(∞) superscripts correspond to the values of the nucleation and completion stresses in the virgin ($\lambda = 0$) and fully-trained ($\lambda = \infty$) states of the material, respectively.

The instantaneous nucleation stresses for forward and reverse transformation are given by,

$$\sigma_{MN}^*(\lambda, T) = \alpha \sigma_{MN}(\lambda, T) + (1 - \alpha) \sigma_{MF}(\lambda, T) \quad (4-18)$$

$$\sigma_{AN}^*(\lambda, T) = \alpha \sigma_{AN}(\lambda, T) + (1 - \alpha) \sigma_{AF}(\lambda, T) \quad (4-19)$$

where the parameter α is determined according to the procedures described in Appendix A for each case.

The initiation of transformations in the forward direction are triggered according to the following conditions,

$$F_{A \rightarrow M}(\sigma, \gamma, T, \lambda) = 0, \quad \gamma < 1 \quad (4-20)$$

whereas the initiation of reverse transformation during unloading is identified by the following conditions:

$$F_{M \rightarrow A}(\sigma, \gamma, T, \lambda) = 0, \quad \gamma > 0 \quad (4-21)$$

$F_{A \rightarrow M}$ and $F_{M \rightarrow A}$ in equations (4-20) and (4-21) are transformation potential functions given by,

$$F_{A \rightarrow M}(\sigma, \gamma, T, \lambda) = \sigma - (1 - \gamma) \sigma_{MN}^*(T, \lambda) - \gamma \sigma_{MF}(T, \lambda) \quad (4-22)$$

and,

$$F_{M \rightarrow A}(\sigma, \gamma, T, \lambda) = \sigma - \gamma \sigma_{AN}^*(T, \lambda) - (1 - \gamma) \sigma_{AF}(T, \lambda) \quad (4-23)$$

Substitution of (4-18) and (4-19) into (4-22) and (4-23) yields,

$$F_{A \rightarrow M}(\sigma, \gamma, T, \lambda) = \sigma - \alpha(1 - \gamma) \sigma_{MN}(\lambda, T) - (1 - \alpha + \alpha\gamma) \sigma_{MF}(T, \lambda) \quad (4-24)$$

and,

$$F_{M \rightarrow A}(\sigma, \gamma, T, \lambda) = \sigma - \alpha \gamma \sigma_{AN}(\lambda, T) - (1 - \alpha \gamma) \sigma_{AF}(T, \lambda) \quad (4-25)$$

The evolution of transformation during the forward transformation is governed by the following incremental kinetic relationship,

$$dF_{A \rightarrow M}(\sigma, \gamma, T, \lambda) = \frac{\partial F_{A \rightarrow M}}{\partial \sigma} d\sigma + \frac{\partial F_{A \rightarrow M}}{\partial \gamma} d\gamma + \frac{\partial F_{A \rightarrow M}}{\partial T} dT = 0, \quad d\gamma > 0 \quad (4-26)$$

and during the reverse transformation by the following condition,

$$dF_{M \rightarrow A}(\sigma, \gamma, T, \lambda) = \frac{\partial F_{M \rightarrow A}}{\partial \sigma} d\sigma + \frac{\partial F_{M \rightarrow A}}{\partial \gamma} d\gamma + \frac{\partial F_{M \rightarrow A}}{\partial T} dT = 0, \quad d\gamma > 0 \quad (4-27)$$

Note that the variation of the cyclic identifier (λ) during the forward transformation needs to be taken into account when calculating the derivative of the transformation potential function with respect to γ ($\frac{\partial F_{A \rightarrow M}}{\partial \gamma}$). That is,

$$\frac{\partial F_{A \rightarrow M}}{\partial \gamma} = \alpha [\sigma_{MN}(T, \lambda) - \sigma_{MF}(T, \lambda)] - (a_\lambda T + b_\lambda) \left\{ \alpha (1 - \gamma) \frac{\partial \sigma_{MN}}{\partial \lambda} + (1 - \alpha + \alpha \gamma) \frac{\partial \sigma_{MF}}{\partial \lambda} \right\} \quad (4-28)$$

Since the parameter λ does not change during the reverse transformation, the derivation of $F_{M \rightarrow A}$ with respect to γ is given by,

$$\frac{\partial F_{M \rightarrow A}}{\partial \gamma} = \alpha [\sigma_{AF}(T, \lambda) - \sigma_{AN}(\lambda, T)] \quad (4-29)$$

A calculation procedure similar to the one explained in Appendix A may be used to find the increments of stress, martensitic fraction, and cyclic identifier during the forward and reverse transformations based on the elastic-predictor and transformation-corrector method.

4.2.3. Heat of transformation

Since some amount of martensite is retained during the process of cyclic deformation and does not contribute to the subsequent transformations, the latent heat of transformation is reduced during the subsequent cycles loading. To account for this, the stress-free enthalpy changes are assumed to be given by the following relationships:

$$\Delta h_{A \rightarrow M}(\lambda) = \Delta h_{A \rightarrow M}^{(0)} - \left[\Delta h_{A \rightarrow M}^{(0)} - \Delta h_{A \rightarrow M}^{(\infty)} \right] (1 - e^{-\lambda}) \quad (4-30)$$

$$\Delta h_{M \rightarrow A}(\lambda) = \Delta h_{M \rightarrow A}^{(0)} - \left[\Delta h_{M \rightarrow A}^{(0)} - \Delta h_{M \rightarrow A}^{(\infty)} \right] (1 - e^{-\lambda}) \quad (4-31)$$

Additionally, the role of irreversible mechanical work due to the generation of permanent strain must also be considered. Therefore by employing equations (2-27) and (4-11), the heat generation during the cyclic loading is obtained as,

$$\dot{q}_G = \begin{cases} \left[-\rho \Delta h_{A \rightarrow M}(\lambda) + \frac{1}{2} \left(\frac{1}{E_M} - \frac{1}{E_A} \right) \sigma^2 + \sigma \Delta \varepsilon_t(\lambda) + \sigma \Delta \varepsilon_p(\lambda) \right] \dot{\gamma}, & (\dot{\gamma} > 0) \\ \left[\rho \Delta h_{M \rightarrow A}(\lambda) + \frac{1}{2} \left(\frac{1}{E_M} - \frac{1}{E_A} \right) \sigma^2 + \sigma \Delta \varepsilon_t(\lambda) \right] \dot{\gamma}, & (\dot{\gamma} < 0) \end{cases} \quad (4-32)$$

4.3. MODIFICATION OF THE THREE-DIMENSIONAL CONSTITUTIVE MODEL

The generalization of the three-dimensional model developed in Chapter 3 for cyclic loading is straightforward based on the discussions provided in Section 4.2. Therefore for brevity, only a summary of the updated constitutive relations are provided in the following section.

4.3.1. General considerations and stress-strain relationship

The additive decomposition of the total strain tensor into elastic, transformation, and permanent strains yields,

$$\varepsilon_{ij} = D_{ijkl}(\gamma)\sigma_{kl} + \varepsilon_{ij}^{(t)} + \varepsilon_{ij}^{(p)} \quad (4-33)$$

The first term on the right hand side of equation (4-33) is the elastic strain. The compliance tensor (D_{ijkl}) is also given in equation (3-7). Based on the constitutive relations developed in Chapter 3, the transformation strain is given by,

$$\varepsilon_{ij}^{(t)} = \frac{\Delta\varepsilon_t(\lambda)}{\sqrt{\frac{2}{3} \frac{\partial P}{\partial \sigma_{kl}} \frac{\partial P}{\partial \sigma_{kl}}}} \frac{\partial P}{\partial \sigma_{ij}} \gamma \quad (4-34)$$

where $\Delta\varepsilon_t(\lambda)$ is given in equation (4-3) and the definition of λ is the same as before (equation 4-4). The potential function P is also chosen to be the Von-Mises effective stress as described in Chapter 3.

As explained in the introduction, the origin of the permanent strain is the generation of dislocations during forward transformation, which in turn is a result of slip. Therefore it is natural to postulate that the evolution of permanent strain $\varepsilon_{ij}^{(p)}$ follows the flow rule of incremental plasticity as given in equation (3-1). Moreover, it is also assumed that the potential function for plastic deformation (Q) is the same as that for transformation (P). Based on these assumptions, the generation of permanent strain is governed by the following incremental relation:

$$d\varepsilon_{ij}^{(p)} = \frac{\Delta\varepsilon_p(\lambda)}{\sqrt{\frac{2}{3} \frac{\partial P}{\partial \sigma_{kl}} \frac{\partial P}{\partial \sigma_{kl}}}} \frac{\partial P}{\partial \sigma_{ij}} d\gamma, \quad d\gamma > 0 \quad (4-35)$$

where $\Delta\varepsilon_p(\lambda)$ is the cyclic plasticity multiplier and needs to be determined. For this purpose, the *effective permanent strain* is defined as,

$$d\tilde{\varepsilon}^{(p)} = \sqrt{\frac{2}{3} d\varepsilon_{ij}^{(p)} d\varepsilon_{ij}^{(p)}} \quad (4-36)$$

which is assumed to follow the same evolution rule that the one-dimensional permanent strain $\varepsilon^{(p)}$ follows (equation 4-8). That is,

$$\tilde{\varepsilon}^{(p)} = \varepsilon_p^{(\infty)} (1 - e^{-\lambda}) \quad (4-37)$$

Substituting $d\varepsilon_{ij}^{(p)}$ from equation (4-35), and $\tilde{\varepsilon}^{(p)}$ from equation (3-37) into equation (4-36) yields the cyclic plasticity multiplier as,

$$\Delta\varepsilon_p(\lambda) = \begin{cases} (a_\lambda T + b_\lambda) \varepsilon_\infty^{(p)} e^{-\lambda} & d\gamma > 0 \\ 0 & d\gamma \leq 0 \end{cases} \quad (4-38)$$

which is exactly the same as the cyclic plasticity multiplier obtained for the one-dimensional case in equation (4-12).

In summary, the incremental stress-strain relationships from equation (4-33) through (4-38) may be written as,

$$d\varepsilon_{ij} = \begin{cases} \bar{D}_{ijkl}(\gamma) d\sigma_{kl} + \left\{ (D_{ijkl}^{(M)} - D_{ijkl}^{(A)}) \sigma_{kl} + \frac{3}{2} \left(\Delta\varepsilon_t(\lambda) + \Delta\varepsilon_p(\lambda) + \gamma \frac{d\Delta\varepsilon_t}{d\gamma} \right) \frac{S_{ij}}{\bar{\sigma}} \right\} d\gamma & d\gamma > 0 \\ \bar{D}_{ijkl}(\gamma) d\sigma_{kl} + \left\{ (D_{ijkl}^{(M)} - D_{ijkl}^{(A)}) \sigma_{kl} + \frac{3}{2} \Delta\varepsilon_t(\lambda) \frac{S_{ij}}{\bar{\sigma}} \right\} d\gamma & d\gamma < 0 \end{cases} \quad (4-39)$$

4.3.2. Kinetics of transformation

The criteria for initiation of transformations are,

$$\begin{cases} F_{A \rightarrow M}(\sigma_{ij}, \gamma, T, \lambda) = 0, & \gamma < 1 & \text{(Forward transformation)} \\ F_{M \rightarrow A}(\sigma_{ij}, \gamma, T, \lambda) = 0, & \gamma > 0 & \text{(Reverse transformation)} \end{cases} \quad (4-40)$$

where,

$$\begin{cases} F_{A \rightarrow M} = \bar{\sigma} - (1 - \gamma)\sigma_{MN}(T, \lambda) - \gamma\sigma_{MC}(T, \lambda) \\ F_{M \rightarrow A} = \bar{\sigma} - \gamma\sigma_{AN}(T, \lambda) - (1 - \gamma)\sigma_{AC}(T, \lambda) \end{cases} \quad (4-41)$$

In the above equation, σ_{MN} and σ_{MC} are the martensite nucleation and completion stresses as functions of the cyclic identifier according to,

$$\sigma_{MN}(\lambda, T) = \sigma_{MN}^{(0)}(T) - [\sigma_{MN}^{(0)}(T) - \sigma_{MN}^{(\infty)}(T)](1 - e^{-\lambda}) \quad (4-42)$$

$$\sigma_{MC}(\lambda, T) = \sigma_{MC}^{(0)}(T) - [\sigma_{MC}^{(0)}(T) - \sigma_{MC}^{(\infty)}(T)](1 - e^{-\lambda}) \quad (4-43)$$

The nucleation and completion stresses of the inverse transformation are also given by,

$$\sigma_{AN}(\lambda, T) = \sigma_{AN}^{(0)}(T) - [\sigma_{AN}^{(0)}(T) - \sigma_{AN}^{(\infty)}(T)](1 - e^{-\lambda}) \quad (4-44)$$

$$\sigma_{AC}(\lambda, T) = \sigma_{AC}^{(0)}(T) - [\sigma_{AC}^{(0)}(T) - \sigma_{AC}^{(\infty)}(T)](1 - e^{-\lambda}) \quad (4-45)$$

As before, the $^{(0)}$ and $^{(\infty)}$ superscripts correspond to the material properties of the virgin ($\lambda = 0$) and fully-trained ($\lambda = \infty$) materials, respectively.

The following kinetics relations control the evolution of transformations:

$$\begin{cases} dF_{A \rightarrow M}(\sigma_{ij}, \gamma, T, \lambda) = 0 & \text{Forward transformation (d}\gamma > 0) \\ dF_{M \rightarrow A}(\sigma_{ij}, \gamma, T, \lambda) = 0 & \text{Reverse transformation (d}\gamma < 0) \end{cases} \quad (4-46)$$

The variation of the cyclic identifier (λ) during forward transformation must be taken into account when the above kinetics relations are enforced. It should also be noted that the value of λ does not change during the course of reverse transformation.

4.3.3. Heat of transformation

As mention in Section 4.2.3., the heat generation due to plastic work during the forward transformation must be taken into account when calculating the heat generation term. From equation (3-30) the total generated heat during forward/reverse transformations is given by,

$$\begin{cases} \dot{q}_G = \sigma_{ij} \dot{\epsilon}_{ij}^{(t)} + \sigma_{ij} \dot{\epsilon}_{ij}^{(p)} + \left\{ \frac{1}{2} \sigma_{ij} (D_{ijkl}^{(M)} - D_{ijkl}^{(A)}) \sigma_{kl} - \rho \Delta h_{A \rightarrow M}(\lambda) \right\} \dot{\gamma}, & \dot{\gamma} > 0 \\ \dot{q}_G = \sigma_{ij} \dot{\epsilon}_{ij}^{(t)} + \left\{ \frac{1}{2} \sigma_{ij} (D_{ijkl}^{(M)} - D_{ijkl}^{(A)}) \sigma_{kl} - \rho \Delta h_{M \rightarrow A}(\lambda) \right\} \dot{\gamma}, & \dot{\gamma} < 0 \end{cases} \quad (4-47)$$

where $\Delta h_{A \rightarrow M}(\lambda)$ and $\Delta h_{M \rightarrow A}(\lambda)$ are found from equations (4-30) and (4-31).

4.4. NUMERICAL SIMULATIONS

4.4.1. One-dimensional simulation of NiTi wire

The cyclic responses of a NiTi wire at two different temperatures are simulated using the proposed one-dimensional model. The simulation results are compared qualitatively with the experimental observations of Iadicola and Shaw (2002a).

4.4.1.1. Material characterization and FEM model

The numerical analysis presented in this section are based on the experimental observations of Iadicola and Shaw (2002a,b). The experimental setup and the corresponding finite element model are shown schematically in Figure 4-1. NiTi wire specimens, with a diameter of $\phi = 0.765$ mm and gauge length of $L_G = 60$ mm, were subjected to uniaxial displacement-controlled tests. Three thermoelectric modules (Peltier cooler/heater) with an overall length of $L_T = 52$ mm were placed between the wire and an aluminum conduction block (not shown in Figure 4-1a). The aluminum block provides an isothermal heat sink, while the thermoelectric modules maintain a prescribed

temperature difference between the wire and aluminum block. Good thermal contact between the wire and thermoelectric modules was achieved by using a thermally conductive paste. The temperatures of the grips (T_G) were also increased relative to the temperature of the thermoelectric modules (T_T) in order to eliminate the effect of stress-concentration and early nucleation at the grips.

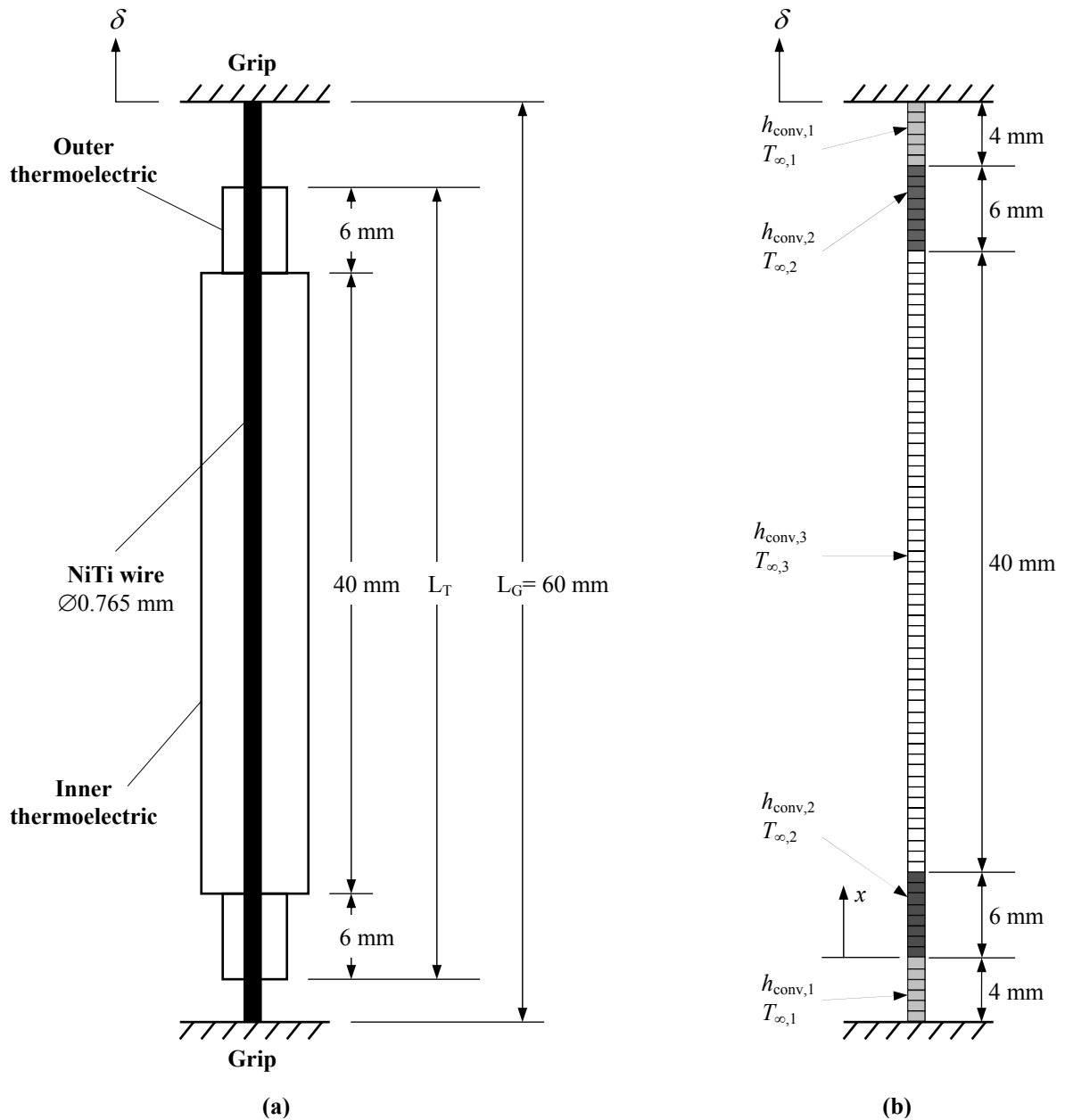


Figure 4-1. (a) Experimental setup (adapted from Iadicola and Shaw, 2002a); (b) Finite element model.

To account for the heat transfer conditions presented by the thermally conductive paste and thermoelectric modules, different convective film coefficients and ambient temperatures are assigned to the corresponding sections of the wire in the FEM model as shown in Figure 4-1(b). The convective film coefficient and ambient temperature associated with the air gap between the outer thermoelectric module and the grip at each end are denoted by $h_{\infty,1}$ and $T_{\infty,1}$, respectively. The respective convective film coefficients assigned to the regions in contact with the outer and inner thermoelectric modules are also denoted by $(h_{\infty,2}, T_{\infty,2})$ and $(h_{\infty,3}, T_{\infty,3})$.

Since the gap was filled with stagnant air, $h_{\infty,1}$ is set equal to $4 \text{ W/m}^2 \text{ K}$ based on the convective film coefficient used in the simulations of Chapter 3. Following a trial-and-error process, it was also found that the combination of thermal paste and electric module can be modeled by assuming a value of $h_{\infty,2} = h_{\infty,3} = 1200 \text{ W/m}^2 \text{ K}$ for the central part of the wire (L_T). Based on these values, the changes in temperature during transformations predicted by the simulations are in the same range as those recorded in the experiments ($\pm 2 \text{ }^\circ\text{C}$).

The pseudoelastic properties of the virgin samples are measured using the uniaxial tests reported by Iadicola and Shaw (2002b) at different temperatures. In both tests, the nucleation events during the forward and reverse transformations were forced to occur in the central part of the wire by adjusting the distributions of temperature. This method allowed for the accurate measurements of nucleation stresses without having to deal with the stress-concentration effects at the grips. Assuming a linear relationship with temperature, the nucleation and finish (propagation) stresses of the virgin material are obtained from the experimental results as,

$$\sigma_{\text{MN}}^{(0)}(T) = 10 T + 295 \text{ (MPa)}$$

$$\sigma_{\text{MF}}^{(0)}(T) = 8.17 T + 244.92 \text{ (MPa)}$$

$$\sigma_{\text{AN}}^{(0)}(T) = 2.07 T + 98.32 \text{ (MPa)}$$

$$\sigma_{\text{AF}}^{(0)}(T) = 4.02 T + 128.52 \text{ (MPa)}$$

Note that in the above relations the temperature is measured in ($^{\circ}\text{C}$) and the stresses are the nominal (or engineering) values.

The elastic moduli of austenite and martensite ($E_{\text{A}}, E_{\text{B}}$) are assumed to be constant and equal to the average values reported by Iadicola and Shaw (2002a). The transformation strain of the virgin material ($\Delta\varepsilon_{\text{t}}^{(0)}$) is the average of the values measured directly from the stress-strain curves reported by Iadicola and Shaw (2002b). Since the wire samples were partially transformed during the tests, the localization of transformation has been considered in the calculation of $\Delta\varepsilon_{\text{t}}^{(0)}$.

The material properties necessary to describe the cyclic behavior are obtained from the results of the cyclic experiments performed by Iadicola and Shaw (2002a) on the same type of NiTi wire that was used by Iadicola and Shaw (2002b). Two sets of displacement-controlled cyclic experiments were performed at nominal specimen temperatures of $T_{\text{T}}=16.5^{\circ}\text{C}$ and $T_{\text{T}}=24.6^{\circ}\text{C}$ and an elongation rate of $\dot{\delta}/L_{\text{G}} = 10^{-3} \text{ s}^{-1}$. During the first cycle of both experiments, the entire length of the material within the central part of the wire (L_{T}) was transformed, and then completely unloaded. Subsequent cycles were performed by loading-unloading of the sample between $\delta/L_{\text{G}} = 0.013$ and $\delta/L_{\text{G}} = 0.047$.

The cyclic parameters a_{λ} and b_{λ} , and the transformation finish stresses (propagation stresses) associated with the fully trained material ($\lambda = \infty$) are calculated based on the experimental measurements of the drop in propagation stresses with the number of cycles. For this purpose, it is assumed that the propagation stresses are linear functions of stress; that is,

$$\sigma_{MF}^{(\infty)}(T) = a_{MF}^{(\infty)} T + b_{MF}^{(\infty)}$$

$$\sigma_{AF}^{(\infty)}(T) = a_{AF}^{(\infty)} T + b_{AF}^{(\infty)}$$

Based on experimental observations, the temperature of the transformation fronts during the tests were approximately constant, and 2 °C higher/lower than the nominal temperature of the specimen (T_T) due to the heat generation. Based on these assumptions, and equations (4-4), (4-15), and (4-17), the evolution of propagation stresses during the tests is approximated by,

$$\left(\sigma_{MP} - \sigma_{MP}^{(0)}\right)\Big|_{T_T} = -\left[\sigma_{MF}^{(0)}(T_T + 2) - a_{MF}^{(\infty)} \times (T_T + 2) - b_{MF}^{(\infty)}\right] \left(1 - e^{(-a_\lambda \times (T_T + 2) - b_\lambda)(N-1)}\right)$$

$$\left(\sigma_{AP} - \sigma_{AP}^{(0)}\right)\Big|_{T_T} = -\left[\sigma_{AF}^{(0)}(T_T - 2) - a_{AF}^{(\infty)} \times (T_T - 2) - b_{AF}^{(\infty)}\right] \left(1 - e^{(-a_\lambda \times (T_T - 2) - b_\lambda)N}\right)$$

where N is the cycle number. By fitting the above values to those measured from the experiments using a least squares optimization method, the six parameters a_λ , b_λ , $a_{MF}^{(\infty)}$, $b_{MF}^{(\infty)}$, $a_{AF}^{(\infty)}$, $b_{AF}^{(\infty)}$ are obtained as,

$$a_\lambda = 3.444 \times 10^{-3}, \quad b_\lambda = -2.322 \times 10^{-3}$$

$$a_{MF}^{(\infty)} = 2.4655 \text{ (MPa/}^\circ\text{C)}, \quad b_{MF}^{(\infty)} = 230.16 \text{ (MPa)}$$

$$a_{AF}^{(\infty)} = 6.2371 \text{ (MPa/}^\circ\text{C)}, \quad b_{AF}^{(\infty)} = 64.835 \text{ (MPa)}$$

Unfortunately, the available experimental results do not provide much information about the variation of nucleation stresses (σ_{MN} , σ_{AN}) with cyclic deformation. In order to find the values of the nucleation stresses, it is assumed that the ratios of the nucleation stresses to propagation stresses do not change during the cyclic tests. That is,

$$\left. \frac{\sigma_{MN}^{(\infty)}}{\sigma_{MF}^{(\infty)}} \right|_{T=T_T} = \left. \frac{\sigma_{MN}^{(0)}}{\sigma_{MF}^{(0)}} \right|_{T=T_T}, \quad T_T = 16.5, 24.6 \text{ } ^\circ\text{C}$$

$$\left. \frac{\sigma_{AN}^{(\infty)}}{\sigma_{AF}^{(\infty)}} \right|_{T=T_T} = \left. \frac{\sigma_{AN}^{(0)}}{\sigma_{AF}^{(0)}} \right|_{T=T_T}, \quad T_T = 16.5, 24.6 \text{ } ^\circ\text{C}$$

Assuming a linear relationship with temperature, the nucleation stresses are obtained from the above conditions as,

$$\sigma_{MN}^{(\infty)}(T) = 3.0510 T + 277.77 \text{ (MPa)}$$

$$\sigma_{AN}^{(\infty)}(T) = 3.6359 T + 53.95 \text{ (MPa)}$$

Using the obtained values of a_λ and b_λ , the maximum permanent strain ($\varepsilon_p^{(\infty)}$) can be obtained from equation (4-8) and the measured value of residual strain at the end of cyclic loading in the experiment. Similarly, the value of transformation strain at the saturation limit ($\Delta\varepsilon_t^{(\infty)}$) may also be obtained by measuring the transformation strain in the last cycle, and using equation (4-7).

The zero-stress enthalpy changes for the virgin material $\Delta h_{A \rightarrow M}^{(0)}$ ($= -\Delta h_{M \rightarrow A}^{(0)}$) are assumed to be the same as those used in the previous chapters. To find the values of $\Delta h_{A \rightarrow M}^{(\infty)}$ ($= -\Delta h_{M \rightarrow A}^{(\infty)}$), it is assumed that the enthalpy changes are proportional to the value of transformation strain $\Delta\varepsilon_t^{(\infty)}$; that is,

$$\frac{\Delta h_{A \rightarrow M}^{(\infty)}}{\Delta h_{A \rightarrow M}^{(0)}} = \frac{\Delta h_{M \rightarrow A}^{(\infty)}}{\Delta h_{M \rightarrow A}^{(0)}} = \frac{\Delta\varepsilon_t^{(\infty)}}{\Delta\varepsilon_t^{(0)}}$$

The above assumption is based on the fact that the latent heat of transformation and transformation strain are both reduced due to the residual martensite trapped during the cyclic deformation.

Other thermo-physical properties of the material such as density ρ , thermal conductivity k , and specific heat capacity C_p are assumed to be independent of cyclic loading, and their values are taken from Chapter 2. Table 4-1 summarizes the mechanical and thermal properties of the NiTi wire. The values of stresses and strains in Table 4-1 are the engineering (nominal) values.

Table 4-1. Mechanical and thermal properties of the NiTi wire

Parameter		Value
Elastic modulus of Austenite	E_A (GPa)	73.5
Elastic modulus of Martensite	E_M (GPa)	34
Cyclic thermal parameter	a_λ (K^{-1})	3.444×10^{-3}
Cyclic thermal parameter	b_λ	-2.322×10^{-3}
Transformation strain (virgin material)	$\Delta \varepsilon_t^{(0)}$	0.0539
Transformation strain (fully-trained material)	$\Delta \varepsilon_t^{(\infty)}$	0.0485
Maximum residual strain	$\varepsilon_p^{(\infty)}$	0.00572
Martensite nucleation stress (virgin material)	$\sigma_{MN}^{(0)}$ (MPa)	$10 T^{(C)} + 295$
Martensite nucleation stress (fully-trained material)	$\sigma_{MN}^{(\infty)}$ (MPa)	$3.0510 T^{(C)} + 277.77$
Martensite finish stress (virgin material)	$\sigma_{MF}^{(0)}$ (MPa)	$8.17 T^{(C)} + 244.92$
Martensite finish stress (fully-trained material)	$\sigma_{MF}^{(\infty)}$ (MPa)	$2.4655 T^{(C)} + 230.16$
Austenite nucleation stress (virgin material)	$\sigma_{AN}^{(0)}$ (MPa)	$2.07 T^{(C)} + 98.32$
Austenite nucleation stress (fully-trained material)	$\sigma_{AN}^{(\infty)}$ (MPa)	$3.6359 T^{(C)} + 53.949$
Austenite finish stress (virgin material)	$\sigma_{AF}^{(0)}$ (MPa)	$4.02 T^{(C)} + 128.52$
Austenite finish stress (fully-trained material)	$\sigma_{AF}^{(\infty)}$ (MPa)	$6.2371 T^{(C)} + 64.835$
Zero-stress enthalpy change (virgin material)	$\Delta h_{A \rightarrow M}^{(0)}$ ($J kg^{-1}$)	-12.3×10^3
Zero-stress enthalpy change (fully-trained material)	$\Delta h_{A \rightarrow M}^{(\infty)}$ ($J kg^{-1}$)	-11.07×10^3
Thermal conduction coefficient	k ($W m^{-1} K^{-1}$)	18
Specific heat capacity	C_p ($J kg^{-1} K^{-1}$)	837
Density	ρ ($kg m^{-3}$)	6.5×10^3

The gauge length of the wire (L_G) is divided into 120 elements. A small geometric imperfection is introduced in the center of the wire by reducing the cross-sectional area of the two elements located in the mid-span. The role of this imperfection is to force nucleation to occur at this location, and simulate a material defect that causes a small stress-concentration. The FEM formulations and solution methods are similar to those described in Chapter 2 and Appendix C for the one-dimensional case.

4.4.1.2. Simulation I

The cyclic behavior of the wire sample shown in Figure 4-1 is simulated at an ambient temperature of $T_T = 16.5$ °C. The applied thermal and mechanical boundary conditions are as follow,

$$T|_{x=-4 \text{ mm}} = T|_{x=56 \text{ mm}} = T_G = 46 \text{ }^\circ\text{C}$$

$$T_{\infty,1} = 25 \text{ }^\circ\text{C}$$

$$T_{\infty,2} = T_{\infty,3} = T_T = 16.5 \text{ }^\circ\text{C}$$

$$u|_{x=-4 \text{ mm}} = 0$$

$$u|_{x=56 \text{ mm}} = \delta, \quad \frac{\dot{\delta}}{L_G} = 10^{-3} \text{ s}^{-1}$$

where x is the axial coordinate measured from the bottom end of the outer thermoelectric module, and u is the displacement component along the x - axis as shown in Figure 4-1(b). The initial temperature distribution of the wire resulting from the above thermal conditions is compared to the experimental measurement in Figure 4-2. There is a clear discrepancy between the measured temperature distribution and that from the FE calculation. This is because of the approximate thermal properties used in the model, and uncertainty of the assumed thermal boundary conditions.

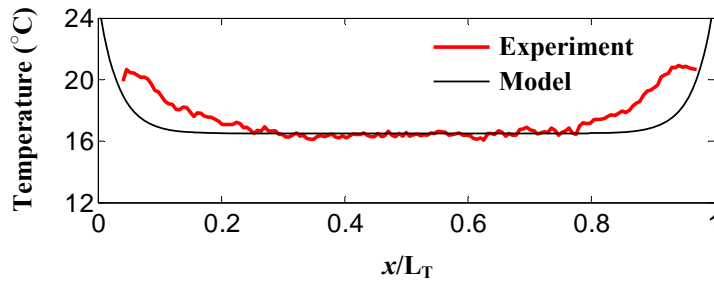
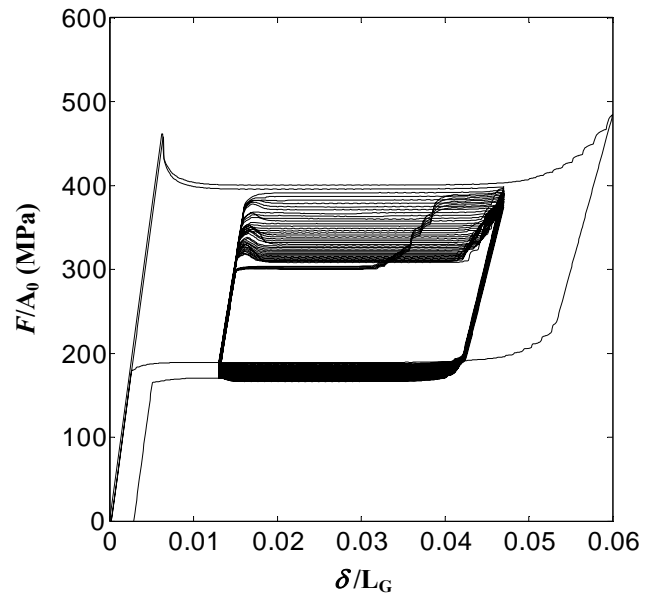


Figure 4-2. Initial temperature distribution along the wire length (experimental data taken from Iadicola and Shaw, 2002a).

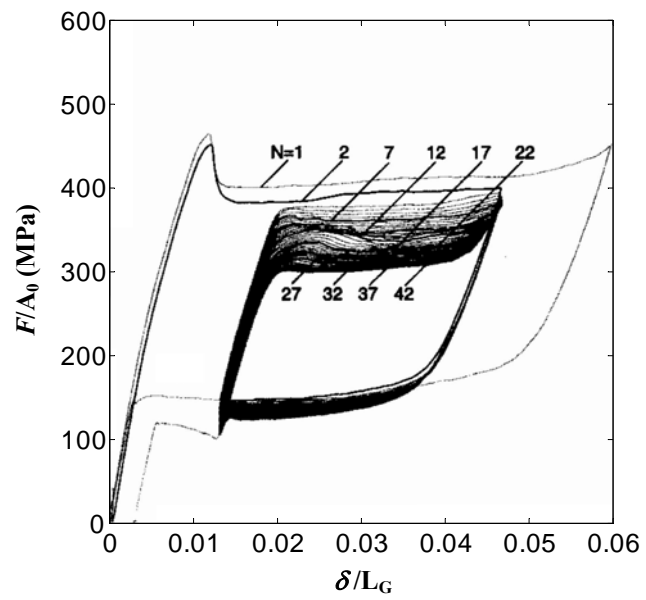
The wire is subjected to displacement-controlled loading-unloading cycles at an elongation rate of $\dot{\delta}/L_G = 10^{-3} \text{ s}^{-1}$. During the first cycle, the wire is strained to $\delta/L_G = 0.06$ followed by unloading to zero strain. In subsequent cycles, the wire is cycled between $\delta/L_G = 0.013$ and $\delta/L_G = 0.047$. At the end of the 42nd cycle, the wire is fully unloaded again to zero stress and the simulation ends.

In Figure 4-3(a), the predicted nominal stress is plotted against the global elongation for the entire test. The experimental stress-strain response reported by Iadicola and Shaw (2002a) is provided in Figure 4-3(b) for comparison. Except for the last few cycles, the predicted mechanical response of the wire is in good agreement with experimental data. The changes in propagation stresses of forward and reverse transformation ($\Delta\sigma_{A \rightarrow M}, \Delta\sigma_{M \rightarrow A}$) with cycles are shown in Figure 4-4. The predicted propagation stress in each cycle was assessed at $\delta/L_G = 0.03$ for loading and at $\delta/L_G = 0.025$ for unloading.

During the first cycle, a gradual rise in stress-strain response is observed at the end of loading ($\delta/L_G = 0.06$). This behavior is also seen in the experimental stress-strain response. The reason is that the transformation fronts nucleated in the central part of the wire enter the hotter regions of the wire near the grips (Figure 4-2) which requires a higher propagation stress.

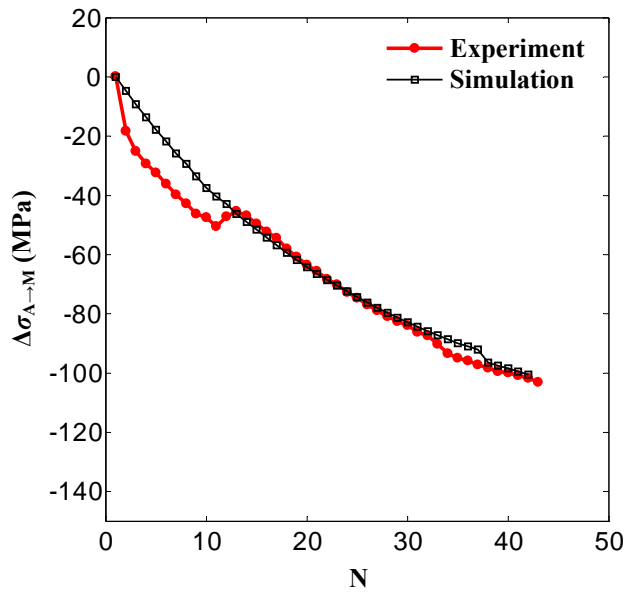


(a)

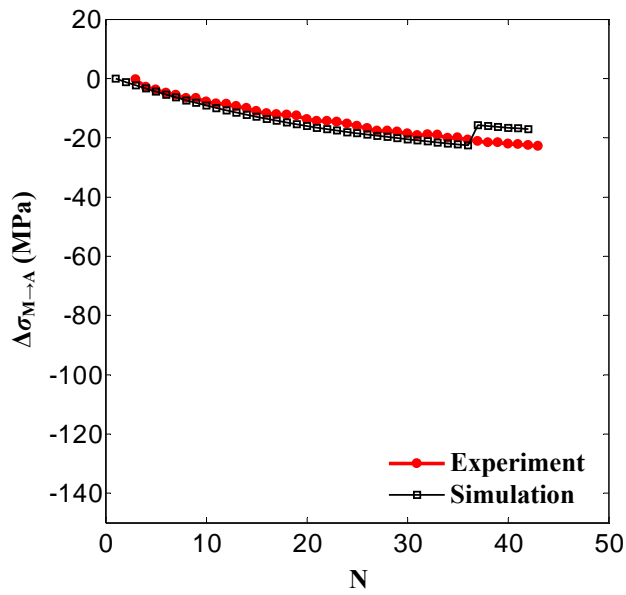


(b)

Figure 4-3. Nominal stress-strain response of the NiTi wire during cyclic loading at $T_T = 16.5 \text{ }^\circ\text{C}$. (a) Simulation (b) Experiment (reproduced with permission from Iadicola and Shaw, 2002a).



(a)



(b)

Figure 4-4. Change in propagation stress relative to cycle 1 during cyclic loading at $T_T = 16.5^\circ\text{C}$. (a) Forward transformation; (b) Reverse transformation.

A common feature in the measured and simulated stress-strain responses in Figure 4-3 is that as the global elongation (δ/L_G) approaches its maximum value of 0.047, the stress increases and reaches the same maximum value seen in the previous cycles. This behavior can be explained by examining the evolution of the transformation fronts during cyclic loading.

The evolution of the phases and the propagation of the transformation fronts based on the simulation are shown in Figure 4-5(a). The corresponding time-history predictions of the nominal stress during cyclic loading are also plotted in Figure 4-5(b). The nucleation of forward transformation in the first and second cycles occurs at $x/L_T=0.5$ where the geometric imperfection is located. A nucleation event for reverse transformation does not take place since the transformation fronts already exist. Also starting from cycle 3, the specimen is partially unloaded, and therefore the nucleation of forward transformation disappears for the same reason.

In each cycle, the transformation fronts move slightly into regions which did not transform in the previous cycle. This can be seen in Figure 4-5(a) as a gradual growth in the length of the fully transformed region during the forward transformation in each cycle. As the transformation fronts move through the regions that have experienced fewer previous transformations, the stress tends to increase since those regions have been less affected by the cyclic loading and require a higher transformation stress. This effect has been experimentally observed by Miyazaki et al. (1981) and Iadicola and Shaw (2002a). Based on the simulation results presented here, it was found that the gradual decrease in the transformation strain with cyclic loading (equation 4-7) is the underlying mechanism for an overall increase in the fraction of transformed material during cyclic loading. Since the maximum global strain is held constant during the cycles ($\delta/L_G = 0.047$), the decrease in the transformation strain is compensated by pushing the transformation fronts further into the less cycled parts of the specimen.

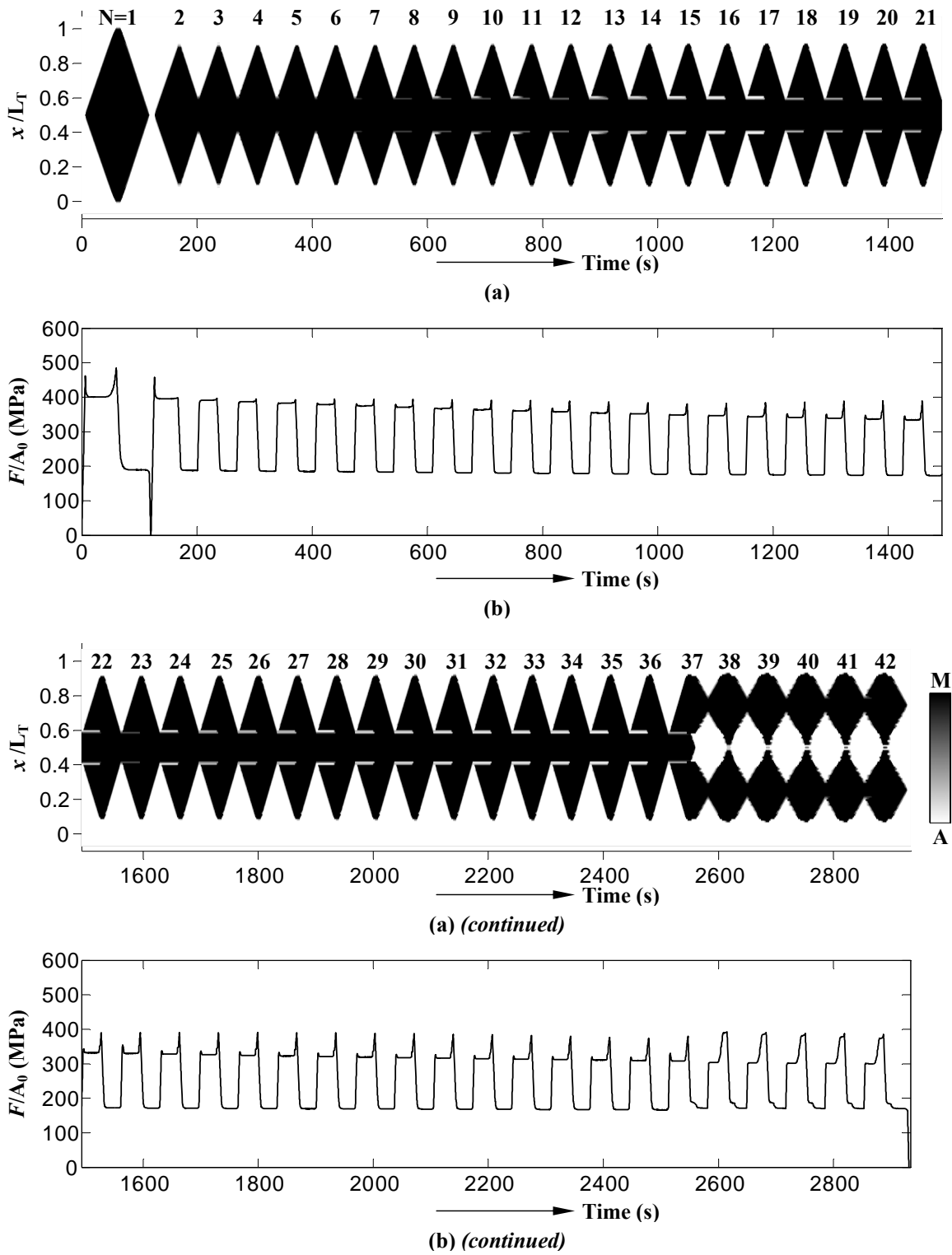


Figure 4-5. Evolution of (a) phases, and (b) nominal stress with cycles at $T_T = 16.5$ °C (simulation).

Similar to the gradual growth in the amount of martensitic phase produced in each cycle, the amount of recovered austenite at the end of each cycle also increases with the number of cycles. This effect is due to introduction of a permanent deformation ($\varepsilon^{(p)}$) during forward transformation which does not recover upon unloading. Since the overall elongation of the wire at the end of unloading in each cycle is the same ($\delta/L_G = 0.013$), some amount of the remaining martensite from previous cycles must be recovered in order to compensate for the introduction of the permanent deformation.

As more austenitic material is recovered at the end of each cycle, a higher stress is required to transform it into martensite. A higher stress is required because the areas just transformed into austenite are less affected by cyclic deformation compared to those that have experienced a larger number of transformations. Therefore, the newly recovered austenite areas do not initially transform during loading, but transform later when the stress is rising at the end of loading. The residual pockets of austenite appear as two parallel white strips in the contour plots of Figure 4-5(a) from cycle 7. However, the occurrence of this phenomenon cannot be verified from the experiments of Iadicola and Shaw (2002a) where they used infrared images of temperature profiles at 1-second intervals to track the propagation of transformation fronts.

In the simulation results, the propagation of only two co-existing transformation fronts is repeated during the first 36 cycles. The predicted transformation behavior of the specimen changes in the last six cycles by switching to four co-existing transformation fronts during the forward and reverse transformations. The change in the transformation behavior starts in cycle 37, where the reverse transformation initiates at four different points along the wire. Although it is difficult to distinguish in Figure 4-5(a), some small pockets of austenite at the mid-span of the wire do not fully transform to martensite during the loading segment of this cycle. The residual austenitic points later become preferred nucleation points during the reverse transformation. Moreover, since these pockets

of residual austenite have experienced a small number of transformations, the stress required to transform them to austenite is relatively high which allows them to transform in the early stages of unloading.

The change in the transformation behavior of the wire has a pronounced effect on the overall stress-strain response in the last few cycles which can be seen in Figure 4-3(a) and 4-5(b). For better illustration, the time history of stress during selected cycles is shown in Figure 4-6. The first change in behavior appears in cycle 36 during which the lower stress plateau initially exhibits a higher stress level compared to its previous cycle followed by smooth transition to a lower value. This behavior is also repeated in the subsequent cycles. As explained earlier, the nucleation and propagation of the reverse transformation in the mid-section of the wire requires a higher stress compared to other sections of the wire that have been subjected to a higher number of transformations. This results in a higher stress plateau during the reverse transformation. As the transformation fronts enter the highly cycled regions again (Figure 4-5a), the plateau stress drops to a lower value.

A similar “staircase” effect (Abeyaratne and Kim, 1997) is also observed during the forward transformation starting from cycle 38. As seen in Figure 4-5(a), the forward transformation in this cycle starts at about $x/L_T \approx 0.25$ and $x/L_T \approx 0.75$. These locations have experienced a high number of transformations in the preceding cycles. Therefore the transformation stress is relatively low in these regions. As the transformation fronts enter the central part of the wire, the plateau stress gradually rises to an upper level.

Based on the above discussion, it may be concluded that the change in the number of co-existing transformation fronts effectively stabilizes the overall mechanical response of the specimen through the “staircase” effect.

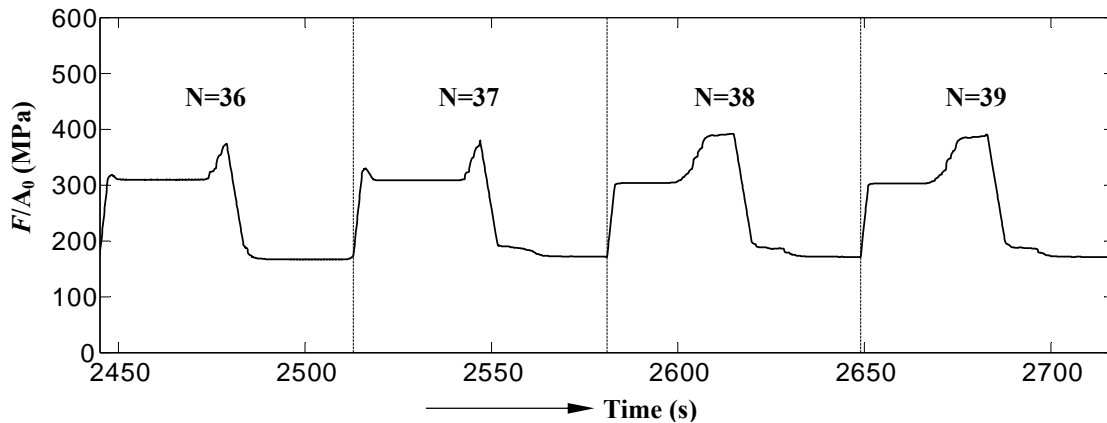
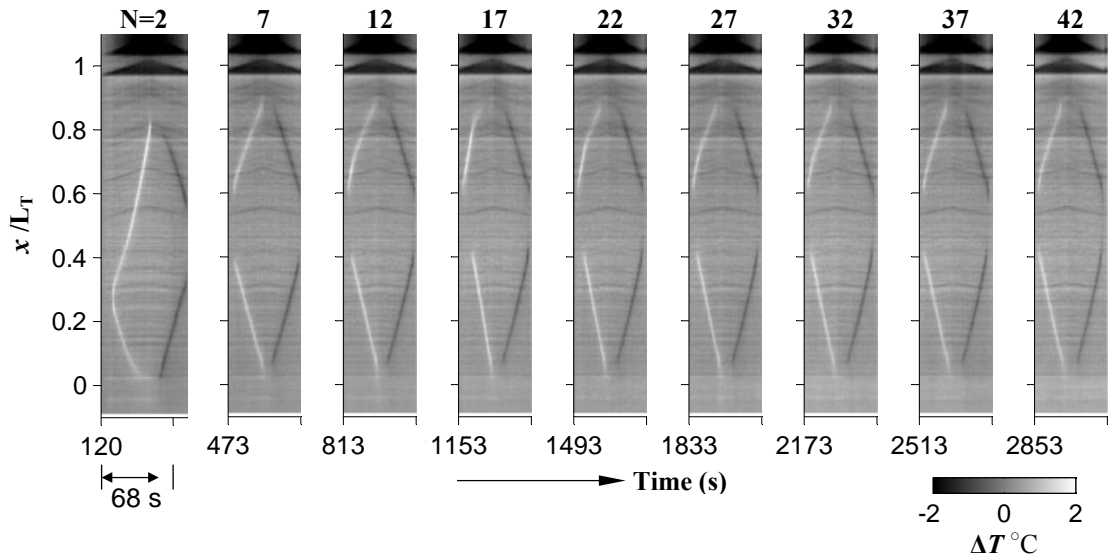
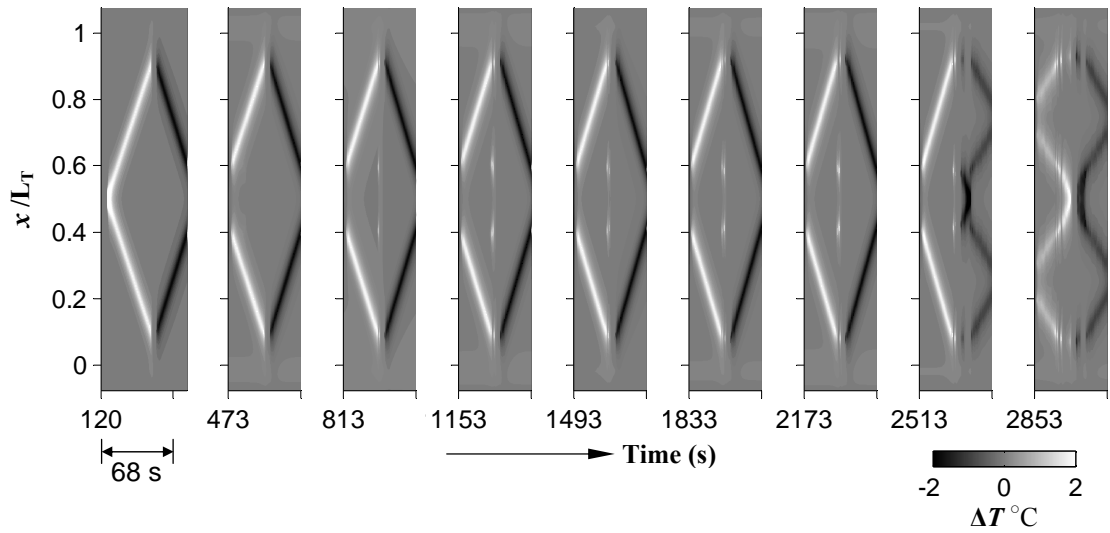


Figure 4-6. Time history of stress during selected cycles.

In Figure 4-7, the temperature change profiles obtained from the simulation are compared to those reported by Iadicola and Shaw (2002a) at selected cycles. The temperature variations are obtained by subtracting the initial temperature profile shown in Figure 4-2 from the subsequent temperature profiles. The number on top of each diagram (N) corresponds to its respective cycle number. The selected cycles are also marked on Figure 4-3(b). Only two transformation fronts move back and forth throughout the entire test in the experiment, while a change in transformation behavior takes place as of cycle 37 in the simulation results which was explained earlier. As shown in the next section, a change in the number of propagating transformations has been observed during an experiment conducted at a higher temperature.



(a)



(b)

Figure 4-7. (a) Infrared images of temperature variation at selected cycles (reproduced with permission from experiments of Shaw and Kyriakides, 2002a); (b) Simulated profiles of temperature variation during cyclic loading at $T_T = 16.5^\circ\text{C}$.

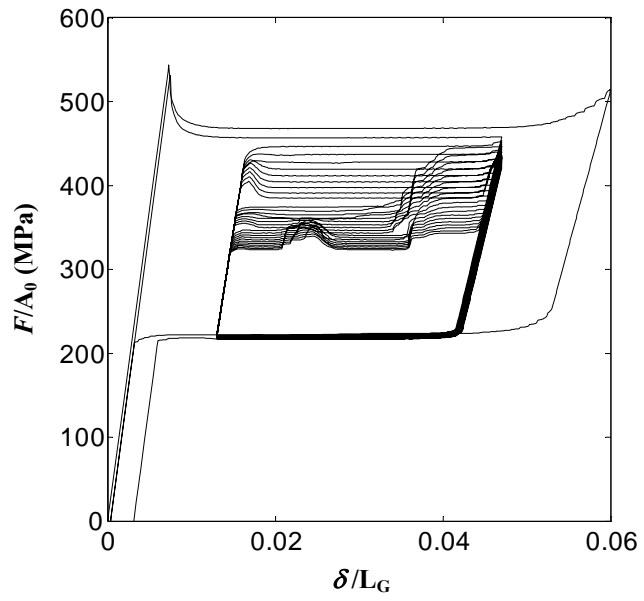
In the simulation results, the transformation of residual pockets of austenite at the end of the forward transformations in each cycle is identified by a momentarily flare of increased temperature in the central part of the wire. As mentioned earlier, this behavior was not observed in the infrared measurements of this experiment. It is probably because the stress concentration that exists at the interface of highly cycled and less cycled regions cannot be effectively modeled with a one-dimensional model. This allows some residual austenite to survive during the early stages of forward transformation in the simulation. The discrepancy between the simulation and experiment may also be due to the inaccuracy of thermal measurements. As shown later, momentary high-temperature spots have been observed occasionally during a cyclic test performed at a higher temperature.

4.4.1.3. Simulation II

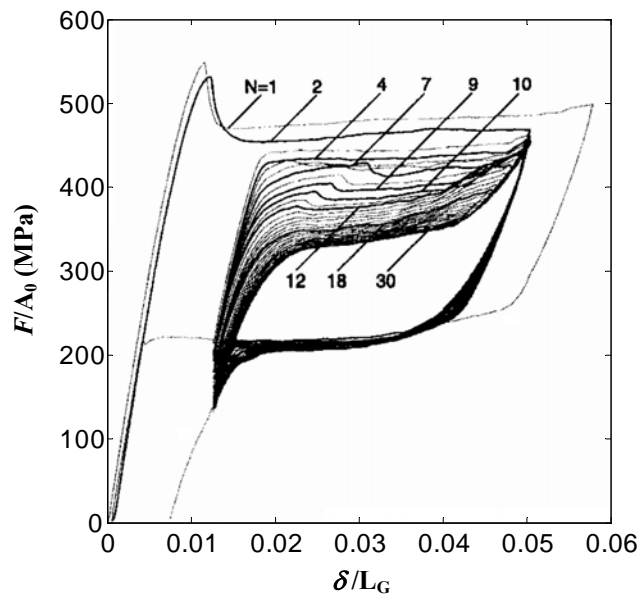
The cyclic behavior of the NiTi wire shown in Figure 4-1 is simulated in this section for a higher ambient temperature of $T_T = 24.6$ °C. The thermal and mechanical boundary conditions are similar to those explained in the previous section, except for the following condition:

$$T_{\infty,2} = T_{\infty,3} = T_T = 24.6 \text{ °C}$$

The applied cyclic loading is exactly the same as that described in the previous section for the lower temperature case (Simulation I). The only difference is that the wire is subjected to only 32 cycles in the present case. The predicted and measured pseudoelastic responses of the wire during cyclic loading at this temperature are shown in Figure 4-8. The changes in propagation stresses during forward and reverse transformations ($\Delta\sigma_{A \rightarrow M}$, $\Delta\sigma_{M \rightarrow A}$) with cycles are also plotted in Figure 4-9. The cyclic changes are larger at this temperature, and the material response approaches its fully-trained state at a faster rate. This behavior is not surprising since the temperature sensitivity of the cyclic parameters has already been embedded in the constitutive model through equation (4-6).

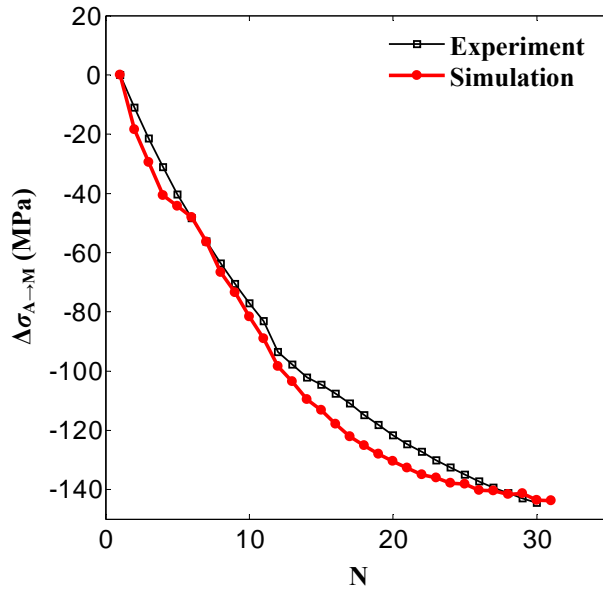


(a)

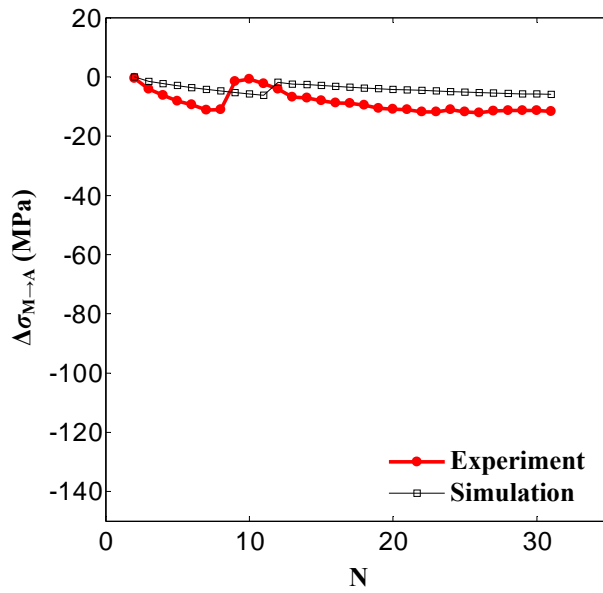


(b)

Figure 4-8. Nominal stress-strain response of the NiTi wire under cyclic loading at $T_T = 24.6\text{ }^\circ\text{C}$. (a) Simulation (b) Experiment (reproduced with permission from Iadicola and Shaw, 2002a).



(a)



(b)

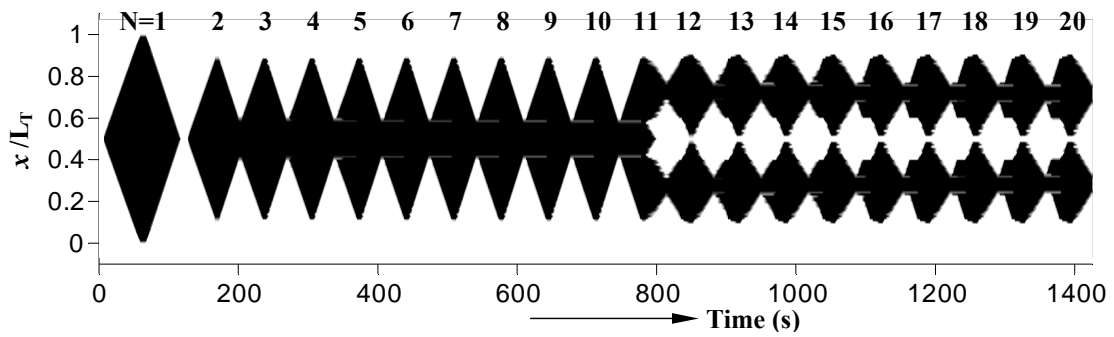
Figure 4-9. Change in propagation stress relative to cycle 1 during cyclic loading at $T_T = 24.6^\circ\text{C}$. (a)

Forward transformation; (b) Reverse transformation.

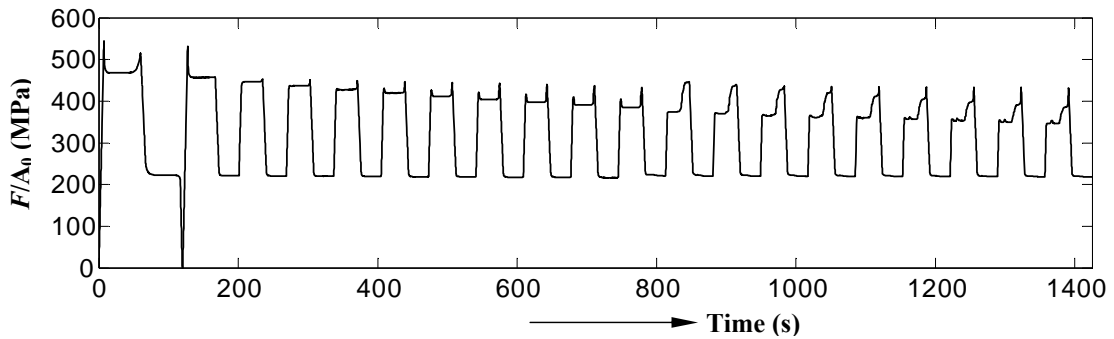
The final residual strain at the end of cycles in the experimental results is higher than the permanent strain predicted by the present model. The primary reason is slippage at the grips which was also reported by Iadicola and Shaw (2002a) with the experimental results.

Observing both the predicted and experimental results, the overall mechanical response of the wire at this temperature ($T_T=24.6$ °C) is more stable compared to that at the lower temperature ($T_T=16.5$ °C). This trend may be explained by investigating the localized transformation behavior of the material. The predicted evolution of phases and the propagation of transformation fronts are shown in Figure 4-10(a). The time-history of the nominal stress during cyclic loading is also plotted in Figure 4-10(b). The change in transformation behavior from two fronts to four co-existing transformation fronts occurs much earlier (cycle 11) compared to the previous case. This is due to the faster rate of accumulation of cyclic effects at the present temperature. As a result, the stress-strain response of the specimen exhibits a more stable behavior.

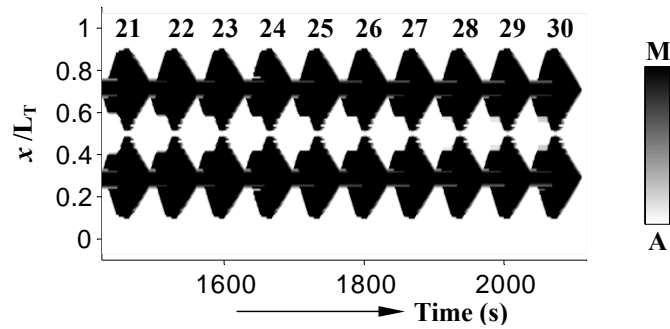
The change in the number of transformation fronts with cycles in this case was also verified by the experimental observations. The temperature variations during cyclic loading measured by the infrared imaging system are shown in Figure 4-11(a). The predicted temperature changes along the wire length are shown in Figure 4-11(b). In both cases, two transformation fronts propagate back and forth during the early cycles. As the number of cycles increases, the number of transformation fronts increases to three or four co-existing fronts. However, there are some differences in the predicted and measured behaviors. Starting from cycle 16, the predicted transformation behavior during loading shows some deviations from the experiment, but the reverse transformation behaviors from the experiment and simulation are more or less the same throughout the test.



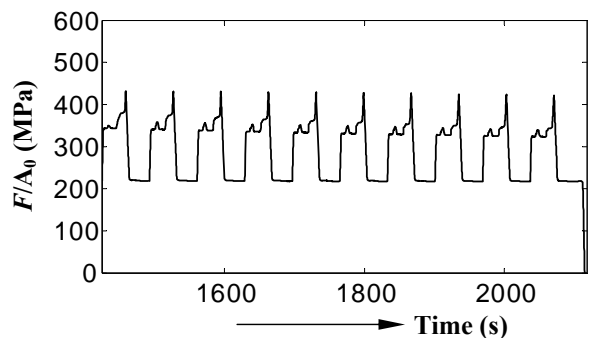
(a)



(b)



(a) (continued)



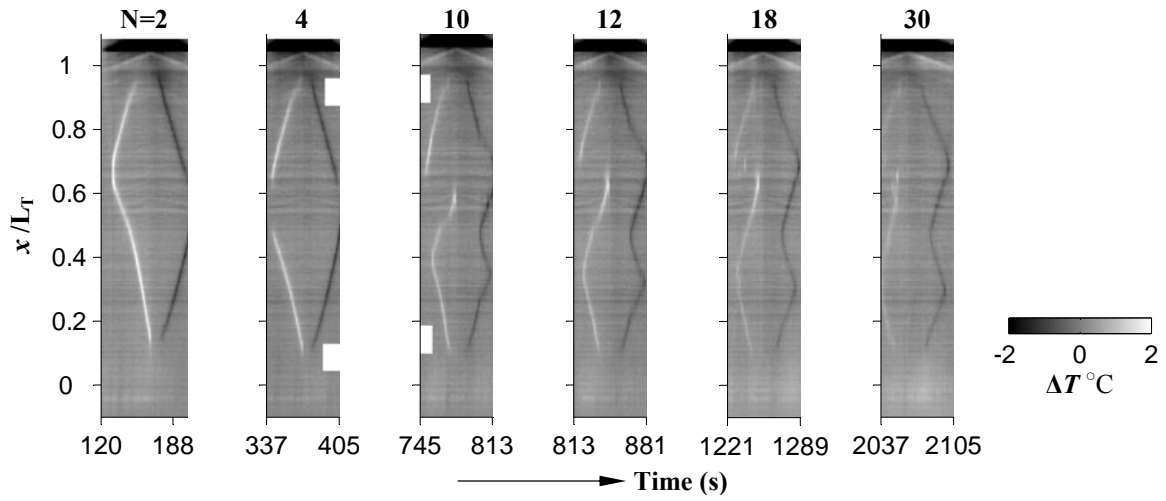
(b) (continued)

Figure 4-10. Evolution of (a) phases, and (b) nominal stress with cycles at $T_T = 24.6^\circ\text{C}$ (simulation).

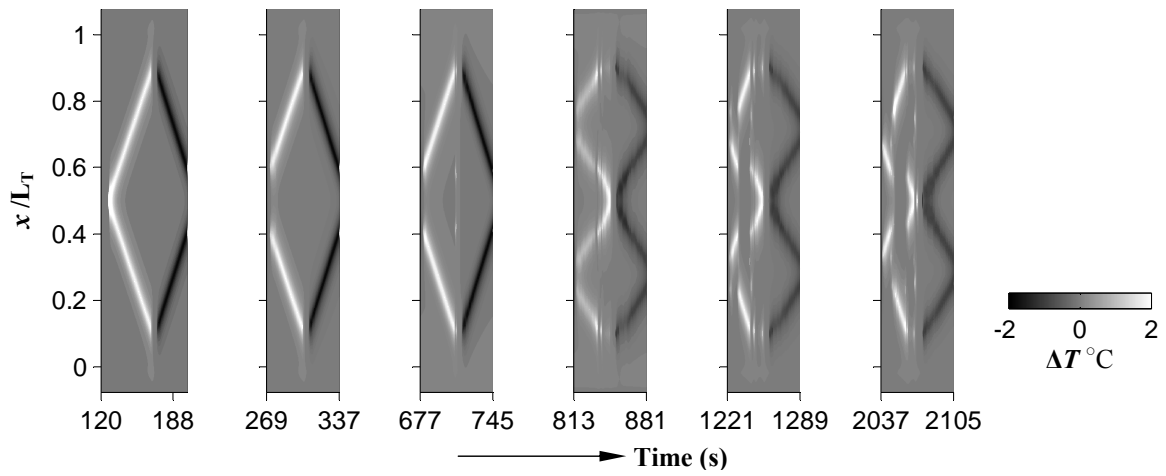
In cycle 16, a second change in the predicted transformation behavior of the wire occurs. At the beginning of loading in this cycle, the two inner transformation fronts start propagating toward each other while the outer transformations do not move. This is again because the stress concentration at the interface of the highly cycled austenitic areas and less cycled martensite areas cannot be accurately accounted for by the present one-dimensional model. In cycle 16, this results in a more favorable transformation condition at the inner transformation fronts. The inner transformation fronts stop propagating when they reach the central part of the wire. The reason is that a higher stress is required to transform this region. As a result, the inner transformation fronts stop and the outer transformation front start propagating. Therefore, starting from cycle 16 only two transformation fronts propagate at each time.

As described in the previous section, the underlying mechanism of the change in the transformation behavior is a combination of the effects of the residual permanent strain, and residual austenite particles which do not fully transform during the forward transformation. The transformation of a residual isolated pocket of austenite at the end of a loading segment appears as a momentarily high-temperature spot in the simulated temperature variation profiles (Figure 4-11b). Similar high-temperature spots are occasionally observed in the experimental infrared (e.g., cycles 18 and 30 in Figure 4-11a). Nevertheless, the above hypothesis cannot be completely verified by the existing experimental evidence and requires further theoretical and experimental investigation.

It should be noted that the difference between the simulation and experimental results is also related to the chosen thermomechanical parameters. Especially the values chosen for the nucleation stresses of the full-trained material are probably far from their real values.



(a)



(b)

Figure 4-11. (a) Infrared images of temperature variation at selected cycles (reproduced with permission from experiments of Shaw and Kyriakides, 2002a); (b) Simulated profiles of temperature variation during cyclic loading at $T_T = 24.6^\circ\text{C}$.

4.4.2. Three-dimensional simulation of the wire

The pseudoelastic response of the NiTi wire is simulated using the three-dimensional model, in an effort to understand the role of the transformation-induced plasticity in nucleation and propagation of transformation fronts. Although the wire can be effectively simulated by a one-dimensional model, studying certain features of the transformation front and distributions of residual stress and strain are better suited to a full multi-dimensional analysis.

The geometry of the wire and FE mesh are shown in Figure 4-12. The wire is discretized using 8-node quadratic axisymmetric elements. The radius of the wire is divided into 3 elements while its length is divided into 400 elements. The applied mechanical and thermal boundary conditions are,

$$\begin{aligned}u_r|_{x=0} &= u_x|_{x=0} = 0 \\u_r|_{x=L} &= 0 \\u_x|_{x=L} &= \delta, \quad \frac{\dot{\delta}}{L} = 2 \times 10^{-3} \text{ s}^{-1} \\T|_{x=0} &= T|_{x=L} = 25 \text{ }^\circ\text{C}\end{aligned}$$

where u_r and u_x are the displacement components in the radial (r) and axial (x) directions.

The ambient media is assumed to be stagnant air at $T_\infty = 25 \text{ }^\circ\text{C}$. A convective film coefficient of $h_{\text{conv}} = 4 \text{ W/m}^2 \text{ K}$ is assigned to the outer surface of the wire to represent the thermal interaction of the wire and the environment. The material is assumed to be the same NiTi wire used in the previous section, with the thermomechanical properties given in Table 4-1. The values of the nominal stresses and engineering strains were converted into the corresponding 2nd Piola-Kirchhoff and Green-Lagrange values for use in the three-dimensional model.

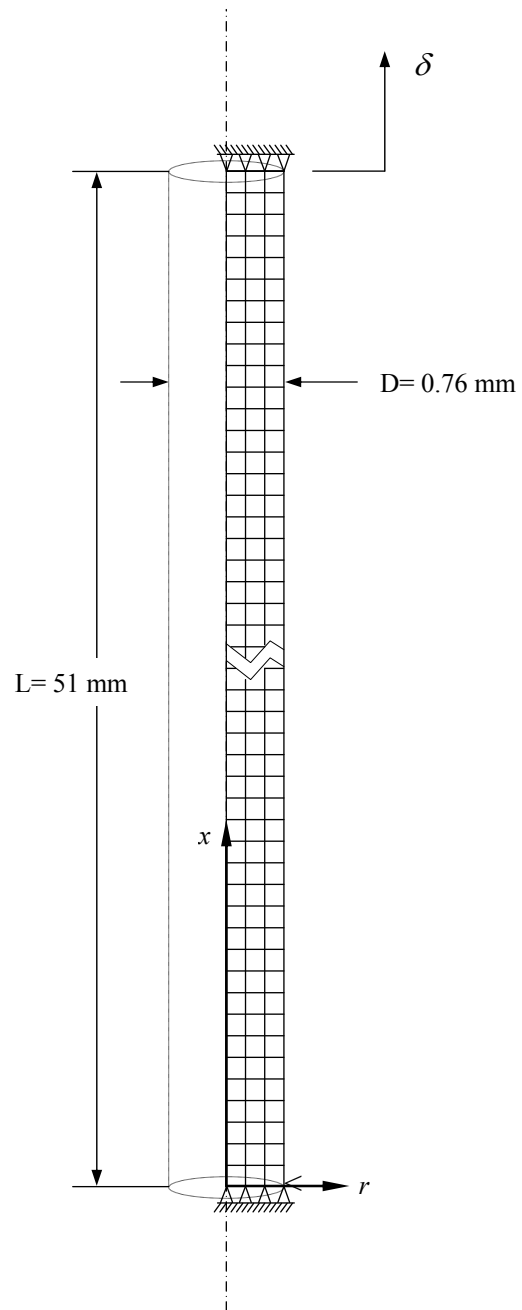


Figure 4-12. Geometry of the wire and axisymmetric finite element mesh.

As pointed out in Chapter 4, the transformation completion stresses in the multi-axial constitutive model (σ_{MC}, σ_{AC}) are different from the transformation finish stresses used in the one-dimensional model (σ_{MF}, σ_{AF}). By fitting the isothermal propagation stresses from the simulations to those from the experiments of Iadicola and Shaw (2002b), the completion stresses are obtained as,

$$\sigma_{MC} = 5.9354 \times T^{(C)} + 169.27 \text{ (MPa)}$$

$$\sigma_{AC} = 5.8675 \times T^{(C)} + 160.28 \text{ (MPa)}$$

A very small geometric imperfection is introduced at the lower corner of the wire (i.e., at $r=D/2$ and $x=0$) to control the location of the first nucleation event. No other artificial effect is introduced.

The wire is subjected to displacement-controlled loading-unloading at a strain rate of $\dot{\delta}/L = 2 \times 10^{-3} \text{ s}^{-1}$. The global stress-strain response of the wire is shown in Figure 4-13. Contour plots of the distribution of martensitic fraction throughout the sample during loading and unloading are shown in Figure 4-14. Due to the symmetry of the wire, the contour graphs are plotted on the r - x plane (Figure 4-12).

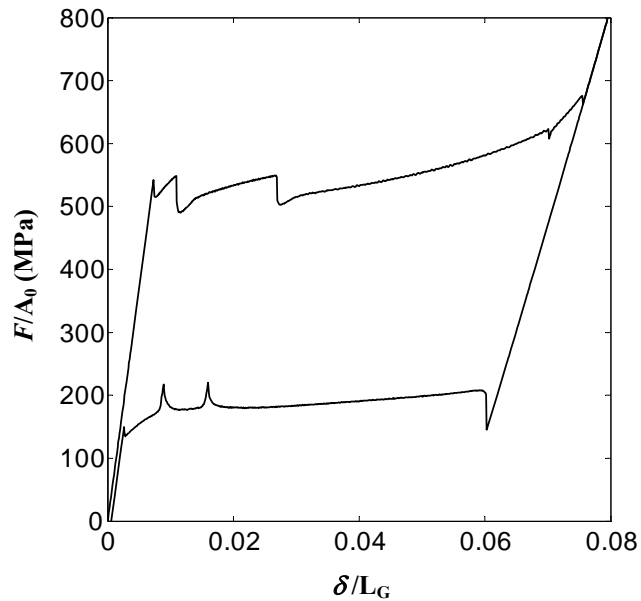


Figure 4-13. The nominal stress-strain response of the NiTi wire.

During loading, the forward transformation is first nucleated at the lower end of the wire followed by a second nucleation at the upper end due to the stress concentrations imposed by the geometric imperfection (lower end) and boundary conditions (upper end). As the transformation fronts propagate toward the central part of the wire, the temperature of the specimen increases which elevates the level of stress as seen in Figure 4-13. As a result, a third nucleation event takes place in the mid-span of the wire. Each nucleation event is accompanied by a drop in the stress-strain curve.

As the transformation fronts approach each other, the effect of heat generation is intensified and the stress continuously rises without occurrence of any additional nucleation event. The first two transformation fronts meet each other at $x/L = 0.67$, followed by the coalescence of the two remaining fronts at $x/L = 0.29$. By the end of loading segment, the entire length of the wire has transformed into martensite.

A 5-minutes delay is assumed between loading and unloading to allow the temperature of the specimen to return to the ambient temperature. The specimen is then unloaded at the same elongation rate of $\dot{\delta}/L = -2 \times 10^{-3} \text{ s}^{-1}$. It is seen that the nucleation of the reverse transformation occurs at the exact same locations that the fronts coalesced during the forward transformation. This is an interesting result which has also been repeatedly observed in various experiments (Shaw and Kyriakides, 1995; Shaw and Kyriakides, 1997; Iadicola and Shaw 2002a,b). According to these observations, the coalescence sites of the transformation fronts become the preferred nucleation points for the subsequent transformations.

To better understand the interaction of two converging transformation fronts, the distribution of the Von-Mises effective stress ($\bar{\sigma}$) before and after the coalescence of two transformation fronts are depicted in Figures 4-15(b) and 4-15(c). The distribution of phases before the two fronts merge is also shown in Figure 4-15(a). Despite the introduction of the permanent deformation, the distribution of stress is quite uniform in the transformed regions ($\gamma = 1$). However, after the two fronts merge together, the effective stress does not exhibit a uniform distribution at the site of coalescence. This is because the two transformations propagate in opposite directions and the resulting permanent strains have mismatching directions.

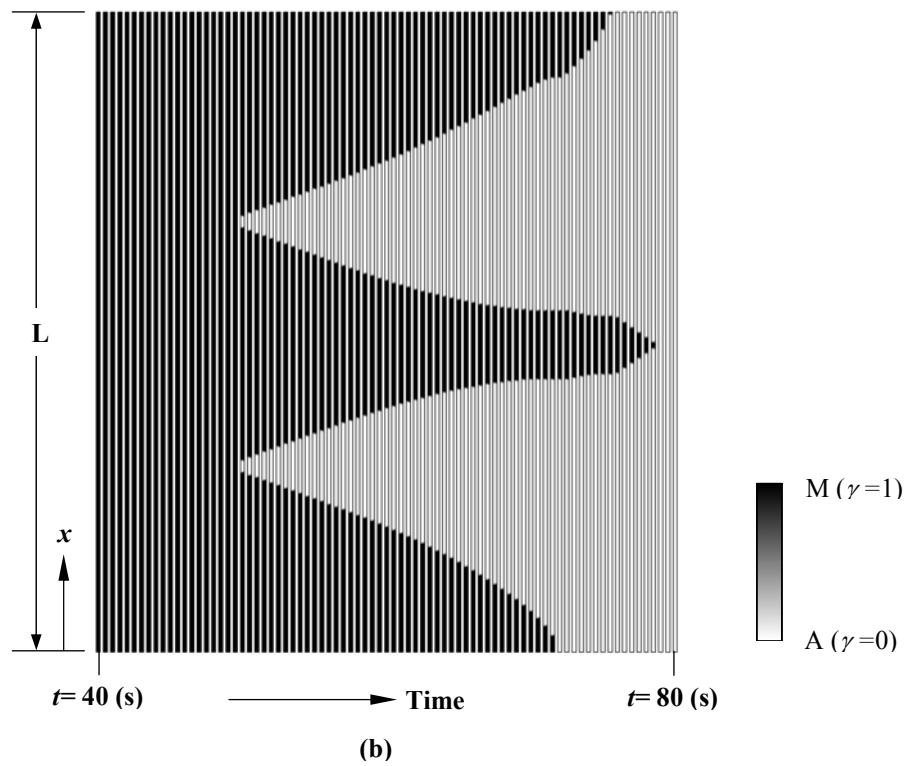
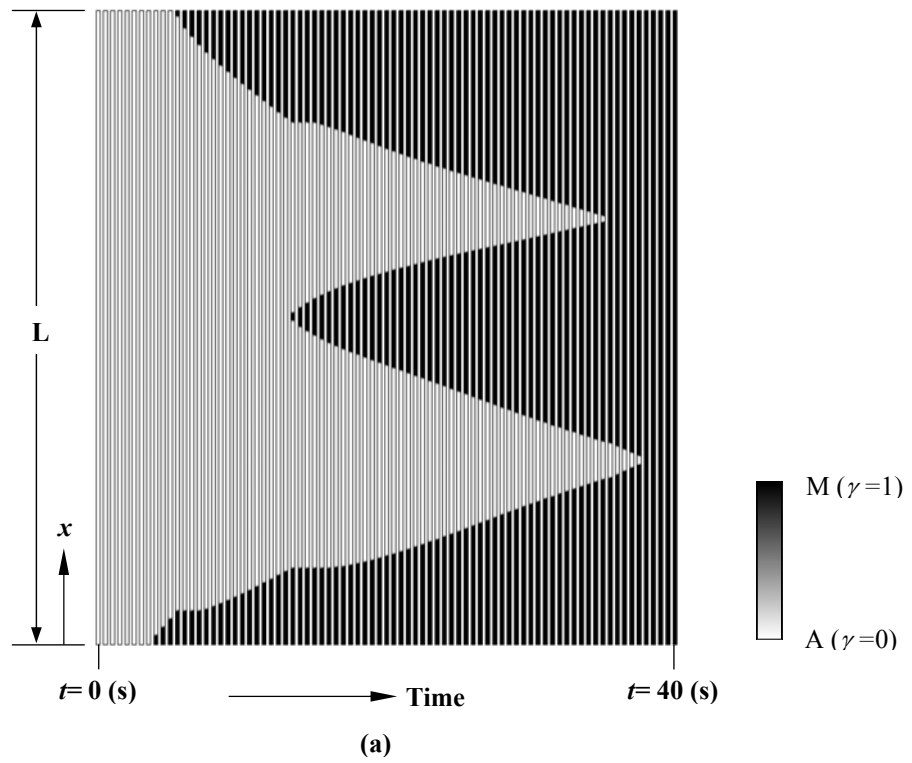


Figure 4-14. Sequence of martensitic fraction contours. (a) Loading; (b) Unloading.

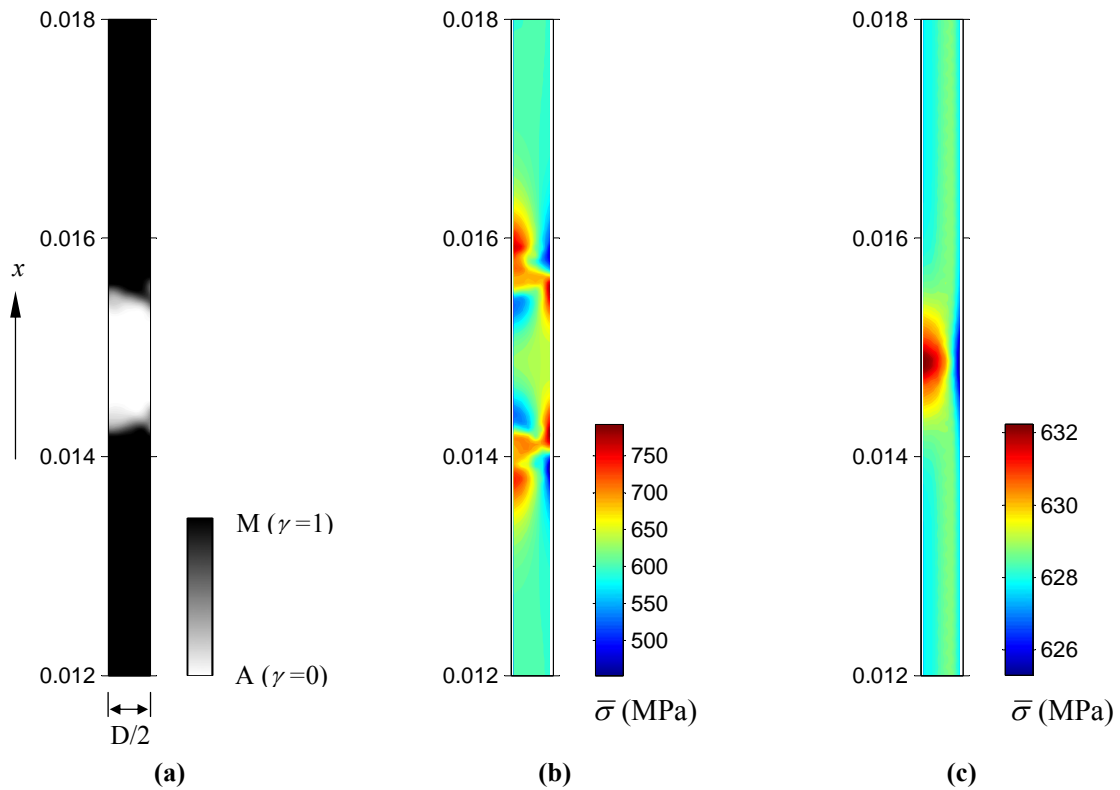


Figure 4-15. (a) Distribution of phases before the coalescence event; (b) Distributions of effective stress corresponding to figure (a); (c) Distributions of effective stress after the coalescence.

As explained in Chapter 3, the state of stress at the transformation front is three-dimensional due to a severe deformation gradient. As a result, the permanent deformation ($\epsilon^{(p)}$) produced during the transformation is not uniaxial and depends on the gradient of the stress tensor (equation 4-35). Unlike the transformation strain ($\epsilon^{(t)}$) which can reorient itself after the completion of transformation, the direction of permanent strain does not change once the transformation front passes over. Since the permanent strains produced at a coalescence site are in opposite directions, a residual *macroscopic* stress field is produced which facilitates the nucleation of subsequent transformations.

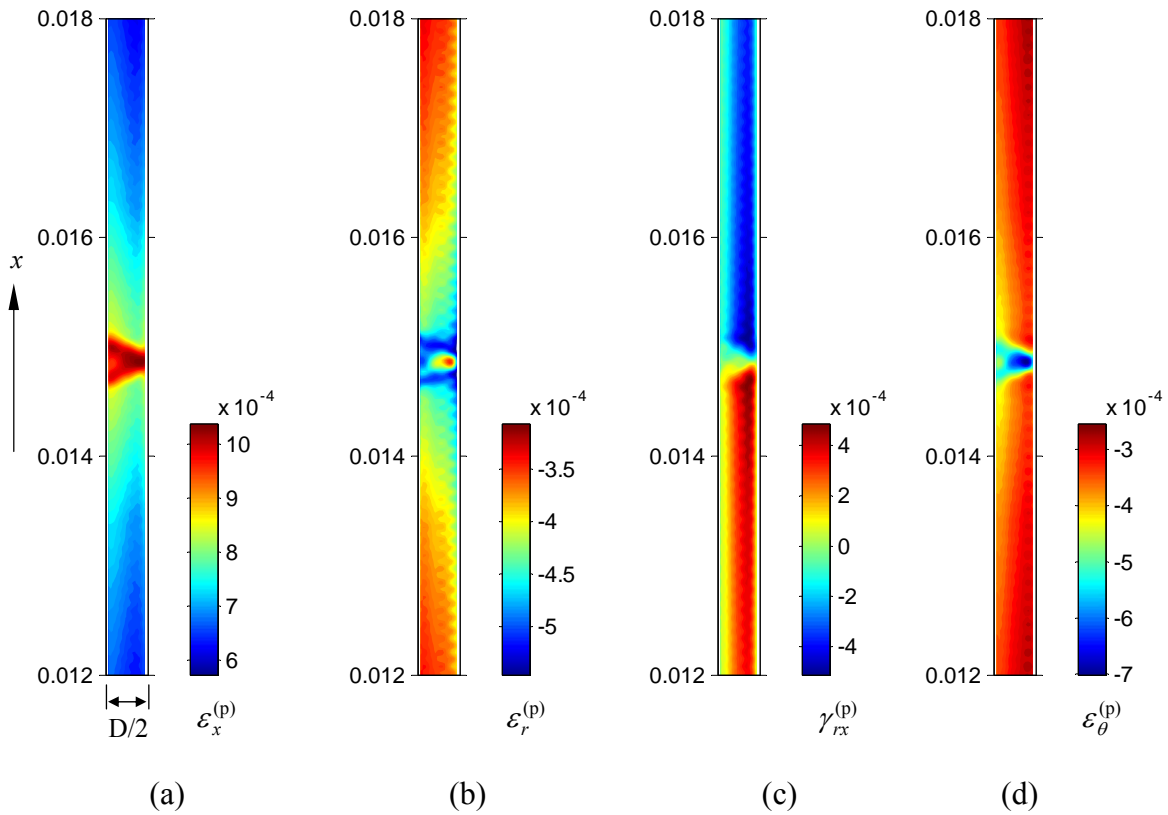


Figure 4-16. (a) Axial strain, $\varepsilon_x^{(p)}$; (b) Radial strain, $\varepsilon_r^{(p)}$; (c) Shear strain, $\gamma_{rx}^{(p)}$; (d) Hoop strain, $\varepsilon_\theta^{(p)}$

The distributions of permanent strains produced at the site of the coalescence are given in Figure 4-17. The distribution of shear strain ($\gamma_{rx}^{(p)}$) is particularly interesting. The directions of shear strain on the opposite sides of the coalescence site are exactly opposite to each other. The non-uniform distribution of permanent strain at this point is clearly responsible for the residual stress field observed in Figure 4-15.

As a final remark, it should be noted that the residual permanent strain calculated in the present model is a macroscopic quantity, and differs from the concept of microscopic plastic strain. As explained in the introduction, the microscopic plastic deformation occurs at the grain boundaries

and results in a microscopic residual stress field which assists the nucleation of transformation. The macroscopic residual strain on the other hand, may or may not produce a considerable residual stress field as shown by the above example.

4.5. BIBLIOGRAPHY

- Abeyaratne, R., Kim, S.J., 1997. Cyclic effects in shape-memory alloys: A one-dimensional continuum model. *International Journal of Solids and Structures* 34, 3273-3289.
- Abeyaratne, R., Knowles, J.K., 1993. Continuum model of a thermoelastic solid capable of undergoing phase transitions. *Journal of the Mechanics and Physics of Solids* 41, 541-571.
- Bo, Z., Lagoudas, D.C., 1999. Thermomechanical modeling of polycrystalline SMAs under cyclic loading, Part I: Theoretical derivations. *International Journal of Engineering Science* 37, 1089-1140.
- Boyd, J.G., Lagoudas, D.C., 1994a. A thermodynamical constitutive model for the shape memory effect due to transformation and reorientation. *Proceedings of the SPIE - The International Society for Optical Engineering* 2189, 276-88.
- Boyd, J.G., Lagoudas, D.C., 1994b. Thermomechanical response of shape memory composites, *Journal of Intelligent Material Systems and Structures* 5, 333-346.
- Gong, J.M., Tobushi, H., Takata, K., Okumura, K., Endo, M., 2002. Cyclic superelastic deformation of TiNi shape-memory alloy. *Materials Science Forum* 394-395, 245-248.
- Iadicola, M.A.; Shaw, J.A., 2002a. The effect of uniaxial cyclic deformation on the evolution of phase transformation fronts in pseudoelastic NiTi wire. *Journal of Intelligent Material Systems and Structures* 13, 143-155.

- Iadicola, M.A., Shaw, J.A., 2002b. An experimental setup for measuring unstable thermo-mechanical behavior of shape memory alloy wire. *Journal of Intelligent Material Systems and Structures* 13, 157-166.
- Lagoudas, D.C., Bo, Z., 1999. Thermomechanical modeling of polycrystalline SMAs under cyclic loading, Part II: Material characterization and experimental results for a stable transformation cycle. *International Journal of Engineering Science* 37, 1141-1173.
- Lagoudas, D.C., Entchev, P.B., 2004. Modeling of transformation-induced plasticity and its effect on the behavior of porous shape memory alloys. Part I: Constitutive model for fully dense SMAs. *Mechanics of Materials* 36, 865-892.
- Lexcellent, C., Bourbon, G., 1996. Thermodynamical model of cyclic behaviour of Ti-Ni and Cu-Zn-Al shape memory alloys under isothermal undulated tensile tests. *Mechanics of Materials* 24, 59-73.
- Liu, Y., Houver, I., Xiang, H., Bataillard, L., Miyazaki, S., 1999. Strain dependence of pseudoelastic hysteresis of NiTi. *Metallurgical and Materials Transactions A: Physical Metallurgy and Materials Science* 30, 1275-1282.
- Miyazaki, S., Imai, T., Otsuka, K., Suzuki, Y., 1981. Lüders-like deformation observed in the transformation pseudoelasticity of a Ti-Ni alloy. *Scripta Metallurgica* 15, 853-856.
- Miyazaki, S., Imai, T., Igo, Y., Otsuka, K., 1986. Effect of cyclic deformation on the pseudoelasticity characteristics of Ti-Ni alloys. *Metallurgical Transactions A (Physical Metallurgy and Materials Science)* 17A, 115-120.
- Shaw, J.A., Kyriakides, S., 1995. Thermomechanical aspects of NiTi. *Journal of the Mechanics and Physics of Solids* 43, 1243-1281.

- Shaw, J.A., Kyriakides, S., 1997. On the nucleation and propagation of phase transformation fronts in a NiTi alloy. *Acta Materialia* 45, 683-700.
- Sittner, P., Lukas, P., Neov, D., Lugovyy, D., 2003. Martensitic transformations in NiTi polycrystals investigated by in-situ neutron diffraction. *Materials Science Forum* 426-432, 2315-20.
- Strnadel, B., Ohashi, S., Ohtsuka, H., Miyazaki, S., Ishihara, T., 1995. Effect of mechanical cycling on the pseudoelasticity characteristics of Ti-Ni and Ti-Ni-Cu alloys. *Materials Science & Engineering A (Structural Materials: Properties, Microstructure and Processing)* A203, 187-96.
- Tanaka, K., 1986. A thermomechanical sketch of shape memory effect: one-dimensional tensile behavior, *Res Mechanica* 18, 251-263.
- Tanaka, K., 1990. A phenomenological description on thermomechanical behavior of shape memory alloys. *Transactions of the ASME, Journal of Pressure Vessel Technology* 112, 158-163.
- Tanaka, K., Hayashi, T., Itoh, Y., Tobushi, H., 1992. Analysis of thermomechanical behavior of shape memory alloys. *Mechanics of Materials* 13, 207-215.
- Tanaka, K., Nishimura, F., Hayashi, T., Tobushi, H., LExcellent, C., 1995. Phenomenological analysis on subloops and cyclic behavior in shape memory alloys under mechanical and/or thermal loads. *Mechanics of Materials* 19, 281-292.
- Tobushi, H., Yamada, S., Hachisuka, T., Ikai, A., Tanaka, K., 1996. Thermomechanical properties due to martensitic and R-phase transformations of TiNi shape memory alloy subjected to cyclic loadings. *Smart Materials and Structures* 5, 788-795.
- Tobushi, H., Pieczyska, E., Gadaj, S., Nowacki, W.K., Hoshio, K., Makino, Y., 2005. Characteristics of energy storage and dissipation in TiNi shape memory alloy. *Science and Technology of Advanced Materials* 6, 889-94.

Chapter 5: Summary and Conclusions

The mechanical instability of some SMAs results in localized transformation and Lüders-like deformation. Previous experimental and theoretical investigation has shown that nucleation and propagation of the localized transformation bands have important implications for the dynamic pseudoelastic response of SMAs. In particular, the sensitivity of an SMA's response to strain rate and cyclic degradation is directly influenced by inhomogenous transformation. Motivated by the above facts, the main objectives of this research have been:

- 1) to develop a reliable and convenient constitutive model for engineers to predict the dynamic, unstable pseudoelastic response of SMAs, including their cyclic response, and
- 2) to provide a better understanding of the mechanical origin of shape recovery occurring through unstable propagation of transformation bands.

5.1. SUMMARY OF MODEL DEVELOPMENT

A one-dimensional thermomechanical model was developed to describe the unstable pseudoelastic behavior of SMAs and to simulate the nucleation and propagation of transformation front(s) in an SMA wire. A key assumption in the model is that the untransformed particles located close to the transformation fronts are less stable than those further away from these interfaces. This constitutive model was used to simulate the pseudoelastic behavior of a thin SMA wire at various strain rates. The results of the simulations were in good agreement with previous experimental observations. The behavior of a NiTi wire subjected to various thermal loadings under constant-stress or constant-strain conditions was also studied numerically.

The one-dimensional model was extended to a multi-axial constitutive model of unstable pseudoelastic response. The model was developed based on a total deformation constitutive relation

(the deformation theory of plasticity). In this model, the total transformation strain is expressed in terms of the gradient of an effective stress. This feature allows the simultaneous accommodation of the transformation and the reorientation of transformation strain according to the current state of stress. The model was implemented in a finite element code to simulate the Lüders-like behavior and localized transformations occurring during the uniaxial extension of NiTi strips. Special attention was paid to the multi-axiality of the stress state at the transformation fronts during the forward and reverse transformations. The effects of heat generation and boundary conditions on the nucleation and propagation of transformation fronts were also studied. The simulation results proved to be in good agreement with previous experimental observations.

The one-dimensional and three-dimensional constitutive models of unstable pseudoelastic behavior were extended to include the effects of transformation-induced plasticity and cyclic deformation. For this purpose, a new internal state variable (cyclic identifier) was defined that characterizes the amount of preceding cyclic deformation at various temperatures. The generation of an irreversible plastic deformation during the forward transformation was also incorporated. The updated one-dimensional model was applied to simulate the pseudoelastic behavior of a NiTi wire subjected to cyclic loading. The model was able to qualitatively capture the effect of cyclic loading on the overall mechanical response of the specimen, as well as the nucleation and propagation of transformation fronts.

5.2. CONCLUSIONS

The following conclusions can be drawn from the numerical simulations of the NiTi wire under various loading conditions based on the one-dimensional model:

- The one-dimensional constitutive model proved to be successful in describing the dynamic unstable pseudoelastic response of SMA wires subjected to various loading

conditions. The effects of loading rate and heat generation on the overall pseudoelastic response, and nucleation and propagation of transformation fronts, are captured by the model.

- Defects and impurities in the material can be effectively included in the FEM analysis by introducing a random deviation from the original cross-sectional area along the wire length, which results in a more realistic model and prevents the transformations from occurring homogeneously throughout the wire. However, a higher mesh density is required in the FE model to achieve convergence in this case.
- The simulations of the pseudoelastic response at various strain rates revealed that the height of the hysteresis loop does not always increase with increased loading rate. In fact, if the heat generated during the forward transformation is not dissipated fast enough during elastic unloading, the reverse transformation occurs at a higher stress level than might be expected. This effect reduces the height of the hysteresis loop.
- Simulating the temperature-induced transformation in a wire at constant stress revealed that the required change in temperature for full transformation of the specimen strongly depends on the cooling rate. As the cooling rate increases, the drop in ambient temperature required to transform the specimen increases.

Based on the simulations of NiTi strip samples using the three-dimensional model, the following conclusions can be drawn:

- The total transformation strain model is clearly successful in describing the nucleation and propagation of transformation fronts during both loading and unloading. Although the model was applied to simulate the uniaxial extension of NiTi strips, the analysis was multi-axial in nature and involved calculation of the two-dimensional stresses and strains.

Therefore, the model is able to capture the unstable pseudoelastic behavior in problems that involve multi-axial loading.

- It was shown through a numerical example that the reversibility of transformation strain in a constitutive model for uniform stress fields does not automatically guarantee the recovery of inelastic deformation when strain localization takes place. As shown in the simulations, the state of stress at a transformation front is very complex due to rapid changes in the strain tensor across the front. Upon unloading, the mismatch in the strain tensor between the neighboring transformed and untransformed regions may further intensify the stress concentration. This effect may prohibit the occurrence of the reverse transformation. Consequently, some localized martensitic areas are locked inside the parent phase, and the transformation strain is not fully recovered throughout the material.
- The reorientation of the transformation strain plays an important role in the reversibility of inelastic deformation during unstable pseudoelastic behavior, preventing particles from being locked in localized high stress concentration zones during reverse transformation. Due to reorientation, the direction of the transformation strain tensor is continuously updated according to the current direction of stress, which minimizes the mismatch between the transformed and untransformed areas. The reorientation of transformation strain also results in a fairly uniform distribution of stress across the transformed areas.
- The success of a purely mechanical approach in correctly describing the forward and reverse transformations verifies that the continuum-level phenomena are the major drivers in the nucleation and propagation of martensitic transformation and its reverse transformation in NiTi shape memory alloys, regardless of the detailed microstructural root of the material instability.

- The number of propagating transformation fronts is an important factor in determining the overall mechanical response of the material in non-isothermal conditions. The number of coexisting transformation fronts influences the local variations of temperature at individual fronts, which in turn affects the overall pseudoelastic response.
- The comparison between the calculated temperature drop during reverse transformation and experimental measurements clearly indicates that the zero-stress enthalpy change (stress-free latent heat) of forward transformation must be greater than that of the reverse transformation. This conclusion, however, does not agree with reported DSC measurements. Further experimental and theoretical analysis is required to clarify this difference.
- The numerical analysis of the effect of boundary conditions on the evolution of transformation fronts indicated that the front morphology is sensitive to imperfections and misalignments in the boundary conditions, especially during the reverse transformation.

The following conclusions can be drawn based on the numerical simulations of cyclic deformation:

- Residual pockets of austenite that gradually accumulate during cyclic loading may change the transformation behavior of a wire specimen, and result in the nucleation and propagation of multiple transformation fronts throughout the sample.
- The change in transformation pattern (number of propagating fronts) during cyclic deformation has a pronounced effect on the overall pseudoelastic response of the material.

- An increase in the number of transformation fronts tends to stabilize the stress-strain response of the material via a “staircase” effect. The forward transformation tends to initiate in regions that are highly cycled. As the transformation fronts enter the less cycled areas, the stress increases. This effect results in a positive slope for the stress-strain response curve.
- The stress concentration that exists at the interface of highly cycled and less cycled regions cannot be effectively modeled using the one-dimensional model. This limitation results in some differences between the simulation results and experimental observations. It is expected that a three-dimensional analysis can overcome this deficiency.
- The simulation of the pseudoelastic response of a NiTi wire using the multi-dimensional model revealed an interesting effect of transformation-induced plasticity. It was demonstrated that the mismatch in the permanent strain produced at the coalescence site of two transformation fronts results in a non-uniform macroscopic residual stress field. The residual stress field makes the coalescence site a preferred nucleation point for the subsequent forward or reverse transformations.

5.3. PROPOSED FUTURE WORK

The main focus of the present research was on the pseudoelastic behavior of SMAs. In addition to pseudoelasticity, SMAs exhibit other important behaviors, such as the one-way shape memory effect, two-way shape memory effect, and ferroelasticity. In these behaviors, the transformation or detwinning strain is not recovered by mechanical unloading, but rather results in a residual strain that can be recovered by raising the temperature of material. In the present three-dimensional constitutive model, however, the transformation strain becomes singular at stress equal

to zero, and therefore, it cannot be used to describe the above-mentioned behaviors. Extending the present modeling effort to include such behaviors should be the subject of a future study.

Although the FE analyses of the NiTi strips presented in this work were multi-dimensional, the applied external loads were uniaxial. The localization of deformation under more complex loading conditions, such as torsion, tension-torsion, and biaxial extension, requires investigation. Some experimental observations suggest that the localization of deformation is not observed during torsion or compression in alloys that exhibit Lüders-like deformation in uniaxial tension. The origin of such inconsistency in the material response at various loading conditions is currently being investigated by a number of researchers using different experimental and theoretical methods. It would be interesting to numerically investigate the response of a SMA sample under such loading conditions while material behavior is unstable. It is suspected that some structural effects, such as geometric distortion, might result in the hardening in spite of the inherent instability of the constitutive behavior of material.

An important topic for future work is the three-dimensional analysis of the evolution of phase transformations during cyclic loading. Numerical simulations of the cyclic effects presented in this research were based on a one-dimensional model in which the stress concentration at the transformation fronts was incorporated in the analysis using the “radius of influence” concept. This was shown to exhibit some deficiencies during partial cyclic loading. A full three-dimensional analysis, on the other hand, will naturally take into account the effect of stress concentration, and is expected to provide valuable information about the nature of cyclic effects.

Finally, the experimental study of the in-situ localized behavior of NiTi SMAs is another exciting topic for further investigations. In particular, the reorientation of transformation strain as a result of the martensite-to-martensite conversion can be experimentally investigated using neutron

diffraction techniques. Neutron diffraction is a crystallographic method that uses a neutron beam to accurately measure the lattice strains in a representative volume of material during mechanical loading.

Appendix A. Details of Calculations Based on the Transformation Evolution Rule (One-Dimensional Model)

Based on the transformation evolution rule described in Section 2.2.3, a numerical procedure that calculates the increments of stress and martensitic fraction in terms of the increments of strain and temperature during one-dimensional forward transformations was developed. In this procedure, the value of stress is initially calculated based on the elastic prediction; if the result is outside the stability region, the value of stress is corrected so that the stress-temperature vector (σ, T) lies on the corresponding transformation line (this procedure is similar to the well-known *elastic-predictor and plastic-corrector* scheme used in the numerical implementation of plasticity theory).

A.1. FORWARD TRANSFORMATION

To start, consider a material particle whose initial state of stress-temperature-transformation is specified by the point $a(\sigma_a, T_a, \gamma_a)$ in Figure A-1, which is located either below or on the instantaneous martensite transformation line. It is assumed that the instantaneous nucleation line is given by:

$$\sigma_{MN}^*(T) = \alpha \sigma_{MN}(T) + (1 - \alpha) \sigma_{MF}(T) \quad (\text{A-1})$$

where the parameter α varies between 0 and 1 and characterizes the relative location of the instantaneous nucleation line. Two different cases are identified as follows:

CASE 1: For an austenitic material point ($\gamma_a = 0$) which is surrounded by other austenite particles far from any transformation front, α is equal to 1 which implies that the instantaneous nucleation line coincides with the martensite nucleation line $\sigma_{MN}(T)$.

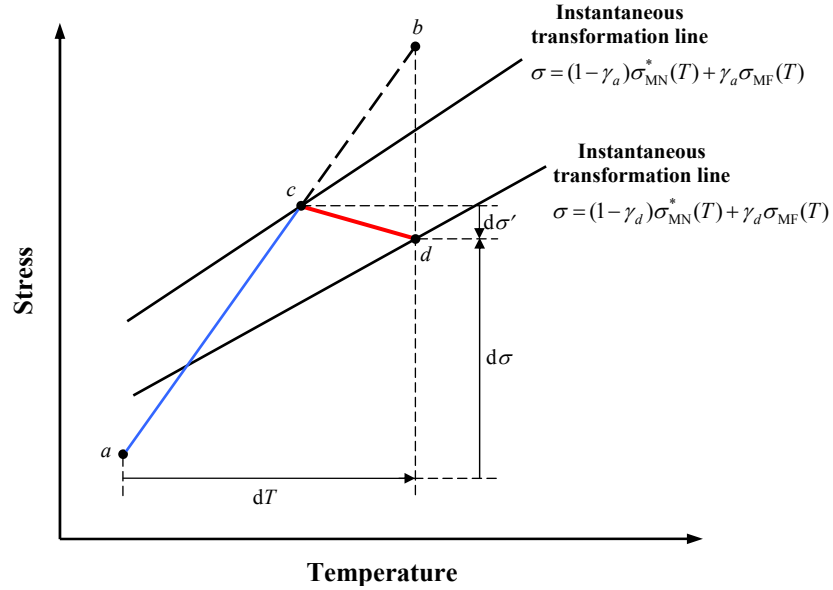


Figure A-1. Calculation of incremental changes during the forward transformation (elastic prediction and transformation correction).

CASE 2: For a partially transformed particle ($0 < \gamma_a < 1$), or an austenite particle ($\gamma_a = 0$) that is located in the close vicinity of a transformation front, the values of α is obtained by imposing the following condition:

$$F_{A \rightarrow M}(\sigma_a, \gamma_a, T_a) = \sigma_a - \left[(1 - \gamma_a) \sigma_{MN}^*(T_a) + \gamma_a \sigma_{MF}(T_a) \right] = 0 \quad (\text{A-2})$$

This implies that the current stress-temperature vector (σ_a, T_a) must be located on an instantaneous transformation line characterized by the martensitic fraction γ_a . Since the instantaneous nucleation line cannot be below the transformation finish line, the value of α is assumed to be zero in cases that the stress-temperature vector is located below the martensite finish line. Therefore, the value of α from equations (A-1) and (A-2) is obtained as,

$$\alpha = \max \left\{ 0, \frac{\sigma_a - \sigma_{\text{MF}}(T_a)}{(1 - \gamma_a) [\sigma_{\text{MN}}(T_a) - \sigma_{\text{MF}}(T_a)]} \right\} \quad (\text{A-3})$$

After finding the appropriate value for the parameter α , the final form of function $F_{\text{A} \rightarrow \text{M}}$ becomes,

$$F_{\text{A} \rightarrow \text{M}}(\sigma, \gamma, T) = \sigma - [(1 - \gamma)\alpha \sigma_{\text{MN}}(T) + (1 - \alpha + \alpha\gamma)\sigma_{\text{MF}}(T)] \quad (\text{A-4})$$

If the increments of strain and temperature are given to be $d\varepsilon$ and dT respectively, the final state of material assuming elastic deformation is characterized by point $b(\sigma_b, T_b, \gamma_b)$ in Figure A-1 where:

$$\begin{cases} T_b = T_a + dT \\ \sigma_b = \sigma_a + E(\gamma_a)d\varepsilon \\ \gamma_b = \gamma_a \end{cases} \quad (\text{A-5})$$

If point b is still located below or on the transformation line (i.e., $F_{\text{A} \rightarrow \text{M}}(\sigma_b, T_b, \gamma_b) \leq 0$), the elastic trial has been successful and no further calculation is required. On the other hand, if point b is located beyond the instantaneous transformation line (i.e., $F_{\text{A} \rightarrow \text{M}}(\sigma_b, T_b, \gamma_b) > 0$), the amount of phase transformation must be calculated and the value of stress must also be corrected. In that case, it is assumed that the behavior of material remains elastic until point c , where the line ab crosses the transformation line, and further loading results in phase transformation along the path cd as shown in the figure. The state of material at point c is given by,

$$\begin{cases} T_c = T_a + \beta dT \\ \sigma_c = \sigma_a + E(\gamma_a)\beta d\varepsilon \\ \gamma_c = \gamma_a \end{cases} \quad (\text{A-6})$$

where β is the solution of the following equation,

$$F_{A \rightarrow M}(\sigma_a + E(\gamma_a)\beta d\varepsilon, T_a + \beta dT, \gamma_a) = 0 \quad (\text{A-7})$$

Substituting (A-4) in (A-7) gives,

$$\beta = \frac{\sigma_a - (1 - \gamma_a)\alpha \sigma_{MN}(T_a) - (1 - \alpha + \alpha \gamma_a)\sigma_{MF}(T_a)}{-\left. \frac{\partial F_{A \rightarrow M}}{\partial T} \right|_{(\gamma_a, T_a)} dT - E(\gamma_a) d\varepsilon} \quad (\text{A-8})$$

where,

$$\frac{\partial F_{A \rightarrow M}}{\partial T} = -(1 - \gamma)\alpha \frac{\partial \sigma_{MN}}{\partial T} - (1 - \alpha + \alpha \gamma) \frac{\partial \sigma_{MF}}{\partial T} \quad (\text{A-9})$$

If the state variables at point d are given by,

$$\begin{cases} T_d = T_a + dT \\ \sigma_d = \sigma_c + d\sigma' \\ \gamma_d = \gamma_a + d\gamma \end{cases} \quad (\text{A-10})$$

the incremental changes of stress and martensitic fraction ($d\sigma'$, $d\gamma$) during the transformation (line cd), are obtained by simultaneously enforcing the stress-strain relationship (equation 2-12) and the transformation evolution rule (equation 2-20) that are,

$$(1 - \beta) d\varepsilon = \frac{d\sigma'}{E(\gamma_a)} + \left(\frac{\sigma_c}{E_M} - \frac{\sigma_c}{E_A} + \Delta\varepsilon_t \right) d\gamma \quad (\text{A-11})$$

and

$$dF_{A \rightarrow M} = 0 \quad (\text{A-12})$$

Substituting (A-4) in (A-12) gives,

$$d\sigma' + \left. \frac{\partial F_{A \rightarrow M}}{\partial T} \right|_{(\gamma_a, T_c)} (1 - \beta) dT + \left. \frac{\partial F_{A \rightarrow M}}{\partial \gamma} \right|_{(\gamma_a, T_c)} d\gamma = 0 \quad (\text{A-13})$$

where,

$$\frac{\partial F_{A \rightarrow M}}{\partial \gamma} = \alpha [\sigma_{MN}(T) - \sigma_{MF}(T)] \quad (\text{A-14})$$

Combining equation (A-10) and (A-12) yields the increment of martensitic fraction as,

$$d\gamma = (1 - \beta) \frac{E(\gamma_a) d\varepsilon + \left. \frac{\partial F_{A \rightarrow M}}{\partial T} \right|_{(\gamma_c, T_c)} dT}{-\left. \frac{\partial F_{A \rightarrow M}}{\partial \gamma} \right|_{(\gamma_c, T_c)} + E(\gamma_a) \left(\frac{\sigma_c}{E_M} - \frac{\sigma_c}{E_A} + \Delta\varepsilon_t \right)} \quad (\text{A-15})$$

Substituting $d\gamma$ from above equation back into (A-11) gives the increment of stress $d\sigma'$ as,

$$d\sigma' = (1 - \beta) E(\gamma_a) \frac{-\left. \frac{\partial F_{A \rightarrow M}}{\partial \gamma} \right|_{(\gamma_c, T_c)} d\varepsilon - \left(\frac{\sigma_c}{E_M} - \frac{\sigma_c}{E_A} + \Delta\varepsilon_t \right) \left. \frac{\partial F_{A \rightarrow M}}{\partial T} \right|_{(\gamma_c, T_c)} dT}{-\left. \frac{\partial F_{A \rightarrow M}}{\partial \gamma} \right|_{(\gamma_c, T_c)} + E(\gamma_a) \left(\frac{\sigma_c}{E_M} - \frac{\sigma_c}{E_A} + \Delta\varepsilon_t \right)} \quad (\text{A-16})$$

A.2. REVERSE TRANSFORMATION

A similar procedure can also be followed for calculation of stress and martensitic fraction during the reverse transformation. The details of the procedure are not given here for the sake of brevity. However, some of the fundamental equations are presented.

The graphical representation of elastic-prediction and transformation-correction in this case is shown in Figure A-2. As before, the initial state of material is represented by the point $a(\sigma_a, T_a, \gamma_a)$.

The instantaneous nucleation line is given by:

$$\sigma_{AN}^*(T) = \alpha \sigma_{AN}(T) + (1 - \alpha) \sigma_{AF}(T) \quad (\text{A-17})$$

where the value of parameter α is determined according to the following two cases:

CASE 1: For a martensite particle ($\gamma_a = 1$) located in a martensitic region the values of α is equal to

1.

CASE 2: For a partially transformed particle ($0 < \gamma_a < 1$), or a martensite particle ($\gamma_a = 1$) that is located in the close vicinity of a transformation front, the values of α is obtained by imposing the following condition:

$$F_{M \rightarrow A}(\sigma_a, \gamma_a, T_a) = \sigma_a - [\gamma_a \sigma_{AN}^*(T_a) + (1 - \gamma_a) \sigma_{AF}(T_a)] = 0 \quad (\text{A-18})$$

Substitution of equation (A-17) into the above equation gives,

$$\alpha = \max \left\{ 0, \frac{\sigma_a - \sigma_{AF}(T_a)}{\gamma_a [\sigma_{AN}(T_a) - \sigma_{AF}(T_a)]} \right\} \quad (\text{A-19})$$

The final form of the function $F_{M \rightarrow A}$ becomes,

$$F_{M \rightarrow A}(\sigma, \gamma, T) = \sigma - [\alpha \gamma \sigma_{AN}(T) + (1 - \alpha \gamma) \sigma_{AF}(T)] \quad (\text{A-20})$$

The rest of the calculations based on the elastic-prediction and transformation-correction scheme to find the final state of the material (point d in Figure A-2) are similar to those explained for the forward transformation case.

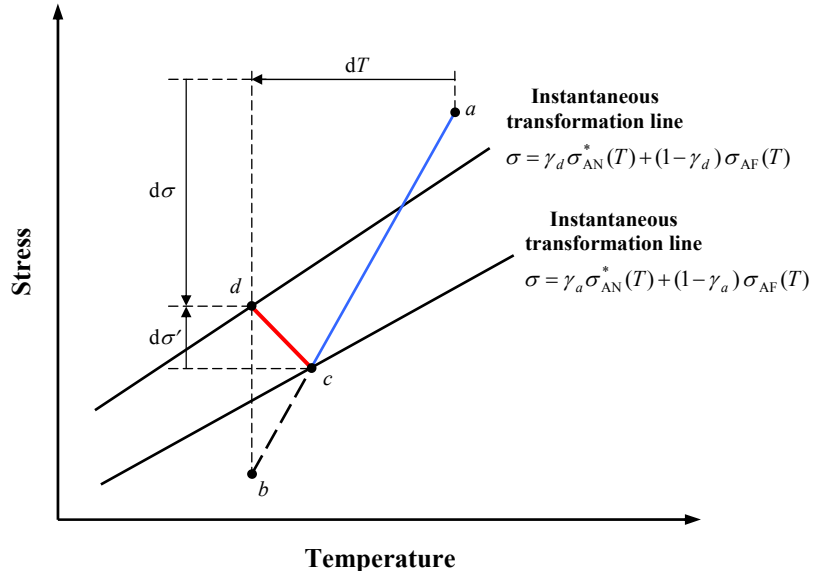


Figure A-2. Calculation of incremental changes during the reverse transformation (elastic prediction and transformation correction).

Appendix B. Outline of Experiments

The setup and testing conditions used in the experiments of Shaw and Kyriakides (1995, 1997) are briefly described in this appendix. The results of these experiments have been used in Chapter 2 and 3 to verify the simulation results.

B.1. DISPLACEMENT-CONTROLLED EXTENSION OF NiTi WIRE (SHAW AND KYRIAKIDES, 1995)

In the experiments of Shaw and Kyriakides (1995), the uniaxial mechanical response of NiTi was established as a function of temperature and loading rate. The experiments were conducted on polycrystalline Ni_{50.1%}Ti wire with a diameter of 1.07 mm. The material processing consisted of 30% cold drawing followed by annealing at 500 °C for 3 min. As a result, the material had an austenite microstructure at temperatures above 50 °C. Each experiment was performed using a virgin specimen.

The experiments were performed with prescribed displacement rates without interruption between loading and unloading. The test specimens had an overall length of 127 mm, and a test section of 63.5 mm. Each end was clamped between hardened flat plates along machined v-grooves in specially designed stainless steel grips.

In order to maintain a reasonably constant specimen temperature during testing, the specimen was placed in an isothermal liquid bath during the test. The bath temperature was controlled to within ± 0.2 °C of a prescribed value by a circulating system. Water was used as temperature control medium for experiments conducted in the range of 10 to 80 °C. To allow for the installation of the specimen into grips inside the liquid bath, relatively long grips had to be used which were designed to be much stiffer than the test specimen.

The load was measured by a 5 kN load cell, and the crosshead displacement was measured by a high resolution optical encoder within the testing machine. Local deformation and temperature were

monitored by miniature extensometers at up to four locations on the test section and by small thermocouples at up to six locations. The extensometers had a gauge length of 2.5 mm, a strain range of $\pm 15\%$, and a mass of less than 13 g. They were held in place by spring loaded clamping rods and knife edges. Each was coated with a flexible waterproof coating and was designed to be self temperature compensating. Corrections were made to the extensometer calibrations before each experiment to account for small changes in the gauge lengths caused by installation and thermal expansion.

The thermocouples were type 'K' with exposed junctions made of fine (0.076 mm) diameter wire. Small clips were used to mount the thermocouples to the specimen, and a thermally conductive paste (Omegatherm 201) was used for electrical insulation and to ensure good thermal contact with the specimen.

According to Shaw and Kyriakides (1995), there were some uncertainties associated with the measurements. The displacement was measured with an uncertainty of less than 0.8%, but grip slippage introduced additional error in the average strain calculated from the displacement. The slippage in the grips was observed when comparing the local and global strain measurements obtained from the miniature extensometer and crosshead displacement. The uncertainty in load measurement was less than 0.1%, but the uncertainty in the reported stress could be as high as 2% due to variation in the diameter of the wire. The miniature extensometer strains were calibrated to have an uncertainty of less than 1%. The thermocouples were also calibrated to measure the temperature with an uncertainty of 1%, but the uncertainty in temperature measurement could be as high as ± 1 °C due to the deformation of the wire and junction. The complex heat transfer conditions at the junction formed by the specimen, the thermocouple, the conductive paste, and the ambient fluid also had some effect on the measured temperature.

B.2. UNIAXIAL TENSION OF NiTi STRIP (SHAW AND KYRIAKIDES, 1997)

Shaw and Kyriakides (1997) presented a methodology for simultaneous full-field monitoring of the deformation and temperature in NiTi strip samples during mechanically unstable regimes. They used polycrystalline Ni_{50.5%}Ti formed into a continuous flat strip with a width of 4 mm and thickness of 0.395(±0.005) mm. After being tailored by thermomechanical processing, the material was in its austenite phase at temperatures above 15 °C. The processing left a thin (5 μm), glossy black oxide layer (TiO₂) on the strip which is a brittle ceramic and tends to shatter when subjected to significant strains such as those associated with the martensitic transformation. This resulted in surface relief and reflectivity changes which under proper lighting could be observed optically. This feature was later used to track the evolution of stress-induced transformations.

Dog-bone test specimens were machined from the strip with an overall length of $L_0 = 100$ mm and gauge section of $39(L_G) \times 2.525(w)$ mm². The wider ends of each specimen were gripped between two hardened flat plates tightly clamped together with four capscrews. In addition, to improve alignment and minimize slippage, each end of the test sample was pinned to the grips with a dowel pin.

The specimens were tested in a standard electromechanical testing machine in room temperature air (25 °C). The load was measured with a 5kN load cell and the end deflection was measured with a high resolution optical encoder. The specimen was first pulled at a constant end-deflection rate ($\dot{\delta}$) to a strain just past the termination of the upper stress plateau. After waiting few minutes, the specimen was unloaded at the same displacement rate. Two experiments were performed at elongation rates of $\dot{\delta}/L_G = 10^{-4} \text{ s}^{-1}$ and $\dot{\delta}/L_G = 10^{-3} \text{ s}^{-1}$. A virgin sample was used in each test to avoid cyclic effects.

The change in surface reflectivity of the specimen as a result of phase transformation and shattering of the oxide layer was recorded by a photographic camera programmed to take photos at 40 s time intervals. Also, an infrared imaging radiometer was used to record the thermal history of the entire test section during the loading/unloading cycle. The thermal camera had a 20 °C measurement range and a 4× zoom. For the particular setup used in the experiments, the spatial resolution of the camera was 0.3 mm, and the accuracy of thermal measurements was within ± 0.1 °C. The measured signal was converted into calibrated color contours which were recorded on video tapes at 30 frames/s. A microphone was placed near the photographic camera to record the sound of its shutter on the video. This sound was later used to synchronize the optical and thermal images.

Appendix C. Finite Element Formulations

An overview of the finite element formulations used to solve the boundary values problems is provided in this appendix.

C.1. THE FINITE ELEMENT FORMULATIONS OF SOLID CONTINUUM

Using the virtual work principle, the weak form of the equilibrium equation is given by,

$$\int_{v^{(e)}} \sigma_{ij} \delta \varepsilon_{ij} dv = \int_{s^{(e)}} f_i \delta u_i ds + \int_{v^{(e)}} b_i \delta u_i dv \quad (C-1)$$

where $v^{(e)}$ denoted the element volume, $s^{(e)}$ is the element surface, u_i is the displacement, f_i is the traction force acting on the surface, and b_i is the body force per unit volume. The above variational equation may be expressed in the vector form as,

$$\int_{v^{(e)}} \delta \boldsymbol{\varepsilon}^T \boldsymbol{\sigma} dv = \int_{s^{(e)}} \delta \mathbf{u}^T \mathbf{f} ds + \int_{v^{(e)}} \delta \mathbf{u}^T \mathbf{b} dv \quad (C-2)$$

It is assumed that the displacement vector \mathbf{u} can be expressed in terms of the nodal displacements as,

$$\mathbf{u} = \mathbf{N} \bar{\mathbf{u}}^{(e)} \quad (C-3)$$

where $\bar{\mathbf{u}}^{(e)}$ denotes the vector of nodal displacements, and \mathbf{N} contains the Lagrange interpolation functions. Furthermore, the strain vector can be derived by differentiating equation (C-3); that is,

$$\boldsymbol{\varepsilon} = \mathbf{B} \bar{\mathbf{u}}^{(e)} \quad (C-4)$$

where \mathbf{B} contains the derivatives of the Lagrange interpolation functions. The matrices \mathbf{N} and \mathbf{B} depend on the element type, and can be found from various FEM books. Substituting (C-3) and (C-4) in (C-2) gives,

$$\delta \bar{\mathbf{u}}^{(e)T} \int_{V^{(e)}} \mathbf{B}^T \boldsymbol{\sigma} dV = \delta \bar{\mathbf{u}}^{(e)T} \int_{S^{(e)}} \mathbf{N}^T \mathbf{f} dS + \delta \bar{\mathbf{u}}^{(e)T} \int_{V^{(e)}} \mathbf{N}^T \mathbf{b} dV \quad (\text{C-5})$$

The above equation must hold for any value of $\delta \bar{\mathbf{u}}^{(e)}$. Hence,

$$\int_{V^{(e)}} \mathbf{B}^T \boldsymbol{\sigma} dV = \int_{S^{(e)}} \mathbf{N}^T \mathbf{f} dS + \int_{V^{(e)}} \mathbf{N}^T \mathbf{b} dV \quad (\text{C-6})$$

The left hand side of the above equation is the *element internal force vector* while the right hand side is the *element external force vector*. After assembling the elements, the above equation results in the following equation:

$$\boldsymbol{\Psi}(\mathbf{U}) = 0 \quad (\text{C-7})$$

where \mathbf{U} denotes the global displacement vector, and $\boldsymbol{\Psi}$ is called the *residual force vector* defined as,

$$\boldsymbol{\Psi} = \boldsymbol{\Phi}(\mathbf{U}) - \mathbf{F} \quad (\text{C-8})$$

In the above equation $\boldsymbol{\Phi}$ is the (*global*) *internal force vector* obtained by assembling the element internal force vectors,

$$\boldsymbol{\Phi} = \sum_{\text{elements}} \left(\int_{V^{(e)}} \mathbf{B}^T \boldsymbol{\sigma} dV \right) \quad (\text{C-9})$$

and \mathbf{F} is the (*global*) *external force vector* obtained by assembling the element external force vectors:

$$\mathbf{F} = \sum_{\text{elements}} \left(\int_{S^{(e)}} \mathbf{N}^T \mathbf{f} dS + \int_{V^{(e)}} \mathbf{N}^T \mathbf{b} dV \right) \quad (\text{C-10})$$

Equation (C-7) is a non-linear equation which can be solved using an iterative numerical scheme. Suppose that the solution of equation (C-7) is known at iteration (i), and the solution at

iteration $(i+1)$ is to be found. Using the Taylor's series expansion, the residual force vector at iteration $(i+1)$ can be approximated by,

$$\boldsymbol{\Psi}(\mathbf{U}^{(i+1)}) = \boldsymbol{\Psi}(\mathbf{U}^{(i)}) + \left(\frac{\partial \boldsymbol{\Psi}}{\partial \mathbf{U}} \Big|_{\mathbf{U}=\mathbf{U}^{(i)}} \right) \delta \mathbf{U}^{(i)} + \dots = 0 \quad (\text{C-11})$$

where $\delta \mathbf{U}^{(i)}$ is the increment. Neglecting the higher order terms in the above equation, $\delta \mathbf{U}^{(i)}$ is obtained as:

$$\delta \mathbf{U}^{(i)} = - \left(\frac{\partial \boldsymbol{\Psi}}{\partial \mathbf{U}} \Big|_{\mathbf{U}=\mathbf{U}^{(i)}} \right)^{-1} \boldsymbol{\Psi}(\mathbf{U}^{(i)}) \quad (\text{C-12})$$

The displacement vector at $(i+1)$ iteration is given by,

$$\mathbf{U}^{(i+1)} = \mathbf{U}^{(i)} + \delta \mathbf{U}^{(i)} \quad (\text{C-13})$$

The iteration is continued until equation (C-7) is satisfied. The above iterative scheme is called the Newton-Raphson method. Newton-Raphson is a fast-converging method that is ideal for most problems in solid mechanics. However, this method fails to trace the equilibrium path near the stationary points (zero tangential modulus). In the vicinity of a stationary point, the Jacobian matrix (i.e., $\frac{\partial \boldsymbol{\Psi}}{\partial \mathbf{U}}$) becomes singular and the Newton-Raphson iteration diverges. Stationary points often appear in problems that involve materials with softening behavior and mechanical instability. Riks and Modified Riks schemes are often used to solve the non-linear equilibrium equations through stationary points. In these methods, the stiffness matrix and its inverse must be calculated at each iteration, which is computationally expensive. To avoid the computational cost of Riks method, a Modified Newton-Raphson scheme is utilized to solve the non-linear equations. In this method, the Jacobian matrix in equation (C-12) is replaced by a constant stiffness matrix. The stiffness matrix and

its inverse are calculated only once at the beginning of the FE calculations, and then used in each of the following iterations. Although the number of iterations required for convergence is much larger in the Modified Newton-Raphson method, the overall computational time is reduced compared to the Riks method in problems that have a large number of elements.

C.2. FINITE ELEMENT FORMULATIONS OF HEAT TRANSFER PROBLEM

The differential form of the heat transfer equation is given by,

$$\nabla \cdot (k \nabla T) + \dot{q}_G - \rho C_p \frac{\partial T}{\partial t} = 0 \quad (C-14)$$

where ∇ is the gradient (nabla) operator, and “.” denotes the scalar product. The weak form of the above equation for an element is given by,

$$\int_{V^{(e)}} w \left(\nabla \cdot (k \nabla T) + \dot{q}_G - \rho C_p \frac{\partial T}{\partial t} \right) dv = 0 \quad (C-15)$$

where w is a weight function. The above equation can be rewritten in the following form,

$$\int_{V^{(e)}} \left(\nabla \cdot (w k \nabla T) - (\nabla w) \cdot (k \nabla T) + \dot{q}_G w - \rho C_p \frac{\partial T}{\partial t} w \right) dv = 0 \quad (C-16)$$

Using the divergence theorem it is obtained,

$$- \int_{S^{(e)}} w q_n ds - \int_{V^{(e)}} (\nabla w) \cdot (k \nabla T) dv + \int_{V^{(e)}} \left(\dot{q}_G - \rho C_p \frac{\partial T}{\partial t} \right) w dv = 0 \quad (C-17)$$

where q_n is the heat flux per unit area defined as,

$$q_n = -k \nabla T \cdot \mathbf{n} \quad (C-18)$$

In the above definition, \mathbf{n} is the unit vector normal on a surface. If a convective film coefficient (h_{conv}) is assigned to the outer surface of the element, the heat flux is given by,

$$q_n = h_{\text{conv}}(T - T_\infty) \quad (\text{C-19})$$

Next, the temperature field is expressed in terms of the nodal temperatures as,

$$T = \mathbf{N}_T \bar{\mathbf{T}}^{(e)} \quad (\text{C-20})$$

where \mathbf{N}_T contains the Lagrange interpolation functions, and $\bar{\mathbf{T}}^{(e)}$ denotes the vector of nodal temperatures. The gradient of temperature can be obtained by differentiating equation (C-20) as,

$$\nabla T = \mathbf{B}_T \bar{\mathbf{T}}^{(e)} \quad (\text{C-21})$$

where \mathbf{B}_T contains the derivatives of the Lagrange interpolation functions. Substituting equations (C-19), (C-20), and (C-21) into (C-17) and following the Galerkin approach, the heat transfer equation becomes,

$$-\left(\int_{s^{(e)}} \mathbf{N}_T^T h_{\text{conv}} \mathbf{N}_T ds \right) (\bar{\mathbf{T}}^{(e)} - T_\infty) - \left(\int_{v^{(e)}} \mathbf{B}_T^T k \mathbf{B}_T dv \right) \bar{\mathbf{T}}^{(e)} + \int_{v^{(e)}} \mathbf{N}_T^T \dot{q}_G dv - \left(\int_{v^{(e)}} \mathbf{N}_T^T \rho C_p \mathbf{N}_T dv \right) \frac{\partial \bar{\mathbf{T}}^{(e)}}{\partial t} = 0 \quad (\text{C-22})$$

Upon assembling the elements, the global heat transfer equation is expressed as,

$$\mathbf{K}\mathbf{T} + \mathbf{C} \frac{\partial \mathbf{T}}{\partial t} + \mathbf{H}(\mathbf{T} - T_\infty) = \mathbf{Q}_G \quad (\text{C-23})$$

where,

$$\mathbf{K} = \sum_{\text{elements}} \left(\int_{v^{(e)}} \mathbf{B}_T^T k \mathbf{B}_T dv \right) \quad (\text{C-24})$$

$$\mathbf{C} = \sum_{\text{elements}} \left(\int_{v^{(e)}} \mathbf{N}_T^T \rho C_p \mathbf{N}_T dv \right) \quad (\text{C-25})$$

$$\mathbf{H} = \sum_{\text{elements}} \left(\int_{s^{(e)}} \mathbf{N}_T^T h_{\text{conv}} \mathbf{N}_T ds \right) \quad (\text{C-26})$$

$$\mathbf{Q}_G = \sum_{\text{elements}} \left(\int_{v^{(e)}} \mathbf{N}_T^T \dot{q}_G dv \right) \quad (\text{C-27})$$

and \mathbf{T} is the global temperature vector.

An implicit time-integration method (Backward Euler) is used to solve equation (C-23). Suppose that the temperature is known at time t_n , and the temperature is to be found at time $t_{n+1} = t_n + \Delta t$. It is assumed that,

$$\frac{\partial \mathbf{T}^{(n+1)}}{\partial t} = \frac{\mathbf{T}^{(n+1)} - \mathbf{T}^{(n)}}{\Delta t} \quad (\text{C-28})$$

Substituting (C-28) into (C-23) yields,

$$\mathbf{K}\mathbf{T}^{(n+1)} + \mathbf{C} \left(\frac{\mathbf{T}^{(n+1)} - \mathbf{T}^{(n)}}{\Delta t} \right) + \mathbf{H}(\mathbf{T}^{(n+1)} - T_\infty) = \mathbf{Q}_G^{(n+1)} \quad (\text{C-29})$$

which can be solved for $\mathbf{T}^{(n+1)}$.

Appendix D. Numerical Solution of the Three-Dimensional Constitutive Relations

In this appendix, a numerical solution of the nonlinear constitutive relations of the proposed multi-axial model during the forward or reverse transformation is provided. If the total strain tensor $\boldsymbol{\varepsilon}$ and temperature T are prescribed during the transformation, it is desired to find the stress tensor $\boldsymbol{\sigma}$ and martensitic fraction γ .

Due to the symmetry of the tensorial stress-strain relation given in Table 3-1, it can be rewritten using the matrix notations as:

$$\{\boldsymbol{\varepsilon}\} = [D(\gamma)]\{\boldsymbol{\sigma}\} + \frac{3}{2}\Delta\varepsilon_t\gamma\frac{1}{\bar{\sigma}}\{S\} \quad (\text{D-1})$$

where,

$$\{\boldsymbol{\varepsilon}\} = \begin{Bmatrix} \varepsilon_{11} \\ \varepsilon_{22} \\ \varepsilon_{33} \\ \gamma_{23} \\ \gamma_{13} \\ \gamma_{12} \end{Bmatrix}; \quad \{\boldsymbol{\sigma}\} = \begin{Bmatrix} \sigma_{11} \\ \sigma_{22} \\ \sigma_{33} \\ \sigma_{23} \\ \sigma_{13} \\ \sigma_{12} \end{Bmatrix}; \quad \{S\} = \begin{Bmatrix} S_{11} \\ S_{22} \\ S_{33} \\ 2S_{23} \\ 2S_{13} \\ 2S_{12} \end{Bmatrix} \quad (\text{D-2})$$

and,

$$[D(\gamma)] = \gamma[D^{(M)}] + (1-\gamma)[D^{(A)}] \quad (\text{D-3})$$

where,

$$[D^{(A)}] = \begin{bmatrix} \frac{1}{E_A} & \frac{\nu_A}{E_A} & \frac{\nu_A}{E_A} & 0 & 0 & 0 \\ \frac{\nu_A}{E_A} & \frac{1}{E_A} & \frac{\nu_A}{E_A} & 0 & 0 & 0 \\ \frac{\nu_A}{E_A} & \frac{\nu_A}{E_A} & \frac{1}{E_A} & 0 & 0 & 0 \\ 0 & 0 & 0 & \frac{2(1+\nu_A)}{E_A} & 0 & 0 \\ 0 & 0 & 0 & 0 & \frac{2(1+\nu_A)}{E_A} & 0 \\ 0 & 0 & 0 & 0 & 0 & \frac{2(1+\nu_A)}{E_A} \end{bmatrix} \quad (D-4)$$

and,

$$[D^{(M)}] = \begin{bmatrix} \frac{1}{E_M} & \frac{\nu_M}{E_M} & \frac{\nu_M}{E_M} & 0 & 0 & 0 \\ \frac{\nu_M}{E_M} & \frac{1}{E_M} & \frac{\nu_M}{E_M} & 0 & 0 & 0 \\ \frac{\nu_M}{E_M} & \frac{\nu_M}{E_M} & \frac{1}{E_M} & 0 & 0 & 0 \\ 0 & 0 & 0 & \frac{2(1+\nu_M)}{E_M} & 0 & 0 \\ 0 & 0 & 0 & 0 & \frac{2(1+\nu_M)}{E_M} & 0 \\ 0 & 0 & 0 & 0 & 0 & \frac{2(1+\nu_M)}{E_M} \end{bmatrix} \quad (D-5)$$

If elastic deformation and reorientation are the only mechanisms of deformation (i.e., $d\gamma = 0$), Newton-Raphson or other iterative methods can be used to solve equation (D-1). When simultaneous elastic deformation, reorientation, and transformation take place, the additional kinetic relation is given by:

$$\bar{\sigma} = Y(\gamma) \quad (D-6)$$

where,

$$Y(\gamma) = \begin{cases} (1-\gamma)\sigma_{MN}(T) + \gamma\sigma_{MC}(T) & \text{Forward transformation} \\ \gamma\sigma_{AN}(T) + (1-\gamma)\sigma_{AC}(T) & \text{Reverse transformation} \end{cases} \quad (D-7)$$

Using (D-6), equation (D-1) can be rewritten in the following form:

$$\{\varepsilon\} = [\hat{D}(\gamma)]\{\sigma\} \quad (\text{D-8})$$

where,

$$[\hat{D}(\gamma)] = [D(\gamma)] + \frac{\Delta\varepsilon_t \gamma}{Y(\gamma)} \begin{bmatrix} 1 & -\frac{1}{2} & -\frac{1}{2} & 0 & 0 & 0 \\ -\frac{1}{2} & 1 & -\frac{1}{2} & 0 & 0 & 0 \\ -\frac{1}{2} & -\frac{1}{2} & 1 & 0 & 0 & 0 \\ 0 & 0 & 0 & 3 & 0 & 0 \\ 0 & 0 & 0 & 0 & 3 & 0 \\ 0 & 0 & 0 & 0 & 0 & 3 \end{bmatrix} \quad (\text{D-9})$$

From (B86) and (D-9) σ can be expressed in terms of ε and γ as:

$$\{\sigma\} = [\hat{D}(\gamma)]^{-1} \{\varepsilon\} \quad (\text{D-10})$$

Substitution of (D-10) back in (D-6) gives an algebraic equation in terms of γ as:

$$f(\gamma) = \bar{\sigma}(\gamma) - Y(\gamma) = 0 \quad (\text{D-11})$$

Newton-Raphson iterative scheme can be utilized to numerically solve the above equation for γ . That is,

$$\begin{cases} \delta\gamma^{(i+1)} = -\frac{f^{(i)}}{\left(\frac{df}{d\gamma}\right)^{(i)}} \\ \gamma^{(i+1)} = \gamma^{(i)} + \delta\gamma^{(i+1)} \end{cases} \quad (\text{D-12})$$

The derivative of the function f with respect to γ needs to be calculated in each iteration.

From equation (D-11) it is obtained that,

$$\frac{df}{d\gamma} = \left\{ \frac{\partial \bar{\sigma}}{\partial \sigma} \right\}^T \left\{ \frac{d\sigma}{d\gamma} \right\} - \frac{d}{d\gamma} Y(\gamma) \quad (\text{D-13})$$

where,

$$\left\{ \frac{\partial \bar{\sigma}}{\partial \sigma} \right\} = \frac{3}{2\bar{\sigma}} \{S\} \quad (\text{D-14})$$

and from (D-10),

$$\left\{ \frac{d\sigma}{d\gamma} \right\} = \frac{d}{d\gamma} \left([\hat{D}(\gamma)]^{-1} \right) \{\varepsilon\} \quad (\text{D-15})$$

Next, it is noticed that,

$$[\hat{D}(\gamma)]^{-1} [\hat{D}(\gamma)] = [I] \quad (\text{D-16})$$

where $[I]$ is the identity matrix. Differentiation the above equation and using (D-3) give:

$$\frac{d}{d\gamma} \left([\hat{D}(\gamma)]^{-1} \right) = -[\hat{D}(\gamma)]^{-1} \frac{d}{d\gamma} \left([\hat{D}(\gamma)] \right) [\hat{D}(\gamma)]^{-1} \quad (\text{D-17})$$

From equation (D-3) and (D-9) it can be shown that,

$$\frac{d}{d\gamma} \left([\hat{D}(\gamma)] \right) = [D^{(M)}] - [D^{(A)}] + \frac{\Delta \varepsilon_t \gamma}{Y(\gamma)^2} \left(Y(\gamma) - \gamma \frac{d}{d\gamma} Y(\gamma) \right) \begin{bmatrix} 1 & -\frac{1}{2} & -\frac{1}{2} & 0 & 0 & 0 \\ -\frac{1}{2} & 1 & -\frac{1}{2} & 0 & 0 & 0 \\ -\frac{1}{2} & -\frac{1}{2} & 1 & 0 & 0 & 0 \\ 0 & 0 & 0 & 3 & 0 & 0 \\ 0 & 0 & 0 & 0 & 3 & 0 \\ 0 & 0 & 0 & 0 & 0 & 3 \end{bmatrix} \quad (\text{D-18})$$

Using equation (D-13) through (D-17) the value of $df/d\gamma$ is finally obtained as,

$$\frac{df}{d\gamma} = -\frac{3}{2} \frac{1}{\bar{\sigma}} \{S\}^T [\hat{D}(\gamma)]^{-1} \frac{d}{d\gamma} \left([\hat{D}(\gamma)] \right) \{\sigma\} - \frac{d}{d\gamma} Y(\gamma) \quad (\text{D-19})$$

The values of γ that is obtained from the iterations in (D-12) can be inserted in equation (D-10) to find the stress vector $\{\sigma\}$.

Appendix E. An Incremental Three-Dimensional Constitutive Model

In this section, an incremental constitutive model for pseudoelastic response is described. The model is able to capture the recovery of transformation strain during reverse transformation for a material point. The incremental flow rules used in this model are in fact similar to those proposed earlier by Boyd and Lagoudas (1994a). The performance of this incremental constitutive model in simulating the unstable pseudoelastic response is examined in Section 3.4 using FEM.

E.1. GENERAL CONSIDERATIONS

The additive decomposition of strain, and elastic strain-stress relations are assumed to be the same as those in the total deformation constitutive model. Therefore,

$$\boldsymbol{\varepsilon}_{ij} = \boldsymbol{\varepsilon}_{ij}^{(e)} + \boldsymbol{\varepsilon}_{ij}^{(t)} \quad (\text{E-1})$$

where

$$\boldsymbol{\varepsilon}_{ij}^{(e)} = D_{ijkl}(\gamma) \boldsymbol{\sigma}_{kl} \quad (\text{E-2})$$

and

$$D_{ijkl}(\gamma) = \gamma D_{ijkl}^{(M)} + (1 - \gamma) D_{ijkl}^{(A)} \quad (\text{E-3})$$

E.2. FLOW RULE OF FORWARD TRANSFORMATION

The transformation strain during the forward transformation is calculated by utilizing the incremental flow rule of equation (3-3) as:

$$d\boldsymbol{\varepsilon}_{ij}^{(t)} = A \frac{\partial P_{A \rightarrow M}}{\partial \boldsymbol{\sigma}_{ij}} d\boldsymbol{\gamma} \quad (\text{E-4})$$

$P_{\Lambda \rightarrow M}$ is the transformation potential function during the forward transformation which needs to be determined. In order to find the corresponding proportionality factor A , it is assumed that:

$$d\tilde{\varepsilon}^{(t)} = \Delta\varepsilon_t d\gamma \quad (E-5)$$

where $\tilde{\varepsilon}^{(t)}$ is an effective transformation strain defined by the following incremental relation,

$$d\tilde{\varepsilon}^{(t)} = \sqrt{\frac{2}{3}} d\varepsilon_{ij}^{(t)} d\varepsilon_{ij}^{(t)} \quad (E-6)$$

It is seen from equation (E-6) that the value of $\tilde{\varepsilon}^{(t)}$ is dependent on the deformation history. Therefore, $\tilde{\varepsilon}^{(t)}$ is referred to as the *path-dependent effective transformation strain* throughout this text to distinguish it from the effective transformation strain defined in equation (3-12).

The parameter $\Delta\varepsilon_t$ has the same meaning as in the total deformation constitutive model in Chapter 3. Substituting equation (E-4) in (E-6) and the subsequent result in (E-5) give the proportionality factor as:

$$A = \frac{\Delta\varepsilon_t}{\sqrt{\frac{2}{3} \frac{\partial P_{\Lambda \rightarrow M}}{\partial \sigma_{ij}} \frac{\partial P_{\Lambda \rightarrow M}}{\partial \sigma_{ij}}}} \quad (E-7)$$

Therefore, the transformation strain is given by:

$$d\varepsilon_{ij}^{(t)} = \frac{\Delta\varepsilon_t}{\sqrt{\frac{2}{3} \frac{\partial P_{\Lambda \rightarrow M}}{\partial \sigma_{kl}} \frac{\partial P_{\Lambda \rightarrow M}}{\partial \sigma_{kl}}}} \frac{\partial P_{\Lambda \rightarrow M}}{\partial \sigma_{ij}} d\gamma \quad (E-8)$$

The forward transformation potential function ($P_{\Lambda \rightarrow M}$) is chosen to be the Von-Mises effective stress $\bar{\sigma}$ defined in equation (3-18). Therefore,

$$d\varepsilon_{ij}^{(t)} = \frac{3}{2} \Delta\varepsilon_t \frac{S_{ij}}{\bar{\sigma}} d\gamma \quad (\text{E-9})$$

E.3. FLOW RULE OF REVERSE TRANSFORMATION

A similar general incremental flow rule is also used for the reverse transformation:

$$d\varepsilon_{ij}^{(t)} = A \frac{\partial P_{M \rightarrow A}}{\partial \sigma_{ij}} d\gamma \quad (\text{E-10})$$

For the transformation strain to be fully recovered upon the completion of reverse transformation (i.e., at $\gamma = 0$), the following conditions must hold,

$$\varepsilon_{ij}^{(t)} \Big|_{\gamma=0} = 0 \quad (\text{E-11})$$

To ensure the complete recovery of transformation strain, the effective transformation strain $\bar{\varepsilon}^{(t)}$ define in equation (3-12) is used during the reverse transformation. It is assumed to be proportional to the martensitic fraction according to,

$$\bar{\varepsilon}^{(t)} = \kappa \Delta\varepsilon_t \gamma \quad (\text{E-12})$$

where κ is a correction factor that accounts for the mismatch between the two effective transformation strain defined in equations (3-12) and (E-6) at the end of forward transformation. That is,

$$\kappa = \frac{\tilde{\varepsilon}^{(t)}}{\bar{\varepsilon}^{(t)}} \Big|_{\text{end of forward transformation}} \quad (\text{E-13})$$

By looking at equations (E-12) and (3-12) it can be easily verified that if $\gamma = 0$ the components of transformation strain tensor ($\varepsilon_{ij}^{(t)}$'s) must also be equal to zero which satisfies the condition in equation (E-11).

Differentiating equations (3-12) and (E-12) gives:

$$d\bar{\varepsilon}^{(t)} = \frac{2}{3} \frac{\varepsilon_{ij}^{(t)} d\varepsilon_{ij}^{(t)}}{\bar{\varepsilon}^{(t)}} = \kappa \Delta\varepsilon_t d\gamma \quad (\text{E-14})$$

Substituting (E-10) into above relation gives the proportionality factor A to be,

$$A = \frac{\kappa \Delta\varepsilon_t \bar{\varepsilon}^{(t)}}{\frac{2}{3} \frac{\partial P_{M \rightarrow A}}{\partial \sigma_{ij}} \varepsilon_{ij}^{(t)}} \quad (\text{E-15})$$

Based on the equations (E-10) through (E-15), the transformation strain should be recoverable along any integration path and for any transformation potential function $P_{M \rightarrow A}$. However, if the transformation strain tensor $\varepsilon^{(t)}$ is normal to the gradient of the potential function $\frac{\partial P_{M \rightarrow A}}{\partial \sigma}$, the denominator on the right hand side of equation (E-15) vanished and the proportionality factor A loses its finiteness. To avoid this situation, it is assumed that the gradient of the potential function is always in the same direction as the transformation strain. That is,

$$\frac{\partial P_{M \rightarrow A}}{\partial \sigma_{ij}} = \varepsilon_{ij}^{(t)} \quad (\text{E-16})$$

or,

$$P_{M \rightarrow A} = \sigma_{ij} \varepsilon_{ij}^{(t)} \quad (\text{E-17})$$

Substituting (E-16) into (E-15) and using (3-18) yields:

$$A = \frac{\kappa \Delta\varepsilon_t}{\bar{\varepsilon}^{(t)}} \quad (\text{E-18})$$

Therefore, from equations (3-22), (3-24) and (3-15) the final form of the reverse transformation flow rule is obtained as,

$$d \varepsilon_{ij}^{(t)} = \kappa \Delta \varepsilon_t \frac{\varepsilon_{ij}^{(t)}}{\varepsilon^{(t)}} d \gamma \quad (\text{E-19})$$

The above flow rule is in fact very similar to the one proposed by Boyd and Lagoudas (1994a) to describe the reverse transformation except for the correction factor κ which does not appear in their model (see equation 1-4). Using equation (E-14), the flow rule of reverse transformation can be rewritten in the following form:

$$d \varepsilon_{ij}^{(t)} = \frac{\varepsilon_{ij}^{(t)}}{\gamma} d \gamma \quad (\text{E-20})$$

Notice that the parameter κ does not appear in the latter form of the flow rule. Equations (E-19) and (E-20) imply that the orientation of the transformation strain tensor does not change during the course of reverse transformation, and only the magnitude of its components are proportionally reduced to zero.

E.4. KINETICS OF TRANSFORMATION

The kinetics of transformation are assumed to be the as those described for the total deformation model in Chapter 3. In summary,

$$\begin{cases} dF_{M \rightarrow A}(\sigma_{ij}, \gamma, T) = 0, & \text{Forward transformation (d } \gamma > 0) \\ dF_{A \rightarrow M}(\sigma_{ij}, \gamma, T) = 0, & \text{Reverse transformation (d } \gamma < 0) \end{cases} \quad (\text{E-21})$$

where,

$$\begin{aligned} F_{A \rightarrow M} &= \bar{\sigma} - [(1 - \gamma) \sigma_{MN}(T) + \gamma \sigma_{MC}(T)] \\ F_{M \rightarrow A} &= \bar{\sigma} - [\gamma \sigma_{AN}(T) + (1 - \gamma) \sigma_{AC}(T)] \end{aligned} \quad (\text{E-22})$$

A simplified summary of the constitutive equations and kinetic relations based on the above assumption is given in Table E-1.

Table E-1. Summary of the incremental constitutive model.

Constitutive Relations	
Forward transformation:	$d\varepsilon_{ij} = D_{ijkl}(\gamma)d\sigma_{kl} + \left\{ (D_{ijkl}^{(M)} - D_{ijkl}^{(A)})\sigma_{kl} + \frac{3}{2}\Delta\varepsilon_t \frac{S_{ij}}{\bar{\sigma}} \right\} d\gamma$
Reverse transformation:	$d\varepsilon_{ij} = D_{ijkl}(\gamma)d\sigma_{kl} + \left\{ (D_{ijkl}^{(M)} - D_{ijkl}^{(A)})\sigma_{kl} + \frac{\varepsilon_{ij}}{\gamma} \right\} d\gamma$
Kinetic Relations	
Forward transformation:	$dF_{A \rightarrow M} = 0 \Rightarrow \frac{3}{2} \frac{S_{ij}}{\bar{\sigma}} d\sigma_{ij} - [(1-\gamma)\sigma'_{MN}(T) + \gamma\sigma'_{MC}(T)]dT - [\sigma_{MC}(T) - \sigma_{MN}(T)]d\gamma = 0$
Reverse transformation:	$dF_{M \rightarrow A} = 0 \Rightarrow \frac{3}{2} \frac{S_{ij}}{\bar{\sigma}} d\sigma_{ij} - [\gamma\sigma'_{AN}(T) + (1-\gamma)\sigma'_{AC}(T)]dT - [\sigma_{AN}(T) - \sigma_{AC}(T)]d\gamma = 0$

Appendix F. Convergence Study of the Finite Element Solution

A mesh-sensitivity study was conducted to examine the convergence of the FEM analysis with respect to the number of elements. A simulation of the short NiTi strip described in Section 3.4.1 was repeated for three different densities of mesh (35×10, 70×20, 105×30). Selected simulation results at different instants during loading are shown in Figure F-1.

Similar results were observed for the nucleation event, and propagation of the transformation front during forward transformation up to $\delta/L = 1.6\%$ for all these cases. However, above this strain some *minor* mesh sensitivity was observed due to the softening behavior embedded in the kinetics of transformation. As stated by Shaw & Kyriakides (1998), the recovery of material stability at the end of the phase transformation has an overall stabilizing effect on the solution, since the localized deformation is eventually arrested. Therefore, the mesh sensitivity has a minor effect on the shape of the propagating transformation front at particular loading/unloading stages (beyond $\delta/L = 1.6\%$). However, the force-displacement response and the overall features of the transformation fronts during forward or reverse transformation were hardly affected by the mesh size.

The CPU times of FE calculations up to an elongation of $\delta/L = 4\%$ for various mesh densities are provided in Table F-1. From the convergence study it was concluded that a mesh density of 70×20 is able to capture all important features with satisfactory convergence and time efficiency.

Table F-1. Approximate CPU times for various mesh densities.

Mesh density	CPU time (loading to $\delta/L = 4\%$)
35×10	4.86 (hrs)
70×20	54.80 (hrs)
105×30	242.18 (hrs)

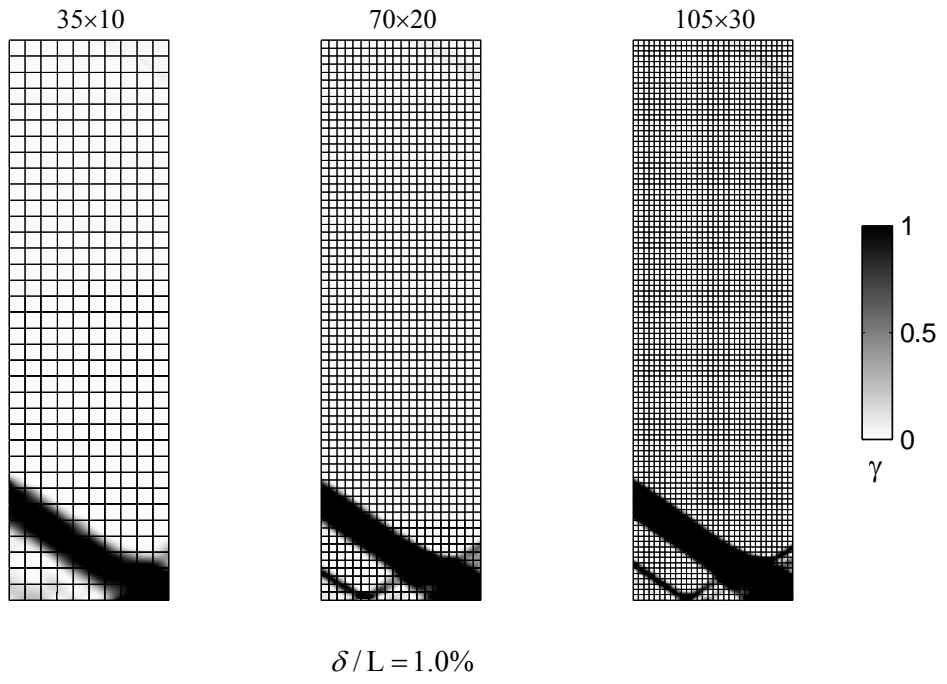
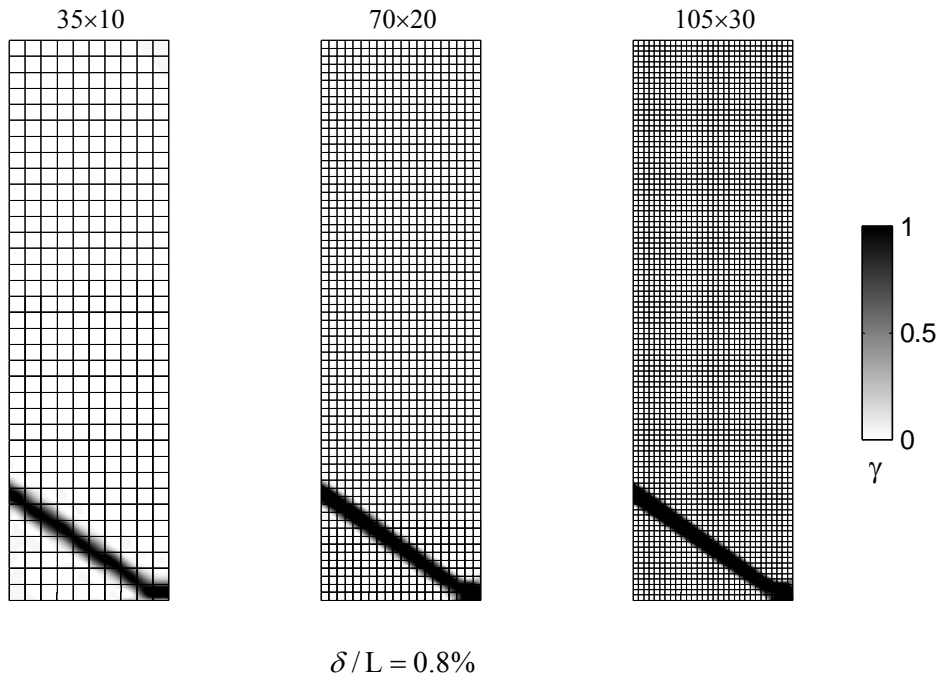
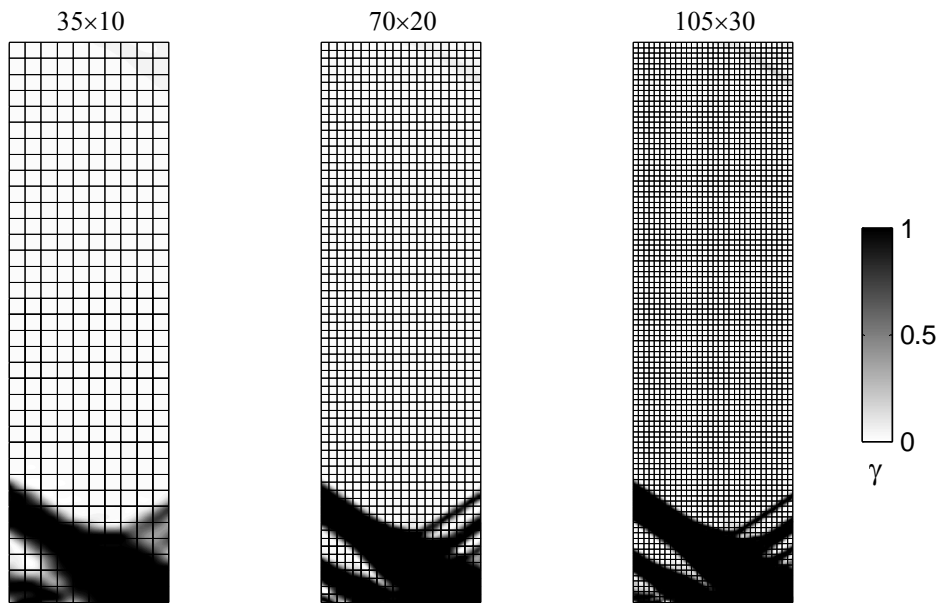
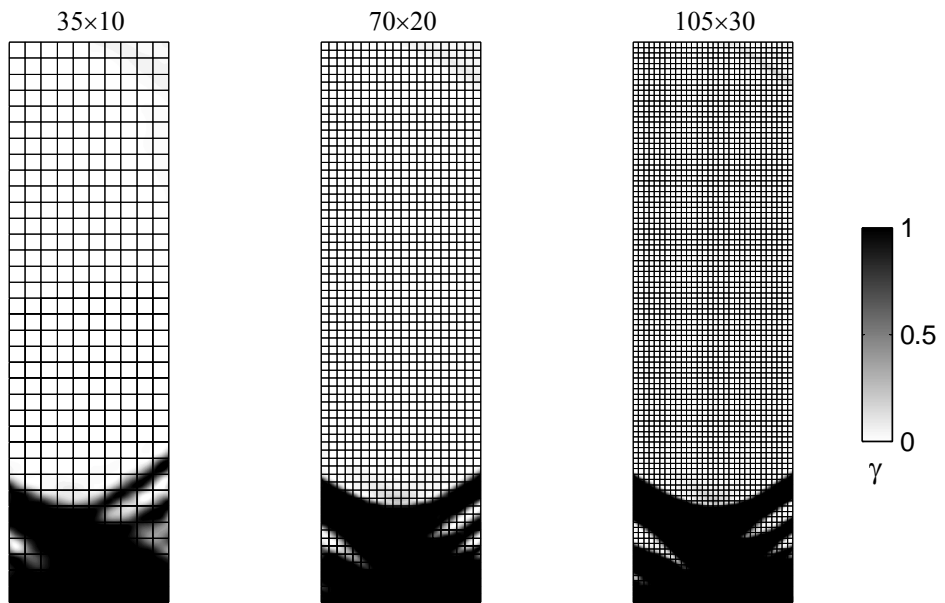


Figure F-1. Distribution of martensitic fraction at selected loading stages.



$\delta/L = 1.2\%$



$\delta/L = 1.4\%$

Figure F-1. (Continued).

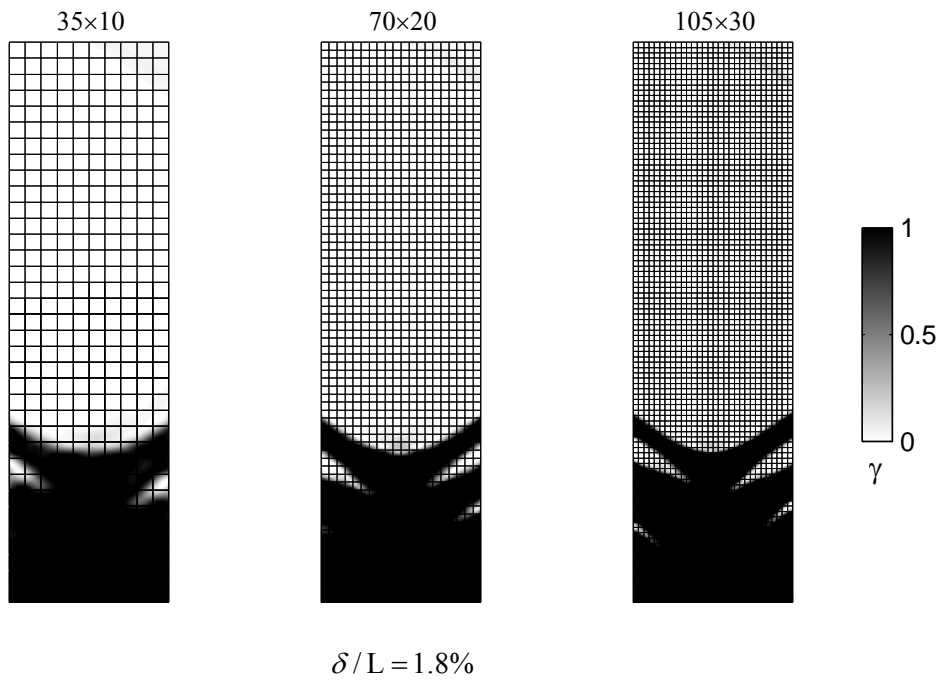
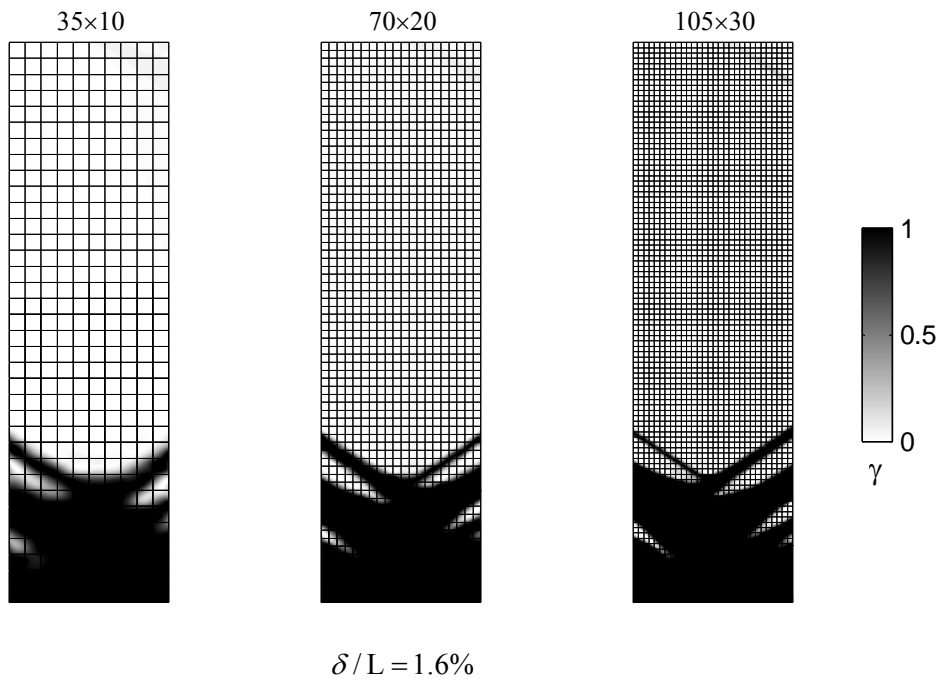
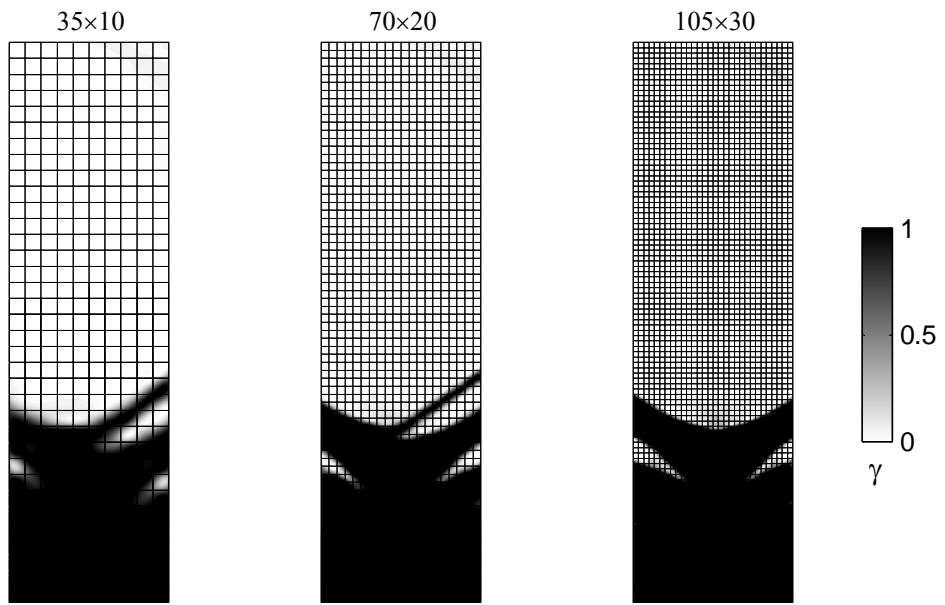
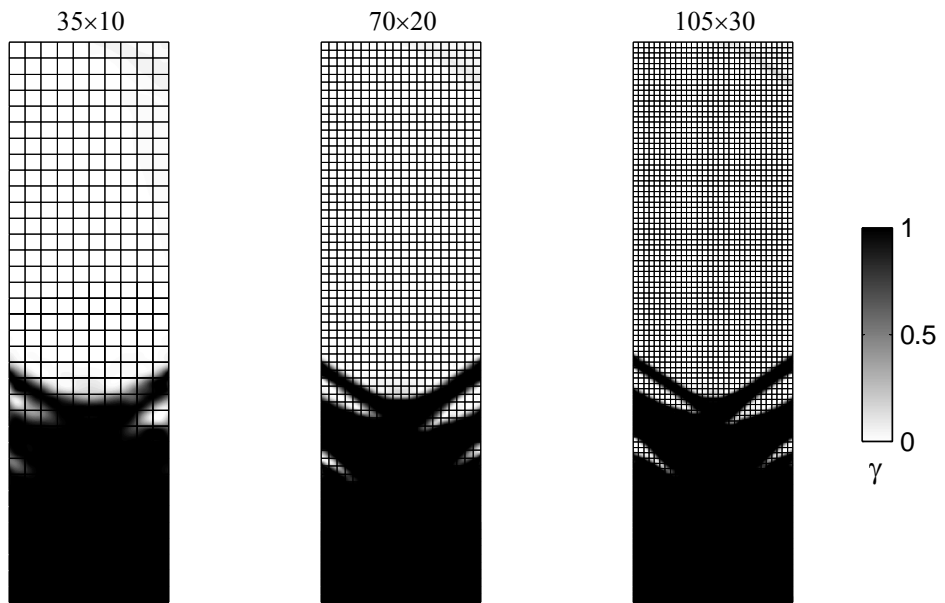


Figure F-1. (Continued).



$\delta/L = 2.0\%$



$\delta/L = 2.2\%$

Figure F-1. (Continued).